Interférométrie X à réseaux pour l'imagerie et l'analyse de front d'ondes au synchrotron

Irène Zanette

UNIVERSITÉ DE GRENOBLE

THÈSE

Pour obtenir le grade de

DOCTEUR DE L'UNIVERSITÉ DE GRENOBLE

Spécialité : **Physique de la Matière Condensée et du Rayonnement**

Arrêté ministérial : 7 août 2006

Présentée par

Irene ZANETTE

Thèse dirigée par **Dr. José BARUCHEL**
et codirigée par **Dr. Timm WEITKAMP**

préparée au sein du **European Synchrotron Radiation Facility**
dans l' **École Doctorale de Physique**

Interférométrie X à réseaux pour l'imagerie et l'analyse de front d'ondes au synchrotron

Thèse soutenue publiquement le **16 Décembre 2011**,
devant le jury composé de :

Prof. Dr. Serge PÉREZ
European Synchrotron Radiation Facility, Grenoble, France, Président
Prof. Dr. Atshushi MOMOSE
University of Tokyo, Kashiwanoha, Japan, Rapporteur
Dr. François POLACK
Synchtoron Soleil, Gif-sur-Yvette, France, Rapporteur
Prof. Dr. Franz PFEIFFER
Technische Universität München, Munich, Germany, Examinateur
Dr. José BARUCHEL
European Synchrotron Radiation Facility, Grenoble, France, Directeur de thèse
Dr. Timm WEITKAMP
Synchtoron Soleil, Gif-sur-Yvette, France, Co-Directeur de thèse

Misura ciò che è misurabile, e rendi misurabile ciò che non lo è.

[Measure what is measurable, and make measurable what is not so.]

G. Galilei

Ce qui importe c'est la cohérence.

[What matters is coherence.]

A. Camus

Abstract

This thesis in on X-ray grating interferometry: an imaging technique demonstrated a few years ago which yields high-sensitivity phase and dark-field images of the investigated specimen and bears tremendous potential for visualization of features producing low absorption contrast. During this thesis, a grating interferometer has been installed at the beamline ID19 of the European Synchrotron Radiation Facility in Grenoble, France, where its excellent performance has been demonstrated on a large variety of soft-tissue biological samples. Moreover, the imaging technique itself has been significantly improved with the demonstration of advanced schemes for grating-based tomography which allow to substantially reduce the dose delivered to the sample, and with the development of a two-dimensional interferometer which gives image signals in multiple directions of the image plane.

Table of Contents

Chapter 1
Introduction

Since the discovery of X rays by W. C. Röntgen in 1895, their property to penetrate opaque matter has been used to take images of inner structures in objects with important application in medical diagnostics, non-destructive testing, security screening and many other fields.

Conventional X-ray absorption imaging consists in illuminating the investigated object with X rays and in measuring, with an area detector placed close behind the object, the two-dimensional profile of the intensity transmitted by the sample. At a given X-ray photon energy, the absorption depends on the density and the elemental composition of the features in the object: features with high density differences produce in general high X-ray absorption contrast. Since the first radiographs in history, bones, which contain calcium (an element with a high atomic number compared to soft tissue), can be clearly distinguished from the surrounding soft tissue whose density is very similar to that of water. However, despite more than a century of advances in X-ray imaging systems and several decades of existence and evolution of digital image processing, absorption contrast may still be insufficient to distinguish different types of soft tissue which have very similar densities. This is, for example, the case of pathological tissue in mammography.

Contrast by details with similar densities has been significantly improved with the development of *X-ray phase-contrast imaging techniques* which use the *phase* of the transmitted X-ray wave for generating contrast. In the X-ray energy range used for imaging, phase contrast can be much higher than absorption contrast because the phase-shift cross section is up to three orders of magnitude larger than the absorption cross section. Exploiting this fact, several phase-sensitive imaging techniques have been developed in the last two decades. The techniques differ in the mechanisms used to transform the phase shift produced by the object into an intensity modulation that can be revealed by the detector.

The most recently developed of these techniques is *X-ray grating interferometry*, which is the subject of this PhD thesis. In its standard implementation, an X-ray grating interferometer consists of two line gratings placed at a distance of several centimetres in the X-ray path between the sample and the detector. The first grating introduces a periodic modulation in the incoming wavefront and generates a periodic intensity pattern at particular distances along the optical axis. This intensity pattern is modified by the presence of the sample and is analyzed by the second grating. The analysis of the intensity pattern yields high-sensitivity differential phase images of the specimen; in these images the signal is proportional to the angle at which X rays are refracted in the direction perpendicular to the grating lines. Moreover, as discovered a few years ago, scattering (or 'dark-field') images of the investigated object can also be retrieved from the analysis of the same intensity pattern. It has since been demonstrated that phase-contrast and dark-field images provided by the X-ray grating interferometer allow the visualization of object features which can not be accessed with conventional absorption contrast.

Unlike other phase-sensitive imaging techniques, X-ray grating interferometry has been proved to work well also at laboratory X-ray generators, which raises hopes for its future implementation in clinical practice. Unique possibilities for the exploitation of this new technique can be found at synchrotron beamlines which provide a large X-ray beam with high spatial coherence and high photon flux.

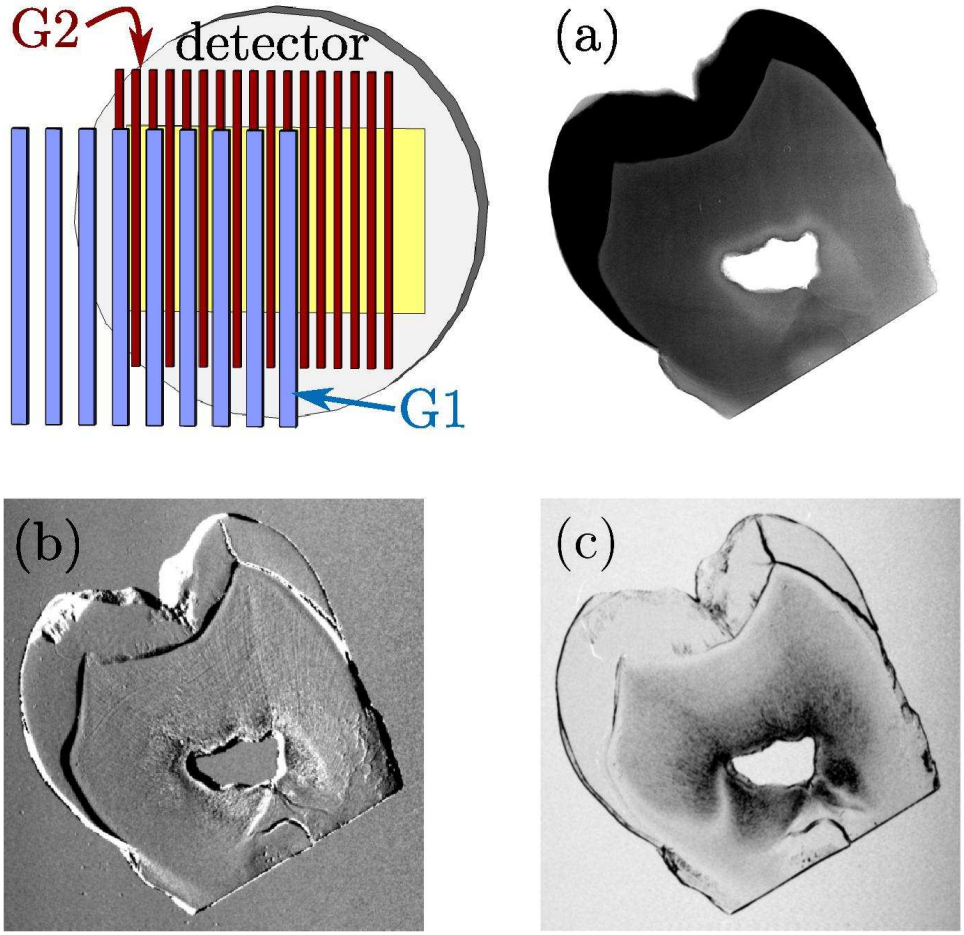

Figure 1.1: Top-left: Schematic representation of an X-ray grating interferometer. G1 and G2 are the two gratings forming the interferometer. Absorption (a), differential phase (b) and dark-field (c) images of a slice of a human tooth measured with the grating interferometer at ID19.

During this PhD thesis an X-ray grating interferometer has been installed, characterized and made available to users at the beamline ID19 of the European Synchrotron Radiation Facility in Grenoble, France. In the past two years, this instrument has been employed to produce high-sensitivity phase-contrast images of soft-tissue biological samples and directional dark-field images of flat specimens.

This thesis is structured as follows. After this introduction, Chapter 2 outlines the fundamentals of X-ray imaging and give an overview of the most common phase-contrast imaging techniques.

Chapters 3-5 describe of the principles of X-ray grating interferometry and grating-based tomography.

Chapter 6 gives a review of recent developments in grating interferometry. These include works by other groups as well as improvements to which the author of this thesis has contributed significantly but not in the leading role. These results have been obtained not only with the device installed at ID19, but also with a laboratory X-ray generator.

Chapter 7 is devoted to instrumentation. It describes the characteristics of the device installed at ID19 with technical details of the interferometer and the procedure commonly used to align the instrument. The last sections of this chapter give information on the data acquisition and analysis systems currently in use.

The main contributions of this PhD project are presented in Chapters 8-11. The principal section of each chapter consists in one or more publication(s) in peer-reviewed journals in which the author of this thesis is the leading author. Other sections, when present, give complementary information or report recent developments, inherent to the topic of the chapter, and not yet published elsewhere.

Chapter 8 reports on the characterization of the X-ray grating interferometer at ID19 through measurements of absorption and phase tomographies of a phantom sample made of known materials. A section of this chapter is dedicated to the description of the phase-wrapping phenomenon and to the analysis, with both experimental results and numerical simulations, of its effects on phase tomography.

Chapter 9 highlights the potential of X-ray grating interferometry in its main application area up to this day, i.e., phase tomographies of soft-tissue biological specimens. Two examples, phase tomographies of a human cerebellum and of the testis of a rat, are presented in this chapter. These results show that grating interferometry provides information which can not be accessed with any other non-destructive technique.

Chapter 10 presents new methods for acquiring and analyzing phase-stepping tomography scans. These methods can reduce the dose delivered to the sample and improve tomography reconstructions. The potential of the new phase-stepping tomography methods is demonstrated with numerical simulations and experimental data.

Chapter 11 reports on the design, implementation and characterization of a two-dimensional (2D) X-ray grating interferometer. This device uses 2D gratings instead of line gratings and, in this way, yields differential-phase and scattering contrast images along multiple directions instead of only along the direction perpendicular to the grating lines as in the standard device. The potential of the 2D grating interferometer for optics characterization and wavefront sensing is demonstrated in the last section of this chapter with a study on parabolic refractive lenses.

Conclusions and perspectives are discussed in Chapter 12.

Introduction en français

Depuis la découverte des rayons X par W. C. Röntgen en 1895, leur propriété de pénétrer la matière opaque a été utilisée pour produire des images de la structure interne de divers objets, avec des applications importantes pour les diagnostics médicaux, les essais non destructifs, la sécurité et de nombreux autres domaines. L'imagerie conventionnelle d'absorption par rayons X consiste à irradier l'échantillon avec des rayons X et de mesurer, à l'aide d'un détecteur bidimensionnel placé juste derrière l'objet, le profil de l'intensité transmise par l'échantillon. L'absorption des photons dépend de la densité et de la composition élémentaire de l'objet: les structures avec des grandes différences en densité produisent en général un fort contraste en absorption aux rayons X.

La premiére radiographie de l'histoire montrait les os de la main. Cette observation est associèe à leur contenu en calcium, un élément avec un numéro atomique élevé par rapport aux tissus mous environnants dont la densité est très similaire à celle de l'eau et dont les éléments constitutifs ont des numéros atomiques beaucoup plus faibles. Cependant, en dépit d'un siècle de recherche dans le domaine et plusieurs décennies de progrès en ce qui concerne le traitement d'images numériques, le contraste d'absorption reste encore insuffisant pour distinguer les différents types de tissus mous, qui ont des propriétés d'absorption très similaires. C'est, par exemple, le cas des tissus pathologiques en mammographie.

Le contraste pour des détails de densité similaire s'est nettement amélioré avec le développement des techniques d'imagerie à rayons X à contraste de phase qui utilisent la phase du faisceau transmis par les rayons X pour produire un contraste. Dans la gamme d'énergies des rayons X utilisée pour l'imagerie, le contraste de phase peut être beaucoup plus important que le contraste d'absorption, car la section efficace associée à la phase est jusqu'à trois ordres de grandeur plus élevée que celle associée à l'absorption. Plusieurs techniques d'imagerie sensibles à la phase ont été développées dans les deux derniéres décennies en exploitant cette caractéristique. Les techniques se différencient par les mécanismes utilisés pour transformer la variation de phase produite par la traversée de l'objet en une modulation d'intensité qui peut être mise en évidence par le détecteur.

Parmi ces techniques, la plus récemment développée est l'interférométrie X à réseaux. Cette derniére fait l'objet de cette thèse. Dans son implantation standard, un interféromètre X à réseaux est constitué de deux grilles placées à une distance de plusieurs centimètres de l'échantillon. La premiére grille introduit une modulation périodique dans le front d'onde entrant et génère une modulation d'intensité périodique à des distances particulières (dites 'distances de Talbot') le long de l'axe optique. Ce profil d'intensité est modifié par la présence de l'échantillon, et est analysé par la deuxiéme grille. L'analyse de la modulation du diagramme d'intensité conduit à des images de phase différentielles de l'échantillon, de haute sensibilité, dans laquelle le signal est proportionnel à l'angle de réfraction. Par ailleurs, comme cela a déjà été mis en évidence, les images de diffusion (ou 'dark-field'*) de l'objet peuvent également être extraites de l'analyse du même diagramme d'intensité. Nous avons, de plus, montré que les images en contraste de phase et les images de diffusion fournies par l'interféromètre X à réseaux permettent la visualisation d'aspects de l'objet qui ne peuvent être obtenus avec un contraste d'absorption conventionnel.*

Contrairement aux autres techniques d'imagerie de phase, l'interférométrie X à réseaux

a aussi donné de bons résultats avec des générateurs de rayons X de laboratoire, ce qui donne des espoirs pour sa future application dans la pratique clinique. D'un autre côté, les synchrotrons qui fournissent un large faisceau de rayons X avec une haute cohérence spatiale et un flux de photons élevé offrent des possibilités uniques pour l'exploitation de cette nouvelle technique.

Pendant les travaux menant à cette thèse, un interféromètre X à réseaux a été installé, caractérisé et mis à la disposition des utilisateurs sur la ligne de lumiére ID19 du European Synchrotron Radiation Facility à Grenoble, France. Au cours des deux dernières années, cet instrument a été employé pour produire des images en contraste de phase à haute sensibilité des tissus mous d'échantillons biologiques et d'images de diffusion directionnelle de spécimens plats.

Cette thèse est structurée comme suit. Après cette introduction, le Chapitre 2 expose les principes de l'imagerie par rayons X et donne un aperçu de la plupart des techniques d'imagerie sensibles à la phase.

Les chapitres 3-5 sont consacrés à la description des principes de l'interférométrie X à réseaux et la tomographie basée sur des grilles.

Le Chapitre 6 donne une revue des améliorations récentes de l'interférométrie à réseaux. Il s'agit notamment du travail produit par d'autres groupes, mais aussi des améliorations auxquelles l'auteur de cette thèse a contribué de manière significative. Ces résultats ont été obtenus non seulement avec l'appareil installé à ID19, mais aussi avec un générateur du rayons X de laboratoire.

Le Chapitre 7 est consacré à l'instrumentation. Il décrit les caractéristiques de l'interféromètre à réseaux installé à ID19 avec des détails sur les moteurs, les grilles, la procédure d'alignement ainsi que les systèmes d'acquisition et d'analyse de données actuellement en usage.

Les partie principale de cette thèse est présentée dans les chapitres 8-11. La section principale de chaque chapitre comprend une ou plusieurs publications dans des revues scientifiques, dans lesquelles l'auteur de cette thèse est l'auteur principal. D'autres sections, lorsqu'elles sont présentes, donnent des informations complémentaires ou incluent des développements récents, liés au sujet du chapitre, et qui n'ont pas encore été publiés.

Le Chapitre 8 donne la procédure et les résultats de la caractérisation de l'interféromètre X à réseaux sur ID19, au moyen de tomographies d'absorption et de phase sur un fantôme fait avec des matériaux connus. Une section de ce chapitre est consacrée à la description et l'analyse du phénomène de d'enroulement de phase ('phase wrapping'*) sur la tomographie de phase. Pour cela, des résultats expérimentaux et des simulations numériques sont utilisés.*

Le Chapitre 9 met en évidence les potentialités de l'interférométrie à réseaux dans son domaine d'application principal jusqu'à ce jour, c'est-à-dire, la tomographie de phase de tissus mous dans des spécimens biologiques. Pour illustrer ces potentialités, deux exemples sont présentés : la tomographie de phase d'un cervelet humain et d'un testicule de rat. Ces résultats montrent que l'interférométrie à réseaux fournit des informations qui ne peuvent être obtenues avec une autre technique non-destructive.

Le Chapitre 10 présente de nouvelles méthodes d'acquisition et d'analyse de tomographie en utilisant un nouveau mode de balayage, le interlaced phase stepping. *Cette nouvelle approche est susceptible de réduire la dose déposée dans l'échantillon et d'améliorer les re-*

constructions en tomographie locale. Le potentiel des nouvelles méthodes de tomographie en phase stepping *est démontré par des simulations numériques et par des données expérimentales.*

Le Chapitre 11 expose la conception, la mise en œuvre et la caractérisation d'un interféromètre X à réseaux à deux dimensions (2D). Cet appareil utilise des grilles 2D au lieu de grilles linéaires. De cette façon, les contrastes de phase différentiels et de diffusion sont obtenus sur des directions multiples (et non seulement dans la direction perpendiculaire aux lignes du réseau comme dans le dispositif standard) sans déplacement de l'échantillon ou rotation du réseaux. La dernière section de ce chapitre présente des résultats de recherche sur des lentilles réfractives paraboliques, ceci montrant comment les interféromètres à réseaux 2D peuvent être utilisés pour la caractérisation optique et pour la détection de fronts d'ondes.

Les conclusions et perspectives sont données au chapitre 12.

Chapter 2
X-ray imaging

Contents

X-ray radiographic imaging consists in recording, in the near field, the intensity of an X-ray beam after it has propagated through an investigated object and, possibly, one or more X-ray optical elements. During the propagation through matter, X rays can be absorbed and/or scattered. Both effects can be used for generating contrast in the final X-ray image. However, while absorption has been used to generate image contrast in radiography since the discovery of X rays in 1895, scattering only started to be actually investigated for X-ray imaging one century later with the availability of third-generation coherent X-ray sources. These sources delivered, for the first time, beams with a substantial degree of transverse coherence.

Phase-contrast imaging has since been receiving great interest, especially for potential applications in the medical field and in materials science. In the past decades, several *phase-contrast imaging techniques* have been developed and demonstrated on soft-tissue biological specimens. Moreover, during the development of these techniques, it was noticed that some of these methods not only provide phase-contrast images but also dark-field maps of the sample.

This chapter presents the theory of X-ray interactions with matter and shows how they can be used for multimodal imaging. The last sections give an overview of the most common phase and dark-field X-ray imaging techniques.

2.1 X-ray interactions with matter

This section presents the fundamental aspects of the theory of X-ray interaction with matter that are needed to explain the principles of X-ray imaging. An exhaustive treatment of this topic can be found in several books, for example, in Refs. [Paganin 2006] and [Als-Nielsen & McMorrow 2010].

The interactions between X rays and matter depend on the properties of the radiation and the characteristics of the object. In the following, we assume that the X rays [1] are not polarized and we treat the case of a monochromatic plane wave with frequency ω.

Propagation of electromagnetic waves is in general described by Maxwell's equations. However, under the hypotheses above, and for the boundary conditions of X-ray imaging, Maxwell's equations can be reduced to simpler equations of the scalar wavefield $E(x, y, z)$ such as the Helmholtz equations.

In order to study interactions of X rays with matter, let us consider waves E_A and E_B shown in Fig. 2.1. Wave E_A travels in free space and wave E_B propagates through a homogeneous block of length L. While E_A remains unperturbed, wave E_B is modified during the passage through matter. In particular, the amplitude of E_B is reduced and the wavelength becomes larger. These changes can be described by the complex-valued refractive index $n_\omega(x, y, z)$:

$$n_\omega(x, y, z) = 1 - \delta_\omega(x, y, z) + i\beta_\omega(x, y, z) \ . \tag{2.1}$$

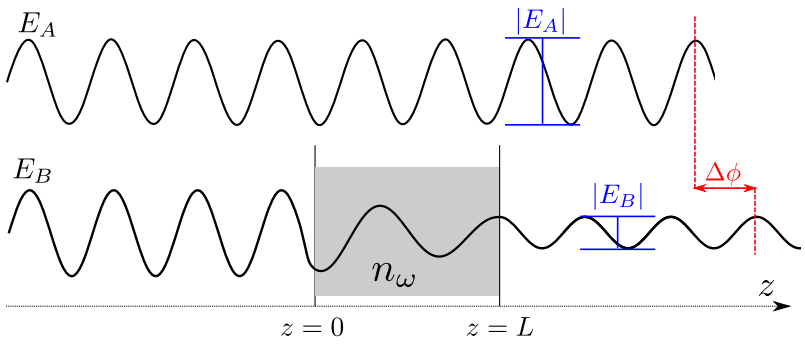

Figure 2.1: Waves E_A and E_B are part of a monochromatic plane wavefront. While E_A propagates in vacuum and remains unperturbed, wave E_B passes through a block of length L with refractive index $n_\omega(x, y, z)$. The amplitude and wavelength of E_B are modified during the passage through matter.

In Eq. (2.1), δ_ω and β_ω are real-valued quantities that depend on the material and on the frequency ω of the radiation. This definition of the refractive index implies that δ_ω, the decrement of the refractive index, is related to the phase-shift and β_ω, the imaginary part

[1] The theory can be extended to polychromatic beams by considering the polychromatic beam as superposition of monochromatic beams.

of the refractive index, is related to the attenuation of the X rays. The refractive index of vacuum is unity, i.e. $\delta_\omega = \beta_\omega = 0$.

If the wavefield $E_0(x, y, z)$ propagating along z impinges at $z = 0$ on a homogeneous object with refractive index $n_\omega(x, y, z)$ and length L, the wavefield inside and directly downstream of the object can be calculated with the following equation:

$$E(x, y, z) = E_0(x, y, 0)e^{ik\int_0^z n_\omega(x,y,z)dz} = E_0(x, y, 0)e^{ik\int_0^z [1-\delta_\omega(x,y,z)]dz}e^{-\int_0^z \beta_\omega(x,y,z)dz} \quad , \tag{2.2}$$

where k is the wave number $k = 2\pi/\lambda$ and λ is the wavelength of the radiation. The above equation holds for $0 \leqslant z \leqslant L$ assuming that the object is infinitely extended along x and y. The wavefield for $z > L$ is calculated with the formalism outlined in Sec. 3.1.

2.1.1 Attenuation

Attenuation of X rays is related to the loss in amplitude of the wave. The physical processes that cause attenuation are described in Sec. 2.2.

The intensity $I(x, y, z)$ of the beam is given by $I(x, y, z) = |E(x, y, z)|^2$ and the transmission $B(x, y, z)$ is

$$B(x, y, z) = \frac{I(x, y, z)}{I(x, y, 0)} = \frac{|E(x, y, z)|^2}{|E(x, y, 0)|^2} = e^{-2k\int \beta_\omega(x,y,z)dz} \quad . \tag{2.3}$$

The attenuation is $A(x, y, z) = 1 - B(x, y, z)$.

Equation 2.3 states the exponential dependence of the transmitted radiation from an object on the imaginary part of its refractive index integrated along the beam path. This equation can be written as the Lambert-Beer formula

$$B(x, y, z) = e^{-\int \mu_\omega(x,y,z)dz} \quad , \tag{2.4}$$

where the quantity $\mu_\omega(x, y, z)$,

$$\mu_\omega(x, y, z) = 2k\beta_\omega(x, y, z), \tag{2.5}$$

is the *linear attenuation coefficient*.

If the object is a block of homogeneous material with linear attenuation coefficient μ_ω and length L as the one represented in Fig. 2.1, the transmission is:

$$B(x, y, L) = e^{-\mu_\omega L} \quad . \tag{2.6}$$

2.1.2 Phase shift

The change in wavelength of the X rays inside the object is described by the decrement of the refractive index δ_ω and corresponds to a phase shift $\Delta\phi$ which X rays undergo while passing through matter. The phase shift is measured with respect to the X rays that did not pass through the object

$$\Delta\phi(x,y,z) = k\int \delta_\omega(x,y,z)dz \ . \tag{2.7}$$

The phase shift by a homogeneous block of thickness L (see Fig. 2.1) is

$$\Delta\phi(x,y,L) = k\delta_\omega L \ . \tag{2.8}$$

2.1.3 The transmission function

Equation (2.2) shows that the wavefield propagating through matter is obtained as a multiplication of the incident wavefield $E_0(x,y,0)$ with a function of the refractive index of the object. This function is the so-called *object transmission function* and will be indicated in the following with $\mathcal{T}(x,y)$. Using the transmission function $\mathcal{T}(x,y)$, Eq. (2.2) can be written as

$$E(x,y,z) = E_0(x,y,0)\mathcal{T}(x,y,z) \tag{2.9}$$

where, using the relations of Eqs. (2.4) and (2.7),

$$\mathcal{T}(x,y,z) = B(x,y,z)\exp[-i\Delta\phi(x,y,z)] \ . \tag{2.10}$$

2.1.4 From phase shift to refraction

In the previous sections, propagation of X rays in matter has been treated in the *projection approximation* which assumes that X rays change negligibly their propagation direction while passing through the object. In this approximation, X rays are assumed to propagate through matter along paths corresponding to those that would have existed if matter was replaced by vacuum.[2] Although the changes in propagation direction are usually very tiny (with respect to the size of the detector elements), the scattered X rays impinging on the detector provide the phase and dark-field image signals.

In this section we concentrate on the phenomenon of refraction. The refraction angle is the quantity directly measured by some phase-contrast imaging techniques, one of those is grating interferometry.

Let us consider a plane wave propagating along the z axis and impinging on a prism of homogeneous material and refractive index n_ω. Since absorption does not affect refraction, we can safely assume that the prism is a non-absorbing phase object but the results of our considerations will be valid for absorbing objects too. The refractive index of a phase object can be written as $n_\omega = 1-\delta_\omega$. Let θ, substantially smaller than unity, be the angle that the face PQ of the prism in Fig. 2.2 forms with the x axis. In the same figure, X rays impinging on the prism are represented with the waves A to E. These X rays undergo a different phase shift depending on the position along the x axis at which they imping on the prism. Since

[2] Any effect originated from structures in the object on length scales comparable to the wavelength of the of the X rays, e.g. diffraction on crystal lattices, but also fluorescence and inelastic scattering are neglected in the projection approximation.

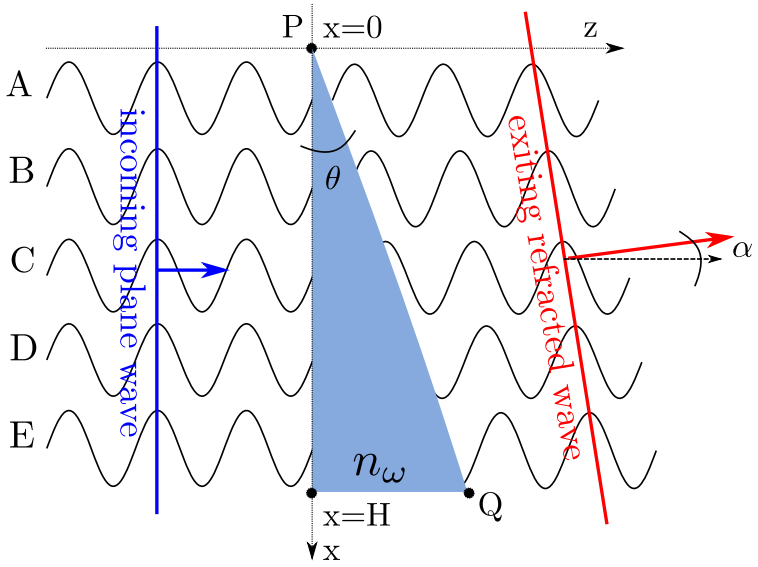

Figure 2.2: Schematic representation of the phenomenon of refraction by a prism. For more explanations, see text.

the phase shift increases with the thickness of the object (see Eq. (2.8)), X rays impinging on the prism at the bottom will undergo a larger phase shift than the X rays impinging on the prism at the top.

According to Eq. (2.8), the phase shift $\Delta\phi$ at which the X rays undergo is

$$\Delta\phi(x) = -k\delta_\omega t(x) = -k\delta_\omega x \tan(\theta) \quad \text{for } 0 \leqslant x \leqslant H \tag{2.11}$$

where $t(x) = x\tan(\theta)$ is the projected thickness of the prism.

Downstream of the prism, the lines connecting the crests of the phase-shifted waves form an angle α with the x axis. The vector orthogonal to this line (red bold arrow in Fig. 2.2) indicates the propagation direction of the X rays downstream the object. The angle at which X rays are refracted by the prism is equal to α.

The refraction angle α can be derived with geometrical considerations from Fig. 2.2, see for example Ref. [Paganin 2006]. With the approximation $\sin(\alpha) \approx \alpha$, the refraction angle is

$$\alpha \approx \theta\delta_\omega = \frac{2\pi}{\lambda}\frac{\partial\phi(x)}{\partial x} \quad . \tag{2.12}$$

More generally, if a plane wave propagates along the z axis through an object with refractive index $n_\omega(x,y,z)$ and $\phi(x,y)$ is the phase of the wavefront at the observation plane downstream the object, the refraction angles along x and y, $\alpha_x(x,y)$ and $\alpha_y(x,y)$ respectively, can be calculated as

$$\alpha_x(x,y) = \frac{2\pi}{\lambda}\frac{\partial\phi(x,y)}{\partial x} = \frac{\partial}{\partial x}\int \delta_\omega(x,y,z)dz \tag{2.13}$$

$$\alpha_y(x,y) = \frac{2\pi}{\lambda}\frac{\partial\phi(x,y)}{\partial y} = \frac{\partial}{\partial y}\int \delta_\omega(x,y,z)dz \quad . \tag{2.14}$$

2.2 Absorption versus phase shift

In the previous section we have related the absorption and phase shifting properties of the sample with its complex-valued refractive index. In this section, we discover the typical magnitudes of δ and β[3] for hard X rays in the energy range typically used in imaging (10-150 kev) and we relate these numbers with the absorption and phase signals in the radiographic images.

Let σ^a and σ^p be the atomic attenuation and phase-shift cross sections respectively. The imaginary and real parts of the refractive index can be expressed in terms of σ^a and σ^p as [Momose *et al.* 2009c]:

$$\beta = \frac{\lambda}{4\pi} \sum_l N_l \sigma_l^a \quad \text{and} \tag{2.15}$$

$$\delta = \frac{r_0 \lambda^2}{2\pi} \sum_l N_l (Z_l + f_l') = \frac{\lambda}{2\pi} \sum_l N_l \sigma_l^p \quad , \tag{2.16}$$

where $\sigma_l^p = r_0 \lambda (Z_l + f_l')$ and r_0 is the classical electron radius $r_0 = 2.82 \times 10^{-5}$Å. In the above equations N_l is the atomic number density, Z_l is the atomic number and f_l' is the real part of the anomalous atomic scattering cross section of the element l. The quantity f_l' is relevant only near to the absorption edges of the material. Far from the absorption edges, f_l' can be considered zero.

The attenuation cross section σ_l^a is given by the sum of the cross sections of three contributing processes:

1. the photoelectric effect (pure absorption);
2. Rayleigh (elastic) scattering;
3. Compton (inelastic) scattering:

$$\sigma_l^a = \sigma_l^{\text{photoelectric}} + \sigma_l^{\text{Rayleigh}} + \sigma_l^{\text{Compton}} \quad . \tag{2.17}$$

These processes are thoroughly described and their cross sections are calculated elsewhere, see for example Ref. [Als-Nielsen & McMorrow 2010]. For light materials such as water and at low photon energies below 30-50 keV, the photoelectric effect is the dominant process. For the same type of materials and above 50 keV, Compton scattering is the process with the largest cross section.

The photoelectric effect cross section has a strong dependency on both the energy E of the X-ray photons and atomic number Z_l of the material [Wang 2007]:

$$\sigma_l^{\text{photoelectric}} \propto \frac{Z_l^5}{E^{3.5}} \quad . \tag{2.18}$$

Far from the absorption edges, the phase-shift cross section increases linearly with the wavelength of the radiation and with Z_l (see Eq. (2.16)):

[3] In this section, in order to lighten notation, we eliminate the subscript ω from δ and β.

$$\sigma_l^p \propto \frac{Z_l}{E} \tag{2.19}$$

At the low photon energies used for imaging light materials, the cross section for the attenuation process, which is dominated by the photoelectric effect, drops down more rapidly with the energy than the phase-shift cross section (cf. Eq. (2.18) and (2.19)). This means that slightly increasing the X-ray energy significantly reduces the absorption in the sample without causing a dramatic reduction of phase contrast; this aspect makes phase-contrast methods attractive for imaging low-Z dose-sensitive samples.[4] Another advantage of phase-contrast imaging versus absorption-contrast imaging is the much larger cross section of the phase shift process respect to the attenuation process. This is discussed in more detail in the following.

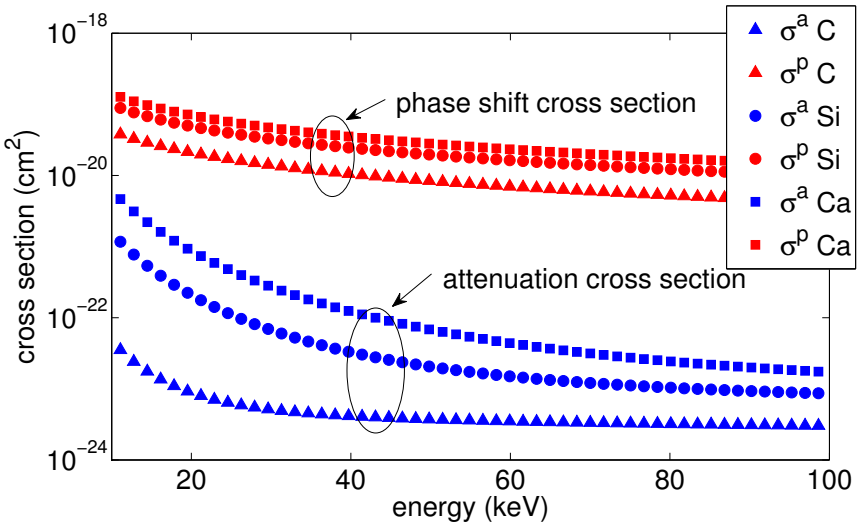

Figure 2.3: Phase and attenuation cross sections for three low-Z materials: C, Si and Ca calculated in the energy range 15-100 keV.

The theoretical values of the cross sections are usually obtained from tabulated values. Several databases are available for this purpose, most of them are included in the XOP software [Sanchez del Rio & Dejus 2004].

In order to estimate the difference in magnitude of the absorption and phase shift cross sections, we calculated, with XOP and the XCOM database, σ_l^a and σ_l^p for three different materials: carbon (Z=6), silicon (Z=14) and calcium (Z=20) over an energy range from 15 keV to 100 keV. The results are shown in Fig. 2.3. The values of σ_l^p exceed those of σ_l^a by two or three orders of magnitude. Thus, if the phase information is used to produce the image contrast, the image signal can be increased by up to a thousand times.

Values of β and δ, calculated, from the results plotted in Fig. 2.3, with Eq. (2.15) and Eq. (2.16), are shown in Fig. 2.4. These values can be used to calculate absorption and phase shift produced by simple objects. For example, a silicon particle of 20 μm diameter in an aluminium matrix (as might be observed in an Al-Si composite material) will give

[4]For a detailed treatment of the dose see, for example, Ref. [Attix 1986].

absorption contrast of only 0.2% but the difference in phase shift between the aluminium and the silicon particle is 0.1 π, i.e., 5% of the X-ray wavelength. For a polymer blend of acrylic glass and polystyrene (PMMA/PS) with the same feature dimensions (20 μm), the difference in phase shift between the two materials is still 3% of the X-ray wavelength, but the absorption contrast is negligible, only 0.03%.

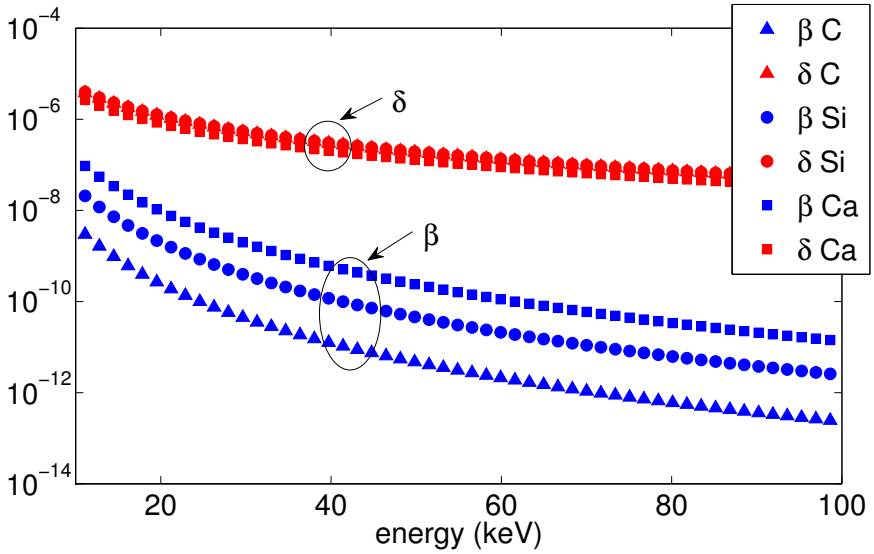

Figure 2.4: Calculated values for δ and β for three low-Z materials: C, Si and Ca calculated in the energy range 10-100 keV.

2.3 Phase-sensitive X-ray imaging techniques

In the previous sections we have seen that using phase shift rather than the absorption information allows to significantly increase the image contrast. However, in conventional absorption imaging, the detector, which records the intensity of the incoming wavefront, is placed directly downstream of the sample and in this way any information on the phase shift created by the sample is lost. This is because, the wavefield $E(x, y, z)$ downstream of the sample is given by Eq. (2.9) and the intensity is:

$$\begin{aligned} I(x,y,z) = |E(x,y,z)|^2 &= |E_0(x,y,0)|^2 |\mathcal{T}(x,y,z)|^2 \\ &= |E_0(x,y,0)|^2 |B(x,y,z)|^2 \quad . \end{aligned} \tag{2.20}$$

Phase-contrast imaging techniques use additional optical elements and/or exploit free-space propagation (see Sec. 3.1) to transform phase shift caused by the sample into an intensity modulation that can be revealed by the detector. The way in which this intensity modulation is related to the phase shift is different for the different techniques.

In this section, we give an overview of the most common phase-contrast techniques. They can be divided into four groups: (a) crystal interferometry, (b) propagation-based imaging, (c) analyzer-based imaging and (d) grating interferometry, see Fig. 2.5. The latter is the subject of this thesis and will be extensively described in the next chapters.

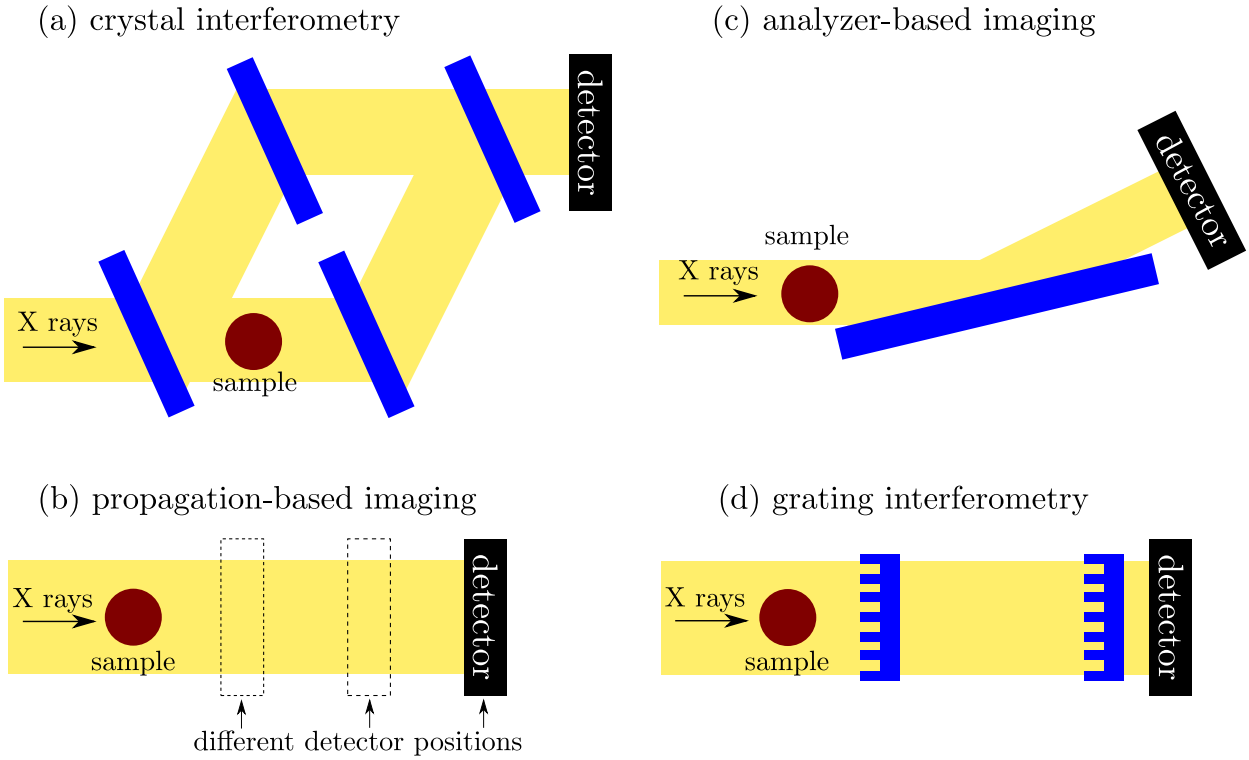

Figure 2.5: Schematic representation of X-ray phase-contrast imaging techniques.

2.3.1 Crystal interferometry

The first implementation of an X-ray interferometer dates back to 1965 [Bonse & Hart 1965]. The crystal interferometer splits and recombine the X-ray beam as shown in Fig. 2.5 (a). The sample is positioned in one of the beams, the interference pattern produced when the two beams recombine contains the phase shift information.

This phase shift is usually retrieved with the phase-stepping technique: a phase shifter is introduced, in the beam that does not go through the sample (the reference beam). Several interference patterns are recorded for different shifts of the reference beam. The analysis of these interference patterns yields the phase information modulo 2π (phase-wrapping effect). Phase-unwrapping techniques [Ghiglia & Pritt 1998] can be used to remove the phase ambiguity if the phase jumps are on a scale larger than the spatial resolution.

The spatial frequency range that can be detected with the crystal interferometer is not limited towards the low frequencies.

The high density resolution of this technique (a value of 4 mg/cm^3 was reported in Ref. [Momose *et al.* 1996]) makes this device well adapted for phase-contrast radiography and tomography of biological and other low-density samples.

The beam requirements are not extreme: the division of the incident beam into a diffracted and forward-diffracted beam acts a coherence filter since this process involves monochromatization and collimation [Momose 2003]. However, coherence filtering also filters out most of the incoming radiation making the exposure times very long (e.g. 18 s per phase map with synchrotron radiation in Ref. [Momose *et al.* 2000]).

Mechanical stability is the most difficult aspect of crystal interferometry. The path length difference between the two beams should be constant and of the same order of the wavelength of the X rays (subangstrom stability). Although this remains a very delicate task, it is easier to fulfil stability and alignment constraints when the interferometer is obtained from a single Si ingot. However, the field of view of the monolithic interferometer is limited from the size of the ingot itself. Crystal interferometers with two independent blocks that permit to increase the field of view in both transversal directions were realized, see for example [Becker & Bonse 1974]. They require laborious procedures to obtain the desired mechanical stability and rigidity of the system.

The spatial resolution is affected by the blurring in the analyzer lamella downstream the sample originated by the X rays refracted by the object [Momose 2003]. This blurring can be reduced by thinning down the analyzer crystal as reported in Ref. [Hirano & Momose 1999] where the authors calculate that, with an analyzer lamella thinner than 100 μm, a spatial resolution of about 10 μm can be achieved.

2.3.2 Propagation-based imaging

Phase-sensitive imaging methods which do not require any optical element in the beam path except the sample and the detector are called "propagation-based" [Snigirev *et al.* 1995, Cloetens *et al.* 1996, Nugent *et al.* 1996], see Fig. 2.5 (b). This techniques are based on the detection of the Fresnel diffraction pattern produced when the object is illuminated by spatially coherent radiation. The radiation can be polychromatic and propagation-based imaging can be applied to laboratory X-ray generators [Wilkins *et al.* 1996].

In order to detect the interference fringes, the detector should be a high-resolution detector. Since there are no optical elements in the beam, the spatial resolution, which is limited by blurring introduced by the presence of the interference fringes, can be very high: it can reach values of the order of the micron or less [Cloetens *et al.* 2006].

The image contrast in the near field is proportional to the second derivative of the phase of the wavefront. Therefore this technique is mainly sensitive to abrupt variations of the decrement of the refractive index (edge-enhancement).

Images exhibiting edge-enhancement already provide qualitative phase-contrast information and can be used as they are, without any further processing. If the object is homogeneous, the three-dimensional distribution of δ can be obtained as a solution of the transport of intensity equation [Paganin *et al.* 2002]. The formula proposed by Paganin et al. is simple and easy to implement. For this reason, this method is used also with inhomogeneous materials to produce an "artificial" and non-quantitative phase map of the object which often makes the sample features information easier to visualize and segment [Weitkamp *et al.* 2011].

In *holotomography* [Cloetens *et al.* 1999], tomographies taken with monochromatic radiation at different sample-to-detector distances are combined together. In this way, the quantitative δ tomogram of the investigated object, even if it is composed of multiple materials, can be extracted. The defocusing distances are chosen in order to map all the accessible spatial frequencies on the observation plane. However, low frequencies are imaged with less contrast than higher frequencies (the zero frequency is not accessible) and it remains difficult

to retrieve them. Low-frequency artifacts can be reduced in holotomography with the use of more sophisticated phase retrieval algorithms [Langer 2008]. Unlike crystal interferometry, free-space propagation does not suffer from the phase-wrapping effect.

2.3.3 Analyzer-based imaging

As crystal interferometry, analyzer-based imaging (also known as diffraction-enhanced imaging) uses a crystal, placed between the sample and the detector, see Fig. 2.5 (c) [Förster *et al.* 1980, Ingal & Beliaevskaya 1995, Davis *et al.* 1995]. The sample is illuminated by a monochromatic collimated beam usually produced by a double crystal monochromator. The analyzer crystal is positioned in Bragg geometry and is used as an angular selector; it accepts or rejects photons refracted or scattered by the sample. In fact, only the photons satisfying the Bragg condition reach the detector and contribute to the image formation. The typical angular acceptance of an analyzer-based imaging system, which is from few microradians to tens of microradians, is related to the full width at half maximum of the rocking curves of the crystals. The crystals used in an analyzer-based imaging setup have less stability requirements than the crystals used in crystal interferometry. However, the analyzer crystal in an analyzer-based imaging setup needs to be flat and the beam needs to be parallel so that the whole field of view is at the same point of the rocking curve. This constraint effectively limits the field of view.

The contrast in the image is associated to the angle at which rays are refracted by the sample and therefore to the differential phase of the incoming wavefront. Differently than crystal interferometry and propagation-based imaging, analyzer-based imaging provides the phase information only in one direction, i.e., the diffraction direction. It is thus not sensitive to angular deviations on the plane perpendicular to the diffraction plane.

Being a differential phase technique, analyzer-based imaging is not as sensitive as crystal interferometry to low spatial frequencies.

As in crystal interferometry, the spatial resolution in the final image is limited by the passage through the analyzer crystal and depends on the properties of the crystal. The blurring due to the analyzer element is explained by the dynamical theory of diffraction and amounts to a few micrometers.

A single image, taken for a single position of the analyzer crystal, gives a qualitative information of the refraction properties of the sample. The quantitative differential phase information can be retrieved by recording images for different detuning positions of the analyzer crystal on the rocking curve. Several algorithms can be used to extract information for the rocking curve. These algorithms, not only give the refraction angle information but they also provide the scattering signal [Pagot *et al.* 2003].

The first analyzer-based tomography is reported in Ref. [Dilmanian *et al.* 2000].

2.3.4 Grating interferometry

Grating interferometry is the most recently developed X-ray phase-contrast imaging technique first reported in 2002-2003 [David *et al.* 2002, Momose *et al.* 2003], see Fig. 2.5 (d).

This technique is also known as "Talbot interferometry" because the principle on which it is based, the self-imaging phenomenon, was discovered by H. F. Talbot in 1836 [Talbot 1836].

The standard and so far most widely-used X-ray grating interferometer (also used in this thesis) is the one described in Ref. [Momose *et al.* 2003, Weitkamp *et al.* 2005a] and shown in Fig. 2.5. Variations in the technique and/or phase-extraction methods have been implemented in the past years. They will be discussed in Chap. 6.

The main optical element of the grating interferometer is a phase grating which acts as a beam splitter. The beams departing from the phase grating (+1 and -1 diffraction orders) are separated by less than a milliradian and practically remain superimposed until they reach the observation plane. The pattern formed by the interference of the two beams is distorted, blurred and attenuated by the presence of the sample which can be placed either upstream or downstream of the phase grating. The interference pattern thus modified contains, besides the conventional absorption information, the differential phase and scattering signals in the direction perpendicular to the grating lines.

The period of this interference pattern is usually a few micrometers which can not be conveniently resolved by most image detectors (for further explanation see Sec. 4.1). This is why an absorption grating is used as analyzer. The analyzer grating is placed at one of the positions along the optical axis at which the fringes show maximum contrast.

The interferometer can operate in two different modes: the image signals can be extracted by analyzing the moiré fringes (see Sec. 4.4) formed by a slight rotation of one of the two gratings around the optical axis or with the phase-stepping technique. The latter method provides higher spatial resolution in the final images but requires multiple exposures recorded for different transverse positions of one of the two gratings to obtain the final images. The moiré technique allows to perform high-speed tomography (0.5 s for tomography scan [Momose *et al.* 2009b]) and single-shot radiography with spatial resolution in the diffraction direction limited by the period of the moiré fringes. The spatial resolution obtained with the phase-stepping technique is related to the grating period and to the distance between the two gratings; in parallel beam geometry, it is typically is of the order of few micrometers.

The density sensitivity of grating interferometry, calculated from the standard deviation of a region of constant phase in the phase tomogram, is extremely high: for example, a density sensitivity value of 0.5 mg/mm^3 was measured, for aqueous specimens, with the interferometer built in the present PhD thesis, see Chap. 9. For this reason, this technique is extremely attractive for X-ray imaging of soft-tissue biological samples.

The interferometer needs a high-precision translation stage for the scan of the stepped grating, the mechanical stability and rigidity of the device should be good enough to guarantee the alignment of the two gratings with a precision of a few tenth of nanometers. The parameters of the interferometer installed at a synchrotron beamline during this PhD project are reported in Chap. 7.

Grating interferometry, as crystal interferometry, measures the phase shift modulo 2π. As analyzer-based imaging, grating interferometry has a limited sensitivity to the low spatial frequencies. The sensitivity to this frequencies is in any case better than in propagation-based imaging which measures the Laplacian of the phase shift.

2.4 Dark-field X-ray imaging techniques

Phase-contrast imaging techniques measure, as described in the previous sections, phase shift from structures which are larger than the spatial resolution of the imaging system.

Sample features which cannot be resolved by the imaging system (typically in the micrometer or nanometer range) still affect the image signal in many phase-sensitive imaging techniques. However, the signal produced by unresolvable features can not be easily related to their optical or physical properties. This signal is usually associated with a local loss in coherence of the X-ray beam [Nesterets 2008] and is called "scattering contrast" or "dark-field imaging" [Pfeiffer *et al.* 2008a]. The term "dark-field" comes from light and electron microscopy and indicates that the unscattered beam does not produce image signal.

As mentioned in the previous sections, analyzer-based and grating-based imaging allow, in most of the cases, to measure the scattering contribution from the unresolvable features in the sample and separate it from phase and absorption information.

In analyzer-based imaging, the scattering information is extracted by measuring the width of the rocking curve of the analyzer crystal which is broadened by the presence of scattering features [Pagot *et al.* 2003].

In grating interferometry, the dark-field signal is accessed by measuring the local loss in visibility of the interference pattern produced by the phase grating [Pfeiffer *et al.* 2008a].

Both techniques yield images of the component of the scattering signal in the direction parallel to the diffraction vector.

Analyzer-based and grating-based methods are the most common among the full-field, parallel beam X-ray scatter-imaging techniques. Other scattering-contrast techniques such as small (or ultrasmall) angle X-ray scattering use a pencil beam and a scanning-based setup to measure, in the far field, the scattering signal produced in the interactions between X rays and different areas of the specimen, see, for example, Ref. [Bunk *et al.* 2009]. These scanning techniques have the advantage that they provide resolution in momentum transfer (i.e., scattering angle), which gives selectivity in the size of the scattering structures. On the other hand, despite the recent advances in detector technology, they remain much slower than full-field techniques.

Chapter 3
The Talbot (self-imaging) effect

Contents

The principles of X-ray grating interferometry are often explained on the basis of the Talbot effect: a self-imaging phenomenon reported for the first time in 1836 by Henry Fox Talbot [Talbot 1836] (in the following the terms 'Talbot effect' and 'self-imaging effect' will be used equivalently). Talbot observed that an absorbing periodic object illuminated by spatially coherent radiation produces self images at different distances along the optical axis. He wrote that: *"It was very curious to observe that though the grating was greatly out of the focus of the lens, yet the appearance of the bands was perfectly distinct and well defined"* [Talbot 1836]. The Talbot effect was analytically explained by Lord Rayleigh in 1881 [Rayleigh 1881] who showed that the self-imaging phenomenon is a consequence of Fresnel diffraction. He calculated that, for a plane wave, the distances D_m at which the self-imaging phenomenon occurs (the so-called Talbot distances) are proportional to the square of the period p of the object and inversely proportional to the wavelength λ of the radiation:

$$D_m = m\frac{2p^2}{\lambda} \quad \text{where } m = 1, 2, 3, ... \tag{3.1}$$

The first observation of the Talbot effect with hard X rays was reported in 1997, see Ref. [Cloetens *et al.* 1997]. Cloetens et al. used the Talbot effect to measure the coherence of a synchrotron X-ray beam in a way that will be described in Sec. 3.3.2.3. Instead of using an absorbing periodic object, Cloetens et al. used a phase grating, i.e., a grating whose lines only negligibly absorb X rays, but induce a substantial phase shift. The self-imaging phenomenon for phase objects resembles to the self-imaging phenomenon for absorbing objects. The periodic phase shift induced by the object is transformed into a periodic intensity

modulation at particular distances along the optical axis. These distances, which are given in the following sections, are *fractions* of the Talbot distances D_m calculated for absorbing objects. For this reason, the self-imaging phenomenon from phase objects, is usually called *fractional Talbot effect*.

In an X-ray grating interferometer, the fractional Talbot effect from a line phase grating is used to obtain a high-contrast periodic intensity pattern at several centimetres from the grating. The distortions of this intensity pattern caused by a sample placed close to the grating gives information on the optical properties of the specimen. Image formation in grating interferometry is the subject of the next chapter.

The following sections present the theory of the Talbot effect under coherent plane-wave illumination and discuss the effects of the partial coherence of radiation and of a spherical wavefront on the Talbot images generated by gratings. Understanding the properties of the intensity pattern generated by a line grating and the effects caused by an imperfect beam is fundamental to understand the performances of the grating interferometer under different illumination conditions.

3.1 Propagation of X rays in free space

In Sec. 2.1 we have seen what happens to a non-polarized and monochromatic X-ray plane wave that passes through a homogeneous object. In particular, we have derived the wavefront immediately downstream of the object as a function of the transmission function $\mathcal{T}(x, y)$ of the sample (Eq. (2.9) (page 10)). We have seen that the phase information is not accessed when the detector is placed immediately downstream of the object (Eq. (2.20) (page 14)) and we have said that propagation of X rays between the sample and the detector is fundamental for retrieving the phase information. In the following, we outline the theory of free-space propagation and we use this theory to explain the self-imaging phenomenon by periodic objects.

Let $E_0(x_0, y_0)$ be the wavefield at the aperture plane $z = z_0$ and let $E_1(x, y)$ be the wavefield at the observation plane $z = z_1$. The wavefield $E_1(x, y)$ can be calculated from $E_0(x_0, y_0)$ with the *Huygens-Fresnel principle* by superposition of spherical waves originated from each point of the aperture plane [Born & Wolf 1998]:

$$E_1(x, y) = \frac{1}{i\lambda} \int\int E_0(x_0, y_0) \frac{\exp(ikr)}{r} \cos(\mathbf{n}, \mathbf{r}) dx_0 dy_0 \quad . \tag{3.2}$$

In the above equation, known as the *Fresnel-Kirchhoff diffraction formula*, $\cos(\mathbf{n}, \mathbf{r})$, the so-called obliquity factor, is the cosine of the angle between the propagation direction $\mathbf{n}$ and the vector $\mathbf{r}$, see Fig. 3.1. For hard X rays, this angle is often very small (on the order of the microradian or less) and the obliquity factor can be neglected, i.e. $\cos(\mathbf{n}, \mathbf{r}) \approx 1$. Under the same assumption of very tiny diffraction angles (this approximation is called *small-angle or paraxial approximation*), the quantity r, which is rigorously equal to

$$r = \sqrt{\zeta^2 + (x - x_0)^2 + (y - y_0)^2} \tag{3.3}$$

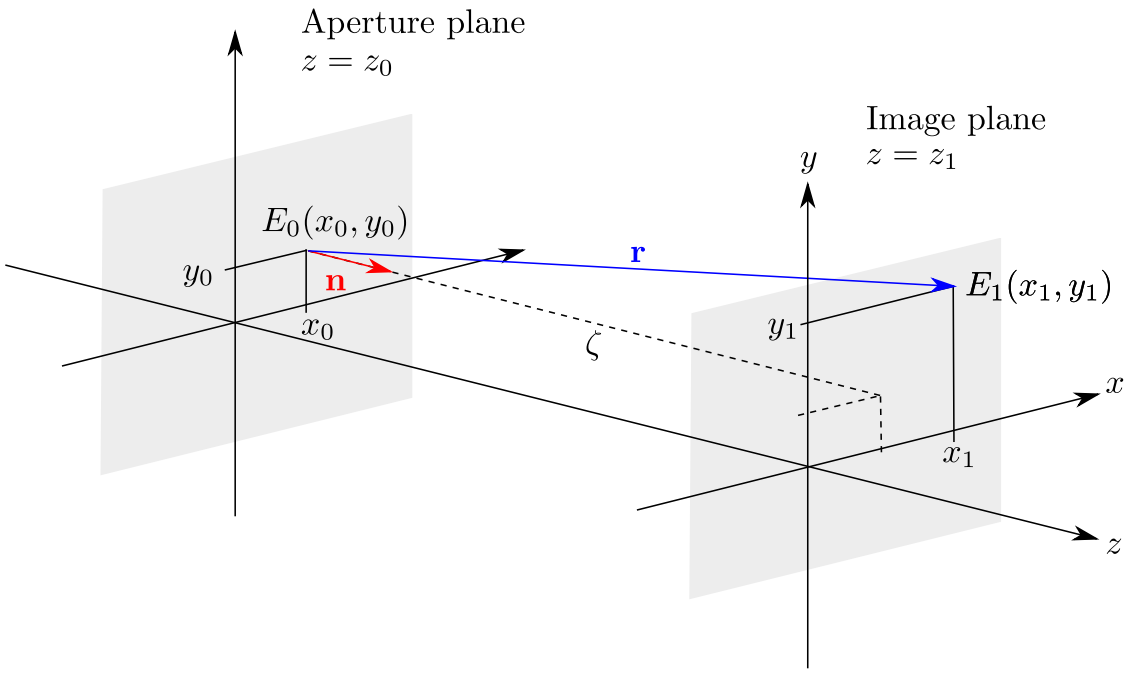

Figure 3.1: Geometry used for describing the free-space propagation theory. The quantities indicated in this figure are used in the formalism reported in the main text. Figure adapted from Ref. [Weitkamp 2002].

where the inter-plane distance, $\zeta = z_1 - z_0$, can be approximated in both the numerator and the denominator of the fraction in Eq. (3.2). In the denominator, r can be considered equal to ζ and taken out of the integral. In the exponent at the numerator we can substitute r with the first term of the binomial expansion,

$$r \approx \zeta + \frac{(x - x_0)^2 + (y - y_0)^2}{2\zeta} \quad , \tag{3.4}$$

so that Eq. (3.2) can be re-written as:

$$E_1(x, y) = \frac{e^{ik\zeta}}{i\lambda\zeta} \int\int E_0(x_0, y_0) \exp\left[i\pi \frac{(x - x_0)^2 + (y - y_0)^2}{\lambda\zeta}\right] dx_0 dy_0 \quad . \tag{3.5}$$

Equation (3.5) can be seen as a real-space convolution (the convolution operator will be indicated with the symbol "$\star$") of the initial wavefield $E_0(x_0, y_0)$ with a propagator function $P_\zeta(x, y)$:

$$E_1(x, y) = E_0(x_0, y_0) \star P_\zeta(x - x_0, y - y_0) \quad , \tag{3.6}$$

where

$$P_\zeta(x, y) = \frac{1}{i\lambda\zeta} \exp\left[i\frac{\pi}{\lambda\zeta}(x^2 + y^2)\right] \quad . \tag{3.7}$$

The phase factor $\exp(ik\zeta)$ in Eq. (3.7) has been dropped since it disappears when calculating the intensity.

Using the convolution theorem, Eq. (3.6) can be re-written as:

$$E_1(x,y) = \mathcal{FT}^{-1}\left\{\mathcal{FT}\left[E_0(x_0,y_0)\right] \times \mathcal{FT}\left[P_\zeta(x,y)\right]\right\} \tag{3.8}$$

where $\mathcal{FT}$ is the Fourier transform, $\mathcal{FT}^{-1}$ is the inverse Fourier transform and $\mathcal{FT}\left[P_\zeta(x,y)\right]$ is given by:

$$\mathcal{FT}[P_\zeta(x,y)] = \widetilde{P_\zeta}(f,g) = \exp\left[-i\pi\lambda\zeta(f^2+g^2)\right] \quad . \tag{3.9}$$

3.1.1 Simulation

Equations (3.8) and (3.9) are of practical interest for numerical calculations of wavefront propagation. These equations allow to calculate the final image produced by a relatively complex imaging setup where a series of known objects are present in the beam path. The objects are described by their transmission function (Sec. 2.1.3). A simulation of this kind practically consists in a series of multiplications and Fourier transforms. As part of this work, a simulation code based on the formalism presented in the previous section has been written in Matlab and has been used for simulating grating interferometry setups. All the wavefront simulations presented in this thesis have been obtained with this software.

3.2 The Talbot effect

The self-imaging phenomenon (or Talbot effect) is a consequence of the Fresnel diffraction on a periodic wavefront generated, for example, by a periodic object. The theory of wavefront propagation outlined in the previous section is used here to analytically describe the self-imaging phenomenon.

3.2.1 The Talbot effect for absorption objects

In the following we consider an object periodic along x and we indicate with p its period. We assume that the object is illuminated by a plane monochromatic wave with wavelength λ travelling along z axis, perpendicular to x. Moreover, we make the hypothesis that the period p of the object is much larger than the wavelength λ so that the beams are diffracted in the forward direction. In this case, the wavefield at the aperture plane directly downstream the object is given by the one-dimensional transmission function $\mathcal{T}(x)$ of the object which can be written in a Fourier series as [Momose *et al.* 2003]:

$$\mathcal{T}(x) = \sum_l a_l \exp\left(i2\pi\frac{lx}{p}\right) \quad , \tag{3.10}$$

where a_l are the Fourier coefficients. For the one-dimensional wavefield at the aperture plane $E_0(x_0) = \mathcal{T}(x_0)$, Eq. (3.5) becomes:

$$E(x,z) = \int \mathcal{T}(x_0)\exp\left[i\pi\frac{(x-x_0)^2}{\lambda z}\right]dx_0 \quad . \tag{3.11}$$

It has been shown that, by substituting Eq. (3.10) into the above equation, the wavefield $E(x,z)$ at a distance z from the periodic object can be written as [Guigay 1971, Momose *et al.* 2003]:

$$E(x,z) = \sum_l a_l \exp\left(i2\pi\frac{lx}{p}\right)\exp\left(-i\pi\frac{l^2 z\lambda}{p^2}\right) \quad . \tag{3.12}$$

Equation 3.12 shows that:

(1) the wavefront is periodic along z with period $2p^2/\lambda$: $E(x,z) = E(x,z+2p^2/\lambda)$;

(2) self images are generated at the distances of Eq. (3.1) predicted by Lord Rayleigh. At these distances $\exp(-i\pi l^2 z\lambda/p^2) = 1$ and the wavefield is equivalent to the transmission function of the object;

(3) self images laterally shifted by $p/2$ are generated at integer multiples of the distance $z = p^2/\lambda$. At the distances $z = p^2/\lambda$, $\exp(-i\pi l^2 z\lambda/p^2) = \exp(-i\pi l^2)$ and $E(x,z) = \mathcal{T}(x+p/2)$.

Points (2) and (3) above can be summarized by the following formula:

$$E(x, m'p^2/\lambda) = \begin{cases} \mathcal{T}(x), & \text{if } m' \text{ is even} \\ \mathcal{T}(x+p/2), & \text{if } m' \text{ is odd.} \end{cases} \tag{3.13}$$

Since the intensity at these particular distances is given by the modulus square of the transmission function of the object, the self images of the object do not contain any information on its phase profile. This means that a pure phase object produce no contrast at these distances. In the following sections we show that periodic phase objects produce an intensity modulation related to the phase profile at fractions of the distances $z = m'p^2/\lambda$ [Guigay 1971].

3.2.2 The fractional Talbot effect for phase objects

The intensity modulation generated by a phase object at the fractional Talbot distances is not exactly the self image as meant for absorption objects because the intensity profile at the fractional Talbot distances is different from that at the object plane and is also different, in general, from the phase profile of the object.

In this section we derive, based on the results reported by Guigay [Guigay 1971], the intensity profile generated by a phase periodic object at the fractional Talbot distances and we see how this intensity pattern is related to the phase profile of the object. In the following, the fractional Talbot distance will be indicated as F_{m_1,m_2}:

$$F_{m_1,m_2} = \frac{m_1}{m_2}D_1 = \frac{m_1}{m_2}\frac{2p^2}{\lambda} \quad , \tag{3.14}$$

where m_1 and m_2 are integer numbers and D_1 is the first Talbot distance defined in Eq. (3.1)[1]. Guigay calculated that the wavefield $E(x, F_{m_1,m_2})$ is a superposition of laterally shifted replicas of the object [Guigay 1971]:

[1] We limit our calculation to D_1 because D_1 is the period of the wavefront along z.

$$E(x, F_{m_1,m_2}) = C \sum_{q=1,2,\ldots,m_1m_2} \mathcal{T}\left(x + q\frac{p}{m_2}\right) \exp\left(\frac{i\pi q^2}{2m_1m_2}\right) [1 + i^{m_1m_2}(-1)^q] \quad , \tag{3.15}$$

where:

$$C = \frac{\exp(2\pi iz/\lambda - i\pi/4)}{\sqrt{2m_1m_2}} \quad . \tag{3.16}$$

Guigay used Eq. (3.15) to show that a phase object with transmission function $\mathcal{T}(x) = \exp[i\phi(x)]$, where $\phi(x)$ is periodic with period p, produces a wavefield $E(x, F_{1,4})$ given by [2]:

$$E(x, F_{1,4}) \propto \mathcal{T}(x)e^{-i\pi/4} + \mathcal{T}(x + p/2)e^{i\pi/4} \quad , \tag{3.17}$$

The intensity distribution $I(x, F_{1,4})$ at this distance is:

$$I(x, F_{1,4}) = |E(x, F_{1,4})|^2 = 1 + \sin\left[\phi(x) - \phi(x + p/2)\right] \quad . \tag{3.18}$$

The above equation states that there is a simple relation between the phase profile of a periodic phase object with period p and the intensity pattern generated by this object at the distance $F_{1,4}$. Note that these results are valid for any shape (e.g. triangular, rectangular, sinusoidal, ...) of the periodic object and that, accordingly to Eq. 3.18, the intensity distribution has not necessarily the same shape as the object transmission function.

3.2.3 The Talbot effect for binary gratings

In this section we consider the Talbot effect for binary gratings in which absorbing and/or phase shifting lines are alternated by clear parts with transmission function 1 (Fig. 3.2). Line gratings of this type are the optical elements forming a grating interferometer; their transmission function can be written as:

$$\mathcal{T}(x) = \begin{cases} 1, & \text{if } 0 \leqslant (x \bmod p) < \gamma p \\ A\exp[i\phi], & \text{if } \gamma p \leqslant (x \bmod p) < p \end{cases} , \tag{3.19}$$

where "mod" denotes the modulo operation. In the above equation γ is the duty cycle defined as the ratio between the width w of the grating lines and the period of the grating: $\gamma = w/p$ (Fig. 3.2). In the following we will consider gratings with $\gamma = 0.5$ except when otherwise indicated.
Depending on the transmission function at the working energy, gratings can be classified as:

- **absorption gratings** if $A \ll 1$;
- **phase gratings** if $\phi \gg |1 - A|$.

[2] Note that, since $m_1m_2 = 4$, the terms of the sum in Eq. 3.15 with q odd are zero.

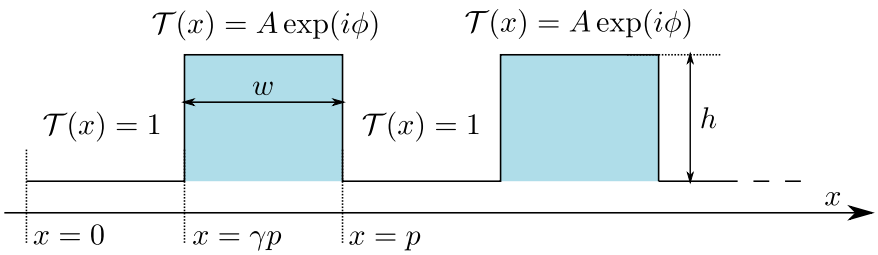

Figure 3.2: Transmission function of a binary grating with duty cycle γ.

3.2.3.1 The Talbot effect for absorption gratings

The grating lines of an ideal absorption grating are totally opaque structures. This kind of grating produces self images at the distances $z = m'p^2/\lambda$ with $m' = 1, 2, 3, ...$ discussed on Pag. 25. Fig. 3.3 (a) shows the intensity calculated at different positions along the optical axis after an ideal absorption grating with $p = 2$ μm illuminated by 20-keV X rays. Images like the ones in Fig. 3.3, which display the evolution of the wavefront generated by a periodic one-dimensional object, are usually called *Talbot carpets*. In the Talbot carpet of Fig. 3.3 (a), the first revival of the transmission function of the object is indicated by a dashed line.

3.2.3.2 The Talbot effect for phase gratings

The transmission function of a phase grating with period p, $\phi-$shifting lines and $\gamma = 1/2$ can be written as

$$\mathcal{T}(x) = \begin{cases} 1, & \text{if } 0 \leqslant (x \bmod p) < p/2 \\ \exp(i\phi), & \text{if } p/2 \leqslant (x \bmod p) < p \end{cases} . \tag{3.20}$$

According to Eq. (3.18), the image $I(x, F_{1,4})$ generated by this grating at the distance $F_{1,4}$ is equal in shape to its phase profile: [3]

$$I(x, F_{1,4}) = \begin{cases} 1 - \sin(\phi), & \text{if } 0 \leqslant (x \bmod p) < p/2 \\ 1 + \sin(\phi), & \text{if } p/2 \leqslant (x \bmod p) < p \end{cases} . \tag{3.21}$$

The contrast of the intensity pattern can be measured with the visibility v defined as

$$v = \frac{I_{\max} - I_{\min}}{I_{\max} + I_{\min}} , \tag{3.22}$$

where $I_{\min}$ and $I_{\max}$ are, respectively, the minimum and maximum values of the intensity pattern.

The visibility of the intensity pattern generated by a phase grating at $F_{1,4}$ depends on the phase shift ϕ induced by the grating lines and is, according to Eqs. (3.21) and (3.22):

$$v = \sin(\phi) . \tag{3.23}$$

The maximum visibility $v = 1$ is observed in the interference pattern generated by a $\pi/2$-shifting grating. A Talbot carpet generated from a phase grating with $\pi/2$-shifting lines

[3] The fractional Talbot distances for these gratings are also referred to as *Lohmann distances* and their "self images" are also called *Lohmann images* [Suleski 1997].

is shown in Fig. 3.3 (b); the dashed line indicates the position of the distance $F_{1,4}$. Since the amplitude of the wavefield at $F_{1,4}$ is the same as the wavefield immediately after an absorption grating with the same period, the Talbot carpet generated by the $\pi/2$-shifting phase grating is analogous to the Talbot carpet generated by the absorption grating shifted by $F_{1,4}$ along the optical axis.[4] An image identical to the one observed at $F_{1,4}$, but laterally shifted of $p/2$ is observed at the distance $F_{3,4}$. This distance is indicated in Fig. 3.3 (b) by a dotted line.

If the phase shift induced by the grating lines is a value different than $\pi/2$, Talbot carpets similar to the one shown in Fig. 3.3 (b) are obtained. However, the visibility of the image generated by these gratings at the fractional Talbot distances is smaller than 1. The visibility goes to zero when $\phi = 0, \pm\pi$. This means that a $\pi-$shifting phase grating does not produce any contrast at $F_{1,4}$.

A Talbot carpet generated by a $\pi-$shifting phase grating is displayed in Fig. 3.3 (c). It can be calculated from Eq. (3.15) that a $\pi-$shifting grating produces images with a rectangular profile and visibility 1 at the distance $F_{1,16}$ (Appendix A) and at its odd multiples. The intensity profile after a π-shifting grating has half the period of the grating. Moreover, it should be noted that, unlike for $\pi/2$ gratings, there is no contrast inversion between the positions of maximum visibility along the optical axis.

Notation used in the following for describing the fractional Talbot distance of a phase grating A phase grating is the main optical element of the X-ray grating interferometer. Phase gratings are used because of their higher photon efficiency compared to absorption gratings. Phase gratings with $\pi/2-$ or $\pi-$shifting lines are chosen because they produce rectangular intensity patterns with maximum visibility. In the following, we will refer to the phase grating as G1 and we will indicate with p_1 its period. As discussed in the previous sections, the fractional Talbot distances at which these gratings produce rectangular profiles with visibility 1 depend on the phase shift induced by the grating lines, i.e., odd multiples of $F_{1,4}$ for a $\pi/2-$shifting phase grating and odd multiples of $F_{1,16}$ for a $\pi-$shifting phase grating.

In order to generalize notation, we introduce, following the scheme presented in Ref. [Weitkamp *et al.* 2006], the parameter η and we write the fractional Talbot distances f_n as:

$$f_n = n\frac{p_1^2}{2\eta^2\lambda} \quad \text{where} \quad \eta = \begin{cases} 1, & \text{if } \phi = \pi/2 \\ 2, & \text{if } \phi = \pi \end{cases}, \tag{3.24}$$

where $n = 1, 3, 5, ...$ indicates the fractional Talbot order. Thus, for example, when we speak of the third fractional Talbot distance, we mean the distance $f_3 = 3p_1^2/(2\lambda)$ if the grating is a $\pi/2-$shifting phase grating and $f_3 = 3p_1^2/(8\lambda)$ if the grating is a $\pi-$shifting phase grating. At the distances f_n, the period of the interference pattern is p_1/η.

Finite lateral dimensions of the gratings In the formalism and in the simulations presented so far, the object has been considered to be infinitely extended along x, which

[4] Except for the photon efficiency: 100% of the incoming radiation is transmitted by the phase grating and 50% is transmitted by the absorption grating.

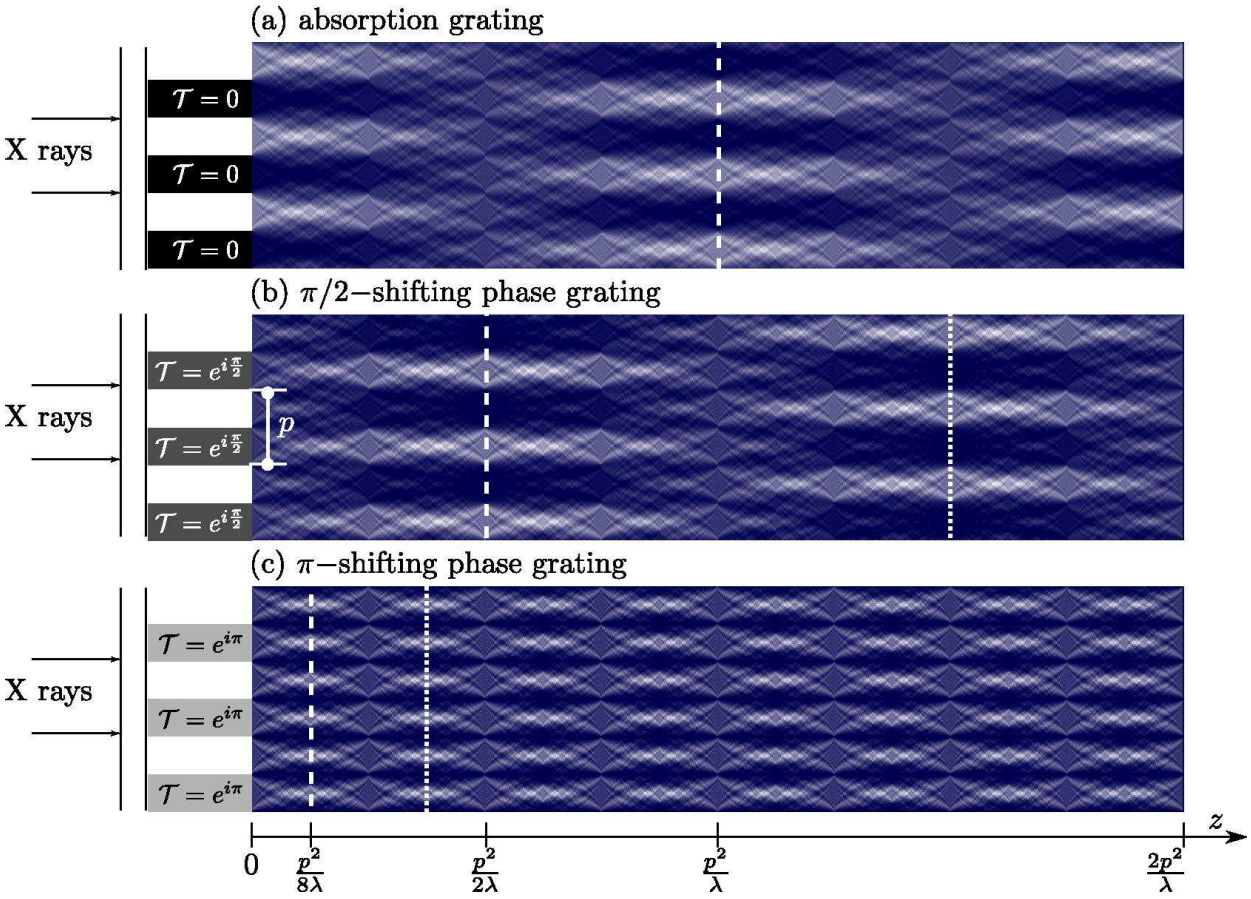

Figure 3.3: Talbot carpets generated, up to the first Talbot distance $2p^2/\lambda$, by different types of binary gratings with duty cycle 0.5 illuminated by a plane monochromatic wave with full transverse coherence. The first positions along the optical axis at which the interference pattern is a rectangular profile with period p or $p/2$ (the latter for a $\pi-$shifting grating) and visibility 1 are indicated with dashed white lines. In panels (b) and (c), the second positions are indicated with dotted white lines. Figure after Ref. [Weitkamp *et al.* 2006].

obviously is not the case for real gratings. However, the gratings used in a grating interferometer have a high line density and they are extended for several thousand periods in the x direction. At these conditions, the effect of the grating borders on the intensity pattern can be neglected [Arrizón & Rojo-Velázquez 2001].

Two-dimensional Talbot effect The results presented so far can be easily extended to wavefronts periodic not only along x, but also along y. In particular, if p_x is the period along x and $p_y = kp_x$ is the period along y, Talbot images are observed if k^2 is a rational number. Discussions about two-dimensional gratings with $k = 1$ can be found in Chap. 11 and Ref. [Zanette *et al.* 2010a].

3.2.3.3 Phase grating as a beam splitter

The fractional Talbot effect can be seen also as the result of the *interference* between two beams diffracted by the grating. In fact, the phase grating acts as a beam splitter which divides the incoming beam mostly in the +1 and -1 diffraction orders. The angle θ_1 at which these beams are diffracted is [Paganin 2006]

$$\theta_1 = \frac{\lambda}{p_1} \quad . \tag{3.25}$$

For $\lambda = 0.62$ Å corresponding to 20-keV X rays and $p_1 = 4$ μm, the angle θ_1 is approximately 16 μrad.

The separation distance s_n of the two beams at the fractional Talbot distance f_n is

$$s_n = 2f_n\frac{\lambda}{p_1} = n\frac{p_1}{\eta^2} \quad . \tag{3.26}$$

If $n = 7$, $\eta = 2$ and $p_1 = 4$ μm, then $s_7 = 7$ μm. As we will see in the following (Sec. 4.3.1), the distance s may affect the spatial resolution of the final images in the diffraction direction.

3.3 Effects of partial coherence and spherical wavefront

So far the Talbot effect has been described for coherent plane-wave illumination. However, in a real experiment, the wavefront is never perfectly coherent and its curvature is always finite. These effects cause deviations of the intensity patterns at the (fractional) Talbot distances from the ideal profiles calculated in the previous sections.

In the following, we will discuss qualitatively and quantitatively the effects of the spherical wavefront, source size and polychromaticity of the X-ray beam on the interference pattern generated by a phase grating G1.

3.3.1 Spherical wavefronts

The formalism outlined in the previous sections assumed a plane wave illumination produced, for example, by an X-ray source positioned at infinite distance from the grating.

When the source is situated at a distance R from the object plane, the one-dimensional spherical wavefront incident on the object can be written as

$$E_0(x) = \exp[i\pi x^2/(\lambda R)] \quad . \tag{3.27}$$

The effects of the spherical wavefronts, which can be rigorously obtained by inserting expression of Eq. (3.27) into Eq. (3.12), are to induce a magnification M in the interference pattern and a modification in the (fractional) Talbot distances. The magnification M of the pattern at a distance z from the object is [Cloetens 1999]

$$M = \frac{R+z}{R} \quad . \tag{3.28}$$

This means that, at the distance z, the period of the interference pattern is not exactly p/η but Mp/η. Moreover, the distances d_n at which the magnified interference pattern is observed are larger than the fractional Talbot distances f_n for a plane wave and given by [Cloetens 1999]

$$d_n = f_n \frac{R}{R - f_n} \quad . \tag{3.29}$$

At the beamline ID19 at European Synchrotron Radiation Facility in Grenoble, France where most of the experimental part of the present thesis was carried out, the source-to-G1 distance is $R = 150$ m. The magnification at a distance $z = 500$ mm is $M = 1.003$ which, if $p = 4$ μm and $\eta = 2$, leads to a period of the interference pattern of 2.007 μm instead of a period of 2.000 μm which would be obtained for plane wave illumination. Even if this difference is very tiny, it should be taken into account for the design of the grating interferometer in order to avoid artifacts in the final images. This aspect will become more clear in the next chapters and in particular in Sec. 4.3.2 and Appendix B.

At conventional X-ray tubes, the source-to-G1 distance is much shorter than at synchrotrons and the wavefront is strongly spherical. This strong curvature affects not only the fractional Talbot distance and the period of the interference pattern but also the angle at which X rays impinge on the grating lines. This will be discussed with more detail in Sec. 6.1.1.

3.3.2 Partial coherence

Besides the plane wave approximation, a second assumption that is usually unfulfilled is that of a perfectly coherent wavefront. A coherent wavefront, such as the one produced by a single electron, is a wavefront in which phase differences between all pairs of points have definite values which are constant with time [Born & Wolf 1998].

Real X-ray sources, such as synchrotron radiation sources and conventional X-ray tubes, are extended in space and each point of the source emits radiation independently of the others. Moreover, they deliver polychromatic radiation. These characteristics decrease the coherence of the radiation. The transverse coherence is related to the source size and the longitudinal coherence is related to the polychromaticity of the beam.

The partial coherence of the X-ray beam affects the visibility v of the interference pattern (Eq. (3.22)): a smaller degree of coherence corresponds to a lower visibility and a totally incoherent radiation will give $v = 0$.

In the following sections we discuss the effects of the partial coherence on the shape and visibility of the interference pattern generated by a phase grating at the fractional Talbot distances. For a complete treatment of the optical coherence theory we refer to textbooks such as Ref. [Born & Wolf 1998].

3.3.2.1 Partial transverse coherence

The transverse coherence of the radiation is related to the angular size of the X-ray source. The radiation from an extended source can be described as a superposition of mutually incoherent spherical waves from different points x in the source plane. If the distance R between the source and G1 is much larger than the distance z between G1 and the observation plane and than the source size, then the spherical waves can be approximated by plane waves. The projected distribution of the source profile at the observation plane z downstream of G1 is demagnified by a factor z/R. The distribution of the source profile at the source plane $g(x)$ can often be approximated by a Gaussian distribution

$$g(x) = \frac{1}{\sigma_s\sqrt{2\pi}} \exp\left(-\frac{x^2}{2\sigma_s^2}\right) \quad , \tag{3.30}$$

where σ_s is the standard deviation of the intensity distribution. In this case, the projected distribution of the source at the observation plane z becomes:

$$s(x) = \frac{1}{\sigma_o\sqrt{2\pi}} \exp\left(-\frac{x^2}{2\sigma_o^2}\right) \quad , \tag{3.31}$$

where the standard deviation σ_o is given by $\sigma_o = \sigma_s z/R$.

The intensity $I_s(x)$ at the observation plane is given by the intensity pattern $I(x)$ that would be obtained with a point source convoluted with the projected intensity distribution of the source $s(x)$:

$$I_s(x) = I(x) \star s(x) \quad . \tag{3.32}$$

This effect is shown in the Talbot carpet of Fig. 3.4 (a) which has been calculated for typical conditions at ID19: a source size of $\sigma_s = 150$ μm and a source-to-G1 distance of 150 m. The profiles shown in Fig. 3.4 (b) are taken at four different fractional Talbot distances indicated by dashed lines in the Talbot carpet. At small values of σ_o, the intensity pattern is very similar to the one that would be obtained with a fully coherent wavefront, i.e., at the fractional distance it has a rectangular shape. By increasing the propagation distance, the grating image is convoluted with a Gaussian of increasing width. This convolution makes the shape of the intensity pattern similar to a sinusoidal function and reduces the visibility of the intensity pattern. For very large values of σ_o, any intensity modulation will be washed out.

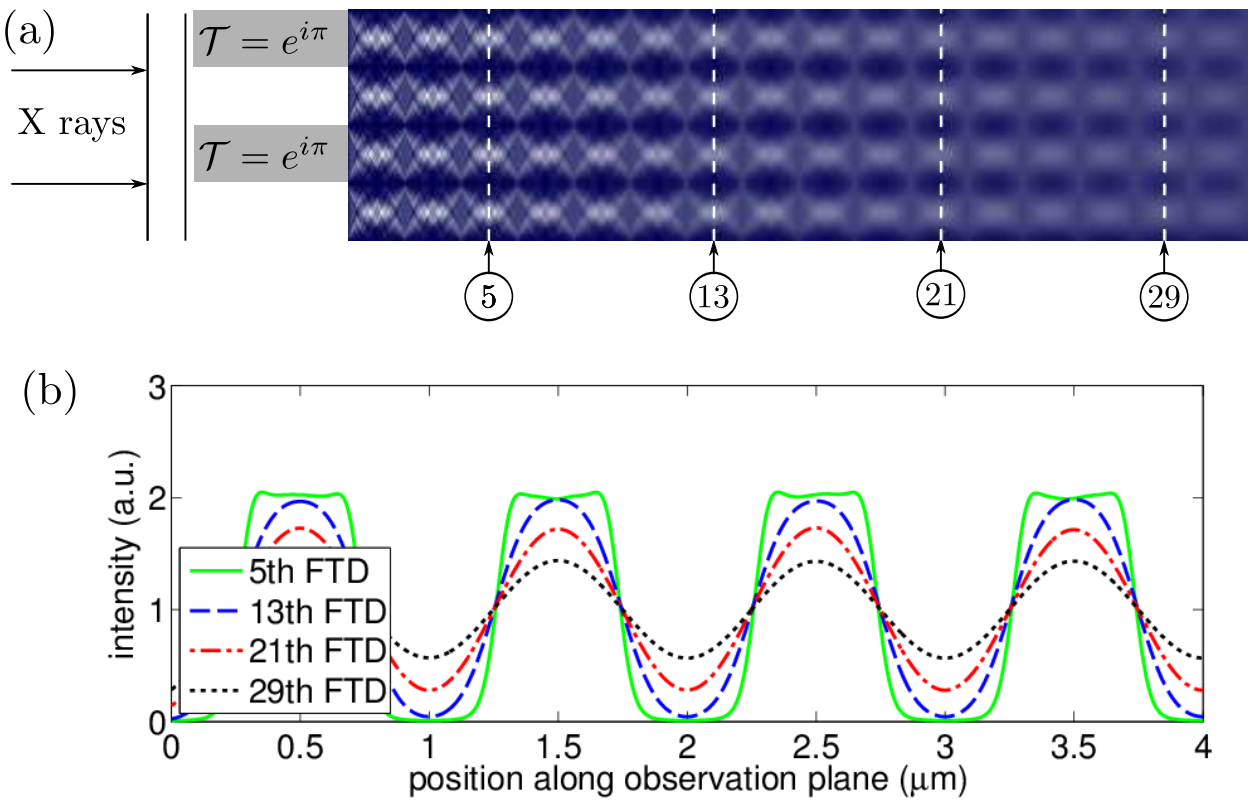

Figure 3.4: (a) Talbot carpet generated, up to the second Talbot distance, from a $\pi-$shifting phase grating with period p_1=2 μm illuminated by 20-keV X rays. In this simulation, a Gaussian distribution of the source profile with a size of σ_s = 150 μm and a source-to-G1 distance of 150 m have been considered. (b) Profiles extracted at the positions indicated by dashed lines in the Talbot carpet of panel (a).

Bech, in his PhD thesis [Bech 2008], neglecting imperfections in the grating and assuming a Gaussian source distribution, showed that, when $\sigma_o/p_1 \geqslant 1/(2\pi)$, the visibility decreases exponentially with the projected source size:

$$v(\sigma_o) = \frac{8}{\pi^2} \exp\left[-2\pi^2 \left(\frac{\sigma_o}{p_1}\right)^2\right] \quad . \tag{3.33}$$

A similar result has been obtained in Ref. [Weitkamp *et al.* 2006]. Bech further showed that, for $\sigma_o/p_1 < 1/(2\pi)$, the visibility decays linearly with σ_o/p_1.
Inverting Eq. (3.33), one can calculate the projected source size for a given required minimum visibility v_0:

$$\sigma_o < \frac{p_1}{\pi}\sqrt{-\frac{1}{2}\ln\left(\frac{\pi^2}{8}v_0\right)} \quad . \tag{3.34}$$

Equation above holds for $\sigma_o/p_1 \geqslant 1/(2\pi)$. For example, in order to have a visibility of 20% when p_1 = 4.8 μm, the projected source size should be smaller than 1.3 μm. This can be easily obtained at ID19 where R = 150 m and σ_s = 150 μm. However, for typical parameters at an X-ray tube, where the source size is usually larger than the one at the synchrotrons

and the distance R is almost always much shorter (around 1 m), it is extremely difficult to reach a projected source size as small as 1.3 μm. It is in practice possible to slit down the source to a required minimum value but this would result in a significant loss of beam intensity. This is why an alternative method, discussed in Sec. 6.1.1, has been proposed for implementing grating interferometry at low-brilliance sources [Pfeiffer *et al.* 2006].

3.3.2.2 Partial longitudinal coherence

The degree of longitudinal coherence is another factor that can affect the visibility of the intensity pattern generated by a binary phase grating. However, its effect is usually not as dramatic as that of limited transverse coherence.

The visibility of the interference pattern obtained with a polychromatic X-ray beam can be expressed as a weighted sum of the visibilities obtained with the monochromatic X rays of the photon energy spectrum [Engelhardt *et al.* 2008]. Engelhardt et al. describes in detail the effect of a broad spectral width. The authors show that that, provided sufficient transverse coherence, the interference pattern shows acceptable fringe contrast even with a polychromatic X-ray spectrum produced by an X-ray tube. The calculations of Engelhardt et al. have been confirmed by experimental results, see, for example, Refs. [Bech 2008, Donath *et al.* 2010, Rizzi *et al.* 2011].

The energy spread of a quasi-monochromatic beam (with $\Delta E_\gamma/E_\gamma \approx 10^{-2}$ or less, where E_γ indicates the X-ray energy) obtained from a monochromator device at a synchrotron beamline has negligible effect on the visibility of the interference pattern generated by the grating. An example is given in Fig. 3.5. This figure shows intensity profiles generated by a phase grating which gives a phase shift of π when it is illuminated by X rays with energy E_γ^0. The ideal profile at E_γ^0 (black solid line in Fig. 3.5) is plotted against the profile generated by the same grating illuminated by X rays with energy $E_\gamma^0 + \Delta E_\gamma$ where $\Delta E_\gamma = 0.01 E_\gamma^0$. Since at this energy the phase shift caused by the grating lines is slightly different than π, the signal of the fundamental harmonic, which corresponds to half of the period of the grating, is disturbed by an oscillation which has the period of the grating itself (red dashed line in Fig. 3.5). The difference in visibility between the two profiles is only 0.6%.

3.3.2.3 Measurement of the coherence of the X-ray beam with a binary grating

In Sec. 3.3.2.1, we have seen that the decrease of visibility in the interference pattern from a phase grating along the optical axis is related to the projected source size. Measurements of the visibility at several propagation distances can be used to retrieve the source size and the spatial coherence properties of the X-ray beam without the need of knowing the grating and detector properties. This was exploited for the first time in 1997 by Cloetens et al. who measured the coherence of the X-ray beam at ID19 [Cloetens *et al.* 1997]. The author of this thesis has contributed in a more recent experiment, in which the self-imaging phenomenon has been used to measure the coherence after different types of multilayer monochromators [Rack *et al.* 2010, Rack *et al.* 2011].

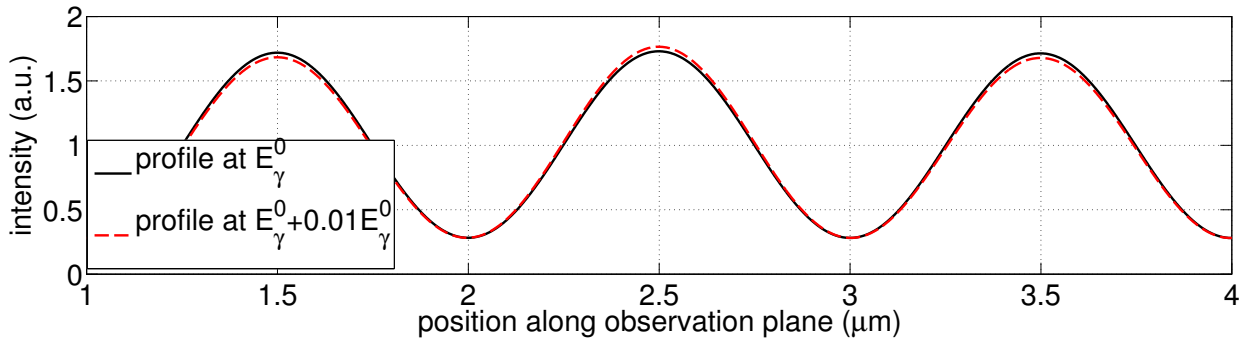

Figure 3.5: Profile plots obtained from a phase grating with period $p_1 = 2$ μm at the 21st fractional Talbot distance under the same conditions (source size and source-to-G1 distance) used for the simulation shown in Fig. 3.4. The grating gives a phase shift of π at the energy E^0_γ=20 keV. The profile obtained at 20 keV is shown with a solid black line. The red dashed line shows the profile obtained at the energy $E^0_\gamma + 0.01E^0_\gamma$.

Chapter 4

X-ray grating interferometry

Contents

This chapter presents the principles of X-ray grating interferometry. Sections 4.1 and 4.2 describe the function of the two gratings forming the interferometer and present the procedure, based on the phase-stepping technique, usually adopted to collect and analyze data. The three image signals obtained from the analysis of the raw interferograms, i.e. attenuation, differential phase and dark-field signals, are presented in Sec. 4.1.4. Section 4.3 discusses the aspects which should be considered for a practical implementation of an X-ray grating interferometer, such as the inter-grating distance and the grating parameters, and outlines their effect on the final image quality. The last section (Sec. 4.4) is dedicated to moiré imaging, which is an alternative to the phase-stepping technique to obtain image signals when spatial resolution is not an issue and single-shot imaging is required.

4.1 Principles

4.1.1 The phase grating

In an X-ray grating interferometer, the fractional Talbot effect from a phase grating (G1 with period p_1) is used to generate a high-contrast periodic interference pattern at several centimeters downstream the grating. The fractional Talbot effect from a phase grating has been described, under different illumination conditions, in the previous chapter. For convenience, we restate the fundamental aspects here.

Phase gratings are used because of their higher photon efficiency compared to absorption gratings. Gratings giving a phase shift of $\pi/2$ or π are preferred because they generate high-contrast interference patterns with period p_1 and $p_1/2$ respectively (Sec. 3.2.3.2). The position of the fractional Talbot distances along the optical axis depends on the phase shift ϕ induced by the grating lines. If the grating is illuminated by a monochromatic plane wave, the fractional Talbot distances f_n can be written as:

$$f_n = n\frac{p_1^2}{2\eta^2\lambda} \quad \text{with} \quad \eta = \begin{cases} 1 & \text{if } \phi = \pi/2 \\ 2 & \text{if } \phi = \pi \end{cases}, \tag{4.1}$$

where λ is the wavelength of the radiation and n is an odd number and p_1 is the period of G1. At the distances f_n, the period of the interference pattern is p_1/η.

If the incoming wavefront is a spherical wave and if the X-ray source is situated at a distance R from G1, the fractional Talbot distances become:

$$d_n = f_n\frac{R}{R - f_n} \ . \tag{4.2}$$

At the distances d_n the period of the interference pattern is magnified by a factor $M = (R + d_n)/R$.

For large radii of curvature (e.g., several meters), the interference pattern produced by fully coherent radiation has a rectangular profile. Partial transverse and longitudinal coherence of the X-ray beam affect the shape of the interference pattern which, in a typical experiment, has a sinusoidal profile as described in Sec. 3.3.

The interference pattern observed when a sample is in the X-ray path, situated either downstream or upstream of G1, is different than the reference interference pattern obtained without the sample in the beam. The distortions of the interference pattern caused by the sample carry information on the optical properties of the investigated object (Fig. 4.1). In particular:

1. the average intensity is reduced due to *attenuation*;
2. the interference pattern is laterally shifted due to *refraction*;
3. the visibility is reduced due to *scattering*.

The goal of the method is to analyze the interference pattern observed when the sample is in the beam path and compare it to the interference pattern obtained from the reference beam. In this way, attenuation, refraction and scattering (or dark-field) images of the sample can be retrieved.

4.1.2 The analyzer grating

Usually, the interference pattern generated by G1 cannot be analyzed with a suitable X-ray detector. This is because a very high resolution detector (in general with a correspondingly small field of view) would be needed to resolve an interference pattern with period of a

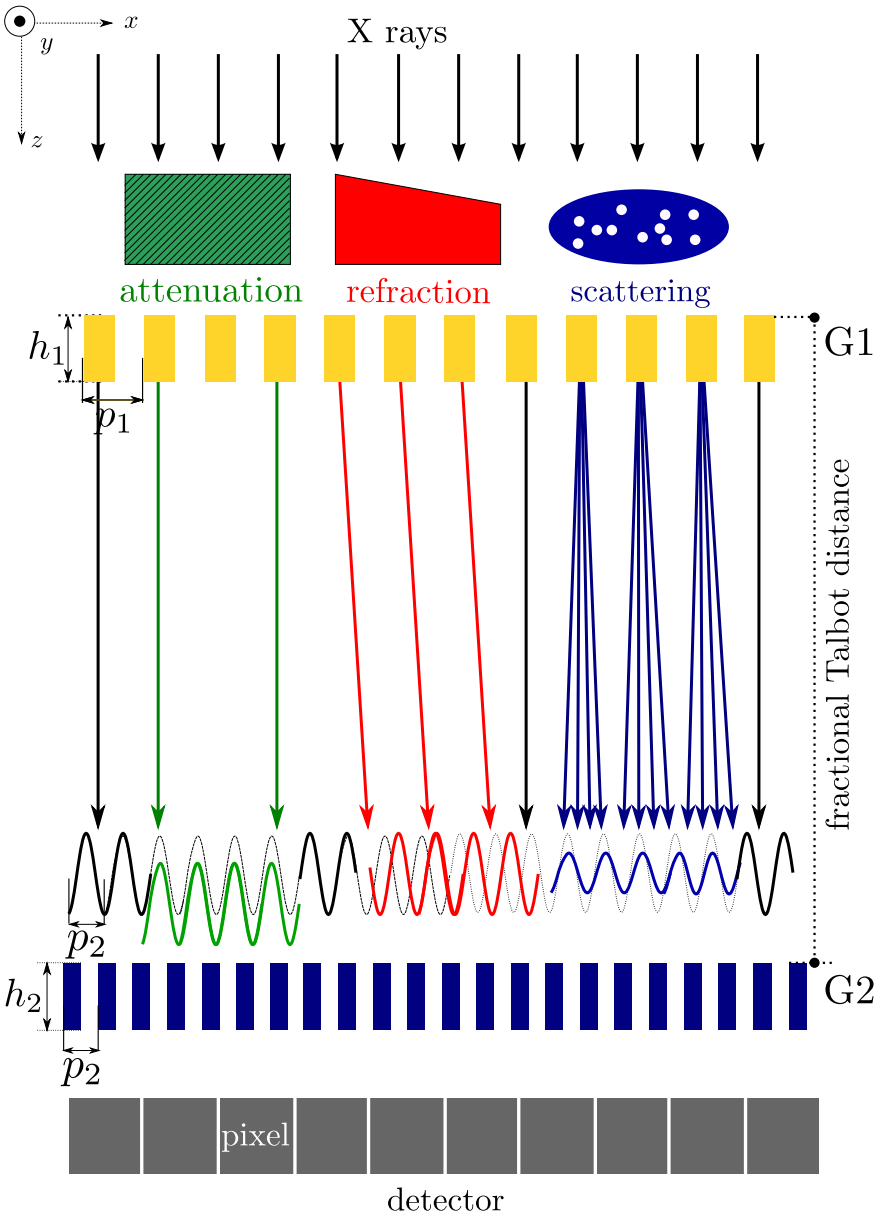

Figure 4.1: Principles of X-ray grating interferometry. The sample is positioned either upstream or downstream of the phase grating G1 which produces a periodic interference pattern at the fractional Talbot distance d_n. Attenuation decreases the average intensity, refraction displaces the interference pattern and scattering decreases its visibility. The absorption grating G2 is situated at a distance d_n from G1 in order to analyze the interference pattern produced by G1.

couple of micrometers. Increasing the period of G1, causes a decrease of the sensitivity of the device and a deterioration of the spatial resolution in the final images. Moreover, requirements on spatial coherence are harder to satisfy at large grating periods. One should also consider mechanical limitations of using large grating periods; the first fractional Talbot distance for a $\pi/2-$shifting phase grating with a period of 20 μm illuminated by 30-keV X rays is approximately 5 m which would be very difficult to implement.

For these reasons, an *analyzer element* is often used to measure fringe position and

amplitude at the observation plane. The analyzer is a second grating with opaque lines which is positioned directly upstream the detector at a fractional Talbot distance from G1, see Fig. 4.1. This absorption grating, which in the following will be indicated as G2, is used as a mask and not as a diffractive element.

The analysis of the interference pattern can be performed with the phase-stepping technique or by direct processing of the moiré pattern generated by the grating pair. During this PhD thesis, the grating interferometer has always been used in phase-stepping mode. The next sections are devoted to the description of the phase-stepping technique in grating interferometry. Moiré imaging will be discussed in the last section of this chapter.

4.1.3 The phase-stepping scan

The phase-stepping (or phase-shifting) technique is widely used in visible light interferometry, see for example Ref. [Creath 1988]. As mentioned in Sec. 2.3.1, it is also used in X-ray crystal interferometry.

In grating interferometry, the phase-stepping technique consists in recording a series of images for different transverse positions of one of the two gratings: either the phase or the absorption grating is scanned perpendicularly to the grating lines over at least one period of the interference pattern in more than two steps per period. In order to avoid moiré fringes which may disturb the final images, the absorption grating has the same period of the interference pattern. Mathematically, the intensity recorded in each pixel during a phase-stepping scan is given by the convolution of the interference pattern impinging on that pixel with the local transmission function of the grating, see Fig. 4.2. In the ideal case of fully coherent radiation and binary gratings without imperfections, the intensity curve observed in each pixel is a triangular function (given by the convolution of two square profiles). In most of the cases, however, the interference pattern can be approximated by a sinusoidal function, which, convolved with the rectangular transmission function of the absorption grating, gives a sinusoidal intensity oscillation as represented in Fig. 4.2.

Since the distortion of the interference pattern caused by the sample is measured with respect to the reference beam, a phase-stepping scan without the sample in the beam is recorded under the same conditions (same number of steps, same grating positions and same exposure time) as the phase-stepping scan with the sample.

Figure 4.3 shows a selection of raw interferograms from the phase-stepping scans recorded for the measurement of an ant - a demonstrator sample. These images show that the intensity in each pixel changes with the grating position x_g. Contrast curves in two detector pixels extracted from the phase stepping scans, taken with and without the sample in the beam, are shown in Fig. 4.4.

4.1.4 The three image signals

Attenuation, differential phase and scattering signals are obtained from the average a_v, phase φ and amplitude a_m of the contrast curves (Fig. 4.4). These quantities are extracted with a pixel-wise analysis of the raw interferograms taken during the phase-stepping scan. In the following, the superscript 's' will indicate quantities extracted from the scan recorded

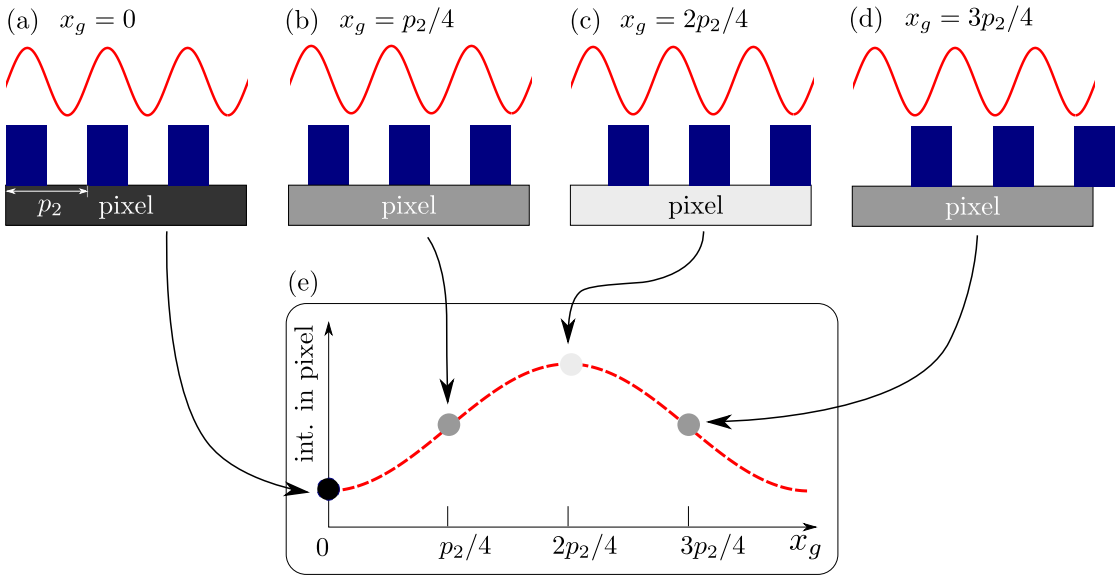

Figure 4.2: Schematic representation of a phase-stepping scan performed over one period in four steps. The lines of G2 are represented by blue rectangles. The intensity pattern produced by G1 impinging on G2 has a sinusoidal profile (red line). At the G2 position $x_g = 0$ (panel (a)), the absorbing lines are aligned with the regions of maximum intensity of the interference pattern. In this case, the intensity recorded by the pixel positioned downstream G2 takes the minimum value. The opposite occurs when the absorbing lines are aligned with the regions of minimum intensity of the interference pattern and the maximum intensity is recorded by the pixel (panel (c)). Panels (b) and (d) show an intermediate situation. Panel (e) shows a plot of the relative intensity values recorded by the pixel during the phase-stepping scan.

with the sample in the beam path; the quantities extracted from the reference scan will be indicated with the superscript 'r'. For example, a_m^{r} denotes the amplitude of the contrast curve in a pixel of the reference phase-stepping scan.

The three image signals are described in the following.

The attenuation image The attenuation is given by:

$$A = 1 - \frac{a_v^{\mathrm{s}}}{a_v^{\mathrm{r}}} \quad . \tag{4.3}$$

The quantity often displayed in the so-called 'attenuation image' is the transmission $B = 1 - A = a_v^{\mathrm{s}}/a_v^{\mathrm{r}}$, cf. Eq. (2.4) (page 9). The attenuation image of the ant is shown in Fig. 4.5 (a); it is very similar to the image that would have been obtained, for otherwise identical conditions, without the interferometer in the beam. The attenuation signal can be mixed with the edge-enhancement (or in-line phase-contrast) effect which has its origin in the propagation of the X-ray beam from the sample to the detector. The edge-enhancement appears in panel (a) as bright and dark stripes at the edges of the object.

The attenuation image provided by the grating interferometer may suffer from a blurring in x with respect to the image obtained without any optical element between the sample and the detector. This blurring arises from the separation of the two beams diffracted from

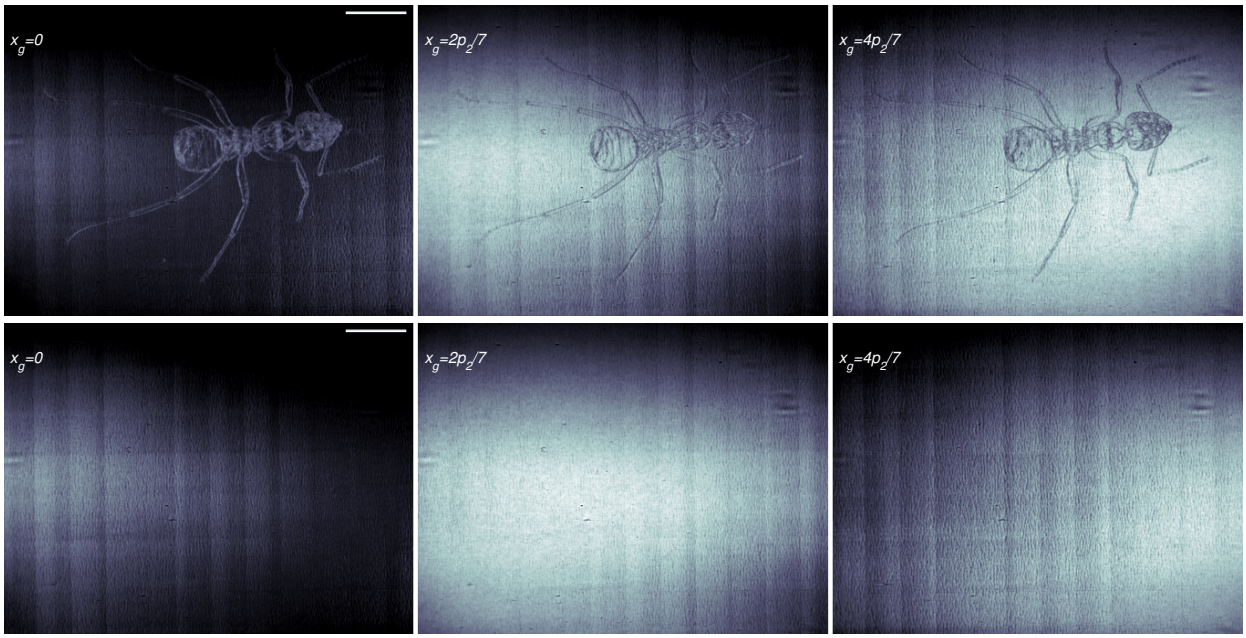

Figure 4.3: Top: selection of images of an ant recorded in a phase-stepping scan performed in 7 steps over one grating period. Bottom: corresponding images recorded during the flat-field phase-stepping scan without the sample in the beam path. The measurements were made at the 9th fractional Talbot distance at 23 keV with a $\pi-$shifting grating. The exposure time per raw image was 1 s. The pixel size was 7.5 μm. The line at the top of the images indicates a length of 2 mm.

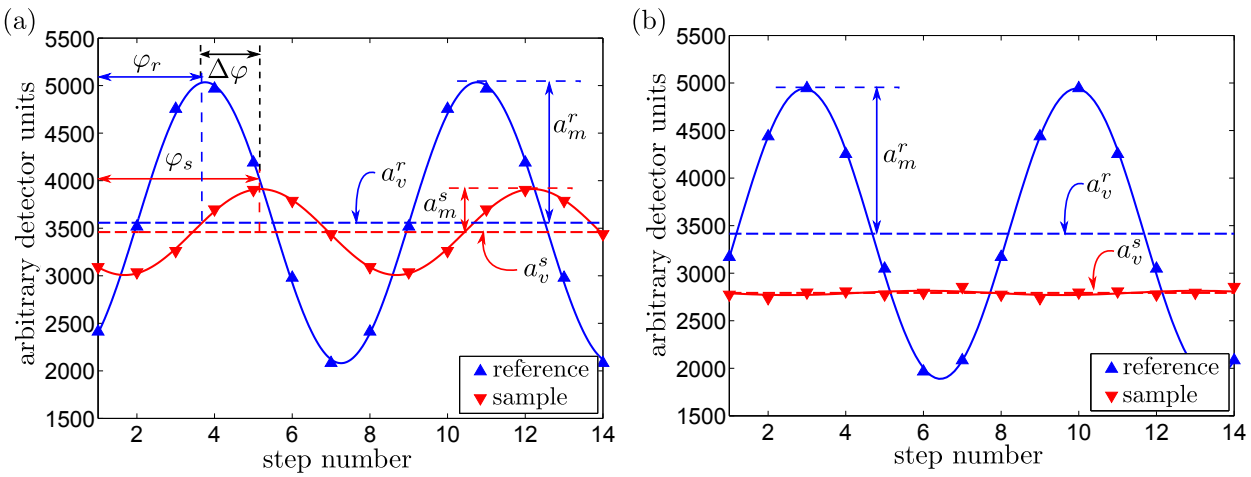

Figure 4.4: Contrast curves extracted from the ant measurements. Red lines and downward-pointing triangles show the contrast curves measured with the sample in the beam; blue lines and upward-pointing triangles are the reference measurements. The presence of the sample strongly modifies the interference pattern produced by G1. In particular, the amplitude is reduced due to scattering and the curve is shifted due to refraction. The intensity modulation can be completely washed out by strong scattering from the sample as shown in panel (b). The phase-stepping scans have been performed over one period. The two-period representation has been obtained by tiling the data.

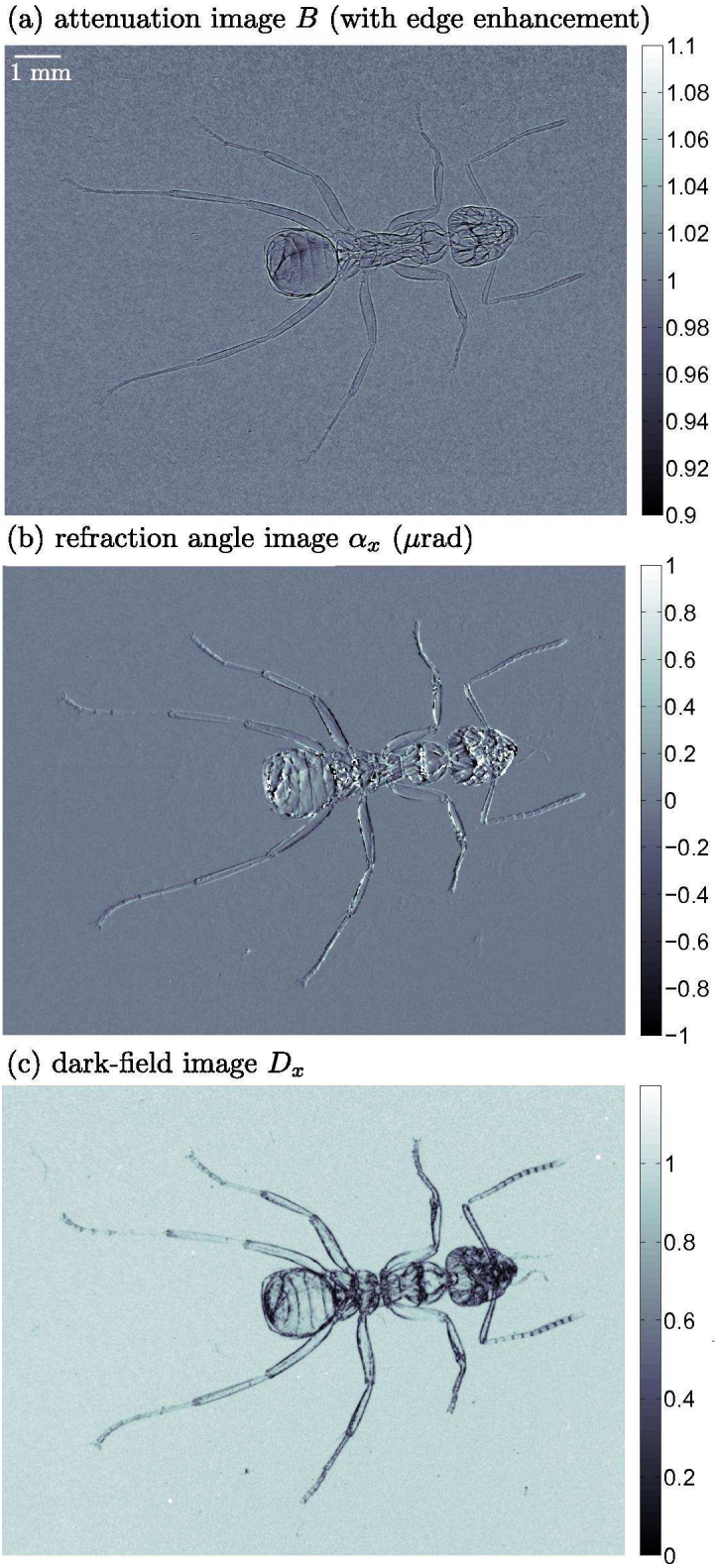

Figure 4.5: Attenuation, refraction angle and dark-field images of an ant extracted from the raw data shown in Fig. 4.3.

G1 (Sec. 3.2.3.3) and can be revealed when the resolution of the detector is better than the separation of the two beams.

The differential phase image The differential phase $\partial\phi/\partial x$ of the incoming wavefront (which is proportional to the refraction angle α_x, cf. Eq. (8.3)) is related to the displacement of the contrast curve $\Delta\varphi = \varphi^{\mathrm{s}} - \varphi^{\mathrm{r}}$:

$$\alpha_x = \frac{2\pi}{\lambda}\frac{\partial\phi}{\partial x} = \Delta\varphi\frac{p_2}{2\pi}\frac{1}{d} \quad . \tag{4.4}$$

The refraction angle image of the ant is shown in Fig. 4.5 (b). While the attenuation signal is isotropic (except for the blurring in x mentioned above), the one-dimensional grating interferometer yields the component perpendicular to the grating lines of the differential phase and dark-field signals. In the measurements of the ant, the grating lines were vertically oriented. For this reason, the horizontal features, which refract X rays mostly in the vertical direction, give much less contrast than the vertical ones. In the refraction angle image, some details, faintly visible in attenuation contrast, can be clearly revealed, such as the segments of the antennas. Note that in some parts of the body of the animal the differential phase signal is corrupted. Three effects can cause the corruption of the differential phase signal:

(i) High attenuation in the sample. In this case, very few photons reach the observation plane, the phase-stepping curve is dominated by noise and its phase is not well defined.

(ii) Strong scattering in the sample. In this case, the visibility of the phase-stepping curve goes to zero (this is shown in Fig. 4.4 (b)) and, as in case (i), the phase of the curve is not well defined.

(iii) Phase-wrapping phenomenon. This phenomenon occurs when the displacement of the interference pattern caused by the sample exceeds one period of the interference pattern. Phase wrapping is a frequent problem in several fields, from medical to military, when the information is extracted from a phase image and several algorithms have been developed for removing the phase ambiguity, see for example Ref. [Ghiglia & Pritt 1998]. A more detailed discussion on the phase-wrapping phenomenon in grating interferometry and on its consequences on the phase tomographies is reported in Sec. 8.2.6.

The dark-field (scattering) image The dark-field signal D_x is calculated as:

$$D_x = \frac{v^{\mathrm{s}}}{v^{\mathrm{r}}} = \frac{a^{\mathrm{s}}_m}{a^{\mathrm{s}}_v}\frac{a^{\mathrm{r}}_v}{a^{\mathrm{r}}_m} \quad , \tag{4.5}$$

where v is the visibility of the intensity oscillation.

The dark-field image of the ant is shown in Fig. 4.5 (c). The dark-field signal obtained with the grating interferometer gives access to features smaller than the spatial resolution of the detector even if these features are not resolved and gives complementary information than the attenuation and differential phase signals, see Ref. [Pfeiffer *et al.* 2008a] and Sec.

2.4 (page 19). In Fig. 4.5 (c), scattering parts in the object, in this case corresponding mainly to the edges of the sample, are represented by dark pixels. Just as the differential phase signal, the scattering signal is directional and horizontal structures show little contrast.

Among recent formalisms developed to describe the scattering signal obtained with the grating interferometer, we point out Refs. [Wang *et al.* 2009, Bech *et al.* 2010, Yashiro *et al.* 2010b, Lynch *et al.* 2011]. In these works, the authors define a scatter coefficient in analogy to the linear attenuation coefficient μ and/or relate the loss in visibility with the geometrical parameters of the microstructures in the investigated objects.

4.2 Data analysis

Since the contrast curve can very often be approximated by a sinusoidal function, it is particularly convenient to obtain average, amplitude and phase of the intensity oscillation by Fourier analysis.

In order to perform this analysis, images are recorded at three or more evenly spaced positions of the scanned grating per period over an integer number of G2 periods. If the phase stepping is performed over P periods in S steps, the intensity measured in the $j-$th step can be written as:

$$I_j = a_v + a_m \cos\left(\frac{2\pi}{p_2} x_{gj} + \varphi\right) \quad , \tag{4.6}$$

where $x_{gj} = jp_2P/S$ with $j = 0, 1, ..., S-1$ is the transverse position of the grating. The vector of recorded intensities can be written as:

$$\bar{I} = (I_0, I_1, ..., I_{S-1}) \tag{4.7}$$

and its Fourier transform $\bar{Y} = (Y_0, Y_1, ..., Y_{S-1})$ has the $k-$th component:

$$Y_k = \sum_{j=0}^{S-1} I_j \exp(-i2\pi kj/S) \quad . \tag{4.8}$$

While the attenuation signal is given by the $0-$th order component, the scattering and the differential phase signals are related to the absolute value and phase of the $P-$th components respectively. Thus, the transmission B, the refraction angle α_x and the dark-field D_x image signals are given by:

$$B = \frac{Y_0^{\mathrm{s}}}{Y_0^{\mathrm{r}}} \quad , \tag{4.9}$$

$$\alpha_x = \frac{p_2}{2\pi}\frac{1}{d}\left[\arg(Y_P^{\mathrm{s}}) - \arg(Y_P^{\mathrm{r}})\right] \quad , \tag{4.10}$$

$$D_x = \frac{|Y_P^{\mathrm{s}}|}{Y_0^{\mathrm{s}}}\frac{Y_0^{\mathrm{r}}}{|Y_P^{\mathrm{r}}|} \quad , \tag{4.11}$$

where "arg" indicates the argument of the complex number.[1]

When higher harmonics are present in the phase-stepping curve, a number of steps greater than three is needed to separate the fundamental from the higher harmonics. The higher harmonics can be present, for example, at small fractional Talbot distances for highly coherent radiation when the intensity profile produced by G1 cannot be approximated by a sinusoidal function.

Stetson et al. calculated the harmonics that cause errors in retrieving the phase of a phase-stepping curve depending on the number of steps [Stetson & Brohinsky 1985]. He showed that, with $P = 5$, the lowest odd order creating errors is the ninth order which is generally very low.[2] The study by Stetson et al. was performed for visible light interferometry and applied by Momose et al. to grating interferometry [Momose *et al.* 2009c]. The author is not aware of any experimental study reported in literature showing the effect of the number of steps on the retrieved image signals. In a standard experiment performed at ID19, phase-stepping scans are performed over one period in three, four or five steps.

4.2.0.1 Alternatives to Fourier analysis

A different way of analyzing phase-stepping data is fitting, pixel by pixel, the intensity curve measured during the scan. The fitting methods are in general computationally expensive and therefore less adapted to process a large amount of data than Fourier analysis. Their main advantage, on the other hand, is that they can be applied to non-sinusoidal contrast curves and/or non-evenly stepped curves. Besides fitting routines and Fourier methods, phase and amplitude of the contrast curve can be extracted with analytical formulas. Several formulas have been introduced with this purpose in phase-stepping visible light interferometry as discussed in Ref. [Hack & Burke 2011]. It should be noticed that one of the most commonly used formulas in visible interferometry, the Bruning's algorithm [Bruning *et al.* 1974], is equivalent to Fourier analysis when phase-stepping scans are performed over one period.

4.2.1 Image noise

Noise in the final images is related to noise in the raw interferograms. Various models describing noise in the radiographs and tomograms obtained with the X-ray grating interferometer have been recently reported in literature, with special focus on the noise in the differential phase signal [Yashiro *et al.* 2008, Engel *et al.* 2011, Revol *et al.* 2010, Raupach & Flohr 2011]. Among these, we report here the main result obtained by Engel et al. [Engel *et al.* 2011]. The authors express the variance σ_d^2 of the differential phase signal measured in a pixel as a function of the total number N_p of photons recorded in the same pixel during the entire phase-stepping scan and of the visibility v of contrast curve [Engel *et al.* 2011]:

[1] Note that every detector frame, i.e. flat-field interferograms and interferograms of the sample, is corrected, before undergoing any further processing, for the dark-signal image which is recorded without the X-ray beam and with the same exposure time than the other images.

[2] Even orders should not be present in the contrast curve since it is given by a convolution of a rectangular profile with a sinusoidal profile.

$$\sigma_d^2 \propto \frac{1}{v^2 N_p} \quad . \tag{4.12}$$

The equation above has been obtained by assuming that higher orders are not present in the phase-stepping curve, that the noise for each exposure is described by photon shot noise and that there is no error in the grating positioning. Equation (4.12) clearly shows the strong influence of the visibility on the quality of the differential phase image.

4.3 Practical implementation

The visibility of the contrast curve, and therefore the quality of the final images, is influenced by a big variety of factors such as partial coherence, grating imperfections, inter-grating distance and detector response. This section discusses the interferometer parameters which should be carefully chosen for the practical implementation of a grating interferometer in order to optimize the performance of this instrument.

4.3.1 Choice of the fractional Talbot distance

The inter-grating distance d_n which satisfies Eq. (4.2) is chosen considering several aspects, such as mechanical limitations (very short or very large fractional Talbot distances may be difficult to realize) and more importantly, it is tuned to optimize spatial resolution and sensitivity.

The spatial resolution in the final images is affected by the shearing distance s of the beams diffracted by G1. This distance, given by Eq. (3.26) (page 30), increases linearly with the inter-grating distance. Therefore, the spatial resolution can be improved by working at small fractional Talbot distances.

The sensitivity here defined as the resolution in the measured refraction angle, is affected by the inter-grating distance d_n in two opposite ways. By decreasing the distance d_n:

1. The displacement of the interference pattern caused by refraction becomes smaller. This decreases the sensitivity of the system.
2. The projected source size becomes smaller and the visibility of the interference pattern becomes larger. This increases the sensitivity of the system.

In the choice of the fractional Talbot distance, one should also consider the phase-wrapping phenomenon which is more likely to occur at large inter-grating distances.

At ID19, inter-grating distances from 150 mm to up to 600 mm have been implemented up to now.

4.3.2 Grating design

The design of the optical elements is another important aspect for the implementation of a grating interferometer. For each grating, the material and three parameters should be defined: the duty cycle γ, the period p and the height h of the grating lines. In the following the subscripts 1 and 2 will indicate which grating these parameters refer to, e.g. γ_1 is the duty cycle of the phase grating G1.

4.3.2.1 The materials

The phase grating must be fabricated in a material with a high δ/β ratio at the working energy in order to have nearly ideal (non absorbing) phase gratings. Among the materials which are used for fabricating phase gratings are silicon and nickel.

The absorption grating must be made of a material with high β. The material most commonly used for fabricating absorption gratings is gold.

4.3.2.2 The duty cycles

The duty cycle of the phase grating must be $\gamma_1 = 0.5$. In this way a $\pi-$shifting phase grating generates an interference pattern with half of the period of the grating and both $\pi-$ and $\pi/2-$shifting phase gratings generate interference patterns with the desired duty cycle of 0.5, see Sec. 3.2.3.

The duty cycle γ_2 of the absorption grating affects the intensity transmitted onto the detector and the visibility of the contrast curve. By increasing the width of the absorbing lines (i.e. by increasing γ_2), the visibility increases whereas the intensity transmitted onto the detector decreases. By considering these two aspects, a numerical study shows that 0.6 is a suitable value for γ_2 [Modregger *et al.* 2011]. In practice, the duty cycle of the absorption grating is often chosen to be γ_2 =0.5.

4.3.2.3 Period and height of the absorption grating

The lines of G2 should be high enough to absorb most of the incoming radiation because transmission by G2 lines reduces the visibility of the contrast curve and therefore degrades the image quality. Figure 4.6 shows results of a simulation which quantifies the effect of unwanted transmission by the G2 lines on the visibility of the contrast curve. The visibility of the contrast curve has been calculated for different transmission of the grating lines, from 0% to 80% (x axis of the image), and for different visibilities, from 0% to 100%, of the sinusoidal interference pattern produced by G1. Figure 4.6 shows, for example, that if the transmission of the grating lines is 10%, the visibility of the contrast curve is almost half of the visibility of the interference pattern.

The absorption gratings should not only have high absorbing lines, but also a very small line width in order to match the period of the interference pattern. The absorption gratings used at ID19 are produced with the LIGA process[3] at the Karlsruhe Insitute of

[3]LIGA is a German acronym which means *LIthographie, Galvanoformung, Abformung*, i.e. lithography, electroplating, and molding.

Technology (KIT, Karlsruhe, Germany) with a period $p_2 = 2.4$ μm [Reznikova *et al.* 2008, Kenntner *et al.* 2010]. Gratings with aspect ratio (the aspect ratio is defined here as line height h_2 divided by line width $p_2/2$) of more than 80 ($h_2 \approx 100$ μm) can be currently produced at KIT and are used at ID19.

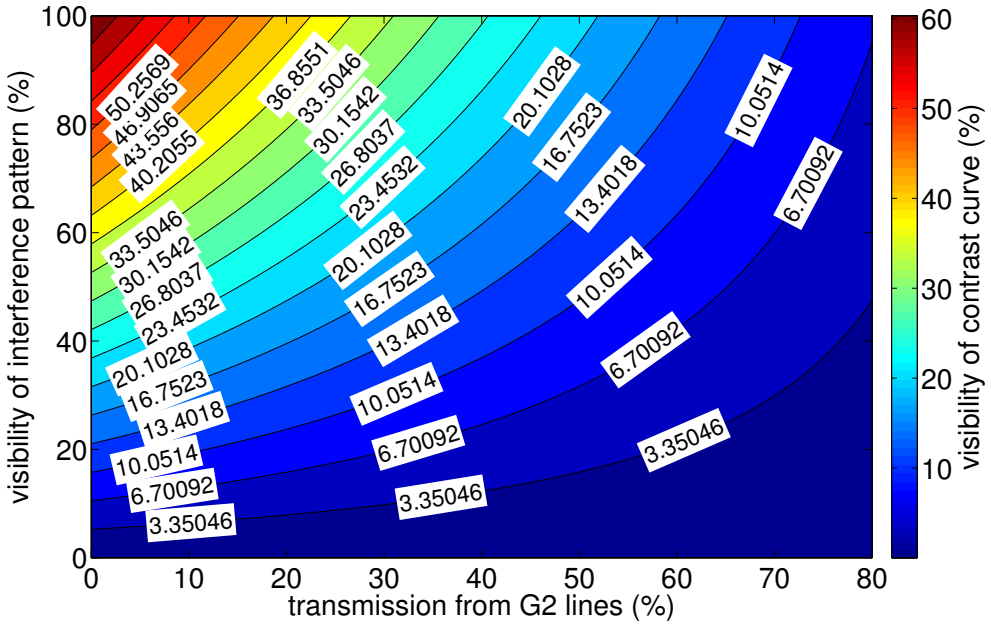

Figure 4.6: Simulated visibility of the contrast curve for different transmission by the G2 lines. The intensity pattern generated by G1 is a sinusoid with visibility from 0% to 100% as reported in the y axis.

4.3.2.4 Period and height of the phase grating

When designing an interferometer for different working energies and/or inter-grating distances, it is convenient to use a single absorption grating with an height sufficient to ensure good absorption at all working energies, and use different phase gratings, one for each configuration, whose period and height are adapted to the distance and photon energy. This is because a phase grating with a given height h_1 produces the desired phase shift only at a particular X-ray photon energy.

Since the material of the grating is known and its refractive index decrement δ at the working energy can be looked up, h_1 can be easily calculated with Eq. (2.8) (page 10). For example, a $\pi-$shifting Si grating at 23 keV should have $h_1 = 29.5$ μm.

In phase-stepping interferometry, the period $p_{1,n}$ of the phase grating should be designed so that its magnified image at the distance d_n has the same period as G2:

$$p_2 = \frac{p_{1,n}}{\eta}\frac{R + d_n}{R} \quad . \tag{4.13}$$

By combining the above equation with Eq. (4.2), which, for convenience, is rewritten here:

$$d_n = n\frac{p_{1,n}^2}{2\eta^2\lambda}\frac{R + d_n}{R} \quad , \tag{4.14}$$

the quantities $p_{1,n}$ and d_n can be derived as a function of p_2, the source-to-G1 distance R and the wavelength of radiation λ:

$$p_{1,n} = \frac{\eta\lambda R}{np_2}\left(\sqrt{1+\frac{2np_2^2}{\lambda R}}-1\right) \tag{4.15}$$

$$d_n = \frac{np_{1,n}^2 R}{2\eta^2\lambda R - np_{1,n}^2} \quad . \tag{4.16}$$

Using Eqs.(4.15) and (4.16) and for $n = 9$, an X-ray photon energy of 23 keV, $R = 150$ m and $p_2 = 2.4$ μm, the period $p_{1,9}$ of the $\pi-$shifting phase grating results $p_{1,9} = 4.785$ μm and the inter-grating distance is $d_9 = 479$ mm.

Figure 4.7 shows intensity profiles produced, under otherwise identical conditions by $\pi-$shifting phase gratings with two types of imperfections: (i) wrong thickness of the grating lines (dotted line in Fig. 4.7) and (ii) wrong duty cycle (dashed line in Fig. 4.7). These profiles should be compared to the one obtained under ideal conditions and plotted with a solid line. Both defects cause the loss of the frequency doubling effect which reduces the visibility of the fundamental harmonic.

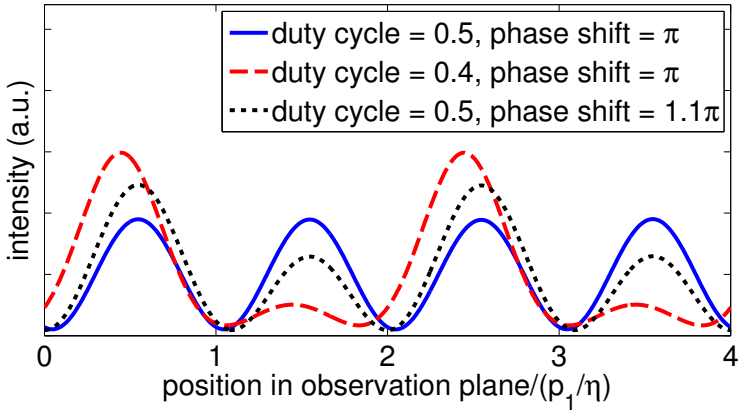

Figure 4.7: Simulated profiles of the interference pattern from phase gratings with different types of imperfections.

Most of the phase gratings used at ID19 are produced at the Paul Scherrer Institute (PSI, Villigen, Switzerland) and made in silicon [David *et al.* 2007]. The fabrication process consists in a sequence of photolithography, anisotropic wet etching and electroplating [David *et al.* 2007]. Some of the phase gratings used at ID19 are produced at KIT in silicon or nickel; their fabrication process is similar to the process used for absorption gratings.

At ID19, several setups for different energies and fractional Talbot distances have been implemented during this PhD project. The list of currently available configurations is reported in Sec. 7.3.

The grating substrate Grating lines are not free standing structures. They are fabricated on a support wafer with thickness of hundreds of micrometers. The typical material of the wafer is silicon. If the substrate is polished on both sides, the presence of the substrate

does not have any effect on the visibility of the phase-stepping curve and, in this sense, does not influence the image quality. However, absorption in the silicon wafer should be taken into account especially at low X-ray energies. Absorption in the wafers increases exposure time and dose delivered to the sample. At ID19, gratings fabricated on Si wafers with thickness from ≈200 to ≈500 μm are used. The absorption in these wafers, calculated from Eq. (2.6) for energies from 15 keV to 50 keV (the absorption is negligible for energies larger than 50 keV), is shown in Fig. 4.8.

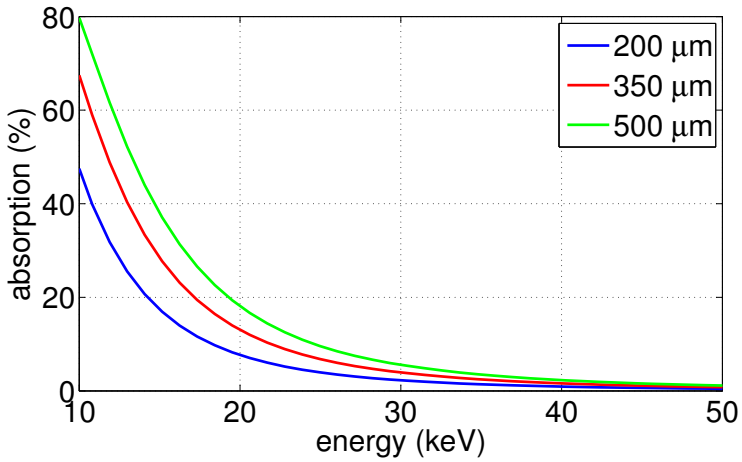

Figure 4.8: Absorption in Si a single wafers, as a function of the photon energy. In different colors are plotted curves calculated for different thickness of the substrates.

4.4 Moiré imaging

In the previous sections we have described the principles of grating interferometry based on the phase-stepping technique. An alternative way to retrieve the differential phase and scattering signals using the same instrument is to directly analyze the single-shot moiré patterns distorted by the sample. Moiré patterns in the raw interferogram are generated by rotating one grating with respect to the other around the optical axis.

The main advantage of moiré imaging is that it is a single-shot technique: as opposed to phase stepping it does not require multiple exposures to retrieve the image signals. However, the spatial resolution is lower than the one obtained with phase stepping.

In moiré imaging, the spatial resolution in the direction orthogonal to that of the moiré fringes is limited by the period of the fringes. For this reason, raw interferograms with a large number of fringes are collected in moiré mode.

The effect of the sample on the moiré pattern is analogous to the effect of the sample on the contrast curve recorded in phase stepping. The phase shift caused by the sample displaces the moiré fringes and scattering scattering causes a blurring of the pattern. Algorithms based on Fourier analysis can be used to extract differential phase and scattering signals from the moiré pattern [Takeda *et al.* 1982].

The moiré technique was used in the first implementations of the two-grating interferometer [David *et al.* 2002, Momose *et al.* 2003] and is currently mainly used for wavefront and

optics characterization [Pfeiffer *et al.* 2005, Weitkamp *et al.* 2005b, Diaz *et al.* 2010] and high-speed tomography [Momose *et al.* 2009b, Momose *et al.* 2011b].

Since moiré imaging requires only one exposure per differential phase and scattering projection, very fast tomography scans can be realized with the grating interferometer operating in moiré mode especially when high photon flux, such as the white beam at a synchrotron beamline, is available. As an example, Momose et al. report on tomography scans performed in 0.5 s [Momose *et al.* 2011b].

Chapter 5

Grating-based tomography

Contents

X-ray computerized tomography, or simply tomography, is a non-destructive technique to visualize internal structures in objects. It consists in recording a series of projection images of the sample, taken from different directions. These projections are combined with appropriate algorithms so that the three-dimensional distribution of an optical property of the investigated object can be retrieved. The reconstructed quantity depends on the signal recorded in the projections. Attenuation, phase and dark-field tomographies can be obtained with an X-ray grating interferometer as described in this chapter.

5.1 Principles of tomography

The development of computerized tomography is attributed to Allan McLeod Cormack [Cormack 1963] and Godfrey Hounsfield [Hounsfield 1973] who both received the Nobel prize in Medicine in 1979 for the development of computer-assisted tomography. An exhaustive description of the principles of tomography can be found in several books, see for example Refs. [Natterer 1986, Kak & Slaney 1987, Hsieh 2003].

Several algorithms can be used for reconstructing volumes from projections: e.g. algebraic reconstruction techniques, iterative methods, direct Fourier transform methods and the filtered-back projection algorithm. When data are recorded with sufficient and regular angular sampling over at least 180° the reconstruction is often performed with the filtered-back projection (FBP) algorithm because it provides accurate reconstructions much faster than the iterative methods. The principles of the FBP algorithm, which has been used to reconstruct the data in this thesis, are outlined in the following.

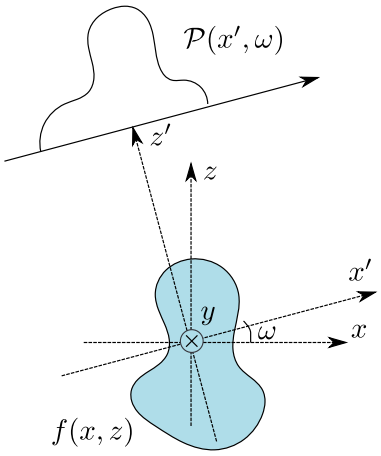

Figure 5.1: Geometry used to explained the principles of the filtered back-projection algorithm. The region shaded in blue represents the support of f. In this representation, the coordinate system (x, z) is fixed with respect to the sample and the coordinate system (x', z') is fixed with respect to the source and detector.

5.1.1 The filtered-back projection algorithm

Let $f(x, y, z)$ be the three-dimensional distribution of an optical property of the investigated object and let y be the rotation axis, as represented in Fig. 5.1. The function $f(x, y, z)$ can be reconstructed with the FBP algorithm, as a stack of slices $f(x, z)$ orthogonal to the rotation axis y, provided that the angular projections of $f(x, y, z)$ are measured for an angular range over at least 180° and assuming sufficient angular and spatial sampling. [1]

In the following, we fix y and we concentrate on a single slice $f(x, z)$ (Fig. 5.1). The projection $\mathcal{P}(x', \omega)$ of the slice $f(x, z)$ at the angle ω can be written as:

$$\mathcal{P}(x', \omega) = \int f(x' \cos\omega - z' \sin\omega, x' \sin\omega + z' \cos\omega) dz' \quad , \tag{5.1}$$

where (x', z') is a coordinate system rotated by an angle ω with respect to the coordinate system (x, z). The central theorem for tomographic reconstructions is the Fourier slice theorem which states that the one-dimensional Fourier transform of the function $\mathcal{P}(x', \omega)$ represents a section of the two-dimensional Fourier transform of the function $f(x, z)$ tilted by and angle ω with respect to the origin.

Using this property, $f(x, z)$ can be reconstructed from the projections $\mathcal{P}(x', \omega)$ with the convolution *back-projection* integral:

$$f(x, z) = \int_0^{\pi} \mathcal{P}_{\mathrm{f}}(x \cos\omega - z \sin\omega, \omega)\, \mathrm{d}\omega \, . \tag{5.2}$$

Here, $\mathcal{P}_{\mathrm{f}}$ is a *filtered* projection

$$\mathcal{P}_{\mathrm{f}}(x', \omega) = \int_{-\infty}^{\infty} k(v) \widetilde{\mathcal{P}}(v, \omega) \mathrm{e}^{\mathrm{i}2\pi v x'}\, \mathrm{d}v \, , \tag{5.3}$$

[1] It can be shown that the sufficient number of angular projections N_{proj} is proportional to the width in pixels of a projection N_{pix} with the relation: $N_{\mathrm{proj}} \approx \pi N_{\mathrm{pix}}/2$.

where $k(v)$ is the filter function in Fourier space, v is the reciprocal space coordinate and $\widetilde{\mathcal{P}}(v,\omega)$ is the one-dimensional Fourier transform of $\mathcal{P}(x',\omega)$.

In grating interferometry, three image signals (i.e. attenuation, refraction angle and dark-field) are measured for each tomography angle ω (Fig. 5.2). Each set of projections yields a different tomographic volume. The reconstruction of the attenuation, phase and dark-field volumes with the filtered back-projection algorithm is described in the following.

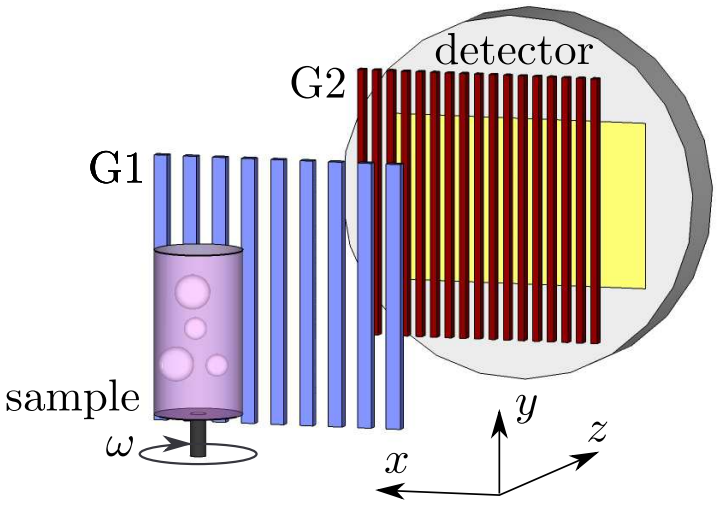

Figure 5.2: Schematic representation of a grating-based tomography setup. In order to retrieve the phase tomograms, the grating lines are parallel to the tomography rotation axis.

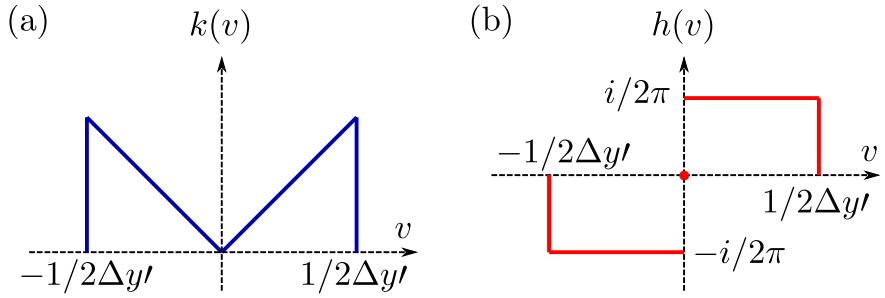

Figure 5.3: Filters used in the back-projection algorithm. The ramp filter (a) is used in the attenuation and dark-field reconstructions. The imaginary sign filter (b) is used in the phase reconstruction from differential phase projections [Pfeiffer *et al.* 2007b]. The sampling of the image detector is not continuous, for this reason, if $\Delta y'$ is the sampling resolution, the filters are defined in the interval $[-1/2\Delta y', +1/2\Delta y']$.

5.2 The attenuation tomogram

The signal measured in the attenuation image is the one reported in Eq. (2.4) (page 9):

$$B(x',\omega) = e^{-\int \mu(x,z)dz'} \quad . \tag{5.4}$$

The projection $\mathcal{P}(x',\omega)$ of the linear attenuation coefficient $\mu(x,z)$ of the object is obtained by taking the logarithm of $B(x',\omega)$: $\mathcal{P}(x',\omega) = -\log\left[B(x',\omega)\right]$. The quantity reconstructed in the tomogram is the linear attenuation coefficient which, for monochromatic radiation, is proportional to the imaginary part of the refractive index of the sample $\beta(x,z)$, cf. Eq. (2.5) (page 9).

The filter $k(v)$ commonly used to retrieve the attenuation volume is a linear ramp filter, $\widetilde{k}(v) = |v|$ (Fig. 5.3 (a)). As thoroughly explained in Ref. [Kak & Slaney 1987], this filter is chosen to compensate for the fact that the sampling density decreases from the regions close to the rotation axis to the regions close to the sample edge.[2]

By substituting the shape of the ramp filter into Eq. (5.3), the filtered projection becomes:

$$\mathcal{P}_{\mathrm{f}}(x',\omega) = \int_{-\infty}^{\infty} |v|\widetilde{\mathcal{P}}(v,\omega)\mathrm{e}^{\mathrm{i}2\pi v x'}\,\mathrm{d}v\,, \tag{5.5}$$

5.3 The phase tomogram

In the phase tomogram, the three-dimensional distribution of δ is retrieved from refraction angle projections $\mathcal{D}(x',\omega) = \alpha(x',\omega)$ which, according to Eq. (8.3) (page 88), are given by

$$\mathcal{D}(x',\omega) = \alpha(x',\omega) = \frac{\partial}{\partial x'}\int \delta(x,z)dz' \quad . \tag{5.6}$$

The quantity from which the tomographic volume $\delta(x,y,z)$ is reconstructed is thus not a projection of δ but a projection of its first derivative in the direction perpendicular to the grating lines. The reconstruction of the phase tomogram thus involves an integration step which can be performed in real space or in Fourier space:

1. *Integration in real space.* Numerically this can be done by integrating the projections, for example with a cumulative sum. Once the projections are integrated, the phase can be reconstructed with the same procedure used for the attenuation data, Eqs. (5.2) and (5.5).

2. *Integration in Fourier space* [Pfeiffer *et al.* 2007b]. It is based on the Fourier theorem for derivatives which states that:

$$\mathcal{FT}\left[\frac{df(x)}{dx}\right] = 2\pi i v\left[\widetilde{f}(v)\right]. \tag{5.7}$$

Using Eq. (5.7), Eq. (5.3) can be written as

$$\mathcal{P}_{\mathrm{f}}(x',\omega) = \int_{-\infty}^{\infty} h(v)\widetilde{\mathcal{D}}(v,\omega)\mathrm{e}^{\mathrm{i}2\pi v x'}\,\mathrm{d}v\,, \tag{5.8}$$

[2]Note that filters different than the ramp filter can be used in the back-projection algorithm in order, for example, to suppress high-frequency noise or reconstruct correctly the low-frequency components. Other filters and their properties are described in Ref. [Kak & Slaney 1987].

where $h(v)$ is the imaginary sign filter:

$$h(v) = \frac{|v|}{2\pi i v} = \frac{1}{2\pi i \mathrm{sign}(v)} \quad . \tag{5.9}$$

The imaginary filter is shown in Fig. 5.3 (b) and it corresponds to Hilbert filtering in the real space [Pfeiffer *et al.* 2007b]. The advantage of this reconstruction method over integration in real space is that no additional steps, such as integration of the differential phase projections, are required in the reconstruction procedure. Moreover, it reduces artifacts in the reconstruction caused by the unknown integration constant as an integration in real space. The latter aspect is particularly important in local tomography. Integration in Fourier space can be performed only if the grating lines are parallel to the rotation axis as shown in Fig. 5.2.

Measurement of the refractive index Sections 5.2 and 5.3 showed that, when the sample is illuminated by monochromatic radiation, the full refractive index of the sample can be measured with grating-based tomography: the real and the imaginary part of the refractive index are reconstructed, respectively, in the phase and the attenuation tomograms. However, several factors can affect the quantitative accuracy of the tomographic measurements, such as the presence of propagation-based phase contrast or the phase-wrapping phenomenon. The effect of phase wrapping in the phase tomogram is discussed in Chap. 8 and Ref. [Zanette *et al.* 2011d].

When polychromatic radiation is used, it is convenient to interpret the measured polychromatic data with an effective refractive index which corresponds to the weighted sum of the values of refractive index obtained with the monochromatic X rays of the photon energy spectrum [Herzen *et al.* 2009]. The refractive index resolution obtained with a polychromatic beam is in general inferior to that obtained with monochromatic radiation and artifacts such as beam-hardening effects may disturb the phase tomogram [Chabior *et al.* 2011].

5.4 The dark-field tomogram

Dark-field projections are usually treated in analogy to attenuation projections. The dark-field volume is obtained by applying the filtered back-projection algorithm with a ramp filter to the logarithm of D_x (Eq. (4.5)). Formalism developed to relate the reconstructed dark-field signal to known physical quantities are under way, see for example Refs. [Wang *et al.* 2009, Bech *et al.* 2010, Lynch *et al.* 2011] in which dark-field tomograms of phantom samples are reported.

5.5 Example: fossilized insect in amber

Figure 5.5 shows attenuation, phase and dark-field tomograms of an insect in opaque amber. Amber is a low-density material, mainly composed of carbon, hydrogen and oxygen with average density around 1.1 g/cm^3 similar to the density of plastic materials. The tomograms

shown in Fig. 5.5 have been reconstructed from 3000 projections recorded over 360°. Each attenuation, differential phase and dark-field projection (see Fig. 5.4) was retrieved from a phase-stepping scan taken over one period in four steps.

Figure 5.4: (a) Attenuation, (b) differential phase and (c) dark-field (c) projections of the insect in amber obtained during the tomography scan which gave the results shown in Fig. 5.5.

The reconstruction algorithm provides slices orthogonal to the rotation axis, these axial slices are shown in the left column of Fig. 5.5 (panels (a), (d) and (g)). When the full volume is reconstructed, it is possible to visualize slices on any arbitrary plane. Sagittal slices extracted in planes orthogonal to the axial slices are shown in the central and right columns of the figure.

The signal produced by the fossilized insect is much stronger in the phase than in the attenuation tomogram. In the attenuation images, the edge-enhancement effect is present as a couple of bright and dark stripes along the borders of the insect. The edges of the insect are the parts which give the strongest contrast in the dark-field tomogram. Note that the wings of the animal can be more easily detected with the dark-field and phase signals than with the attenuation signal, see circle in Fig. 5.5 (c), (f) and (i). The dark-field signal is also sensitive to the presence of cracks in the amber. For example, the crack indicated with arrows in Fig. 5.5 (h) can only be seen with the dark-field signal.

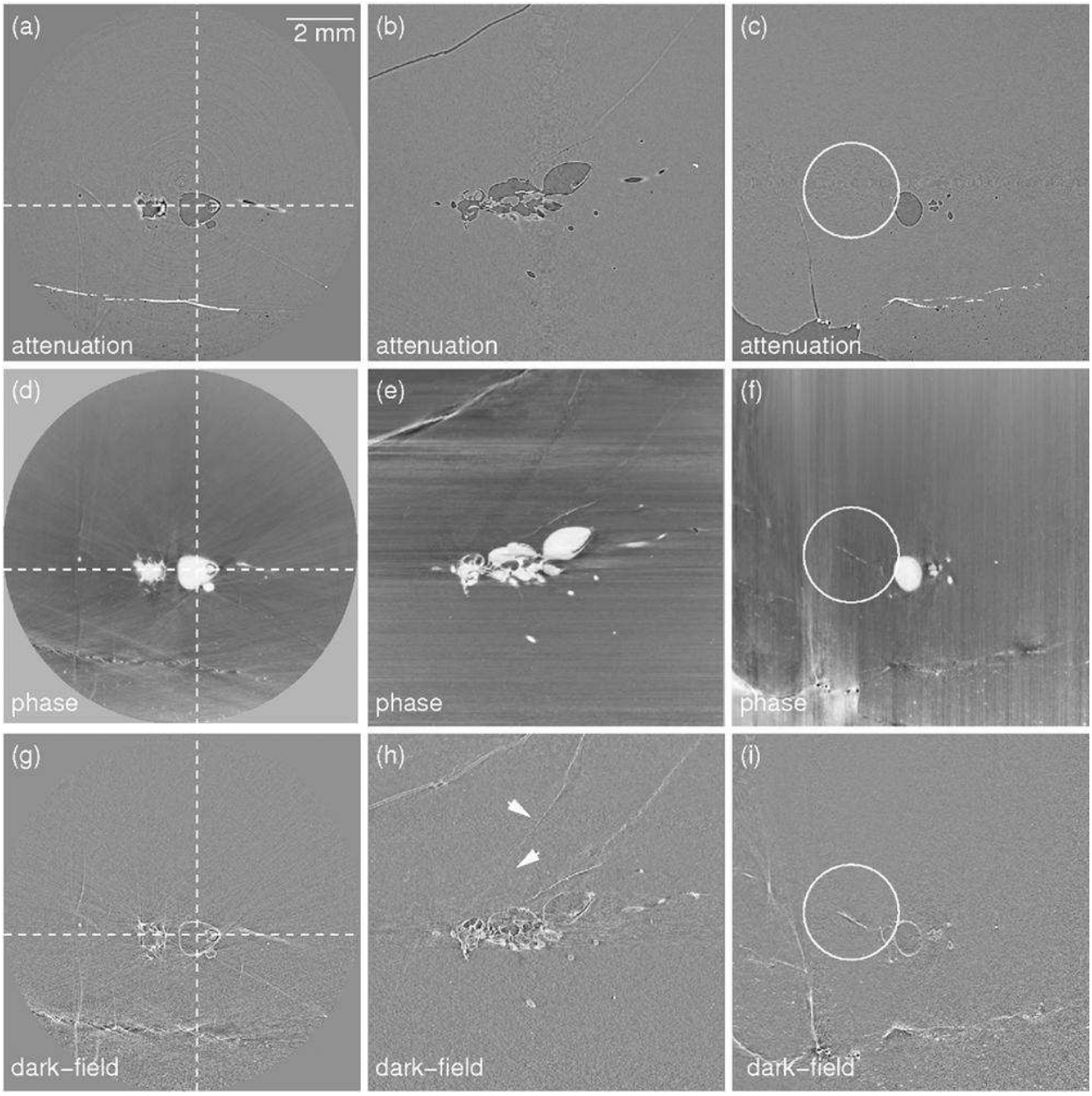

Figure 5.5: Attenuation (a)-(c), phase (d)-(f) and dark-field (g)-(i) tomograms of an insect in opaque amber. The first column shows axial slices. The center and right columns display sagittal slices in planes orthogonal to each other and orthogonal to the axial slices at the left. Positions at which these sagittal slices are extracted from the volume are indicated in the axial slices with dashed lines. This measurement has been performed at beamline ID19 with the interferometer described in the next chapters at an X-ray photon energy of 35 keV. The distance between the $\pi-$shifting G1 and G2 was 404 mm corresponding to the 5th fractional Talbot order. The pixel size was 5 μm and the exposure time per interferogram was 2 s.

Chapter 6
State of the art of X-ray grating interferometry

Contents

X-ray grating interferometers as the one described in Chap. 4 have been been implemented at third-generation synchrotrons such as the ESRF (the interferometer at ESRF-ID19 was implemented during this thesis project, see Chap. 7), the Swiss Light Source in Switzerland [McDonald *et al.* 2009] and Spring-8 in Japan.

In the past years, variations to the standard device described in the previous chapter have been proposed to adapt the interferometer to low-brilliance sources, improve image quality and reduce the dose delivered to the sample. The purpose of this chapter is to describe the state of the art of grating interferometry by presenting recent contributions in this field.

This chapter consists of two sections:

(i) Section 6.1 gives a review of developments which have been implemented outside of this thesis project, mostly by other groups;

(ii) Section 6.2 presents recent works to which the author has significantly contributed during her thesis project.

The achievements of the author's work in which she had a leading role are not listed here because they are extensively presented in Chapters 10 and 11.

6.1 Developments by other groups

6.1.1 X-ray Talbot-Lau grating interferometer

Chapter 4 describes the principles of a two-grating interferometer which works at a third-generation synchrotron beamline where the transverse coherence of the radiation is enough to observe good fringe visibility up to large inter-grating distances of tens of centimeters. As explained in Sec. 3.3.2.1, an interferometer like this would not work on laboratory X-ray tubes and on second-generation synchrotrons because of the limited transverse coherence of the radiation provided by these sources. Moreover, at these facilities, it would not be practically feasible to simply slit down the source to increase the visibility because this would also decrease the photon flux to unacceptably low values.

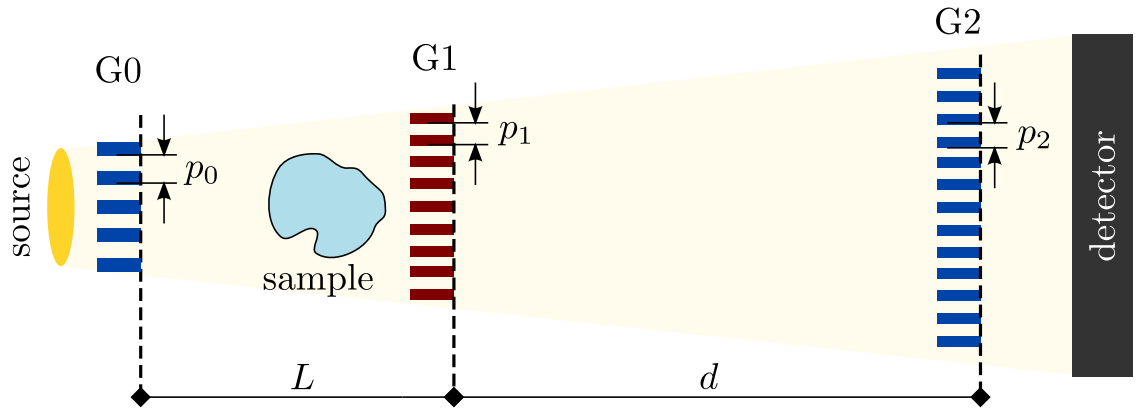

Figure 6.1: Schematic representation of a Talbot-Lau interferometer.

A solution to this problem was found by Pfeiffer et al. [Pfeiffer *et al.* 2006] who implemented the so-called Talbot-Lau[1] interferometer, see Fig. 6.1. This interferometer is very similar to the standard grating interferometer except that an additional line grating G0 is inserted in the beam path. G0 is an absorption grating placed between the source and the phase grating in order to create an array of line sources. The period p_0 of G0 is chosen so that the intensity pattern originated by each of these apertures adds constructively on the observation plane. The period p_0 is given by:

$$p_0 = p_2 \frac{L}{d} \quad , \tag{6.1}$$

where L is the G0-to-G1 distance, p_2 is the period of G2 and d is the G1-to-G2 distance. The different possible geometrical configurations satisfying Eq. (6.1), e.g. $L < d$, $L = d$ or $L > d$, have been studied and their effect on the image quality has been discussed in Ref. [Donath *et al.* 2009].

As the grating G2, the grating G0 is usually made of gold. The duty cycle is chosen as a compromise between visibility (gratings with larger duty cycles give higher visibility)

[1]The Lau effect is the generation of a fringe pattern by a pair of gratings under incoherent illumination [Lau 1948].

and photon flux on the observation plane (gratings with larger duty cycles transmit less photons).

The radiation produced by a conventional X-ray generator is polychromatic. The phase grating and the inter-grating distance d are designed for the mean energy of the polychromatic beam. The quality of phase and absorption tomographies obtained with a Talbot-Lau interferometer have been studied by Herzen et al. [Herzen *et al.* 2009] using a laboratory source without a monochromator at the Paul Scherrer Institute (Villigen, Switzerland). With the same set up, the potential of the Talbot-Lau interferometer for future clinical applications has recently been investigated on human ex-vivo samples [Donath *et al.* 2010, Stampanoni *et al.* 2011].

Another aspect to consider in the implementation of a grating interferometer at conventional X-ray sources is that, at these sources, the wavefront is strongly spherical. X rays impinge on the grating lines with different angles depending on the distance from the optical axis. With increasing incidence obliquity the projected profiles of the gratings first become trapezoidal, then triangular and eventually more and more washed out. For this reason, at conventional X-ray generators, the visibility decreases with the distance from the optical axis. A way to reduce this problem is to adapt the gratings to the shape of the wavefront by curving them [David *et al.* 2005, Revol *et al.* 2011].

Other developments in three-grating interferometry go in the direction of minimizing the number of optical elements in the beam path. Momose et al. proposed to substitute the source grating G0 with a grooved rotation anode [Momose *et al.* 2009a]. In a more recent work, Momose et al. suggested the implementation of a Lau interferometer by completely removing the absorption grating G2 [Momose *et al.* 2011a].

The Talbot-Lau interferometer was developed at X-ray laboratory sources and has subsequently been implemented at the second-generation synchrotron DORIS, Hamburg, Germany see Ref. [Herzen *et al.* 2010] A first implementation of a three-grating interferometer at the Brazilian Synchrotron, Laboratório Nacional de Luz Síncrotron in Campinas, Brazil has been performed during this PhD project.

6.1.2 Grating interferometry without phase stepping

In Sec. 4.4 we have seen that a grating interferometer operating in moiré mode can be used for single-shot (without phase stepping) differential phase and scattering imaging. We have also seen that the main disadvantage of moiré imaging is that the spatial resolution is limited by the period of the moiré fringes.

Recently, two different methods have been proposed for single-shot grating interferometry which does not consist in recording a moiré pattern and thus do not degrade the spatial resolution of the imaging system [Zhu *et al.* 2010, Diemoz *et al.* 2011]. Although the methods proposed by Zhu et al. and Diemoz et al. differ in the acquisition procedure and the retrieved signal, they have some aspects in common:

(1) they require a perfect alignment of the gratings: all over the field of view the relative position of the two gratings should be adjusted so that the signal recorded in each pixel

is at the same position on the flank (point at which the derivative is maximum) of the contrast curve;

(2) the signal retrieval is based on a linearization of the curve around its flank;

(3) dark-field signal is not accessed.

Zhu et al. propose to combine the projection taken for a viewing angle of ω degrees (where $\omega \in [0, \pi[$) with the projection taken for the viewing angle of $\pi + \omega$ degrees [Zhu *et al.* 2010]. They demonstrate that a linear combination of these two projections allows to separate the differential phase signal from the absorption signal.

Diemoz et al. exploit the fact that raw interferograms contain both absorption and differential phase information [Diemoz *et al.* 2011]. If images are taken at the flank of the contrast curve, the quantity reconstructed in the tomogram can be approximated by a linear combination of the attenuation coefficient and the gradient of the decrement of the refractive index provided that the rotation axis is orthogonal to the grating lines (thus perpendicular to the direction in the standard implementation).

The main limitation of the methods proposed by Diemoz et al. and Zhu et al. is that, for being in the flank of the contrast curve over all the field of view, the gratings must be extremely carefully aligned which is a difficult task already at synchrotron beamlines where the radius of curvature of the wavefront is very large. At conventional X-ray tubes, where the wavefront is much more divergent, this alignment would be more difficult.

6.1.3 Single or double grating set-up in magnified geometry

Magnified geometry is used in order to increase the spatial resolution at the object plane.

In Ref. [Engelhardt *et al.* 2007a], the authors report on the implementation of a grating interferometer with a laboratory microfocus X-ray source. Since the source size is of few micrometers, the source grating is not needed in such a setup.

In Ref. [Takeda *et al.* 2008], a two-grating interferometer is implemented with a Fresnel zone plate X-ray microscope at a synchrotron facility. Yashiro et al. used a similar setup with a single phase grating [Yashiro *et al.* 2009] and measured a spatial resolution at the object plane of 480 nm. In this microscope, the large grating-to-detector distance allows to obtain what the authors call *twin phase images* generated by the two beams departing from the grating. Further theory on this subject can be found in Ref. [Yashiro *et al.* 2010a].

It should be noted that, although magnified geometry allows to increase the spatial resolution at the object plane, it also decreases the sensitivity of the imaging system which is inversely proportional to the magnification.

6.1.4 Fourier imaging with a transmission grating

Fourier imaging with gratings is in many ways similar to grating interferometry although it does not exploit the interference effect for generating the image contrast [Wen *et al.* 2009, Bennett *et al.* 2010, Wen *et al.* 2010]. This method was implemented at a laboratory X-ray generator and uses a commercially available grid mask which induces a periodic modulation

in the incoming wavefront. The modulation produced by the mask, after the X rays propagate through the sample, is directly resolved by the image sensor. An algorithm based on the Fourier transform [Takeda *et al.* 1982] applied to the raw images allows to obtain, as in grating interferometry, the component perpendicular to the grating lines of the differential phase and the scattering signal, plus the conventional absorption image.

6.1.5 Phase-contrast imaging with coded apertures

The method based on coded apertures, as the technique presented in the previous section, has been developed at a laboratory source and does not rely on the interference effect to obtain the phase signal. The so-called "coded apertures" are a pair of absorbing gratings placed in the X-ray beam path. These gratings are arranged so that only photons deviated by the sample at certain angles are effectively detected by the image sensor [Olivo & Speller 2007] and the image signal is related to the refraction angle caused by the object.

The first implementations of this technique were performed with line apertures which give access to the refraction in the direction perpendicular to the lines. A more recent work reports on the implementation of this technique with two-dimensional apertures which yield sensitivity in two orthogonal directions [Olivo *et al.* 2009].

6.2 Developments within this PhD project

6.2.1 Grating interferometer with a structured scintillator

In Sec. 4.3.2.3 we have seen that transmission by the grating lines of G2 reduces visibility of the contrast curve and therefore degrades image quality. Unfortunately, grating lines high enough to absorb 100% of the incoming radiation at high X-ray photon energies are very challenging to fabricate.

A method to circumvent this problem has been recently proposed which consists in a structured scintillator, used instead of the conventional absorption grating, as analyzer element [Rutishauser *et al.* 2011a]. The structured scintillator replaces the absorption grating and the continuous scintillator used in the standard setup, see Fig. 6.2. As in the standard setup, the visible light produced in the structured scintillator is guided to a lens system into the CCD camera. The structured scintillator acts as an analyzer element as described in the following.

The lines with scintillator material correspond to the clear areas of the conventional absorbing grating while the non-scintillating lines are totally opaque parts because no visible photons are produced in them, see Fig. 6.2. Since visible photons can not be produced in the non-scintillating lines, the visibility of the contrast curve can be much higher with respect to the one obtained, for otherwise identical conditions, with a standard absorption grating.

In the experiment reported in Ref. [Rutishauser *et al.* 2011a] which was carried out at 60 keV, a visibility of 22% was measured with the structured scintillator while, for the same number of detector counts, a visibility of only 5% was obtained with a continuous scintillator and a conventional absorption grating.

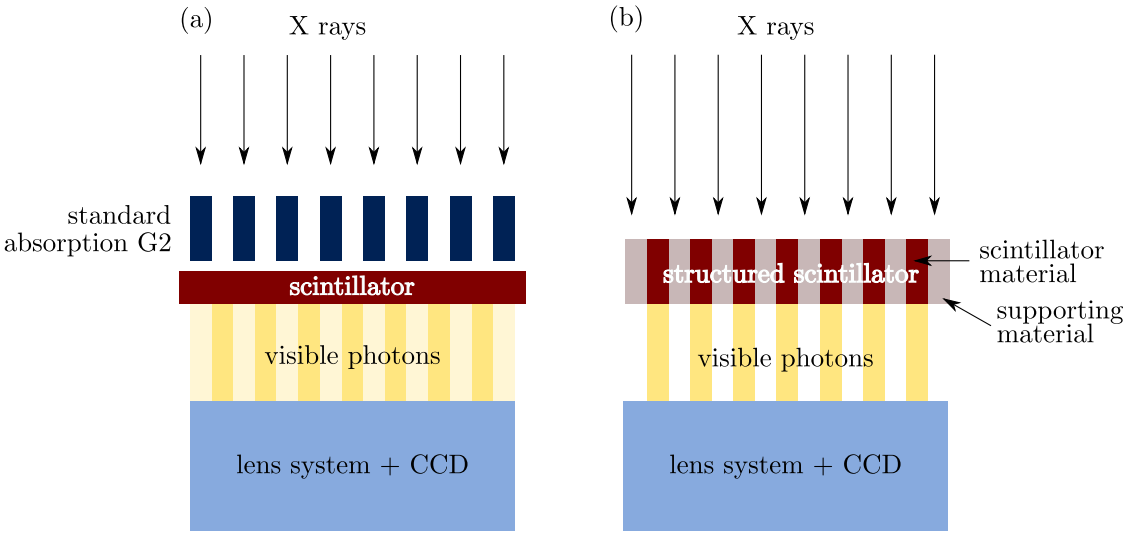

Figure 6.2: A structured scintillator (b) can be used as the analyzer element in a grating interferometer. It substitutes the standard absorption grating G2 and the continuous scintillator usually coupled to the image detector (a). It increases the visibility of the contrast curve if this is limited by transmission from absorption grating lines.

While the proof of principle measurements reported in Ref. [Rutishauser *et al.* 2011a] have been performed at an X-ray tube, the same principle can be applied to interferometers installed at other X-ray sources such as synchrotrons.

6.2.2 Directional dark-field imaging

The anisotropic nature of scattering information obtained with a grating interferometer is at the basis of a new imaging technique called "directional dark-field imaging".

In directional dark-field imaging, the directional dark-field signal produced by an object is recorded at different angular positions of the sample which rotates around the optical axis as shown in Fig. 6.3 (a) [Jensen *et al.* 2010a, Jensen *et al.* 2010b]. These images are combined together to obtain a map of the preferential scattering direction of the features in the object and their scattering strength. In Ref. [Jensen *et al.* 2010b] a theory for describing the directional dark-field signal produced by strongly oriented objects has been developed. In this model, the scattering from a single point on the sample results in a 2D Gaussian scattering intensity profile at the observation plane. With the directional dark-field measurements it is possible to calculate the parameters of the 2D Gaussian and retrieve information on the scattering preferential direction, scattering strength and the degree of orientation of the sample features. A directional dark-field image of a slice of a human tooth measured for validating the theory reported in Ref. [Jensen *et al.* 2010b] is shown in Fig. 6.3 (b).

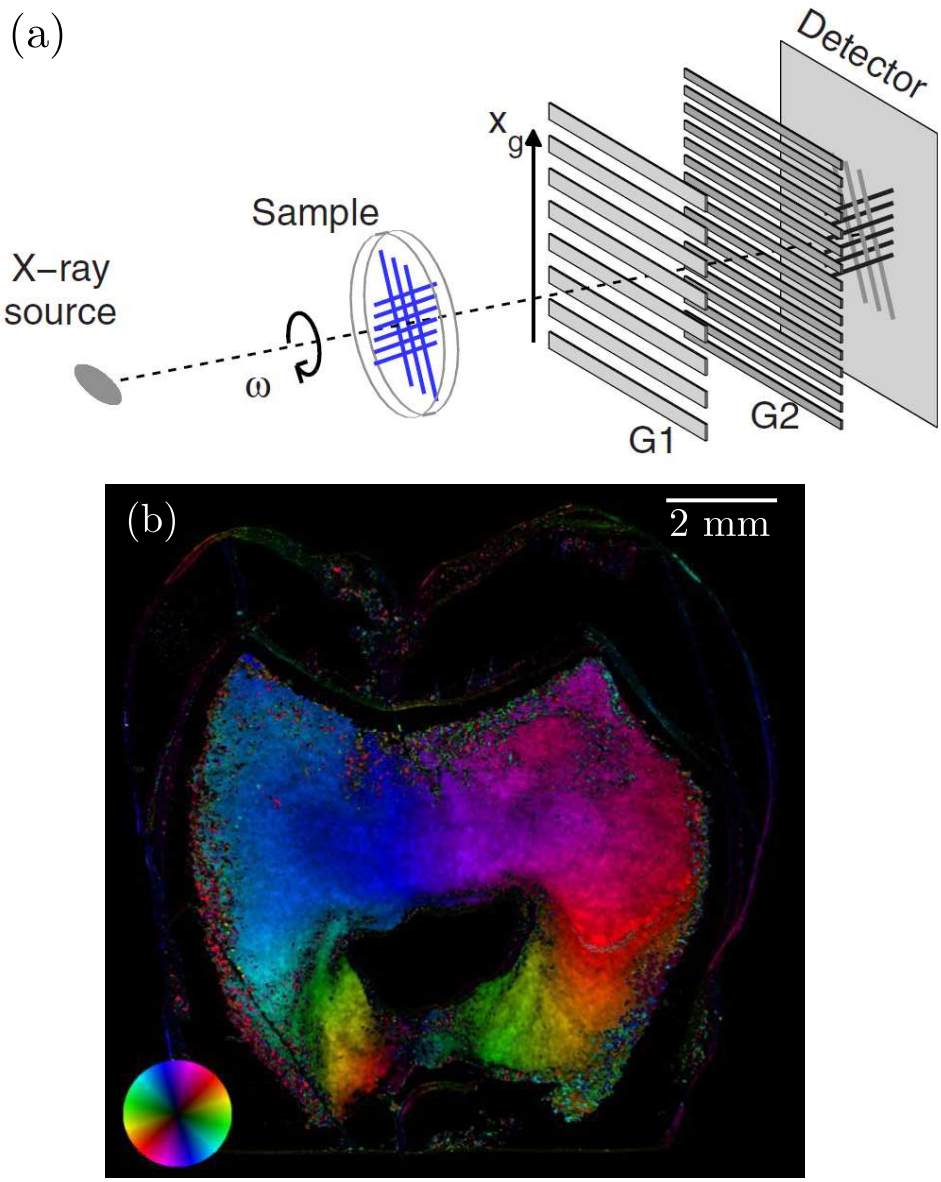

Figure 6.3: (a) Principles of directional dark-field imaging: dark-field images of the sample are obtained for different sample angular positions ω of the sample which rotates around the optical axis. (b) Directional dark-field map of a human tooth. The scattering comes prevalently from the tubuli in the dentin whose diameter of tenth of micrometers decreases from the regions close to the pulp to the regions close to the enamel. The orientation of the scattering features is indicated by the color wheel displayed in the bottom left corner of the image and the brightness is related to the strength of the scattering signal: dark parts are non scattering parts. The pixel size was 8 μm and the X-ray energy 17.6 keV. Images adapted from Ref. [Jensen *et al.* 2010b].

Chapter 7

The grating interferometer at the beamline ID19

Contents

The first task of the experimental part of this thesis was to design, implement and characterize an X-ray grating interferometer for radiography and tomography at the beamline ID19 of the European Synchrotron Radiation Facility in Grenoble, France. This chapter is dedicated to the description of the instrument which is now available to external users. The description includes details on the data acquisition and analysis methods currently in use. Since X-ray source and detector are important parts of the imaging system, their characteristics are reported in the first part of the chapter.

7.1 Synchrotron radiation

Synchrotron radiation is the electromagnetic radiation produced by an accelerated relativistic charged particle [Raoux 1983]. It was observed for the first time in 1947 in a particle accelerator (called synchrotron) and was used at the beginning as parasitic radiation, i.e., the purpose of the accelerator operation was not the generation of synchrotron radiation but the particle beam itself (first-generation synchrotrons). The first dedicated machines entirely devoted to the production of synchrotron radiation and its use for the investigation

of matter started to appear in the 1970s. They are now classified as second-generation synchrotrons. Third-generation synchrotrons are sources with improved trajectory and stability control which make optimum use of insertion devices (IDs) to produce more brilliant radiation than the previous sources. The most powerful third generation sources in the world are the European Synchrotron Radiation Facility (ESRF) in Grenoble (France), PETRA III in Hamburg (Germany), the Advanced Photon Source in Argonne (U.S.) and SPRING-8 in Hyogo (Japan).

An introduction to the physics of synchrotron radiation and storage rings can be found, for example, in Refs. [Raoux 1983, Als-Nielsen & McMorrow 2010]. This section gives a brief review of the important aspects of synchrotron radiation relevant for this PhD project.

The radiation produced by relativistic charged particles is *collimated* and tangential to the particle trajectory. The opening angle of the radiation cone is γ^{-1}, where:

$$\gamma = \frac{1}{\sqrt{1 - v^2/c^2}} \tag{7.1}$$

and v is the speed of the electrons and c the speed of light. It is due to this high collimation that synchrotron radiation has a very high brilliance. The brilliance of the beam produced by an insertion device can go up to 10^{20} photons s^{-1} / (mrad^2 mm^2 source area 0.1% bandwidth) which is about ten orders of magnitude higher than the brilliance of a laboratory X-ray source [Als-Nielsen & McMorrow 2010].

The brilliance of the synchrotron X-ray beam is related to the product of the emittance, i.e. the extent in phase space of the electron beam, in the horizontal (ε_x) and vertical (ε_y) directions, perpendicular to the average electron velocity. In accordance with Liouville's theorem, the emittance is constant over the length of the orbit and is a global parameter of the machine. A small emittance gives an X-ray beam with high brilliance.

The emittance ε_x in the horizontal plane of the orbit is given by the product of the beam size Σ_x and its divergence Σ'_x. An analogous relation holds for the emittance in the vertical direction. Since ε_x and ε_y are constant along the storage ring, a smaller beam size corresponds to a larger distribution of the transverse momentum of the electrons. The emittance in the vertical direction is much smaller than in the horizontal direction since there are no vertical bending magnets in the storage ring. At ESRF, the ratio $\varepsilon_y/\varepsilon_x$ is of the order of 1%. The ratio Σ_x/Σ'_x depends on the position in the orbit and is the so-called β_x function. At ESRF, straight sections with a low-beta value are alternated with straight sections with high-beta values.

Insertion devices (IDs) are inserted in the straight sections to produce X rays. The IDs are formed by an array of magnets that produce magnetic fields of alternate sign and force the electrons to oscillate perpendicularly to their principal direction of motion. Since IDs induce multiple oscillations on the electron beam, they are much more brilliant sources than the bending magnets where electrons travel in a circular arc. Depending on the size of the oscillation of the particles, the insertion devices are called wigglers or undulators. The IDs are described in more detail below.

Wiggler The oscillations of the particles in a wiggler are larger than the opening angle of the radiation cone γ^{-1} and the radiation pattern produced by a wiggler is given by

the *incoherent* sum of the radiation produced by each individual wiggle. This leads to a continuous energy spectrum.

Undulator In an undulator, the electrons execute oscillations smaller than γ^{-1}. In this way, the radiation emitted by an electron at one oscillation is in phase with the radiation emitted at the next oscillation. The resulting radiation is a *coherent* sum of the radiation produced by each individual magnet at one wavelength and its harmonic. Thus, the undulator can produce a quasi-monochromatic beam at a particular energy which can be tuned by changing the strength of the magnetic field. Additionally, the beam from an undulator is more collimated than that of a wiggler, i.e. the emission angle is substantially smaller.

Figure 7.1: Aerial view of the ESRF; the satellite building of ID19 is at the bottom left of the image.

7.1.1 The beamline ID19

This section is dedicated to the description of the beamline ID19 of the European Synchrotron Radiation Facility (ESRF) where an X-ray grating interferometer has been installed during this PhD project. ESRF was the first third generation synchrotron which started operation in 1992.[1] The storage ring of the ESRF has a circumference 844 m and is composed of 32 bending magnets with 32 straight sections (Fig. 7.1). The maximum electron beam current is of 200 mA and the energy of the electrons is 6 GeV.

ID19 was the first long ESRF beamline. It went into operation in June 1996 and is today mainly dedicated to phase- and absorption-contrast parallel-beam full-field imaging with spatial resolution in the micrometer range.

ID19 is located in a low-β_x section of the storage ring where the nominal size of the electron beam is 150×25 μm^2 (horizontal $\times$ vertical, FWHM). The beamline layout is shown

[1] www.esrf.eu.

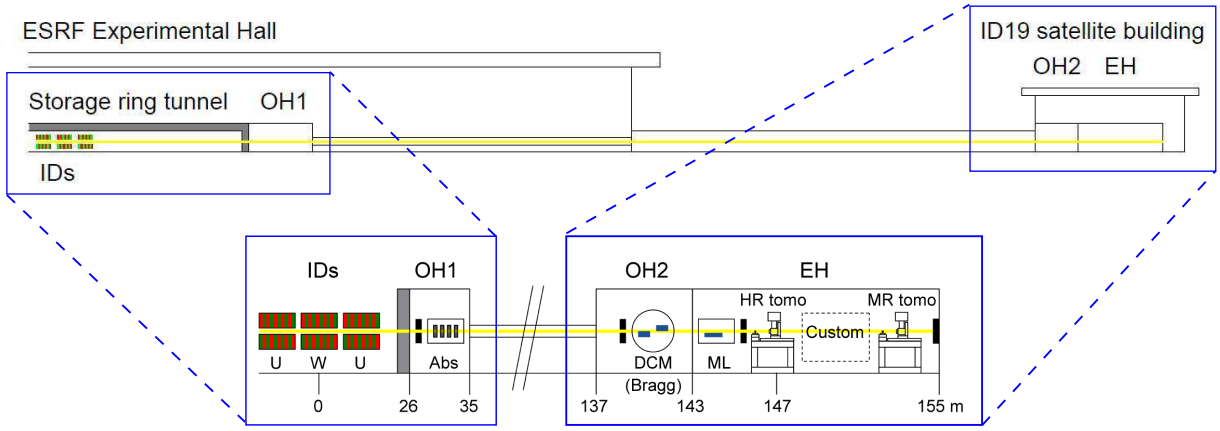

Figure 7.2: Layout of ID19. The beamline has two optics hutches and one experimental hutch. The first optics hutch (OH1) is in the experimental hall and the second optics hutch (OH2), together with the experimental hutch (EH), is situated in satellite building. Bottom: detailed representation of the elements of ID19 and their distance from the center of the straight section. In the EH, a custom space for additional instruments such as a laminograph is available between the high-resolution (HR) tomograph and the medium resolution (MR) tomograph. For more information see main text. These images are adapted from Ref. [Weitkamp *et al.* 2010a].

in Fig. 7.2. In the straight section there are four insertion devices: three undulators (two of them are mounted on a revolver) and one wiggler. The wiggler is situated at the center of the straight section. The beamline has two optics hutches (OH). The first optics hutch OH1, which is located in the main ESRF experimental hall, is not separated by any window from the storage ring vacuum. At ID19, the number of windows in the X-ray beam has been minimized in order to keep the coherence of the X-ray beam as high as possible: any element in the beam can act as a secondary source of much larger angular size than the primary source. This effectively degrades the spatial coherence [2] [Espeso *et al.* 1998]. [3] In OH1 there are attenuators, diaphragms and a set of primary slits.

The second optics hutch OH2 is situated at approximately 140 meters from the center

[2] If the optical element in question is static, the phase correlations in the light field at the sample positions will not be reduced in strength. In this sense, scattering by the optical element will, in principle, not reduce the coherence of the beam as long as the scatterers are constant in time and position. However, they will produce a speckle pattern around each image feature. The characteristic size of the speckles is ac/b, where a is the characteristic modulation period in the scattering object, b is the distance between the scatterer and the sample, and c the distance between sample and detector plane. Since a is often already smaller than the resolution of the imaging system, and, in addition, $c \ll b$ in most cases at synchrotron beamlines, the speckle pattern is usually not resolved. Instead, it takes the form of a halo, and the effect of the scattering filter is therefore equivalent to that of an ideal diffuser screen. The spatial coherence is effectively decreased.

[3] This aspect, which is generally important for X-ray phase-contrast imaging, is fundamental for X-ray grating interferometry. During this PhD project, a grating interferometer was tested at ID17, a beamline of the ESRF very similar to ID19. They are both located in low-β_x sections of the storage ring, the experimental hutches of both beamlines are located 150 m from the source and they use the same type of wiggler. However, at ID17 there are more windows than at ID19, partly because ID17 has another experimental hutch close to the storage ring. In addition, ID17 uses a Laue monochromator. The visibility observed at ID17 was much lower than the visibility observed at ID19, for otherwise very similar experimental conditions.

of the straight section and accomodates a double crystal monochromator (DCM) with two Si (111) crystals in Bragg geometry, as well as a chopper and secondary slits.

A second monochomator, a single bounce multilayer (ML), is situated in the first part of the experimental hutch (EH). Downstream of the ML, there are two tomography stations, called the "high-resolution tomograph" and the "medium-resolution tomograph". As the names suggest, the high-resolution tomograph is optimized for studies with high resolution on light samples and the medium-resolution tomograph is used for studies on samples which require a larger field of view and/or are heavy or bulky.

The beam width in the EH (with DCM or pink/white beams) is limited to 45 mm by apertures. The beam size in the vertical direction can go up to 15 mm. With the DCM the maximum beam height is available up to an energy of approximately 23 keV. At higher energies the beam height decreases (due to the limited dimensions of the monochromator crystals) and reduces to a value of only 3 mm at 80 keV. The maximum beam size obtained with the ML is much smaller and around 15(hor)×4(ver) mm^2.

The beamline operates in white or pink beam modes (i.e., without the use of any monochromator device) or in monochromatic mode by using the DCM or the ML. The energy range is between 7 keV and more than 150 keV. Note that, since the ML is vertically deflecting, the single-bounce monochromator can not be used for the medium-resolution tomograph because of a prohibitively large vertical offset of the ML-reflected beam at the position of the tomograph. The ML provides a monochomatic beam with larger spectral bandwidth and larger photon flux than the DCM: the energy resolution provided by the ML is $\Delta\lambda/\lambda \approx 10^{-2}$ while that of the DCM is of approximately 10^{-4}.

7.2 The detector

Several types of digital image sensors are currently available for X-ray imaging and all of them can be used for grating interferometry. Among them are photographic films, amorphous silicon flat panels, direct conversion pixel detectors [Bech *et al.* 2008] and scintillator lens-coupled CCD cameras. The image sensors used at ID19, in standard tomography as well as in grating interferometry experiments, are scintillator lens-coupled CCD cameras because this scheme combines high spatial resolution with good resistance to highly-intense radiation.

The basic concepts of the detection mechanism are described in the following. X rays impinge on a scintillator material which converts them into visible light photons. Most of the X rays which are not absorbed in the converter screen are stopped by the substrate of the screen or by a lead glass. The visible-light image in the scintillator plane is projected onto a CCD by a system of lenses. In the detectors used at ID19, a mirror in the visible-light beam path avoids exposure of the CCD and electronics to high-energy X rays in the direct beam path.

The thickness and the material of the scintillator have strong effects on both spatial resolution and detection efficiency. Thicker scintillators degrade spatial resolution but provide higher detection efficiency [Koch *et al.* 1998]. At ID19, different types of scintillators including powder scintillators (gadolinium oxysulfide [Gadox] Gd_2O_2S) and crystal scintillators

(yttrium aluminum garnet [YAG] $Y_3Al_5O_12$, lutetium aluminum garnet [LAG] $Lu_3Al_5O_12$ and gadolinium gallium garnet [GGG] $Gd_3Ga_5O_{12}$), doped with different rare earth elements, are available. All the interferometer results presented in this thesis have been obtained with the Gadox scintillator. In powder scintillators, the resolution expressed in terms of the FWHM of the line spread function (LSF), which is one of the quantities used to described the response of a detector, is approximately given by the thickness of the scintillator itself [Swank 1973]. The LSF is the response of the system to illumination by an infinitely narrow line focus. If the detector is linear and spatially invariant, this function can be easily related to the point spread function (PSF) which is the response of the system to a point-like illumination. When the PSF is known, it can be used to correct the recorded image by deconvolution with the detector response. For more information on image detectors and their characterization, see textbooks as Ref. [Knoll 1979].

The CCD detectors used in this PhD project are cameras from the FReLoN (Fast Readout Low Noise) model developed at the ESRF [Labiche *et al.* 1996, Labiche *et al.* 2007]. In these cameras, the background of the images due to dark current is kept low down to approximately 1 electron/pixel/s by cooling the CCD down to -20 °C with a water-cooled Peltier element. Two different models have been used during this thesis project, the "FReLoN 2K" and the "FReLoN E2V". The chips of these cameras have 2048×2048 pixels; both cameras can work in speed or precision mode. The FReLoN E2V is more efficient but slower than the FReLoN 2K; parameters for the two cameras and for the two configurations (precision or speed) are given in Table 7.1. During the grating interferometry experiments, the cameras have been used in precision mode.

	FReLoN 2K		FReLoN E2V	
Official name	F A 7899		F E 230-42	
Pixel size	14 μm		15 μm	
Quantum efficiency for Gadox	40%		90%	
	precision	speed	precision	speed
Dynamic range unbinned	14000:1	8000:1	14000:1	8000:1
Dynamic range binned	14000:1	8000:1	34000:1	21000:1
Effective throughput (Mpixels/s)	40	80	10	20

Table 7.1: Parameters of the two FReLoN cameras used during this PhD project. The quantum efficiency is defined as the number of electron−hole pairs created per visible-light photon. The values reported in this table have been provided by J.-L. Labiche, ESRF.

The effective pixel sizes and scintillators used in this thesis are listed below:

(i) 5 μm with 10 μm Gadox thickness;

(ii) 7.5 μm with 10 μm Gadox thickness;

(iii) 30 μm with 30 μm Gadox thickness.

The values of the effective pixel size above are given for the FReLoN 2K. These values should be multiplied by 15/14 to obtain effective pixel sizes for the FReLoN E2V.

An X-ray exposure shutter is located upstream of the sample position. It has the twofold purpose of (1) limiting the exposure of the sample to the X-ray beam to the periods in which the detector collects photons and (2) avoiding image artifacts that would be caused by X rays hitting the detector during readout.

7.3 The instrument

At ID19, the grating interferometer is a removable add-on of the MR tomography station. Due to the limitations on the spatial resolution imposed by the period of the gratings, the interferometer performs best with moderate resolution detectors with a large field of view. The interferometer has been designed, installed and commissioned during this thesis project in collaboration with partners from Paul Scherrer Institut.

The interferometer is based on the "Macrobech" series of optical mounts by the company Qioptiq Photonics GmbH & Co. KG, Göttingen, Germany (formely: LINOS). The system is based on four parallel rods which hold mounts on which the gratings are fixed, see Fig. 7.3 (a) and (b). The rods ensure stability, rigidity and parallelism of the gratings with respect to each other. The distance between the gratings can be varied manually and different sets of rods are available for implementing different inter-grating distances.

The interferometer gives access to the full beam size at ID19. Phase and absorption gratings are fabricated on wafers with a diameter of 100 mm. The maximum active area of the phase gratings made at PSI is a square of 65×65 mm^2 and the maximum active area of the phase and absorption gratings fabricated at KIT is 60×20 mm^2. Photographs of phase and absorption gratings are shown in Fig. 7.4 (a) and Fig. 7.5 (a).

The phase-stepping scan is usually realized by moving the phase grating. This grating is mounted on a commercial piezo translation stage (HERA model series, by Physik Instrumente PI, Karlsruhe, Germany) with 100 μm travel range and 0.4 nm nominal resolution. The adapter plate shown in Fig. 7.4 (b) was designed in-house and is used as interface for mounting the phase grating on the piezo. Grating and piezo can be mounted on a goniometer used to tilt the grating around the axis parallel to the grating lines in order to reduce the period of the phase grating projected on the plane orthogonal to the optical axis. The goniometer is a MOGO 40 from OWIS GmbH, Staufen, Germany with $\pm 15^\circ$ travel range.

The gratings can be aligned by rotating the absorption grating around the optical axis over a range of a few degrees with a system of flexure hinges that acts as a reduction gear. This mechanism was originally developed at Paul Scherrer Insitut and can be actuated by a micrometer screw. The ESRF version, shown in Fig. 7.4 (b), is made of aluminim and driven by an MMS 19-25-HSM by Owis GmbH, Satufen, Germany. The magnetic grating holder, which allows an easy mounting of the grating on the rotation stage, was designed in-house at ESRF.

A photograph of the sample stage is shown in Fig. 7.3 (c). In a tomography experiment, the sample is fixed on a suspended rotation stage (PRS-110 from miCos GmbH, Eschbach, Germany) which allows to immerse the specimen in a water tank. This configuration is used

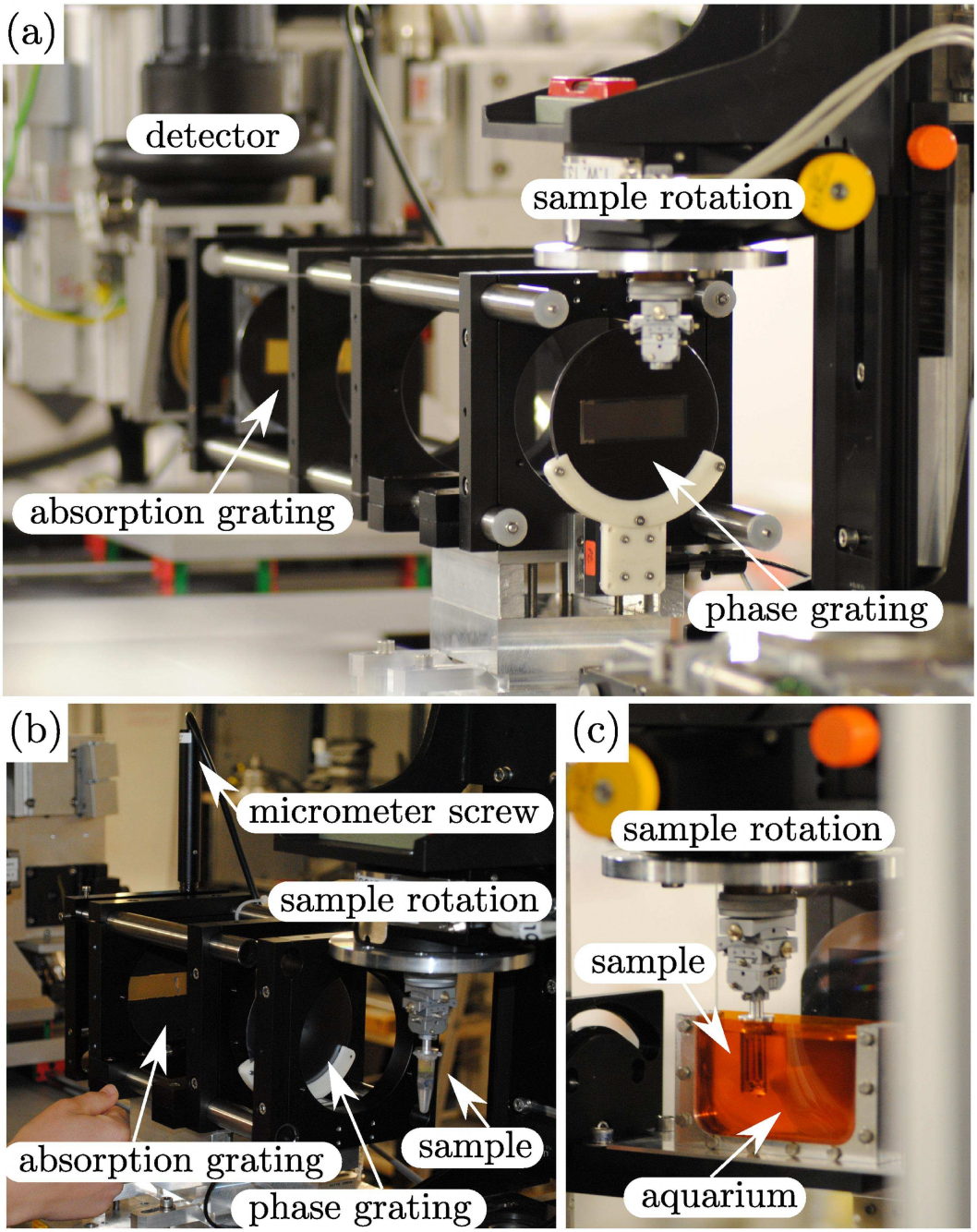

Figure 7.3: Pictures of the grating interferometer installed at ID19. (a) Interferometer with a large inter-grating distance of approximately 500 mm. (b) Interferometer with a short inter-grating distance of approximately 200 mm. (c) Detailed view of the sample stage.

in order to reduce artifacts in the phase tomogram coming from refraction at the sample-air interface. Water tanks of different sizes have been designed inhouse. They are made by kapton foils fixed by screws on an aluminum structure, see Fig. 7.3 (c). The sample can move in both transverse directions for alignment and for acquiring images of the reference beam during a tomography scan.

Up to now, the interferometer has been used with monochromatic radiation from the

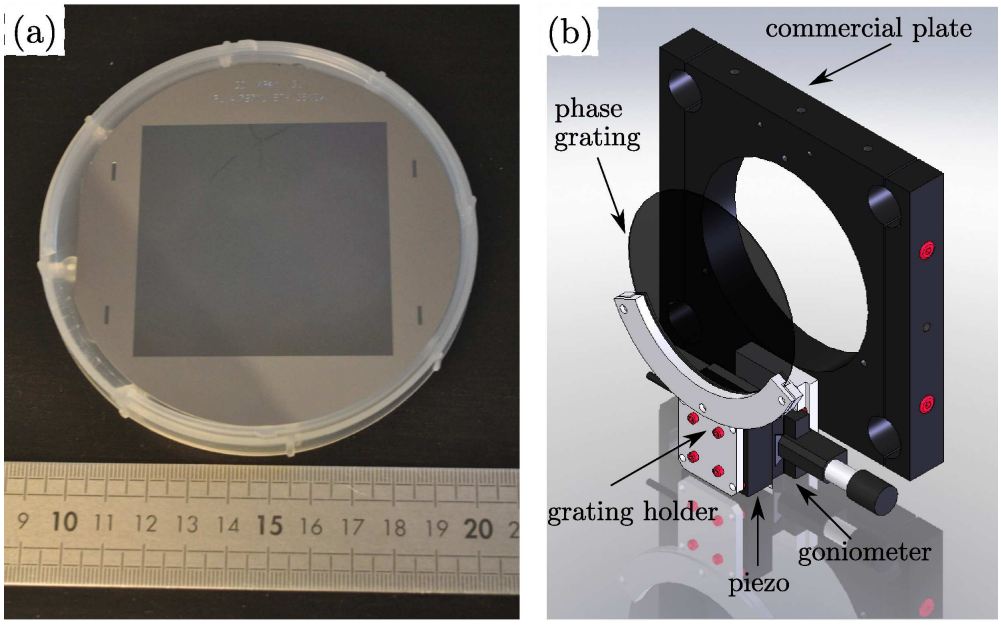

Figure 7.4: (a) Picture of a phase grating. (b) Scheme of the phase grating mounted on the piezo and goniometer.

DCM. The wiggler has been chosen as source of radiation instead of the undulator for two reasons: (i) the size of the beam produced by the wiggler is larger (ii) the visibility, for otherwise identical conditions, is higher with the wiggler than with the undulator. We believe that this is due to the fact that the wiggler is situated at the center of the straight section where the size of the electron beam is smaller. The horizontal transverse coherence length of the X-ray beam at the sample is therefore larger.

Tests for using the pink beam produced by the undulator are planned for the near future.

The grating interferometer described above has been extended for the use of two-dimensional gratings instead of line structures [Zanette *et al.* 2010a, Zanette *et al.* 2010b, Zanette *et al.* 2011c]. The two-dimensional interferometer is described in Chap. 11.

7.3.1 List of available configurations

The gratings currently available at ID19 are listed in Table 7.2.

7.3.1.1 Small interferometer for the high-resolution tomograph

A smaller interferometer for the high-resolution tomograph has recently been implemented in collaboration with partners from Paul Scherrer Institut and from Universität Basel. Gratings for this interferometer belong to the Paul Scherrer Institute, the wafer and the active area of these gratings is smaller than the gratings used in the MR tomograph and the period of the absorption grating is of 2.0 μm. Gratings and some of the mechanical parts of the interferometer are not permanently available at ID19. This "small interferometer" is based on a mounting system similar to that of the large-field interferometer. However, the rods ("Microbench" series by the company Qioptiq Photonics GmbH & Co. KG, Göttingen,

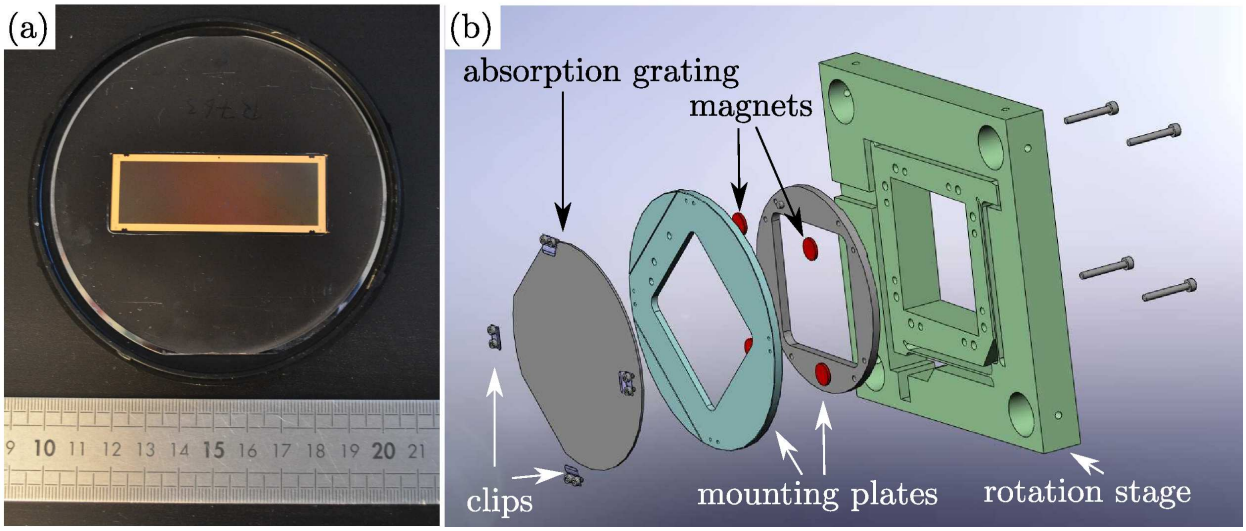

Figure 7.5: (a) Picture of an absorption grating. (b) Rotation stage for the absorption grating.

#	**Type**	**Material**	**Energy** (keV)	Designed **FTD** (mm)	Designed **FTO**	Nominal **Period** (μm)	Nominal **Height** (μm)
1	G1 (π)	Si	17.6 keV	451	11th	4.78	21
2	G1 (π)	Si	23 keV	482	9th	4.785	29.5
3	G1 ($\pi/2$)	Ni	28 keV	–	–	2.4	5.1
4	G1 (π)	Si	35 keV	244	3rd	4.792	44.8
5	G1 (π)	Si	35 keV	408	5th	4.787	44
6	G1 ($3\pi/2$ & $\pi/2$)	Ni	17.6 & 52 keV	–	–	2.4	9.2
7	G1 ($3\pi/2$ & $\pi/2$)	Au	17.6 & 52 keV	–	–	2.4	5.3
8	G1 ($\pi/2$)	Ni	140 keV	–	–	4.8	25
9	G2	Au	–	–	–	2.4	50
10	G2	Au	–	–	–	2.4	74
11	G2	Au	–	–	–	2.4	100
12	G2	Au	–	–	–	4.8	180

Table 7.2: List of gratings available at ID19. FTD is the fractional Talbot distance (inter-grating distance). FTO is the fractional Talbot order (i.e. n in Eq. (4.1) (page 38)). Gratings number 1 through 8 are used as phase gratings (G1), gratings number 9 through 12 as analyzers (G2). Gratings with period 2.4 or 4.8 μm are produced at KIT; the other gratings are produced at PSI. Gratings number 6 and 7 were designed to be used at two energies at which their lines give a phase shift of $\pi/2$ and $3\pi/2$. It can be shown, in fact, that the intensity pattern generated by a $3\pi/2-$shifting phase grating is analogous to the pattern generated by a $\pi/2-$shifting phase grating at the same fractional Talbot distances. Gratings number 8 and 12, designed for being used at 140 keV, have not yet been tested. Successful tests at 82 keV, immediately above the Au absorption edge have been performed. The phase grating used at 82 keV is not listed here because it does not belong to ID19.

Germany) have smaller diameter and length. The piezo used for the phase-stepping scan is the same as the one used in the large-field interferometer. The absorption grating is tilted around the optical axis with a principle very similar to the one adopted in the large-

field interferometer. A picture of the small interferometer installed on the high-resolution tomograph is shown in Fig. 7.6.

This instrument has been used with the monochromatic beam from the multilayer at an energy of the 17.6 keV.

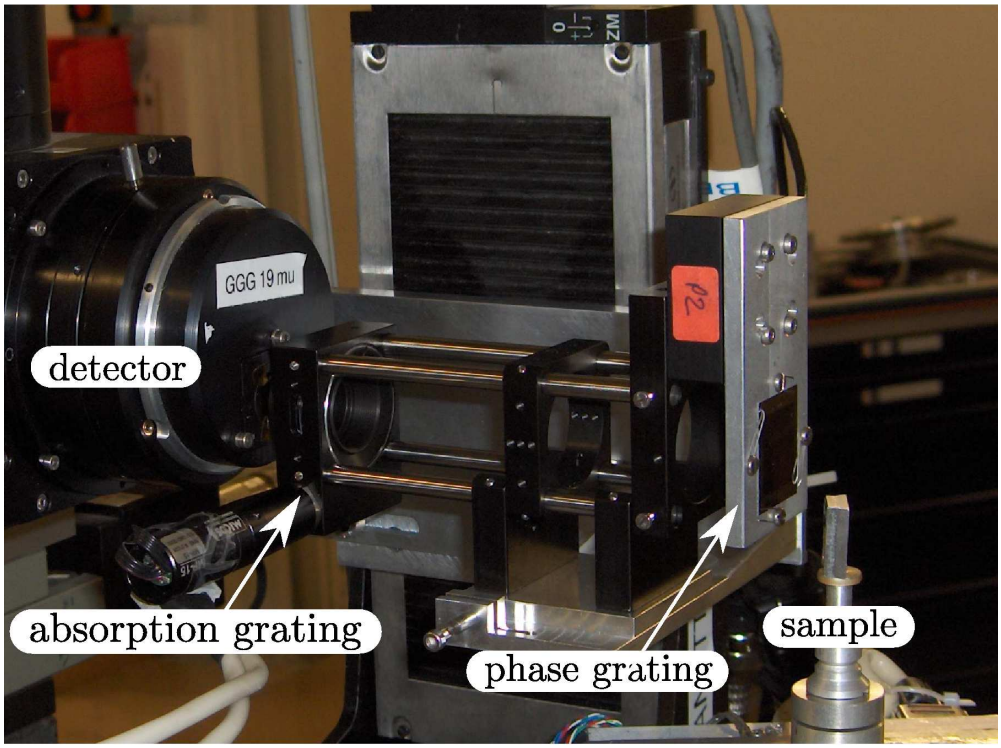

Figure 7.6: Small interferometer installed at the high-resolution tomograph.

7.3.2 Positioning and alignment

In a tomography experiment, the gratings are usually positioned in their respective holders with the lines oriented along the vertical direction (parallel to the rotation axis) for the reasons described in Chap. 5. When the interferometer is used for other applications than tomography, those constraints do not apply. Since the shape of the X-ray source is a flat ellipse, the highest value of visibility is generally reached when the grating lines are horizontal. However, an interferometer with horizontal grating lines is sensitive to vibrations and deformations of vertically deflecting beamline optics. For this reason, gratings at ID19 are usually mounted with their lines vertical. During the mounting, the gratings are manually pre-aligned and the distance between the gratings is set to the value calculated with Eq. (4.14) (page 49).

When the gratings are misaligned, moiré fringes are present in the raw interferograms. The alignment procedure consists in rotating the absorption grating around the optical axis until any horizontal component of the moiré fringes disappears (see Appendix B). If vertical moiré fringes remain in the interferogram, as shown in Fig. 7.7, the period of the interference pattern produced by G1 should be changed so that also vertical fringes are eliminated. This

can be done by adjusting the inter-grating distance or, if the phase grating is mounted on a goniometer, by slightly tilting the phase grating around the axis parallel to the grating lines. Note that the tilt of the phase grating not only reduces the period of the interference pattern but also decreases its visibility because the projected shape of the grating lines on the plane orthogonal to the optical axis is not rectangular. For this reason, having 'ad-hoc' fabricated phase gratings with the correct period is the ideal solution.

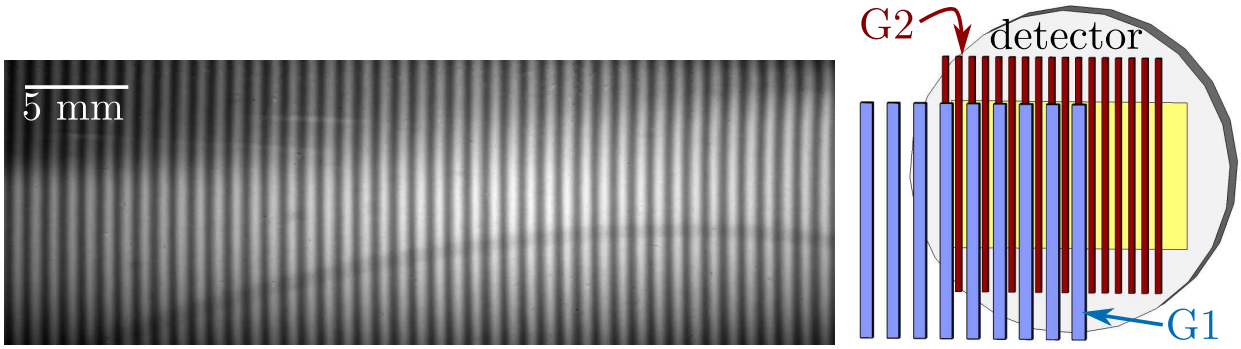

Figure 7.7: Left: raw interferogram with moiré fringes originating from the difference in period between the interference pattern produced by the lines of G1 and the lines of G2. The grating lines were oriented vertically as shown in the schematic representation at the right. The curved dark stripe at the bottom of the interferogram comes from reflection in the silicon substrate.

Another aspect to consider when mounting an interferometer, is the alignment of the surface normal to the grating plane parallel to the optical axis; this is crucial for high aspect ratio G2. This alignment can be done, for example, with the help of the diffraction spots produced by G2 illuminated by a laser aligned parallel to the X-ray beam: the 0th order diffraction spot of the laser should overlap with the incident laser beam.

After the alignment of the instrument and before starting the data acquisition, the period of the piezo motor is calibrated. This calibration is necessary to step the grating over an integer number of interference pattern periods. If the motor is miscalibrated, the Fourier analysis of the phase-stepping curve does not yield correct results and artifacts are observed in the final images.

The calibration procedure consists in taking a phase-stepping scan over approximately four/five periods in many steps. The intensity values recorded during the scan are averaged over small regions of interests in different parts of the field of view. These curves are fitted with a sinusoidal function and in this way the correct stepping period can be calculated. The calibration is performed in different regions of the field of view in order to detect incident variations in period in the image; so far, we have never observed significant period variations.

7.4 The visibility map

The visibility image obtained without the sample in the beam, the so called *visibility map*, is used to evaluate the performance of the interferometer. The visibility is considered as a

figure of merit of the performance of the instrument because the final image quality strongly depends on the visibility of the contrast curve.

Ideally, the visibility map should be homogeneous over the entire field of view. In practice, non uniformities in the wavefront and and defects in the gratings may affect the local visibility. The visibility map can therefore be used either for analyzing the quality of the X-ray beam or for characterizing the gratings. Measurements of the visibility map provide crucial information to the grating producers to understand properties and defects of the optical elements and give information complementary to that obtained through inspection with the scanning electron microscope or the light microscope.

Figures 7.8 (a) and (b) show two visibility maps taken at the same experimental conditions (fifth fractional Talbot distance at 35 keV measured with a detector pixel size of 30 μm) and with the same phase grating but with different absorption gratings. Both absorption gratings were fabricated with a duty cycle of 0.5, a period of 2.4 μm and a line thickness of 50 μm. From the images in Fig. 7.8, features caused by defects in the absorption gratings can be separated from features originating from the other elements in the beam such as the beamline optics, the scintillator or the phase grating. For example, a scratch in the phase grating is visible at the left of panels (a) and (b).

The vertical bright lines present in both images of Fig. 7.8 come from the absorption gratings and have their origin in the electron beam lithography process; the electron beam writes in squares of 1.2×1.2 mm^2. The higher visibility in these regions might be a result of a better electroplating in the stitched areas. The visibility map of panel (a) shows a horizontal gradient (the visibility increases from left to right of the image) which is not present in Fig. 7.8 (b) and is probably due to variation in thickness of the absorption grating lines. Although the visibility map in panel (b) is more homogeneous than the one in panel (a), it shows a lower average visibility (22%) than the one of 26% measured in panel (a) (see colorbars at the bottom of the images).

Figure 7.8 (c) shows a visibility map taken with the same pixel size and photon energy of 35 keV as the maps (a) and (b). However, this visibility map was measured at a different (shorter) fractional Talbot distance than the other maps and with a different phase grating. The absorption grating for the measurement in (c) was the one used for the measurement in (a). The visibility map in (c) presents strong inhomogeneities due to defects in the phase grating.

A visibility map measured with a pixel size of 5 μm is shown in Fig. 7.9 (a). The experimental parameters used in this measurement are reported in caption of Fig. 7.9. This visibility map has been obtained at a lower energy (23 keV) than those shown in Fig. 7.8 but at approximately the same inter-grating distance. Since it was measured at a lower energy, the average visibility in Fig. 7.9 is higher than the visibility obtained at 35 keV and equal to, approximately, 44%. The higher spatial resolution in Fig. 7.9 allows to see with more detail the high-frequency texture which could already be seen in Fig. 7.8. This texture is made of vertical wiggling structures parallel to the grating lines which come from trenches within the resist matrix of the absorption grating. Moreover, horizontal finely spaced lines can be seen in this image, see enlarged detail in Fig. 7.8. These lines are caused by bridges which are inserted between the absorption grating lines to prevent them to collapse. While

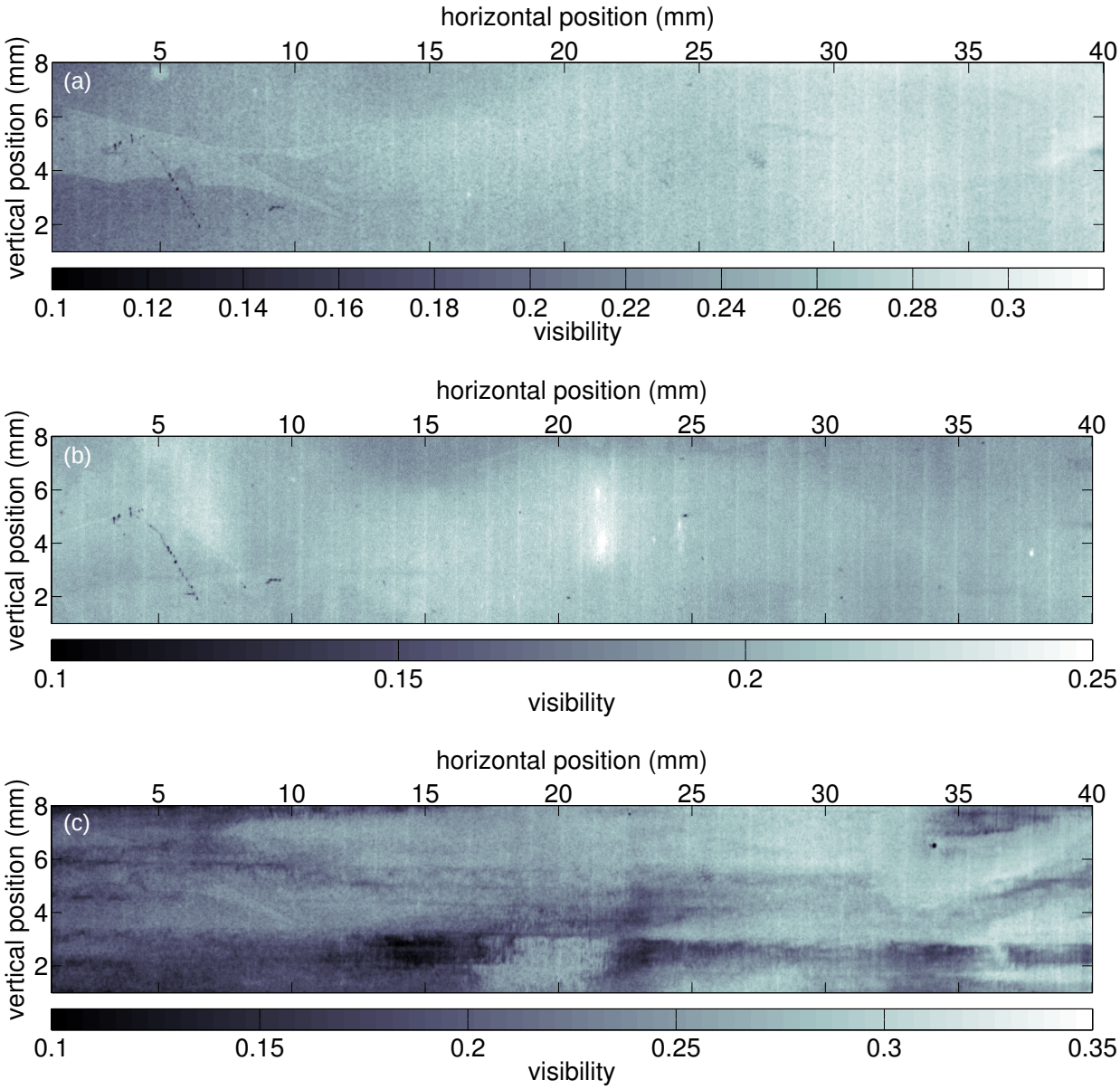

Figure 7.8: Visibility maps measured with a pixel size of 30 μm. Panels (a) and (b): visibility maps measured at the fifth fractional Talbot distance at 35 keV with the same phase grating and a different absorption grating. Panel (c): visibility map taken at the third fractional Talbot distance at 35 keV with the same absorption grating than in (a) and with a phase grating different than the one used in the measurements show in (a) and (b). All phase-stepping scans were performed over two G2 periods in eight steps. The exposure time was 0.3 s per raw image. The gratings were positioned with vertical lines. For more discussion, see main text.

in Fig. 7.8 mainly the vertical lines of the stitching field of the electron beam are visible, in Fig. 7.9 also the horizontal lines can be seen. Note that most of these defects, which can be revealed with the visibility map, are cancelled out with the reference beam correction.

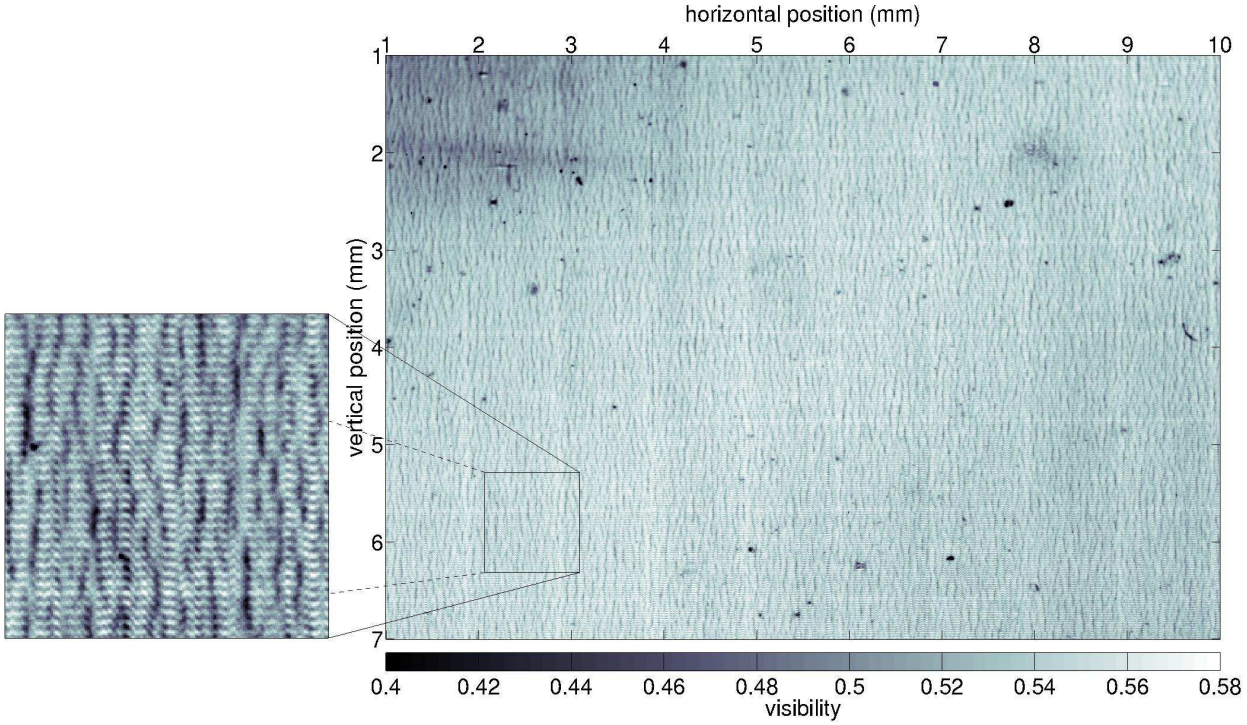

Figure 7.9: Visibility map measured at the 9th fractional Talbot distance at 23 keV with a pixel size of 5 μm. The gratings were positioned with vertical lines. The phase-stepping scans were performed in 4 steps, the exposure time was 1.5 s per image. At the left of the image is shown an enlarged detail of size 1 $\times$ 1 mm^2 in which different grating defects, described in the main text, can be revealed.

7.5 Grating-based tomography

A phase-stepping tomography scan consists in recording images for different grating positions and different viewing angles of the sample: grating scan and sample rotation are most often nested scans (but see Chap. 10 for more advanced acquisition schemes) and can be implemented in several ways.

At ID19, an entire phase-stepping scan is acquired for each angular position of the sample. In order to correct for beam fluctuations, a series of approximately 10 flat field phase-stepping scans is acquired every 100-150 phase-stepping scans of the sample. With this acquisition scheme, the typical acquisition time for collecting 1500 angular views of the sample is of around two hours assuming an acquisition time per raw image of 1 sec and between 3 and 5 steps per phase-stepping scan.

An alternative to this method, less time consuming but less efficient in correcting for beam instabilities, is to use the sample rotation as the fast axis. In this acquisition scheme, a full sample rotation is performed for each grating position. This can reduce the acquisition time because it requires much fewer movements of the phase grating. However, this advantage may come at the cost of artifacts in the reconstructed volumes originating from inadequate flat-field corrections. The presence of these artifacts can be reduced with fast scans which can be obtained, for example, by using the high photon flux of a pink beam.

This possibility will be investigated in the near future.

A significant improvement in the acquisition of phase-stepping tomography scans has been achieved, during this thesis, with the introduction of interlaced phase stepping as discussed in Chap. 10.

7.6 Data analysis

7.6.1 Processing of phase-stepping scans

Raw data acquired during a phase-stepping tomography scan are processed with a software written by T. Weitkamp in IDL, the Interactive Data Language (ITT Visual Information Solution, Boulder, Colorado, U.S.).

This program processes the phase-stepping scans accordingly with a Fourier-based pixel-wise analysis and gives as output the set of absorption, differential phase and dark-field projections and, if desired, the corresponding sets of sinograms.

7.6.2 Tomographic reconstructions with PyHST

PyHST is the standard program used at ESRF for reconstructing tomographies from projections or sinograms. The acronym HST stays for "High Speed Tomography" and the program is currently implemented in Python. It uses the filtered back-projection algorithm described in Chap. 5. More information on the program can be found on the on-line manual.[4] During this thesis project, in collaboration with the PyHST developers, the program was extended in order to reconstruct phase tomographies from differential phase projections measured with the grating interferometer.

In particular, the imaginary sign filter of Eq. (5.9) (page 57) has been implemented in PyHST and the option of inserting some parameters, such as the interferometer geometry, which is needed to retrieve the quantitative δ values, has been included.

[4]HST manual: http://www.esrf.eu/computing/scientific/HST/HST_REF/hst.html.

Chapter 8

Refractive index measurement

Contents

8.1 Introductory remarks

The grating interferometer described in the previous chapter has been characterized with the measurement of the refractive index of a phantom sample made of known materials arranged in a systematic geometry. The results of this characterization are published in the special issue of Physica Status Solidi A containing the proceedings of the 10-th biennial conference on high resolution X-ray diffraction and imaging (XTOP2010) which took place from Monday September 20th to Thursday September 23rd 2010 at the University of Warwick, UK [Zanette *et al.* 2011d]. This chapter contains a reprint of this paper.

8.2 Paper I

This section contains a reprint of the paper published as: I. Zanette, T. Weitkamp, S. Lang, M. Langer, J. Mohr, C. David and J. Baruchel. *Quantitative phase and absorption tomography with an X-ray grating interferometer and synchrotron radiation.* Physica Status Solidi A **208**, 2526-2532 (2011).

8.2.1 Abstract

We report on a study on the accuracy and precision of X-ray phase and absorption tomograms obtained with a grating interferometer using monochromatic synchrotron radiation. The quantitative assessment of the performances of the X-ray grating interferometer is a fundamental aspect in the interpretation of the results obtained with this device. The work presented in this paper consists in the comparison of experimental with calculated three-dimensional distributions of the X-ray refractive index in a phantom sample made of known materials. The quality of phase and absorption tomograms has been determined with respect to their sensitivity and contrast-to-noise ratios. Moreover, the effect of image artifacts typical in phase-contrast imaging based on the phase-stepping technique, especially stripe features generated by the phase-wrapping phenomenon, has been investigated by comparison with numerical simulations. The results show that the artifacts can not only be qualitatively explained by the calculations, but they can even be quantitatively reproduced.

8.2.2 Introduction

Conventional X-ray radiography, in which contrast is obtained from the absorption of the X rays in the specimen under study, finds its limitation when details with similar densities need to be discriminated. For example, inner structures in soft-tissue biological specimens are imaged with poor contrast in conventional absorption X-ray imaging.

Phase-contrast X-ray imaging overcomes this limitation by using the phase shift rather than the absorption as the image signal [Fitzgerald 2000]. In the hard X-ray range, this approach can be several orders of magnitude more sensitive than absorption contrast [Momose 2005]. Among the different phase-contrast imaging techniques, a method based on an X-ray grating interferometer [David *et al.* 2002, Momose *et al.* 2003] provides high-sensitivity phase-contrast images with high resolution. This method has been developed at synchrotron facilities and can be adapted to laboratory X-ray sources [Pfeiffer *et al.* 2006].

The phase and absorption tomographies obtained with the grating interferometer yield the three-dimensional (3D) distribution of the refractive index $n = 1 - \delta + \mathrm{i}\beta$ of the object under study. In particular, δ is retrieved in the phase tomogram and β is reconstructed in the absorption tomogram. The correctness of the quantitative information retrieved in the phase and absorption tomograms is a fundamental aspect in the interpretation of the results given by the X-ray grating interferometer.

The aim of the work reported in this paper is to assess, through comparison of experimental results with calculated data, the quantitativeness of the refractive index measurements obtained with a grating interferometer and monochromatic synchrotron radiation.

A phantom made of known materials was built for this study and was measured with the grating interferometer installed at the beamline ID19 of the European Synchrotron Radiation Facility (ESRF, France) [Weitkamp *et al.* 2010b, Weitkamp *et al.* 2010a].

This work, performed with monochromatic synchrotron radiation, complements previous studies performed with Talbot-Lau interferometers on low-brilliance sources [Herzen *et al.* 2009, Zambelli *et al.* 2010].

8.2.3 The X-ray grating interferometer

An X-ray grating interferometer consists of two line gratings placed in the X-ray path between the sample and the detector (see Fig. 8.1).

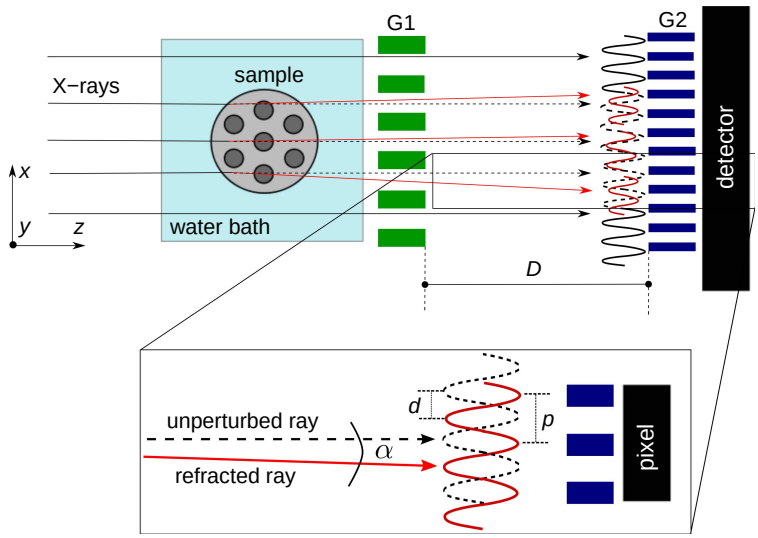

Figure 8.1: Top: schematic representation of an X-ray grating interferometer. The two gratings (G1 and G2) are usually placed between the sample and the detector, the distance D between the gratings corresponds to a fractional Talbot order. During the phase-stepping scan, the grating G1 is moved parallel to the x axis. In a tomography scan, this procedure is repeated for hundreds of different viewing angles of the sample, which rotates around the y axis. Below: detail showing the displacement d of the interference pattern, caused by the refraction in the sample. The refraction angle is indicated with α and p is the period of the interference pattern. The detector pixel size is usually larger than p and the analyzer grating is needed to analyze the interference pattern.

The first grating G1, the 'beam-splitter', is a phase shifting grating which produces an interference pattern of quasi-periodic lines at particular distances D corresponding to fractional Talbot orders [Weitkamp *et al.* 2005a]. The interference pattern, whose period p is typically smaller than the pixel size of the detector, contains information on the optical properties of the sample. The absorbing grating G2, the 'analyzer grating', is positioned directly before the detector to analyze the interference pattern. The period p of the absorbing grating is the same as the period of the interference pattern.

In order to maintain the full spatial resolution of the imaging system, the analysis of the interference pattern is performed with the phase-stepping technique. One of the two gratings is scanned perpendicular to the grating lines and the optical axis over at least one grating period and a series of images is recorded during the scan. The analysis of these images yields pseudo-absorption and refraction angle radiographs [Weitkamp *et al.* 2005a].

The 'pseudo-absorption' radiographs are obtained by averaging all images recorded in the phase-stepping scan. They exhibit absorption contrast and, possibly, edge-enhancing in-line phase contrast. The presence of the in-line phase contrast in the pseudo-absorption images depends on the coherence properties of the radiation and on the sample-to-detector distance. The pseudo-absorption images are very similar to the conventional images that

would be obtained if the interferometer were not in the beam, especially when the shearing distance between the two beams diffracted by G1 is small compared to the detector pixel size.

Where the edge-enhancement effect is not present, the quantity $T(x, y)$ measured in the absorption radiographs is a function of the line integral of the linear attenuation coefficient $\mu(x, y, z)$ of the sample:

$$T(x, y) = \exp\left[-\int \mu(x, y, z)dz\right] \quad , \tag{8.1}$$

where $\mu(x, y, z) = 4\pi\beta(x, y, z)/\lambda$ and λ is the wavelength of the radiation.

The signal recorded in the differential phase radiographs is related to the refraction angle α in the direction perpendicular to the grating lines. The refraction angle is proportional to the differential phase of the wave front $\partial\Phi(x, y)/\partial x$ along x and is related to the integral of the real part of the refractive index [Weitkamp *et al.* 2005a]:

$$\alpha(x, y) = \frac{\lambda}{2\pi}\frac{\partial\Phi(x, y)}{\partial x} = \int \frac{\partial\delta(x, y, z)}{\partial x}dz \; . \tag{8.2}$$

The refraction of the X rays from the sample causes a lateral displacement d of the interference pattern produced by G1, see Fig. 8.1. For small refraction angles, the displacement d is

$$d \simeq \alpha D \; . \tag{8.3}$$

The displacement d is measured by extracting, for each pixel, the phase ϕ of the intensity oscillation measured during the phase-stepping scan. (The oscillation phase ϕ should not be confused with the phase Φ of the wavefront.) The phase ϕ_s measured when the sample is in the beam is corrected for the reference phase ϕ_r measured without the sample in the beam by subtraction. If p is the period of the interference pattern, d is given by:

$$d = p\frac{\Delta\phi}{2\pi} \; , \tag{8.4}$$

where $\Delta\phi = \phi_s - \phi_r$. The phase ϕ is measured in the interval $[-\pi, \pi)$. When the phase is outside this interval, the measurement of the phase difference $\Delta\phi$ and therefore the measurement of α are subject to errors. We discuss in detail the effect of the phase-wrapping phenomenon in Section 8.2.6.

The combination of phase stepping with tomography yields the 3D distribution of the full complex-valued index of refraction $n(x, y, z)$ of the specimen. Tomographic reconstruction of the pseudo-absorption images yields the 3D distribution of the linear attenuation coefficient $\mu(x, y, z)$ which is proportional to the imaginary part of the refractive index $\beta(x, y, z)$ (plus, possibly, some propagation-based edge enhancement). The absorption tomogram is usually obtained with the filtered backprojection (FBP) algorithm and a ramp filter. The FBP with an imaginary sign filter [Pfeiffer *et al.* 2007a] applied to the refraction angle projections yields the 3D distribution of the decrement of the refractive index $\delta(x, y, z)$, henceforward referred to as "phase reconstruction".

8.2.4 Experimental parameters

A grating interferometer [Weitkamp *et al.* 2010b] of the type described in the previous section and installed at beamline ID19 [Weitkamp *et al.* 2010a] of the ESRF has been used to measure the refractive index of a reference sample made of known materials arranged in a systematic geometry.

The measurements were made with 35-keV X rays from a Si (111) double crystal monochromator. The sample was positioned at 150 m from the wiggler source. The grating G1 was situated 100 mm downstream of the sample, which was immersed in a tank filled with water in order to avoid artifacts from the refraction at the interface sample/air. The interferometer was operating at the 5th fractional Talbot order, the distance between G1 and G2 was 405 mm. The detector, a scintillator/lens-coupled Frelon CCD camera with 2048 × 2048 pixels and an effective pixel size of 8.12 μm, was positioned 50 mm downstream of G2. The beam-splitter with $\pi-$shifting Si lines had a period of 4.787 μm [David *et al.* 2007]. The gold lines of G2 had a period of 2.4 μm and a height of approximately 50 μm [Reznikova *et al.* 2008]. Phase-stepping scans were performed at 1500 evenly-spaced angles over 360°. Each phase-stepping scan was performed in 4 steps over one period of G2. The exposure time per image was 1.5 s.

The phantom was a polymethyl methacrylate (PMMA) cylinder of 8 mm diameter with seven cylindrical cavities of 0.8 mm diameter. The cavities were filled with different materials: five cavities contained solutions of dipotassium hydrogen phosphate (K_2HPO_4) in different concentrations, one contained pure water and one was left empty. A wire of Al 99.99% of 125 μm diameter was added at the outer wall of the PMMA cylinder.

Table 8.1 shows the expected values μ_c and δ_c of, respectively, linear attenuation coefficient and decrement of the refractive index of the materials of the phantom. They have been calculated with the software XOP [Sanchez del Rio & Dejus 2004]. The XCOM database was used for the calculation of the linear attenuation coefficient and the Windt database was used for the calculation of decrement of refractive index. The linear attenuation coefficient μ_c takes into account both absorption and scattering effects.

8.2.5 Results and discussion

The pseudo-absorption and phase reconstructions of a slice of the phantom are shown in Fig. 8.2 (a) and (b) respectively.

The numbers in the phase slice indicate the different materials reported in Tab. 8.1. The gray levels of the images in Fig. 8.2 (a) and (b) are the difference of the linear attenuation coefficient $\Delta\mu = \mu - \mu^{H_2O}$ and of the decrement of refractive index $\Delta\delta = \delta - \delta^{H_2O}$ respective to water. They have been obtained by subtracting the average value of the gray levels measured in the capillary occupied by demineralized water.

In the phase slice (Fig. 8.2 (b)), the PMMA cylinder can be distinguished from the surrounding water and all the discs can be discerned from the PMMA cylinder. The two materials that show the weakest contrast are solutions 6 and 7. On the other hand, these liquids can be clearly seen in the pseudo-absorption slice, Fig. 8.2 (a). Here, however, materials 2, 3 and 4 cannot be distinguished. Furthermore, in the absorption slice, the PMMA

#	Material	μ_c (cm^{-1})	δ_c (10^{-7})	Density (g/cm^3)
1	air	0.00	0.000	0.002
2	PMMA	1.19	0.310	2.155
3	H_2O	1.00	0.307	1.881
4	K_2HPO_4 (50 mg/ml)	1.045±0.004	0.369±0.001	1.945±0.008
5	K_2HPO_4 (100 mg/ml)	1.086±0.004	0.429±0.002	2.006±0.008
6	K_2HPO_4 (200 mg/ml)	1.161±0.005	0.550±0.002	2.143±0.009
7	K_2HPO_4 (300 mg/ml)	1.232±0.005	0.662±0.003	2.253±0.009
8	K_2HPO_4 (700 mg/ml)	1.504±0.006	1.081±0.004	2.698±0.011
9	Al	2.70	2.079	4.413

Table 8.1: Densities, linear attenuation coefficient and real part of the refractive index of the materials in the phantom. The solutions of K_2HPO_4 are described with the concentration of the salt in water. The densities of the solutions have been determined by weighing a known volume (25 ml in a calibrated flask) with a high-precision scale. The error associated to the densities measured in this way is 0.4%. Since both the linear attenuation coefficient and the decrement of refractive index are proportional to the mass density of the material, the same error of 0.4% is associated to the μ_c and δ_c values of the solutions. The other densities reported in the table are tabulated values in XOP.

cylinder and materials 3 and 4 are only visible through edge enhancement. This phenomenon helps to identify interfaces but, in the general case of an inhomogeneous specimen, does not give quantitative information and its detectability will generally depend critically on the spatial resolution of the detector.

More information on the image signals can be obtained with histogram analysis. Figures 8.2 (d) and (e) show, respectively, pseudo-absorption and phase histograms of the region-of-interest (ROI) of 715×460 pixels delimited by a white dashed rectangle in Fig. 8.2 (a). The selected ROI is also shown in the background of the histogram plots. The $y-$axis of the histograms represents the frequency of appearance of the gray levels in the ROI.

In the histogram of the absorption-contrast data, Fig. 8.2 (d), only four peaks are present while in that of the phase tomogram (Fig. 8.2 (e)) each of the six materials of the ROI forms a distinct peak. This shows the higher sensitivity of phase contrast compared to absorption contrast in discerning the materials in the ROI. As already discussed, materials 2, 3 and 4, whose gray levels are part of the same peak, cannot be separated in the absorption slice.

Note that all the peaks of the phase histogram except the peak corresponding to the PMMA are asymmetric: they have a tail towards the PMMA peak. We believe that the asymmetry in the histogram peaks is mainly due to the stripe artifacts generated around the capillary containing air (see also detail in Fig. 8.2 (c)). We explain the origin of these artifacts in the next section.

8.2.6 Phase wrapping

In the phase slice of Fig. 8.2 (b), stripe artifacts departing tangentially from the capillary containing air spread throughout the entire slice. A zoom of this capillary is shown in Fig.

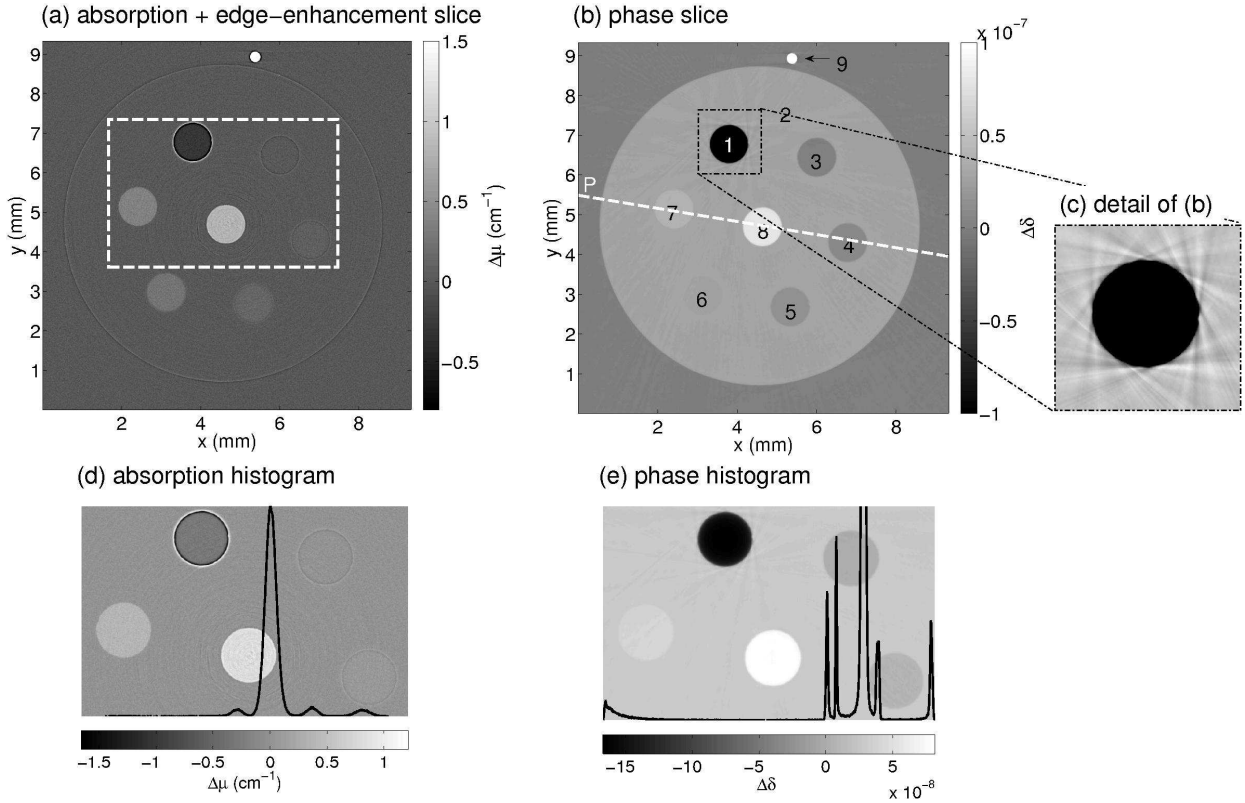

Figure 8.2: Absorption plus edge-enhancement (a) and phase (b) tomographic reconstructions of the phantom sample used in this study. (c) Detail of (b) showing the image artifacts coming from the phase-wrapping effect. (d) Absorption and (e) phase histograms of the ROI indicated by a white dashed rectangle in panel (a). The $y-$axis of the phase histogram has been cut to one eleventh of the height of the peak of PMMA.

8.2 (c) where the contrast has been adjusted in order to highlight these artifacts. The same type of artifacts can be observed around the Al wire. In the following, we show that these artifacts are caused by the phase-wrapping effect introduced in Sec. 8.2.3.

Figure 8.3 shows the sinogram of $\Delta\phi$ values (Eq. (8.4)) from which the phase slice of Fig. 8.2 (b) has been reconstructed. The zoomed insets in Fig. 8.3 are examples of wrapped parts of the sinogram causing the stripe artifacts of Fig. 8.2 (b).

Simple one-dimensional phase unwrapping algorithms and path-following two-dimensional phase unwrapping algorithms [Ghiglia & Pritt 1998] have been tested on our dataset but failed to unwrap it. Here, we prove, by comparison of numerical simulation with the experimental data, that the stripe artifacts of Fig. 8.2 (b) are actually caused by the phase wrapping effect and not by anything else.

By segmenting the phase slice of Fig. 8.2 (b), we obtained the ideal (noise free) phase slice of the phantom and we generated from it the corresponding $\Delta\phi$ sinogram. In order to calculate the $\Delta\phi$ sinogram from the δ values, we used the relations reported in Eqs. (8.2), (8.3) and (8.4). The sinogram computed in this way is a non-wrapped ideal sinogram whose reconstruction gives a phase tomogram free of artifacts, as shown in Fig. 8.3 (b). If, however, we wrap the ideal sinogram into the interval [-π,π), the resulting tomographic

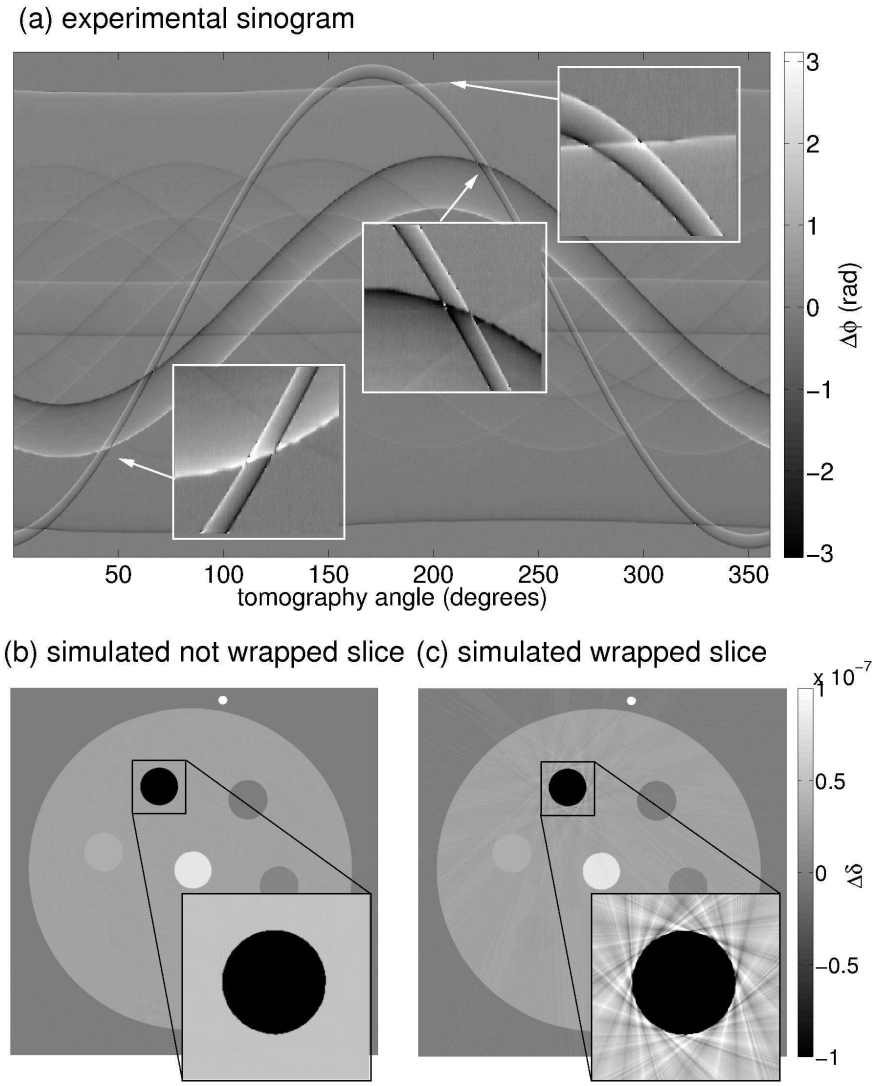

Figure 8.3: (a) Experimental sinogram of $\Delta\phi$ values; the insets show examples of wrapped parts. (b) Phase slice from ideal, noise-free sinogram of $\Delta\phi$, not wrapped. (c) Phase slice from ideal, noise-free sinogram in which $\Delta\phi$ is wrapped.

phase reconstruction (Fig. 8.3 (c)) shows artifacts that are, not only of the same type as those observed in the experimental data (Fig. 8.2), but also show a very similar geometric structure. This geometry is given by the positions in the sinogram at which phase wrapping occurs. In the following quantitative analysis we will see how these errors affect the precision and accuracy of the reconstructed values of the real part of the refractive index.

8.2.7 Quantitative comparison of δ and μ values, sensitivity and contrast-to-noise ratio measurements

Material #	description	Calculated $\Delta\mu_c$ (cm^{-1})	Experim. $\overline{\Delta\mu}$ (cm^{-1})	Std. dev. $\sigma_{\Delta\mu}$ (cm^{-1})	Calculated $\Delta\delta_c$ (10^{-7})	Experim. $\overline{\Delta\delta}$ (10^{-7})	Std. dev. $\sigma_{\Delta\delta}$ (10^{-7})
1	air	-0.307	-0.297	0.046	-1.879	-1.666	0.037
2	PMMA	0.002	-0.007	0.046	0.268	0.269	0.007
3	H_2O	0.000	0.000	0.046	0.000	0.000	0.005
4	K_2HPO_4 (50 mg/ml)	0.062±0.001	0.058	0.045	0.064±0.008	0.067	0.004
5	K_2HPO_4 (100 mg/ml)	0.122±0.002	0.116	0.047	0.124±0.008	0.128	0.004
6	K_2HPO_4 (200 mg/ml)	0.243±0.002	0.241	0.046	0.262±0.009	0.257	0.005
7	K_2HPO_4 (300 mg/ml)	0.354±0.003	0.362	0.047	0.372±0.009	0.380	0.008
8	K_2HPO_4 (700 mg/ml)	0.774±0.004	0.795	0.067	0.816±0.011	0.775	0.007
9	Al	1.771	1.727	0.172	2.532	2.268	0.086

Table 8.2: Comparison between calculated (subscript c) and experimental values of the linear attenuation coefficient and decrement of refractive index. The standard deviations (std. dev.) associated to the measured values are also reported in the table.

The measured values of $\Delta\mu$ and $\Delta\delta$ extracted from the slices of Fig. 8.2 have been compared with the quantities $\Delta\mu_c = \mu_c - \mu_c^{H_2O}$ and $\Delta\delta_c = \delta_c - \delta_c^{H_2O}$ calculated from the numbers in Tab. 8.1 and reported in Tab. 8.2.

The measured values have been obtained by averaging the gray levels in circular ROIs each corresponding to one material in the tomographic slice. The area of the ROIs was of 3848 pixels, with the exception of the Al (314 pixels). The mean values $\overline{\Delta\mu}$ and $\overline{\Delta\delta}$ calculated in this way are reported in Tab. 8.2. The standard deviation of the gray values in the ROIs are displayed with error bars in Fig. 8.4 (a) and (b) and listed in Tab. 8.2.

The measured linear attenuation coefficients match with the calculated data. The decrements of refractive index are, in general, in good agreement with the calculated data. The biggest discrepancies between calculated and measured values are observed for air and Al (materials 1 and 9). They can, at least partly, be attributed to the phase wrapping phenomenon, as can be deduced from inspection of the simulated data. For example, the $\Delta\delta$ value measured in the air disc of the simulated slice shown in Fig. 8.3 (c) is also underestimated with respect to the theoretical value and equal to -1.805×10^{-7}. While the discrepancy to the expected value is inferior than in the experimental data, it is clearly significant.

Another, smaller discrepancy is observed for the highest concentration of K_2HPO_4 (material number 8) probably due to the fact that the solution was saturated. This discrepancy can be detected in the phase slice due to the high sensitivity of the phase signal.

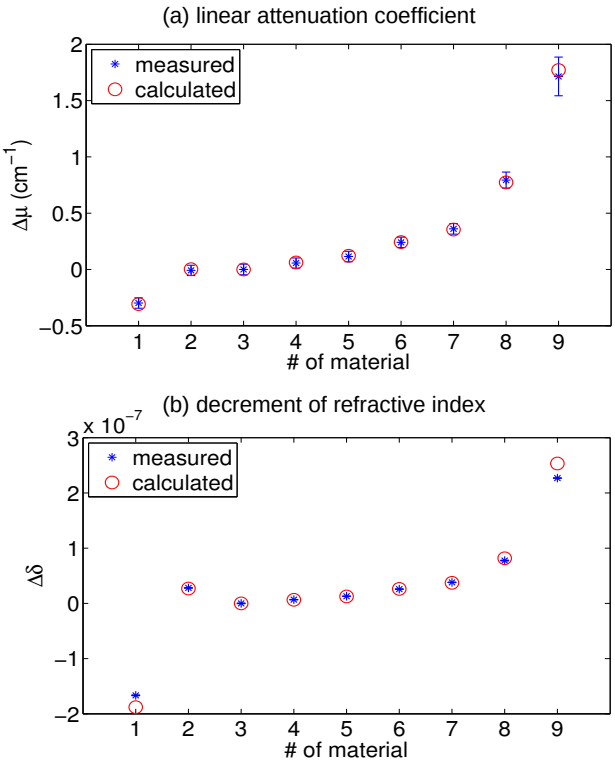

Figure 8.4: Measurements of $\Delta\mu$ (a) and $\Delta\delta$ (b) extracted from slices in Fig. 8.2 and compared with the calculated values reported in Tab. 8.1.

A figure of merit commonly used to assess the sensitivity of phase measurements is the standard deviation of the gray level values in a uniform region in the background of the phase reconstruction [Herzen *et al.* 2009, Pfeiffer *et al.* 2007a, Schulz *et al.* 2010b]. In the data presented here, the standard deviation of a ROI with an area of 3848 pixels extracted from a region of the phase slice occupied by water outside of the PMMA cylinder is 3.4×10^{-10}. This value, which is affected by several factors such as photon statistics, visibility of the interference pattern, presence of image artifacts and size of the ROI, is slightly larger than other sensitivity measurements performed at ID19: Pfeiffer et al. [Pfeiffer *et al.* 2007a] measured a sensitivity of 2.0×10^{-10} at the 9th fractional Talbot distance at 24.9 keV. More recently, Schulz et al. [Schulz *et al.* 2010b] measured a sensitivity of 2.3×10^{-10} at the 9th fractional Talbot distance at 23 keV. Note that the photon energies used for these studies were substantially lower than in the present case.

Herzen et al. [Herzen *et al.* 2009] using a polychromatic beam produced by a laboratory X-ray generator, obtained a higher value for the standard deviation of the background, corresponding to 4.9×10^{-10}. The experiment reported in Ref. [Herzen *et al.* 2009] was performed at 28 keV mean energy, with the interferometer operating at the fifth fractional Talbot distance.

The standard deviation σ_b measured in a ROI of the image background together with the mean value of the ROI, S_b =2.8×10^{-10}, enters in the calculation of the contrast-to-noise ratio (CNR) of the different materials in the phase and absorption tomographies:

$$CNR_x = \frac{|S_x - S_b|}{\sqrt{(\sigma_x^2 + \sigma_b^2)}} , \tag{8.5}$$

where the subscripts x and b refer to the material and the background respectively. The values S_x and σ_x are the ones reported in Tab. 8.2.

Material		CNR	CNR
#	description	μ	δ
1	air	4.5	338.0
2	PMMA	0.1	58.8
3	H_2O	0.2	3.5
4	K_2HPO_4 (50 mg/ml)	1.1	17.7
5	K_2HPO_4 (100 mg/ml)	2.0	30.4
6	K_2HPO_4 (200 mg/ml)	4.0	57.9
7	K_2HPO_4 (300 mg/ml)	5.9	82.4
8	K_2HPO_4 (700 mg/ml)	12.9	165.3
9	Al	27.5	460.1

Table 8.3: Absorption and phase contrast-to-noise ratios calculated with the formula in Eq. (8.5).

Table 8.3 gives a list of the CNR values for δ and μ. Contrary to the results reported in Ref. [Herzen *et al.* 2009], obtained with a polychromatic source, we have observed that the CNR in the phase slice is always substantially better than the CNR of the linear attenuation coefficient

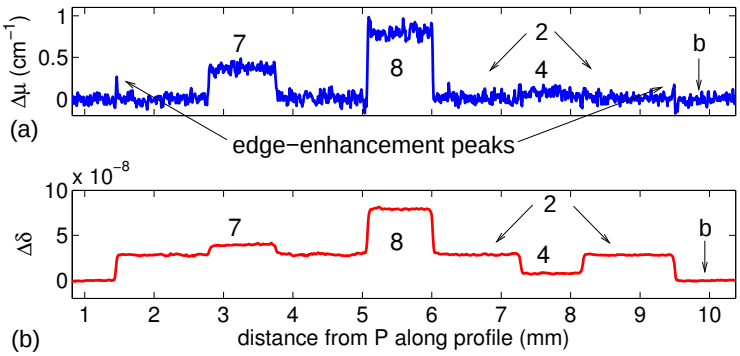

Figure 8.5: (a) Profile extracted from the pseudo-absorption tomogram. (b) Profile extracted from the phase tomogram. The letter 'b' indicates the background: the immersion liquid.

The higher CNR in the phase image compared to the CNR obtained in the absorption tomogram becomes evident in the section profiles of tomographic slices, shown in Fig. 8.5. The position at which the profiles have been extracted is indicated with dashed lines in Fig. 8.2 (a). In the absorption profile, the edge-enhancement peaks are clearly visible.

8.2.8 Conclusions

The present study demonstrates the quantitative correctness of the refractive index values retrieved by interferometric phase tomography. It also shows the superior contrast-to-noise ratio of the phase tomograms with respect to absorption images. Nonetheless, the absorption signal contained in the interferometric data remains a valuable source of complementary information.

We have demonstrated, through simulations based on segmented experimental data, that in the phase tomograms, stripe artifacts tangential to interfaces showing strong contrast are entirely caused by the phase-wrapping phenomenon. The fact that these artifacts can be completely reproduced by simulations indicates that algorithms may be developed to eliminate these artifacts from interferometric tomography data.

In the configuration used in this experiment, with the two-grating setup operated at 35 keV in the 5th fractional Talbot order on a third-generation synchrotron, the refractive index resolution, with a detector pixel size of 8 μm, was 3.4×10^{-10}, expressed in terms of the standard deviation of the real part of refractive index measured in a region of constant phase. The fact that this value is not quite as good as values reported in other studies is most likely influenced by the higher photon energy used here and by the presence of phase-wrapping artifacts generated by sample features showing strong contrast. These artifacts extend into other regions of the image.

These results confirm that grating interferometry with monochromatic synchrotron radiation can be a useful tool for high-accuracy measurements of the refractive index with applications in biological science, materials science and also fundamental physics.

Chapter 9

Phase tomography of soft-tissue biological samples

Contents

9.1 Introductory remarks

Grating interferometry was conceived as an X-ray phase-contrast imaging technique and X-ray phase-contrast imaging of soft-tissue biological specimens is one of its main application areas, see for example Refs. [Pfeiffer *et al.* 2007a, McDonald *et al.* 2009, Schulz *et al.* 2010b]. The high-sensitivity phase tomograms obtained with grating interferometry allow to visualize inner structures in biological specimens which cannot be revealed with any other non-destructive technique. This is because the contrast produced by conventional absorption tomography is in general too weak and the spatial resolution provided by magnetic resonance imaging is currently too low to resolve structures smaller than approximately 50 μm. One of the most commonly used techniques today to obtain microscopic images of soft tissue consists in histological sectioning and in imaging the stained slices of the specimen with a light or electron microscope.

This chapter contains results of two studies, performed during this PhD thesis, which highlight the potential of grating interferometry in giving high-sensitivity phase tomograms of soft-tissue samples.

Reference [Schulz *et al.* 2010b] reports on the comparison between synchrotron-radiation absorption-contrast and phase-contrast tomography of a human cerebellum. Parts of this paper are reported in Sec. 9.2.

The aim of the second study, presented in Sec. 9.3, is to compare the information provided by grating-based phase tomography with histology images of the same specimen. The sample used for this study is a rat testis. The results presented in this section are not yet published elsewhere.

Comparison of grating-based phase tomograms of soft-tissue samples with magnetic resonance images of the same specimen are reported in two co-authored publications [Schulz *et al.* 2010a, Noël *et al.* 2011].

9.2 Absorption vs. phase tomography of a human cerebellum

The aim of the study published in Ref. [Schulz *et al.* 2010b] was to compare absorption-contrast with phase-contrast synchrotron-radiation tomography on a soft-tissue biological specimen. The sample chosen for this comparison was a human cerebellum. For the measurements it was immersed in formalin 4% solution.

Absorption-contrast tomography was recorded at the beamline BW2 at the DORIS storage ring (HASYLAB at DESY, Hamburg, Germany) without the grating interferometer in the beam path and with an X-ray photon energy of 14 keV. This optimal energy was calculated based on the results published in Ref. [Grodzins 1983] in which the author shows that the optimum energy for synchrotron-radiation absorption tomography of a specimen with diameter D is the energy at which the attenuation coefficient μ of the specimen is equal to $\mu = 2/D$. The value of 14 keV was obtained for an aqueous specimen with $D = 1$ cm, i.e. the size of the human cerebellum specimen used in this study.

A slice extracted from the absorption tomogram is shown in Fig. 9.1. The signal in this slice is very poor and hardly allows to visualize features in the sample.

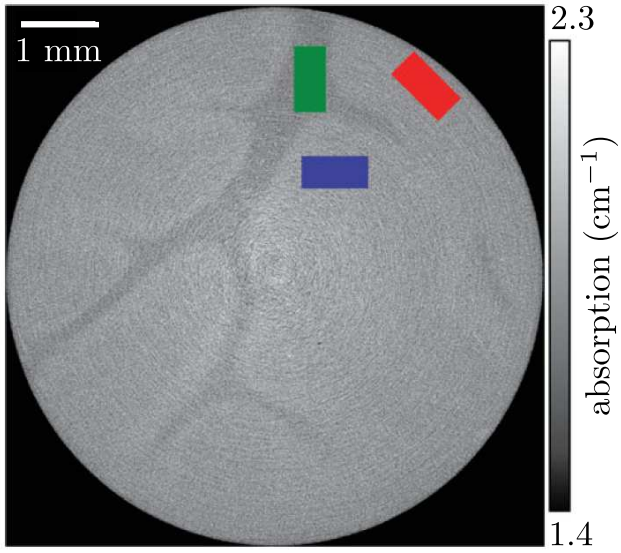

Figure 9.1: Slice of the absorption tomogram of the human cerebellum recorded at beamline BW2 at the DORIS storage ring (HASYLAB at DESY, Hamburg, Germany). Figure adapted from Ref. [Schulz *et al.* 2010b].

As opposed to the poor contrast obtained in the absorption tomogram, the phase signal provided by the grating interferometer allows to clearly distinguish the different tissues which constitute the cerebellum, see Fig. 9.2.

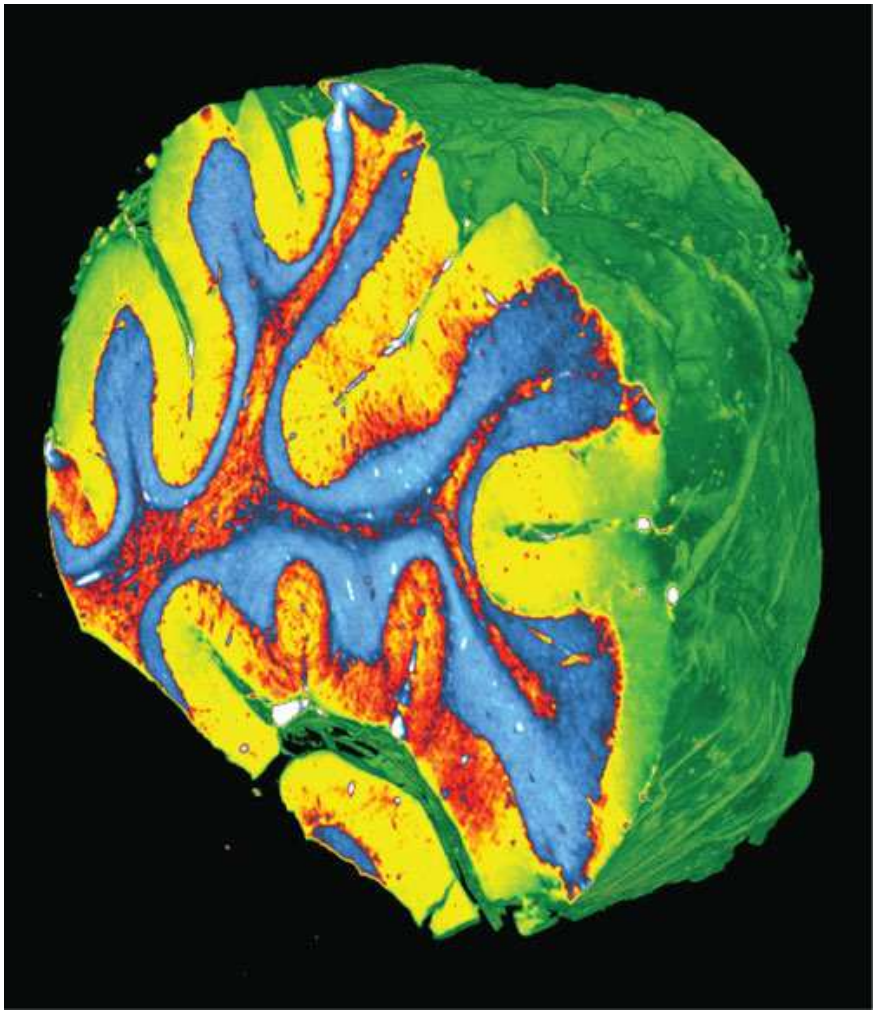

Figure 9.2: Three-dimensional rendering of a human cerebellum measured with the grating interferometer at ID19. The false-color representation has been obtained by simply applying a suitable colormap to the otherwise unsegmented data. The stratum granulosum (blue) separates the white matter (inside) from the stratum moleculare (yellow outside). The diameter of the specimen is 1 cm. Figure adapted from Ref. [Schulz *et al.* 2010b].

Grating-based tomography was performed at ID19 with an energy of 23 keV. The G1-to-G2 distance was 479.4 mm corresponding to the 9th fractional Talbot distance at this energy. The period of the $\pi-$shifting G1 was 4.78 μm; G1 was made in silicon. The analyzer grating G2 was a gold structure with a period of 2.4 μm. The detector pixel size was 5 μm, the exposure time per raw interferogram was 1 s. Four phase steps were scanned for each of the 1500 projection angles. For other experimental parameters, see Ref. [Schulz *et al.* 2010b]. The high sensitivity provided by the instrument at ID19 allowed not only to distinguish between grey and white matter (see false color 3D rendering in Fig. 9.2 and caption), but also to detect the presence of Purkinje cells (Fig. 9.3). These are among the largest neuron cells and have a diameter of around 40 μm. This is the first time that individual cells in the brain are visualized with X rays without any staining agent.

The density resolution (in terms of X-ray refractive index δ) of $\sigma_\delta = 2.3 \times 10^{-10}$ in the

phase tomogram has been obtained by calculating the standard deviation of a homogeneous region in a slice of the tomogram. This corresponds to an electron density resolution of 0.15 electrons/nm^3 and a mass density sensitivity for aqueous specimens of 0.5 mg/cm^3.[1]

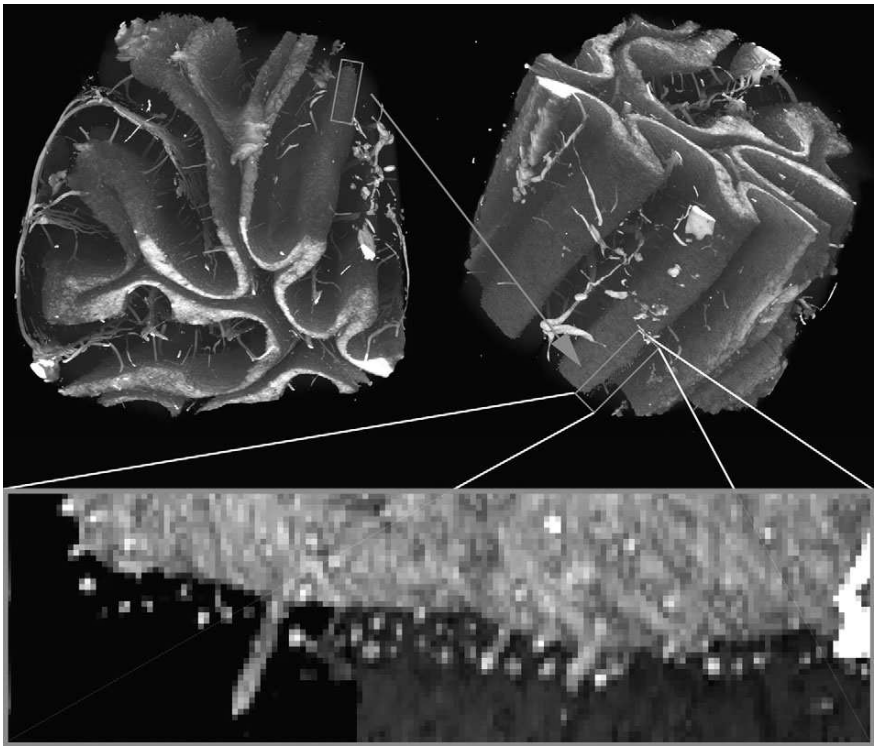

Figure 9.3: Top: three-dimensional rendering of the stratum granulosum and, bottom, enlarged view of the Purkinje cells. The diameter of the specimen is of 1 cm. Figure taken from Ref. [Schulz *et al.* 2010b].

9.3 Histology vs. phase tomography of rat testes

9.3.1 Introduction

As mentioned at the beginning of this section, one of the most commonly used techniques today to obtain microscopic images of soft tissues is histological sectioning and staining, often simply referred to as *histology*. Many advances, for example, in the investigation of diseases and health disorders rely on accurate histopathological analysis of healthy vs. diseased tissue. However, histology is a time-consuming technique which gives distorted images of stained slices. Since histological images are obtained with light or electron microscopes, the spatial resolution can be very high in the cut plane but lower, and limited

[1]The values of the electron density resolution and mass density sensitivity have been obtained, from δ, with the following formulas [Weitkamp 2002]. Far from the absorption edges the electron density ρ_e is given by: $\rho_e = (2\pi\delta)/(\lambda r_e^2)$, where r_e is the classical electron radius. The mass density ρ is related to the electron density by: $\rho = (\rho_e A)/(N_A Z)$ where A is the atomic weight, Z is the atomic number and N_A is the Avogadro number. For aqueous specimens, we can assume that $A/Z = 2$.

to the thickness of the slice (a few micrometers), in the orthogonal plane. Obtaining a three-dimensional dataset with histology through serial sectioning is possible, but extremely laborious. In addition, dimensional accuracy is not certain because distortions are induced in the preparation process of the sections (important when building anatomical atlases, e.g. used for surgical interventions).

This section presents results that show how X-ray phase contrast tomography based on grating interferometry can yield images with similar information content as stained histological cuts but in three dimensions, and without the use of any contrast agent. Moreover, the specimen preparation protocol comprises substantially fewer steps and is drastically less time-consuming since it does not imply dehydration, freezing, embedding into a hard matrix or staining.

The performance of grating-based tomography for histopathology is demonstrated on testes of a rat which were imaged with a grating interferometer and, subsequently, with histological sectioning.

9.3.2 Methods

Orchidectomy (testis ablation) was practised at the ESRF BioMedical Facility on male Fischer rats. After extraction the organs were placed into formalin 10% solution for preservation. All procedures related to animal care conformed to the Guidelines of the French Government under licenses B38 185 10002 and 380825.

9.3.2.1 Grating-based tomography

During the grating-based tomography measurement, the sample was placed in a cylindrical polypropylene tube with 15 mm diameter filled with formalin 10% solution. The sample container, suspended on the tomography axis, was immersed in a water tank with plane-parallel kapton walls and a thickness of 20 mm in the direction of X-ray beam propagation, to avoid artifacts from refraction of X rays on the walls of the cylindrical container.

The X-ray grating interferometer was used with a monochromatic X-ray beam; the X-ray photon energy was 19 keV. The distance between the $\pi-$shifting grating G1 and the absorption grating G2 was 485 mm, corresponding to the 11th fractional Talbot distance at this energy. The grating G1 was made of Si and had a period of $p_1 = 4.78$ μm, the grating G2 was made of Au and had a period of $p_2 = 2.4$ μm. The grating lines and the tomography rotation axis were vertical. The detector was a scintillator-lens coupled CCD Frelon camera (Sec. 7.2) with an effective pixel size of 8 μm.

The tomographic dataset was recorded by phase stepping over one grating period in four steps. A phase-stepping scan was recorded for each of the 1500 equidistant angular positions of the tomography rotation axis over a range of 360 degrees. The exposure time per raw interferogram was 1 s.

The raw interferograms were processed as described in Sec. 4.2 with the software presented in Sec. 7.6.1 and the tomographic reconstructions were obtained as discussed in Chap. 5 and Sec. 7.6.2.

9.3.2.2 Histological slicing and staining

The histological slice shown here was obtained from a different testis than the one imaged with grating-based tomography because the latter was damaged during the slicing procedure. However, the specimen imaged with histology was extracted from the same type of rat of the same age as the one measured with the grating interferometer.

For obtaining the histology image, the testis was embedded in paraffin and cut by using a microtome in longitudinal slices with a thickness of 8 μm. The slices were stained with a HE (Hematoxyllin Erythrosin) stain and imaged with a light microscope.

Histological slicing and imaging was performed at Laboratoire d'Anatomie Pathologique, Centre Hospitalier Universitaire de St. Étienne - 42000 St Étienne, France.

9.3.3 Results

Axial slices in attenuation and phase contrast, obtained from the same grating-based tomography data, are shown, respectively, in Fig. 9.4 (a) and (b). The structures in the testis, which can clearly be seen in the phase slice, are seminiferous tubules, in which the spermatogenesis takes place. As already shown in the previous section for the human cerebellum, almost no structures in the sample can be revealed with attenuation contrast (panel (a)). The dark structure visible at the top and at the bottom right of Fig. 9.4 (a) is the cylindrical container in which the testis was placed during the measurement.

The $\delta-$sensitivity of the phase tomogram was measured as described in section 9.2. The standard deviation σ_δ in a region of constant phase was 2.0×10^{-10}, which corresponds to a mass density sensitivity of around 0.5 mg/cm^3.

A longitudinal slice extracted from the phase tomogram is displayed in Fig. 9.5. Panels (a) and (b) of this figure show the same slice with two different grey scalings as reported in the caption of the figure. In this way, all the features in the image, which has a very high dynamic range, can be visualized.

The phase slice shown in Fig. 9.5 (a) and (b) should be compared with the histology image displayed in Fig. 9.5 (c). In the images of Fig. 9.5, three different parts can be visualized: the testis (indicated with the letter "T"), the epydidimidis (indicated with the letter "E") and adipose tissue (indicated with the letter "A"). The features indicated with the letter "V" are vessels. Enlarged regions of the testis with transversal cuts through the seminiferous tubules are shown in the insets of Fig. 9.5. Both histology and grating-based phase tomography highlight the concentric structure of the tubules which is due to the different stadia of spermatozoa maturation; mature spermatozoa are at the periphery of the tubules.

The immediate access to three-dimensional information provided by grating-based tomography enables three-dimensional visual and quantitative analysis. Figure 9.6 panels (b)-(d) show axial cuts in the phase tomogram taken at three different positions in the volume and panels (a) and (e) show longitudinal cuts in the same tomogram. The false-color representation has been obtained by simply applying a suitable colormap to the otherwise unsegmented data. Figure 9.7 (a) shows a detailed view of the epydidimis and the adipose tissue. The ultra-high sensitivity of the phase tomogram allows the visualization of the

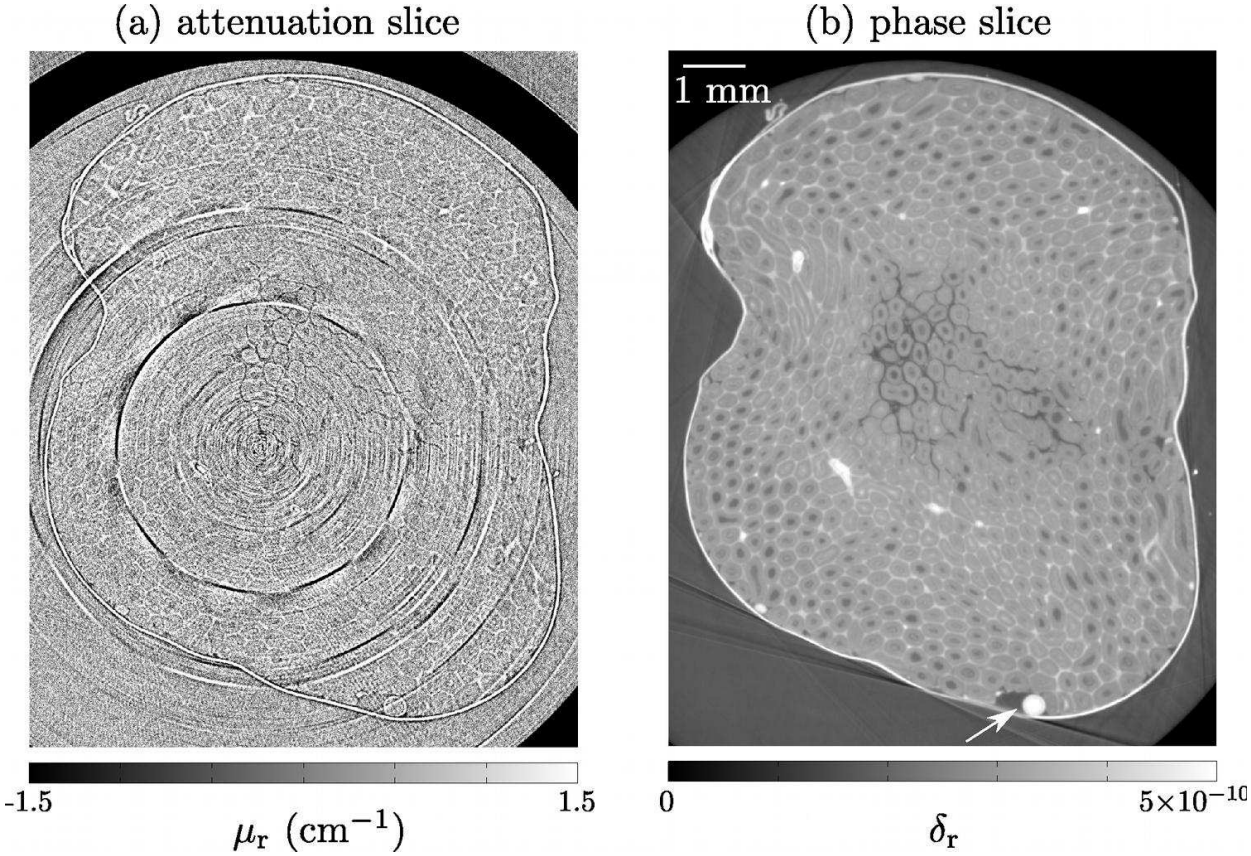

Figure 9.4: (a) Attenuation and phase (b) axial slices of a rat testis obtained with the grating interferometer at ID19. μ_r and δ_r values in the slices are relative to the immersion liquid (water). The circular structures clearly visible in the phase slice are seminiferous tubules. The high-density features (e.g. the one indicated with an arrow at the bottom of the phase slice) are blood vessels.

vascular network inside the testis as shown in Figure 9.7 (b). Note that this image has been obtained without the use of any staining agent and without the application of any particular segmentation algorithm other than global intensity thresholding.

We can conclude that grating-based phase tomography gives information similar to that obtained with histology and provides drastically enhanced image contrast compared to standard X-ray absorption tomography. Moreover, it gives genuine three-dimensional and non-distorted images of the specimen and require less time-consuming sample preparation procedures than serial sectioning in histology.

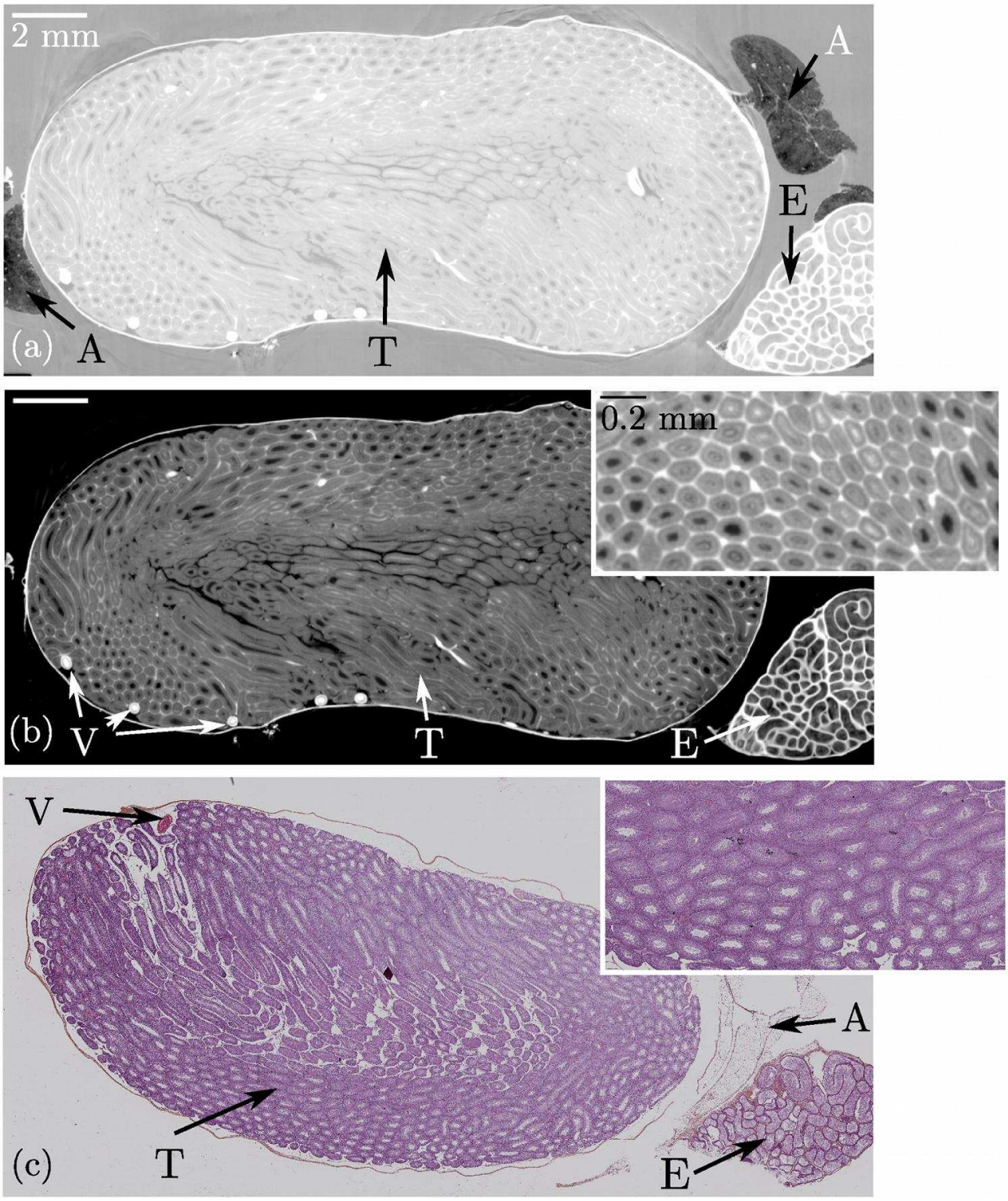

Figure 9.5: (a) and (b): Phase slice of the rat testis displayed with different intensity ranges: $\delta_r \in [-2 \times 10^{-8} 4 \times 10^{-8}]$ in panel (a) and $\delta_r \in [2 \times 10^{-8} 5 \times 10^{-8}]$ in panel (b). (c) Histology of the rat testis. In these images, "A" indicates the adipose tissue, "E" indicates the epydidimis, "T" indicates the testicles and "V" indicates the vessels. Enlarged insets show details of the seminiferous tubules in the testis.

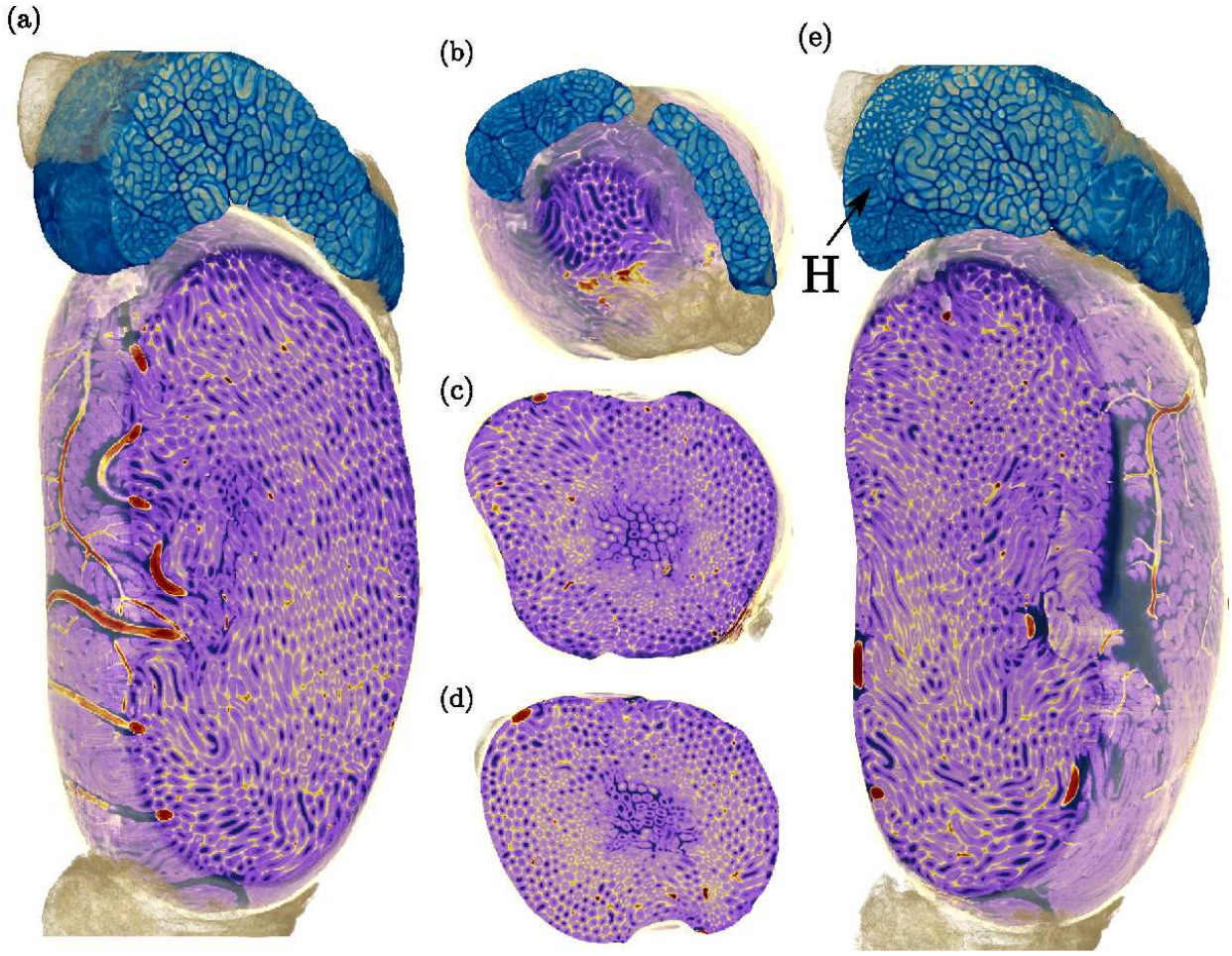

Figure 9.6: (a) and (e): Longitudinal cuts in the phase volume of the rat testis measured with the grating interferometer at ID19. (b)-(d): Axial cuts in the same volume. In these images the testis is colored in violet, the epydidimis in blue and the adipose tissue in yellow. The vessels (in red) are clearly visible at the periphery of the testis. The head of the epydidimis is indicated with the letter "H".

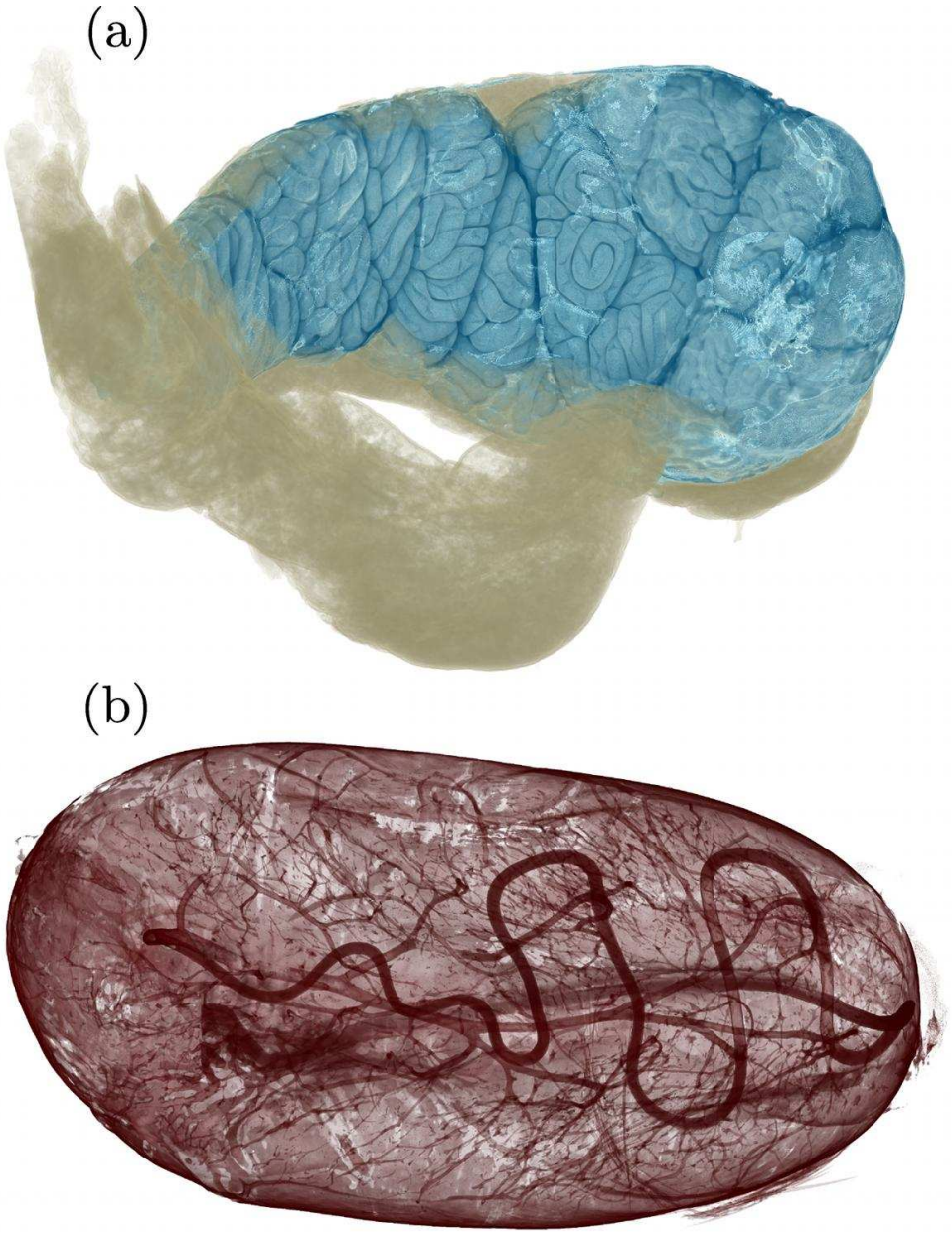

Figure 9.7: (a) Three-dimensional rendering of the epydidimis (light blue) and adipose tissue (yellow). (b) Visualization of the vascular network of the testicle with a simple intensity-based segmentation of the phase volume.

Chapter 10

Advanced phase-stepping schemes

Contents

10.1 Introductory remarks

In the previous chapter we have seen the tremendous potential of X-ray grating interferometry for high-sensitivity imaging of biological soft-tissue samples. The measurements reported in Chap. 9 were performed ex vivo on samples extracted from the body of the animal or the person and placed in proper containers for tomography. In vivo measurements are in general performed in much less favorable conditions: the investigated organ can be deep inside the body of the patient, breathing and blood circulation can cause motion artifacts and the radiation dose becomes an important issue. Thus, especially for in vivo measurements, the following aspects are essential:

(a) the dose delivered to the sample must be kept as low as possible;

(b) the acquisition time must be kept as low as possible to reduce motion artifacts;

(c) features outside of the region of interest may disturb the signal in the internal region.

During this PhD thesis, new phase-stepping tomography methods have developed with the goal of reducing the dose delivered to the sample during a tomography scan and, at the same time, increasing the quality of the region-of-interest reconstruction.

These methods are based on the acquisition of interlaced phase-stepping scans in which each raw interferogram is recorded at a slightly different viewing angle of the sample, rather than at a fixed position of the sample as in the standard method. The following sections contains reprints of the two publications Ref. [Zanette *et al.* 2011a, Zanette *et al.* 2011b].

10.2 Paper II

This section is a reprint of the paper published as: I. Zanette, M. Bech, F. Pfeiffer and T. Weitkamp *Interlaced phase stepping in phase-contrast x-ray tomography* Applied Physics Letters, **98**, 094101 (2011).

10.2.1 Abstract

We report on an interlaced acquisition scheme in grating-based X-ray phase-contrast tomography in which different viewing angles are used to retrieve a single differential phase projection. The interlaced acquisition scheme is particularly beneficial for region-of-interest tomography since it substantially reduces the artifacts caused by the external region and can eliminate the need for stop-and-go motion of the tomography rotation axis. In this Letter, the higher accuracy of the region-of-interest phase reconstructions obtained with the interlaced approach is demonstrated by numerical simulation and experimental results.

10.2.2 Introduction

Conventional computed tomography (CT) is an invaluable tool for the non-destructive investigation of objects belonging to life sciences, environmental sciences and in materials science. However, in conventional absorption contrast CT, weakly absorbing subjects show poor contrast of internal details. This limits its applicability to biological samples and other low-density materials.

Phase-contrast X-ray imaging uses the phase shift rather than the absorption to generate contrast. Since in the hard X-ray range the elastic scattering cross section is much larger than the absorption cross section, increased contrast from low density details can be obtained with phase-contrast imaging [Fitzgerald 2000, Momose 2005].

One of the most recent X-ray phase-contrast imaging techniques is grating-based interferometry [David *et al.* 2002, Momose *et al.* 2003, Weitkamp *et al.* 2005a]. Its outstanding

properties are high sensitivity and, compared to other techniques, good tolerance of polychromaticity and curved wavefronts. Grating interferometry was originally developed at synchrotron radiation facilities and can be adapted to standard X-ray generators [Pfeiffer *et al.* 2006].

In both absorption- and phase-contrast CT, when details deep inside the sample need to be visualized with high resolution and the field of view of the image detector is substantially smaller than the sample itself, high-frequency artifacts in the region of interest (ROI) are generated by the presence of features in the external region. This problem is also known as local tomography or truncated-projection tomography. In ROI absorption CT, tangential averaging of the data far from the rotation center reduces the high-frequency artifacts by blurring the projection of features outside of the ROI [Ramm & Katsevich 1996]. This tangential averaging is usually obtained with continuous tomographic scans, i.e., scans in which the sample rotates at constant speed while images are acquired.

Here we demonstrate, with numerical simulations and experimental results, that a similar principle can be applied to phase-contrast CT based on grating interferometry. In X-ray grating interferometry, differential phase projections are usually retrieved with a procedure known as a "phase-stepping scan" which consists in recording a series of frames for different transverse positions of one of the two gratings [Momose *et al.* 2003, Weitkamp *et al.* 2005a].

While the standard acquisition procedure consists in recording all the frames of the same phase-stepping scan at the same viewing angle, we here propose to perform the sample rotation simultaneously with the phase-stepping scan. In this interlaced approach multiple viewing angles of the sample can be used, as part of the same phase-stepping scan, in order to retrieve a single differential phase image.

It is not obvious that interlaced phase-stepping scans give stable result. In this Letter we not only show that they actually yield accurate phase reconstructions, but that they even significantly reduce high-frequency artifacts in phase-contrast ROI tomography while preserving the sample features.

10.2.3 Interlaced phase stepping

A schematic representation of an X-ray grating-based tomography set-up is shown in Fig. 10.1 (a). The working principles of an X-ray grating interferometer are described elsewhere [Weitkamp *et al.* 2005a]. The phase-stepping scan, in combination with the absorption grating G2, is used to analyze the interference fringes formed by the beam-splitter G1 and distorted by the presence of the sample. In Fig. 10.1 (a), G1 is the stepped grating, its transversal position is indicated with x_g. The sample, which can be described by the 3D distribution of its complex-valued refractive index $1 - \delta(x, y, z) + i\beta(x, y, z)$, rotates around the y axis. Its angular position is denoted with ω.

In phase-contrast tomography, the 3D reconstruction of $\delta(x, y, z)$ is obtained from the differential phase projections resulting from the phase-stepping scans [Momose 2005, Weitkamp *et al.* 2005a Pfeiffer *et al.* 2007b].

In standard phase-stepping CT, all the frames of the same phase-stepping scan are recorded at a given viewing angle of the sample ω. Standard phase-stepping scans thus form vertical lines in the $\omega - x_g$ plane of the diagram of Fig. 10.1 (b) where each dot represents an image recorded by the detector. In the interlaced approach, frames of the same phase-

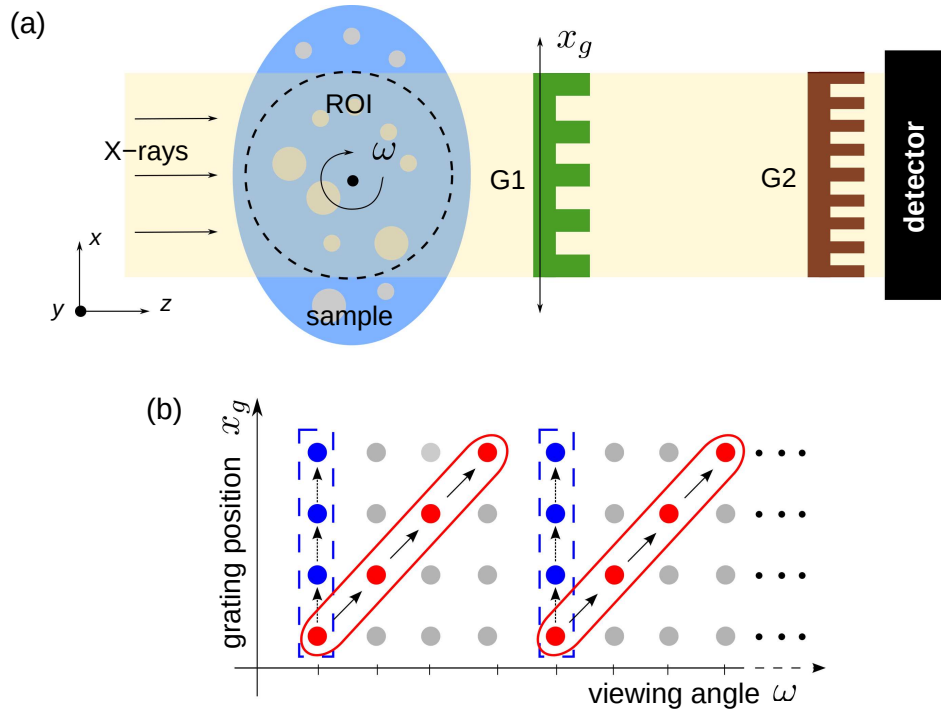

Figure 10.1: (a) X-ray grating-based tomography set-up. (b) Representation of standard and interlaced acquisition schemes in the $\omega - x_g$ plane where each dot represents a frame recorded by the detector. Dots representing standard phase-stepping scans are surrounded by a dashed blue rectangle and form vertical lines. Interlaced phase-stepping scans form diagonal lines and are surrounded by a red solid line.

stepping scan are recorded at slightly different viewing angles: during an interlaced phase-stepping scan, not only the grating is stepped but, at the same time, also the sample is rotated. Interlaced phase-stepping scans form diagonal lines in Fig. 10.1.

Using multiple viewing angles to retrieve the same differential phase projection smears the sample features in the external region while keeping sharp the internal features. This reduces speckle-like noise artifacts in the ROI and increases the accuracy of the ROI phase reconstructions.

10.2.4 Simulation

We validated the interlaced approach and assessed the expected quality of the data with a numerical simulation study on a simple phantom. This simulated object, shown in Fig. 10.2 (a), is a slice of 1500×1500 pixels with discs of different diameter and refractive index. The pixel size is 10 μm. The discs are phase objects with $\delta \in [0.3\times10^{-8}, 5\times10^{-8}]$. The refractive index of the background is unity.

The Radon transform (sinogram) of this slice has been computed for 375 evenly spaced angular steps in the interval $[0, \pi)$ by simulating both the standard and the interlaced acquisition schemes. Phase-stepping scans of four steps were simulated for a π-shifting G1 with period 4.8 μm. The period of G2 was 2.4 μm and the G1-to-G2 distance was 481 mm. The X-ray energy was 23 keV.

The sinograms were then truncated to a detector field of view of 330 pixels. The corresponding ROI is shown in Fig. 10.2 (b) where each number indicates a different grey level and a white rectangle surrounds a cluster of 9 small discs of 40 μm diameter.

The ROI phase reconstructions obtained with the standard and interlaced acquisition schemes are shown in Fig. 10.2 (c) and (d) respectively where high-frequency noise typical of local tomography is present. These artifacts are much weaker in the interlaced slice. While some details of the cluster of small discs are lost in noise in the standard reconstruction, all the features are preserved in the interlaced reconstruction. The increased accuracy is confirmed by the histogram analysis (Fig. 10.2 (e)).

The low-frequency artifacts in the ROIs, also generated by the non-locality of the Radon transform, are not influenced by the acquisition schemes. However, these artifacts, which severely deteriorate conventional ROI reconstructions, are of substantially minor importance in phase CT based on differential phase projections [Pfeiffer *et al.* 2008b].

10.2.5 Experiments

The results of the numerical study have been validated with ROI phase reconstructions of experimental data. The experiment was performed at the beamline ID19 of the European Synchrotron Radiation Facility with 23.0-keV X rays from a Si (111) monochromator. The interferometer, whose geometry was the same as in the simulation, was positioned at 150 m from the wiggler source. The images were recorded with a scintillator / lens coupled CCD camera with 2048×2048 pixels and an effective pixel size of 15 μm.

A dataset of 700 phase-stepping scans of 4 steps each was acquired with the standard scheme for evenly spaced viewing angles in the interval $[0, 2\pi)$. The exposure time per frame was 1 s. In this demonstrator experiment, the sample - a rat kidney - fit entirely in the field of view of the detector. It was fixed in formalin 4% solution and held in a cylindrical plastic container, placed in a water bath to avoid artifacts from the refraction between container walls and air.

A tomogram reconstructed using the full, non truncated dataset is shown in Fig. 10.3 (a). A central ROI of this tomogram with 200 pixels diameter is shown in Fig. 10.3 (b) and was used as a reference when comparing the ROIs obtained with the different acquisition schemes. It should be noted that global reference data of this type will not be available in a typical application experiment.

In order to perform this comparison, two subsets of the raw data with an equal number of frames (1/4 of that of the full dataset) were extracted from the full dataset and were truncated correspondingly to the ROI shown in Fig. 10.3 (b). The first subset, represented in Fig. 10.1 (b) by dots surrounded by a solid line, consists of interlaced phase-stepping scans and the second subset, represented in Fig. 10.1 (b) by dots surrounded by a dashed rectangle, consists of standard phase-stepping scans. In Fig. 10.1 (b), all the dots, surrounded and not, represent the full dataset. Thus, the acquisition schemes are compared for the same dose delivered to the sample corresponding to 1/4 of the dose used for Fig. 10.1 (a) and (b). The standard and interlaced ROI reconstructions are displayed in Fig. 10.3 (c) and Fig. 10.3 (d) respectively.

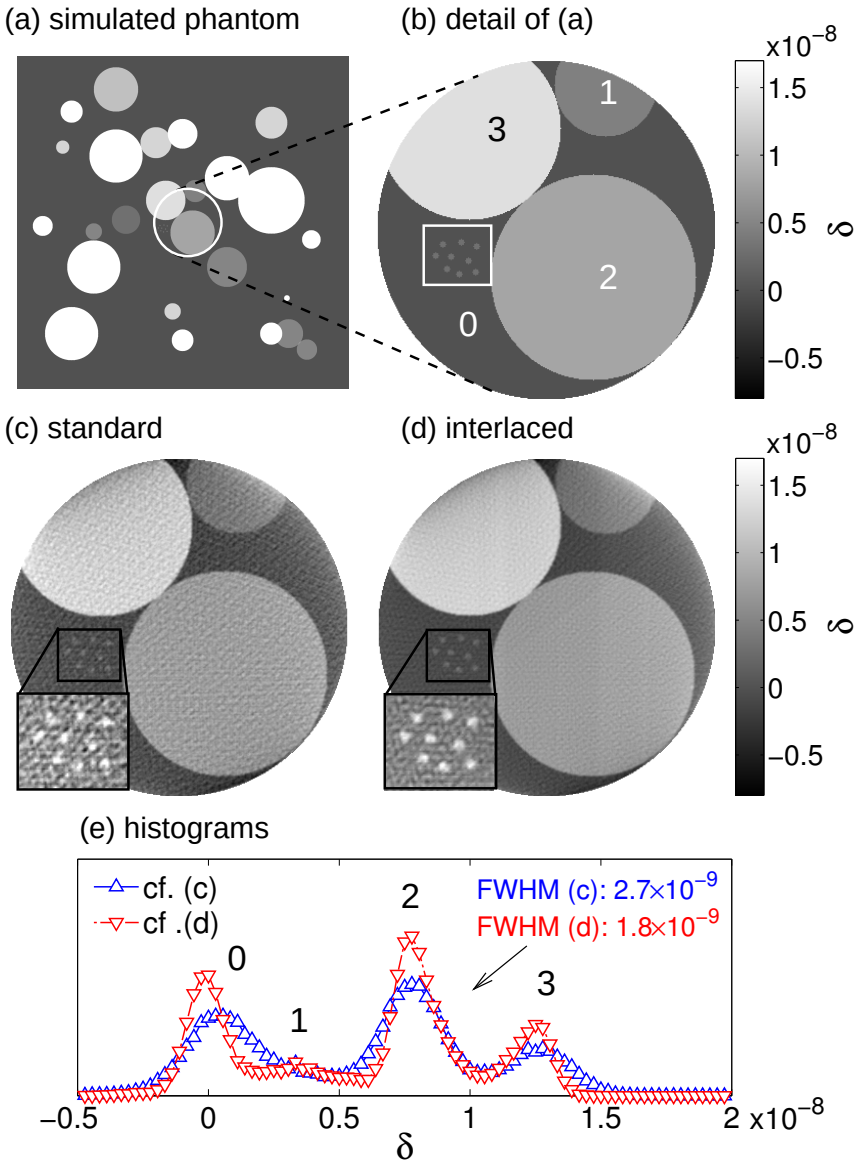

Figure 10.2: (a) Simulated phantom. (b) Zoom of the ROI used for the numerical tests. (c) and (d) Standard and interlaced ROI reconstructions respectively. (e) Histogram analysis.

As in the simulations, high-frequency artifacts are significantly reduced with the interlaced approach without affecting the sharpness of the features. The preservation of the sharpness is confirmed by the profile plots of Fig. 10.3 (e). Squares in Fig. 10.3 (b) indicate detail features visible in local tomography conditions with the interlaced approach that are severely deteriorated when using the standard approach.

Note that all the phase reconstructions have been obtained with exactly the same procedure: the filtered-back projection algorithm with an imaginary sign filter was applied to the differential phase sinograms [Pfeiffer *et al.* 2007b] and no further filtering or processing has been performed on the data.

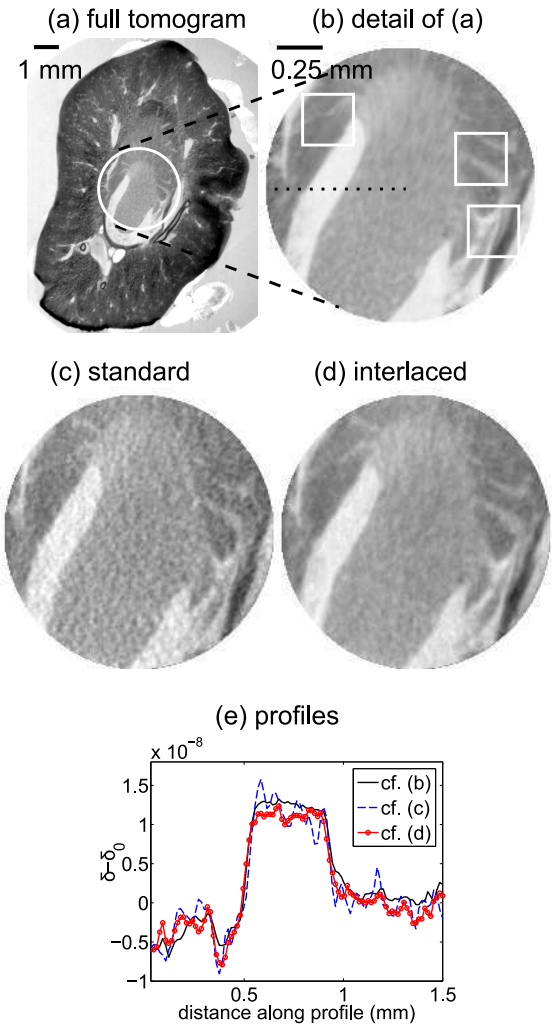

Figure 10.3: (a) Phase slice of a rat kidney obtained with the standard acquisition scheme. (b) Detail selected for the comparison of the acquisition schemes. (c)-(d) ROI reconstructions obtained with the standard and interlaced schemes respectively. (e) Profiles extracted from the central line of the ROIs, δ_0 is the refractive index of the immersion liquid (water).

10.2.6 Conclusions

Compared to other recently proposed schemes for the optimization of data acquisition in grating-based phase CT, which can go as far as abandon the need for phase stepping altogether [Zhu *et al.* 2010], the phase-stepping approach presents less strict requirements on the exact divergence matching of the periods of G1 and G2 - an aspect that makes the interlaced scheme easier to realize, especially for large fields of view. With respect to approaches based on moiré fringe imaging [Momose *et al.* 2009b], the interlaced acquisition scheme retains the full spatial resolution of the detector in the tomograms.

The interlaced approach has the further advantage that it can be implemented in scans with continuous rotation of the sample, as it is common practice in most clinical CT scanners. Moreover, due to the improvement in the image quality provided by the interlaced acquisition scheme, the dose to the sample in phase-stepping CT can be reduced.

In summary, the numerical tests and the experimental data demonstrate that, for the same dose to the sample, interlaced CT provides phase reconstructions of better quality than standard phase-stepping CT. This development is of particular interest for applications where details with small density differences deep inside the object need to be visualized in ROI tomography conditions with high resolution and high sensitivity.

10.3 Paper III

This section contains a reprint of a paper submitted for publication as: I. Zanette, M. Bech, A. Rack, G. Le Duc, P. Tafforeau, C. David, J. Mohr, F. Pfeiffer and T. Weitkamp *Trimodal low-dose X-ray tomography* (2011).

10.3.1 Abstract

X-ray grating interferometry is a coherent imaging technique that bears tremendous potential for three-dimensional tomographic imaging of soft biological tissue and other specimens whose details exhibit very weak absorption contrast. It is intrinsically trimodal, delivering phase contrast, absorption contrast, and scattering ("dark-field") contrast. Recently-reported acquisition strategies for grating-interferometric phase tomography constitute a major improvement of dose efficiency and speed. In particular, some of these techniques eliminate the need for scanning of one of the gratings ("phase stepping"). This advantage, however, comes at the cost of other limitations. These can be a loss in spatial resolution, or the inability to fully separate the three imaging modalities. In the present paper we report a data acquisition and processing method that optimizes dose efficiency but does not share the main limitations of other recently-reported methods. While our method still relies on phase stepping, it effectively uses only down to a single detector frame per projection angle and can extract images corresponding to all three contrast modalities. In particular, this means that dark-field imaging remains accessible. The method is also compliant with data acquisition over an angular range of only 180 degrees, and with a continuous rotation of the specimen relative to the detector.

10.3.2 Introduction

In X-ray phase contrast imaging, contrast is generated by the refraction of X rays as they pass the object under study, and not, as in conventional radiography, by the differences in absorption between the constituents of the object.

Since the real part of the refractive index of hard X rays for light materials is several orders of magnitude higher than its imaginary part (which describes absorption), X-ray phase contrast methods can reveal structures that usually remain invisible in conventional absorption contrast, for example different types of soft biological tissue. However, the angles by which X rays are refracted when passing through macroscopically-sized objects remain so small that sophisticated apparatus is needed to exploit phase contrast.

For these reasons, while some X-ray phase contrast methods had, in principle, already been developed decades ago [Bonse & Hart 1965, Förster *et al.* 1980], the full potential of these methods was recognized only with the availability of modern synchrotron radiation sources and microfocus X-ray generators for the laboratory. A variety of X-ray phase contrast methods based on these sources was developed in the second half of the 1990s [Fitzgerald 2000]. In addition to providing the high contrast of a phase-sensitive method, some of them have the additional advantage of providing yet another complementary contrast modality, i.e., scattering contrast. This is notably the case of analyzer-based imaging

[Davis *et al.* 1995, Chapman *et al.* 1997].

Starting in the early 2000s, X-ray grating interferometry (GIFM) [David *et al.* 2002, Momose *et al.* 2003] emerged as an additional multimodal X-ray imaging technique with particular benefits. It gives access to differential phase contrast (DPC) at ultrahigh sensitivity (density differences down to 0.5 mg/cm^3 can be routinely achieved) [McDonald *et al.* 2009, Schulz *et al.* 2010b]. GIFM also provides dark-field (or scattering) images of the sample which allow to reveal the presence of scattering structures on the nanoscale [Pfeiffer *et al.* 2008a].

A grating interferometer is largely achromatic and can thus be efficiently used with X rays that have a broad spectral distribution [Weitkamp *et al.* 2005a, Rizzi *et al.* 2011]. Another important property of GIFM, which further distinguishes it from many other X-ray phase contrast methods, is that radiation from a low-brilliance X-ray source can be efficiently used [Pfeiffer *et al.* 2006]. This feature and the achromaticity are unique properties that make this method compatible with laboratory X-ray imaging systems and increase its efficiency on synchrotron imaging stations.

The key element of a GIFM setup (Fig. 10.4) is a diffraction grating G1 in transmission geometry. It induces a periodic modulation into the X-ray wavefront. The period p_1 of this grating is much larger than the X-ray wavelength. Its diffraction orders therefore overlap almost completely and form regular interference patterns in planes downstream of G1. An object placed in the beam will cause local modifications of these patterns. A second grating G2, placed before the detector, can be used to encode these modifications into intensity variations on the detector pixels.

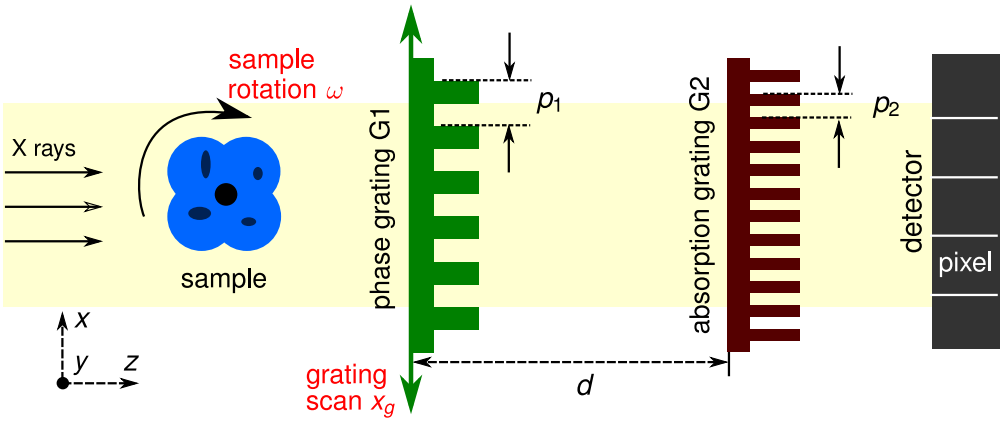

Figure 10.4: Schematic representation of an X-ray grating interferometer setup (not to scale). The phase grating (G1) and the absorption grating (G2) are positioned between the sample and the detector. G2 is placed at the distance d from G1 at which the interference pattern produced by G1 exhibits the maximum contrast.

The DPC and dark-field signals (usually also the absorption image is obtained from the same dataset) can be extracted from the raw interferograms with different approaches. Among these methods, the "phase-stepping" technique, which consists in recording and analyzing a series of interferograms (three or more) for different relative transverse positions of the two gratings [Momose *et al.* 2003, Weitkamp *et al.* 2005a, Zanette *et al.* 2011a], has several advantages. It does not affect the spatial resolution of the imaging system as in the

single-shot approaches [Wen *et al.* 2009, Momose *et al.* 2011b] and it does not have stringent requirements on the period matching of the gratings which is a limitation in the reverse projections (RP) method [Zhu *et al.* 2010]. It should also be noted that, with the RP method, which uses a linear combination of two interferograms taken at sample positions 180° apart, the dark-field signal can not be accessed. On the other hand, since at least three exposures are needed per final projection, the phase stepping method may be slower and may deliver more dose to the sample than other methods.

In this paper we present and demonstrate, through simulated and real data, advanced phase stepping methods, here called oversampled methods, which provide phase and scattering tomographies of quality comparable to the existing phase stepping methods while significantly decreasing (up to a factor of 5) the acquisition time and hence also the dose delivered to the sample.

10.3.3 Oversampled phase stepping

A schematic representation of an X-ray grating interferometer is shown in Fig. 10.4. In a phase-stepping tomography measurement, the scan of one of the gratings is combined with the rotation of the sample as nested scan of two axes. Each raw interferogram recorded during a tomographic scan of this kind is taken at a different transverse position x_g of the grating and/or a different position ω of the sample. Thus, raw images recorded during a tomography scan based on phase stepping can be represented by points in the $\omega - x_g$ coordinate system.

Fig. 10.5 (a) illustrates the standard phase-stepping tomography acquisition scheme. All images belonging to one phase-stepping scan are recorded at a fixed angular position ω of the sample. The sample is rotated only between subsequent phase stepping scans. A first improvement over this scheme was the interlaced phase-stepping method [Zanette *et al.* 2011a] (Fig. 10.5 (c)), in which the sample is also rotated between images belonging to the same phase stepping scan. This acquisition method was developed to improve local tomography reconstructions. In local tomography, the sample is larger than the width of the field of view and only a central region of interested (ROI) is reconstructed. Recording raw images at slightly different positions of the sample, as in interlaced phase stepping, introduces a tangential averaging of the features far from the rotation center. This improves the quality of the ROI reconstruction and makes phase stepping compatible with a continuous rotation of the tomography axis [Zanette *et al.* 2011a].

Although interlaced phase stepping is a significant improvement over the standard method, especially in view of clinical applications of grating interferometry, it shares with the standard method an important limitation: at least three raw images are required to retrieve a differential phase and scattering projection of the sample. This means that if the phase-stepping scans are performed over P steps and if N is the desired number of final projections, $N \times P$ raw images are acquired with the standard and interlaced methods.

Oversampled phase stepping methods, as presented in this paper, allow to significantly reduce this number. The idea at the basis of oversampled phase stepping is that a single raw image, instead of being used in the processing of only one phase stepping scan, can be used in multiple scans. In this way, even if each phase stepping scan still contains P images,

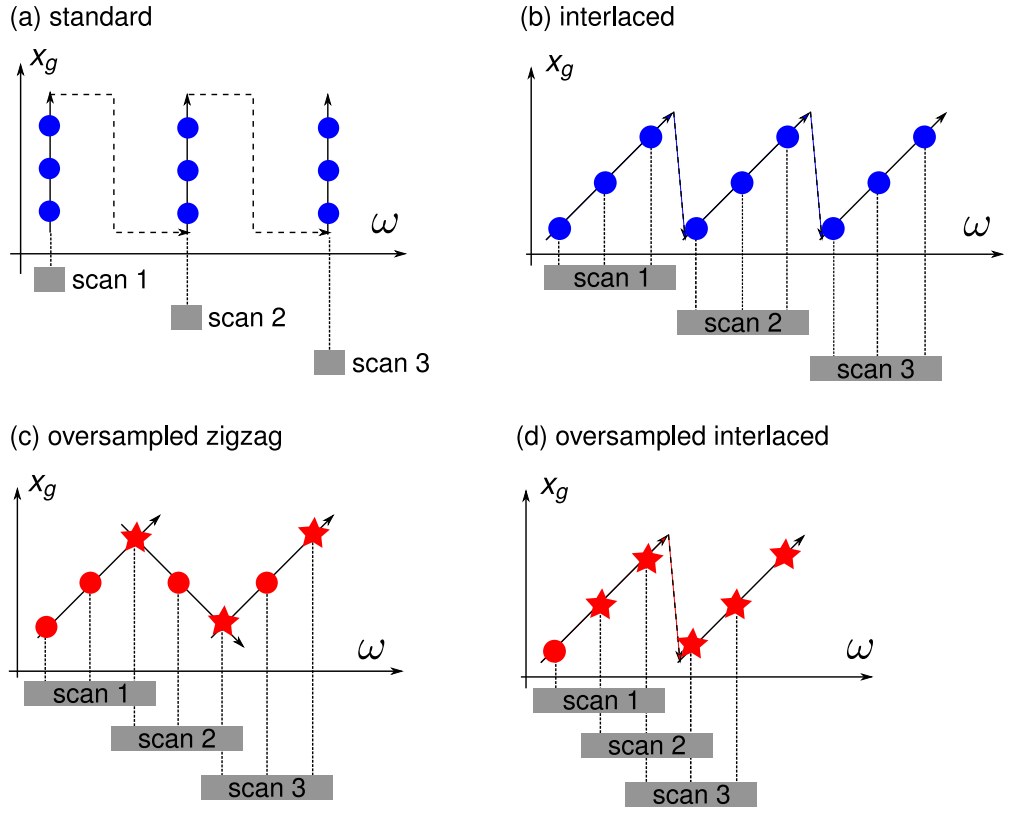

Figure 10.5: Phase stepping methods represented in the $\omega - x_g$ plane. Each colored dot or star represents an image frame recorded by the detector. Frames represented by stars are used in more than one phase stepping scan. (a) Standard phase stepping. (b) Interlaced phase stepping [Zanette *et al.* 2011a]. (c) Oversampled zigzag (OZ) phase stepping: one point of each scan is re-used in the next scan. (d) Oversampled interlaced (OI) phase stepping: all but one point in each scan are re-used in the next scan.

the actual number of images recorded during the full tomography can be much less than $N \times P$.

We propose two ways of implementing oversampled phase stepping scans: one is oversampled zigzag (OZ) phase stepping and the other is oversampled interlaced (OI) phase stepping. While the first method is an advanced way of recording the data, the second approach consists in an efficient way of analyzing the phase stepping scans. The two methods are discussed in the following.

In zigzag phase stepping, images are recorded not only when the grating moves in the forward direction, but also when the grating goes back to its initial position as illustrated in Fig. 10.5 (c). In the zigzag method, one in each P raw images is used for the processing of two phase stepping scans, thus reducing the effective number of images recorded per phase stepping scan to $P - 1$. The raw images contributing to two consecutive phase stepping scans (represented by stars in Fig. 10.5 (c)) are at the vertices of the zigzag line in the $x_g - \omega$ diagram. In this way, the number of raw images actually collected is reduced to $R_{oz} = (P - 1) \times N + 1$. Since the number of projections N is usually large, this can be approximated by $(P - 1) \times N$. For example, if $P = 3$, $R_{oz} = 2 \times N$, i.e., the same number

of raw images needed in the RP method.

With the second method presented in this paper, the oversampled interlaced method (Fig. 10.5 (d)), the number of raw images recorded in the tomography scan can be further reduced. The OI method consists in an efficient analysis of the interlaced phase stepping scans. In fact, if images are recorded with the interlaced scheme, each group of P consecutive raw images is recorded at P different positions of the grating and therefore can form a phase stepping scan. In this way, $P-1$ images of each phase stepping scan can be re-used in the processing of the next phase stepping scan and the number of raw images needed to obtain N final projections goes down to the minimum value of $R_{oi} = N$, independent of the number of steps P.

Thus, compared to existing phase stepping methods, oversampled phase stepping yields the same number of final projections but with significantly fewer raw images recorded during the scan, and consequently a lower dose to the sample. Equivalently, for the same dose delivered to the sample, oversampled methods provide a finer angular sampling of the final projections, which increases the quality of the reconstructions.

Note that, in the oversampled methods, the image signals (including the scattering signal not accessible with the RP method) are extracted with a simple algorithm based on Fourier analysis described for example in Ref. [Pfeiffer *et al.* 2008a] which does not require any linearization of the sinusoidal phase stepping curve.

Since OZ and OI are based on interlaced phase stepping, they can be implemented with continuous movement of the sample and they reduce artifacts caused by the presence of features outside of the field of view.

In the following, the performance of the oversampled methods is demonstrated with numerical simulations and experimental results. The latter have been obtained in both local and global tomography on biological and paleontological samples.

10.3.4 Simulations

We first demonstrate the potential of the oversampled phase stepping methods with simulations. The simulated slice is a pure phase (non absorbing) modified version of the Shepp-Logan phantom with a distribution of real-valued refractive index $n = 1 - \delta$ and zero absorption (see supplementary information). The size of the simulated noise-free slice is 2048×2048 pixels and the pixel size is 5 μm. Four refraction angle sinograms,[1] corresponding to the acquisition methods shown in Fig. 10.5, have been generated from this slice with the same number of 1700 raw images. The parameters used in the simulation are listed in Table 10.1, more details on the simulation can be found in the supplementary material Sec. 10.3.8.

In order to compare the different acquisition schemes in local tomography, the sinograms were truncated and a region of interest (ROI) of 800 pixels diameter was reconstructed. The reconstruction of the ROI obtained with the oversampled interlaced method is shown in Fig. 10.6 (a). The complete set of reconstructions with the different schemes can be found in

[1] The phase tomography is obtained from refraction angle projections. The phase tomographies shown in this paper have been obtained with the filtered back-projection algorithm and a Hilbert filter [Pfeiffer *et al.* 2007b].

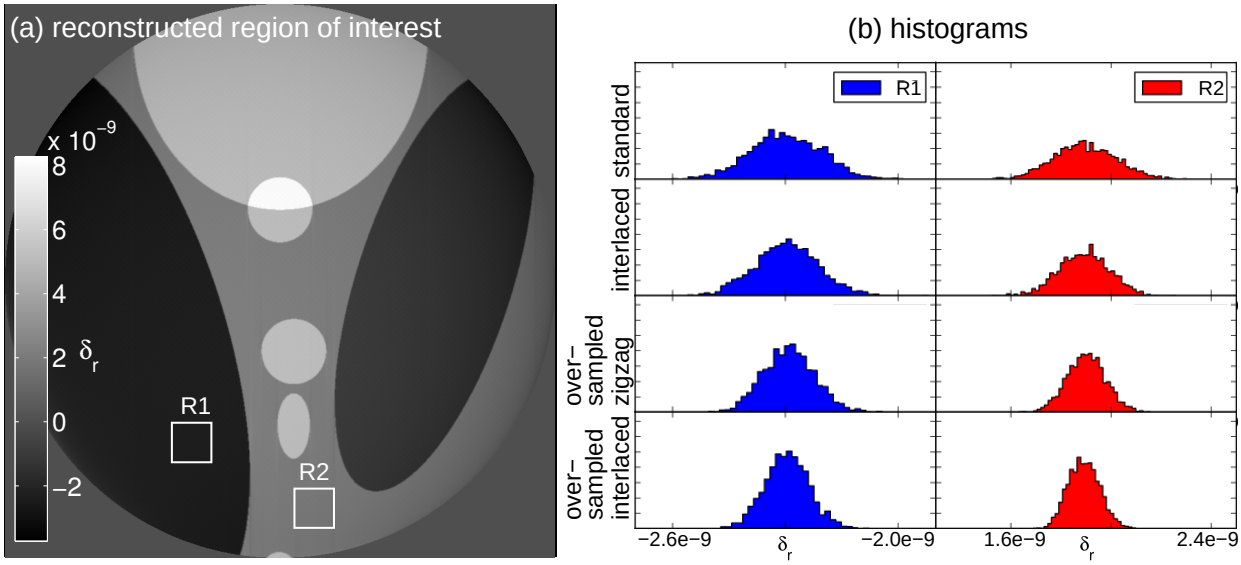

Figure 10.6: (a) ROI of the simulated slice reconstructed with the oversampled interlaced method. The simulated slice and the ROI reconstructions obtained with the other acquisition schemes are shown in supplementary material. (b) Histograms of the two regions R1 and R2 indicated by rectangles in panel (a). The y-axis of the histogram is the frequency of appearance of the grey levels in the ROI. The scale of the y-axis is the same for all the histograms. The histogram analysis shows the potential of the oversampled methods in reducing image noise. In fact, the width of the histogram peaks, which is broadened by the presence of image noise, is much smaller in the histograms extracted from the ROIs obtained with the oversampled methods.

the supplementary material. The histogram analysis on the ROI reconstructions is shown in Fig. 10.6 (b). For each ROI reconstruction, we calculated the histograms of the two regions R1 and R2 of 50×50 pixels indicated by squares in Fig. 10.6 (a).

Angular undersampling in the standard acquisition scheme generates image noise. The strength and position of the undersampling artifacts depend on the features in the sample (inside and outside the ROI) and on the angular sampling. As already discussed in Ref. [Zanette *et al.* 2011a], these artifacts are reduced with the interlaced acquisition scheme. This can be seen with the histograms analysis: the width of the histogram peak, which should ideally be infinitely narrow, is narrower in the histogram extracted from the slice obtained with the interlaced method than in the histogram extracted from the slice obtained with the standard acquisition scheme. By effectively increasing the angular sampling density, oversampled methods further improve the reconstructions and significantly reduce the image noise, as can be seen in Fig. 10.6 (b). The best performance (the narrowest peak) is given by the OI method, which increases the angular sampling density by a factor of P (here, $P = 4$) with respect to the standard and interlaced acquisition schemes.

While this particular study has been performed on a phase object, similar results, showing the superiority of the oversampled phase stepping on the other schemes, can be obtained by simulating the scattering and absorption signals.

10.3.5 Experimental results

We validated the results of the simulations with experimental data. The experiments were performed at the beamline ID19 of the European Synchrotron Radiation Facility (Grenoble, France) [Weitkamp *et al.* 2010b]. We used a monochromatic beam obtained via a Si (111) double crystal monochromator. The interferometer was located 150 m from the source. Its characteristics and the other experimental parameters are reported in Table 10.1.

The detector was a scintillator/lens-coupled CCD camera with 2048 × 2048 pixels. The effective pixel size and the field of view depended on the measurement (see Table 10.1).

	energy (keV)	p_1 (μm)	h_1 (μm)	d (mm)	e (μm)	w (pixels)	t (s)
simulation	23.0	4.80	29.5	480	5	800	-
rat heart	23.0	4.78	29.5	481	7.5	700	1.5
rat eye	23.0	4.78	29.5	481	5	2048	1
amber	35.0	4.78	45	404	5	2048	2

Table 10.1: Parameters of simulation and experiment. p_1 and h_1 indicate, respectively, the period and the height of the phase grating G1, made of Si. The period of absorbing Au structures on the absorption Au grating G2 was p_2 =2.4 μm and their height was h_2 =50 μm. d is the distance between G1 and G2, e the effective pixel size, w the width of the detector field of view, and t the exposure time per step.

We measured three samples: two soft tissue biological specimens (a heart and an eye of a rat) and a fossil (an insect in opaque amber). The samples were placed approximately 100 mm upstream of G1. The rat organs were placed in cylindrical containers filled with formalin 10% solution. They had been extracted from a male Fischer rat (Charles River Laboratories, France) after sacrifice of the animal for another experiment.[2] The containers with the rat organs were immersed in a water tank in order to avoid strong refraction at the sample-air interface. The amber was measured in air.

All the tomography scans were performed over 180°. The exposure time per raw image depended on the sample, but was for each sample kept constant for the two stepping methods. The values of the exposure times are reported in Table 10.1.

10.3.5.1 Phase tomography on soft-tissue biological specimens

A rat heart and a rat eye were chosen to validate the oversampled interlaced method in phase contrast tomography. The internal anatomical structures of these samples, which exhibit very little absorption and scattering contrast, can be visualized with high sensitivity in the phase tomographies obtained with the grating interferometer.

The rat heart was measured in local tomography. The phase tomographies were reconstructed from 750 refraction angle projections. In tomography performed with the standard acquisition scheme, these projections were retrieved from 750×5=3750 raw images and in the oversampled interlaced tomography they were retrieved from only 750 raw images. The

[2]All operative procedures related to animal care strictly conformed to the Guidelines of the French Government with licenses 380825 and B3818510002.

dose delivered to the sample with the oversampled interlaced method was thus only 20% of the dose delivered to the sample with the standard method.

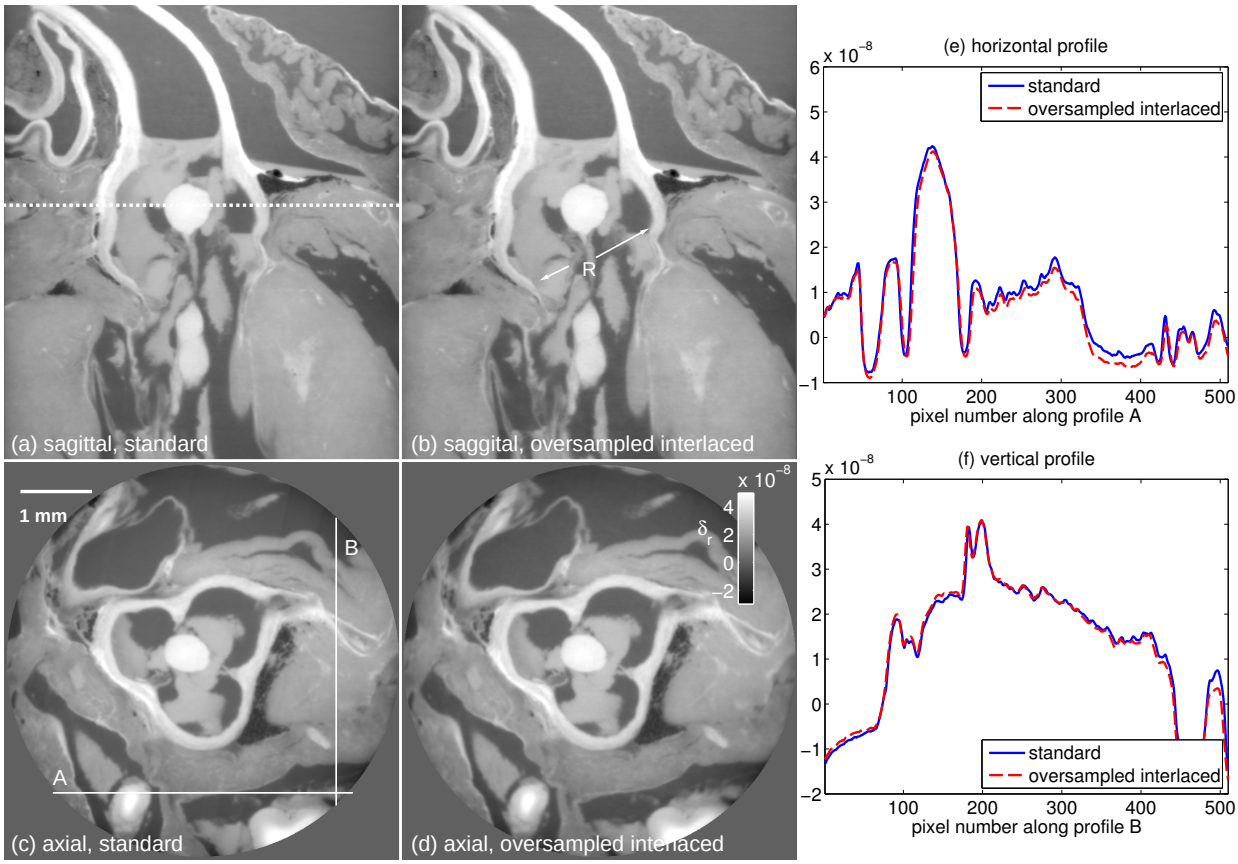

Figure 10.7: Sagittal (top) and axial (bottom) views of phase tomograms of a rat heart. Panels (a) and (c) show images obtained with the standard method and panels (b) and (d) show images obtained with the oversampled interlaced method. Profiles extracted from the standard and oversampled interlaced axial slices along the lines shown in panel (c) are displayed in panels (e) and (f). Despite the high difference in dose delivered in the two tomography scans (the oversampled interlaced scan was obtained by delivering to the sample only 20 % of the dose given to the sample during the standard phase stepping scan), the two reconstructions show very similar quality.

Sagittal views of the phase tomograms obtained with the standard and oversampled interlaced methods are displayed in Fig. 10.7 (a) and (b), respectively. In the sagittal slices the root of the aorta artery is indicated with the letter 'R'. Axial slices at the position indicated by the dashed line in Fig. 10.7 (a) are shown in panels (c) (standard) and (d) (oversampled interlaced). These slices highlight the anatomy of the aortic valve, and especially its tricuspid structure. Profiles have been extracted from the axial slices along the solid lines shown in Fig. 10.7 (c). These profiles are plotted in Fig. 10.7 (e) and (f). The results show that, despite the huge difference in dose delivered to the sample during the tomography scan, standard and oversampled interlaced methods provide phase reconstructions of very similar quality.

The second example is a global tomography of a rat eye. The organ was extracted with

the optic nerve and the extraocular muscles. In this case, the sample was smaller than the field of view of the detector, which had an effective pixel size of 5 μm and a width of 2048 pixels. The volumes were reconstructed from 750 refraction angle projections. The phase stepping scans were performed in 4 steps and the exposure time per raw image was 1 s. The dose delivered to the sample during the tomography acquired with the OI method was four times less than the dose delivered to the sample with the standard acquisition scheme. Figure 10.8 shows the phase reconstructions obtained with the two acquisition schemes. The lens is indicated with the letter 'L' and is the feature with the highest density. The presence of a gradient in the refractive index of the lens (the density decreases far from the center of the lens as shown in the profile plots displayed in panels (c) and (e)), is a known property of the eye lens which has an influence on both the refractive power and the aberrations of the lens [Smith 2003]. The optic nerve and the extraocular muscles (labeled with the letters 'N' and 'M' respectively) can be clearly distinguished in the tomograms. The retina ('R') was probably damaged during the extraction.

As observed in the previous example, the reconstructions obtained with the two acquisition schemes show very similar quality despite the great difference in deposited dose and number of raw images taken. This is also confirmed by the histogram analysis displayed in Fig. 10.8 (d) and (f) where no significant difference can be seen in the grey level distribution provided by the two acquisition methods.

10.3.6 Dark-field tomography of a fossil

So far the potentials of grating interferometry have been mainly exploited for imaging of biological soft tissue samples. Another class of samples which can benefit from the high sensitivity of the phase and dark-field signals obtained with the grating interferometer is the class of paleontological specimens. The tremendous potential of X-ray phase-contrast imaging is already widely used to visualize inner structures in fossils, mostly in the form of propagation-based phase contrast [Tafforeau *et al.* 2006, Lak *et al.* 2008]. However, there are still features which can not be revealed in phase contrast. Some of these can be made visible with the dark-field signal from the grating interferometer. This is demonstrated here with dark-field tomograms of a fossilized insect in opaque amber. The specimen, a Cretaceous maimetshid wasp from opaque amber of the Charentes region (France), was measured in local tomography. This specimen was recently described as a female of Guyotemaimetsha enigmatica, using propagation-based phase contrast microtomography [Perrichot *et al.* 2011]. In the previous examples we compared standard and oversampled interlaced tomography for the same number of projection angles and a different dose delivered to the sample. Here, tomographic scans performed with the two phase stepping methods are compared for the same dose delivered to the sample. A total of 1500 raw images were collected in each tomographic scan with phase stepping scans performed in 4 steps. From the 1500 raw images, 1500/4=375 projections were retrieved with the standard method and 1500 projections were retrieved with the oversampled interlaced method. The two panels on the left of Fig. 10.9 show tomographic sagittal slices of the fossil in "absorption" mode. Due to the low density of amber, the high degree of transverse coherence of the X-ray beam and the long distance of approximately 500 mm between the sample and the detector, these images are actually

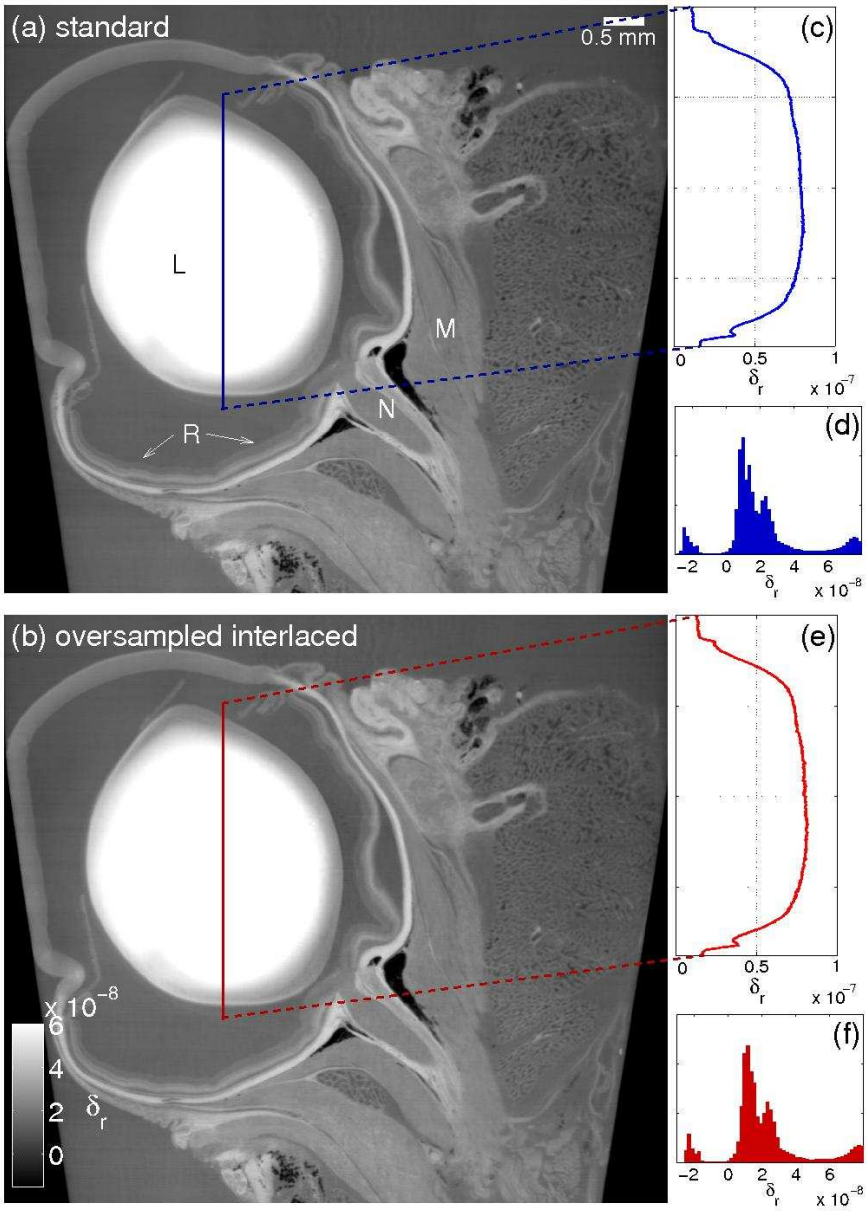

Figure 10.8: Sagittal views of phase tomogramphies of a rat eye obtained with the standard (a) and oversampled interlaced (b) acquisition schemes and the same number of refraction angle projections. The dose delivered to the sample during the tomography performed with standard stepping was 4 times larger than the dose given to the sample during the oversampled interlaced scan. Some of the anatomical features visible in the images are labeled with capital letters, see main text. The profile plots (panels (c) and (e)) show the refractive index gradient present in the lens. The histograms of the whole sagittal slices are shown in panels (d) and (f). The $y-$axis of the histograms is the frequency of appearance of the grey levels in the slices.

dominated by propagation-based phase contrast. The panels on the right of the figure show tomographic slices at the same position and from the same data set, but in dark-field con-

trast. [3] The insect is clearly visible in both imaging modalities. However, the signal in the dark-field images is higher (brighter pixels) at boundaries and interfaces, where there are strong inhomogeneities. Despite the presence of edge enhancement, the wing of the insect is not fully revealed in the absorption/phase-contrast data. On the other hand, with the dark-field signal, which allows to reveal the presence of details smaller than the spatial resolution of the detector [Yashiro *et al.* 2011], the wing of the insect can be clearly revealed in all its length, see arrows in Fig. 10.9 (d). Phase tomograms of the fossil, calculated from the same dataset, are shown in the supplementary material.

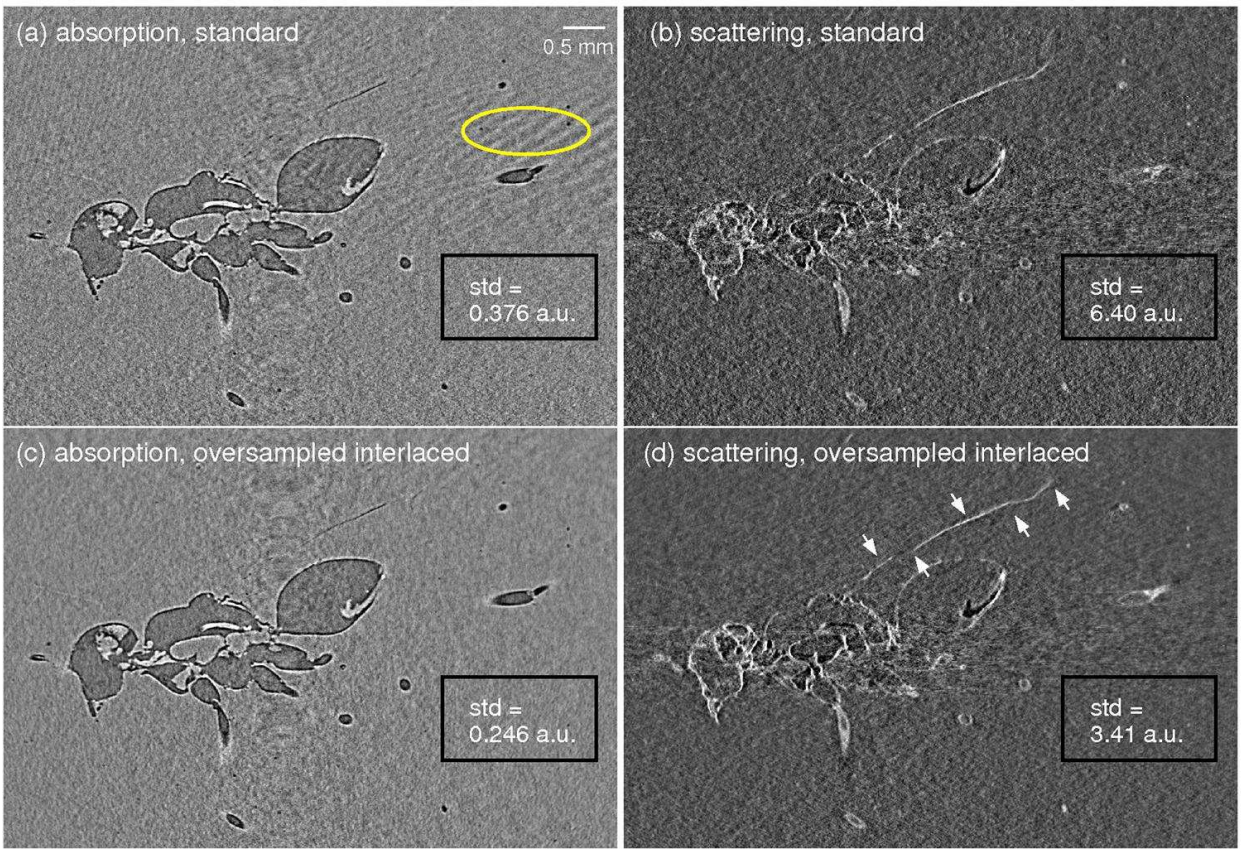

Figure 10.9: Grating interferometry tomograms in absorption and propagation-based phase contrast (left) and dark-field contrast (right) of an insect in opaque amber. Dark-field contrast images show details which are not be fully revealed in the absorption/phase-contrast data, such as the wing of the insect, indicated by arrows in panel (d). The tomograms in the two panels at the top were obtained with the standard phase-stepping method, those in the bottom panels with the oversampled interlaced method, by applying two different reconstruction schemes to the same dataset, one based on the classical system, and the second mimicking the new acquisition scheme presented in this paper. For both absorption and dark-field signals, the image noise is significantly reduced using the oversampled interlaced method as shown by the standard deviation (std) of the grey levels in the uniform region at the bottom right of the images.

The advantages of the oversampled interlaced method over the standard acquisition

[3] The dark-field tomography data were reconstructed using the filtered back projection algorithm and the same ramp filter as in conventional absorption tomography [Bech *et al.* 2010].

scheme are evident in Fig. 10.9. The images at the top, obtained with the standard acquisition scheme, show artifacts from angular undersampling (for example, see region at the right of the absorption image of panel (a) marked by an oval) which are not present in the images obtained with the oversampled interlaced method. The image noise has been evaluated in a uniform region of 370×200 pixels at the bottom right of the images. This region is marked by a solid rectangle in the images of Fig. 10.9. At the center of this rectangle are reported the standard deviation of the grey levels in the regions. As already shown with the simulations, for the same dose delivered to the sample, the oversampled interlaced method significantly reduces the image noise in the tomographic reconstructions. This noise reduction provided by the oversampled interlaced method allows the visualization of features which cannot be detected in the images obtained with the standard method such as details of the head of the insect in the dark-field images.

These results, besides confirming the advantages of the oversampled interlaced method over the standard acquisition scheme in dark-field contrast tomography, also demonstrate the potentials of X-ray interferometry in imaging of fossils.

10.3.7 Conclusions

By increasing the effective angular sampling density, the oversampled phase stepping methods presented in this paper give a substantially improved contrast-to-noise ratio in grating-based tomography over the standard phase-stepping approach commonly used today. The results demonstrate this improvement both for differential phase contrast and for scatter-contrast ("dark-field") tomography.

Moreover, because of the efficient acquisition and processing scheme represented by the oversampled methods, phase and dark-field contrast tomographies of the investigated sample can now be obtained by effectively recording only one raw interferogram per final projection image using the oversampled interlaced OI method.

In addition to demonstrating the improvement in image quality that oversampled phase stepping brings to dark-field tomography, the study on the fossilized insect highlights the potential of grating interferometry for applications in paleontology. The high scatter contrast from the wing of the insect also suggests the exploitation of the dark-field signal in the investigation of sharply-localized features in other application areas, e.g., cracks in biological or man-made materials.

We would like to point out that, while the results shown in this paper have been obtained with synchrotron radiation, oversampled phase stepping can be implemented at any phase-stepping interferometer, including at laboratory X-ray systems or neutron sources.

Oversampled phase stepping is easy to implement, implies no additional requirements on the alignment of the gratings, is compatible with continuous tomography scans, performs well in local tomography and allows to access, with a simple algorithm, three image modalities. These advantages, together with the dose reduction, make it a substantial improvement for low-dose, fast phase-contrast and scatter tomography based on grating interferometry.

10.3.8 Supplementary information

The slice shown in Fig. 10.10 (a) has been used to compare local phase reconstructions provided by the different phase stepping methods. As explained in the main text, slice of Fig. 10.10 (a) is a modified version of the Shepp-Logan phantom with real refractive index $n = 1 - \delta$. The δ values in the phantom are similar to the δ values of the soft tissues measured, with hard X rays, in the experiments reported in the main text.

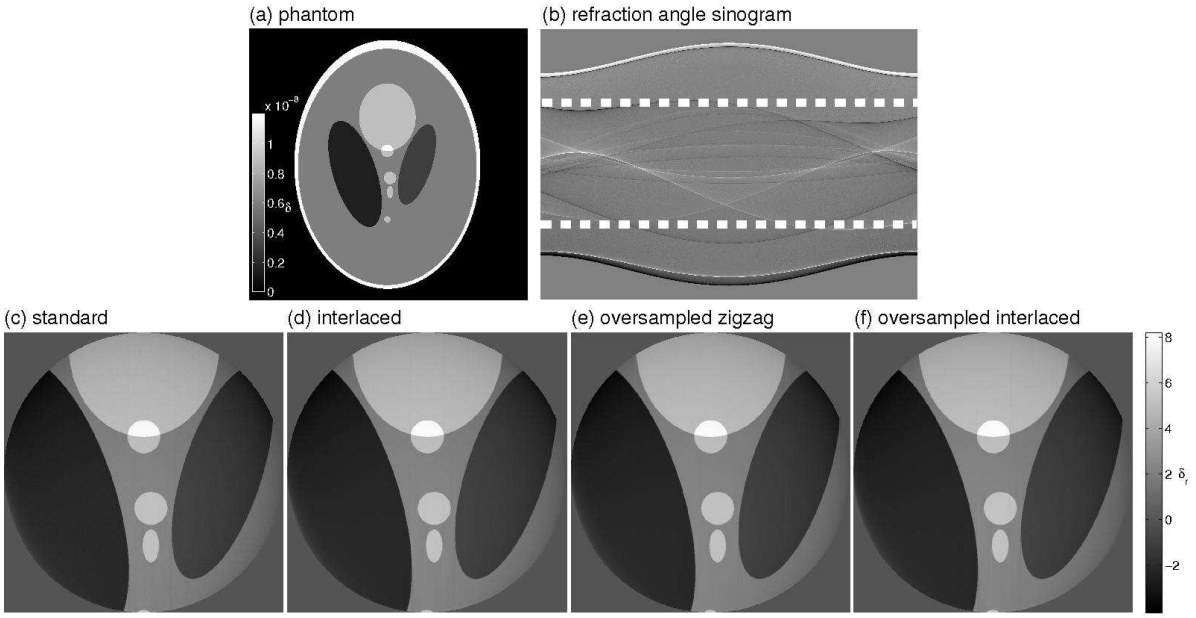

Figure 10.10: (a) Phantom on which the simulations are based. (b) Refraction angle sinogram produced from the phantom by simulating the oversampled interlaced phase stepping method. Dashed lines indicate the region were the sinogram has been truncated. (c) - (f) Regions of interest reconstructed by simulating the different phase stepping methods.

A total of 1700 raw interferograms per phase stepping method have been generated from the phantom exploiting the fact that the quantity directly measured with the phase stepping technique, the refraction angle, is proportional to the differential phase of the wavefront at the object plane. Moreover, the phase shift X rays undergo while passing through the sample is proportional to the line integral along the beam path of the real part of its refractive index [Weitkamp *et al.* 2005a, Pfeiffer *et al.* 2007b].

In each pixel, the intensity oscillation recorded during a phase stepping scan can be written as a sinusoidal function of the grating position x_g and depends also on the sample orientation ω:

$$I(x_g, \omega) = \sin\left[\frac{2\pi}{p_2}\left(x_g + d\int \frac{\partial\delta(x', z')}{\partial x} dz\right)\right] \quad , \tag{10.1}$$

where p_2 is the period of the absorption grating, d is the inter-grating distance and (x', z') is a coordinate system rotated by ω with respect to the coordinate system (x, z), see Fig. 10.4 of main text. In Eq. (10.1), the average of the intensity oscillation has been set to zero and

its amplitude has been set to one since absorption and scattering effects, which are related, respectively to these quantities, are neglected in the simulation.

Using the relation of Eq. (10.1), raw interferograms have been generated, from the starting slice, for different pairs x_g and ω in order to simulate the different phase stepping methods according to the scheme presented in Fig. 10.5 of the main text. For example, a standard phase stepping scan is formed by values $I(x_g, \omega)$ where ω is fixed and x_g assumes values in the interval $[0, p_2[$. In this study, phase stepping scan were simulated over four steps. The four evenly spaced grating positions during a phase stepping scan can be written as $x_g = 0, p_2/4, p_2/2, 3p_2/4$.

Phase stepping scans generated as outlined above, have been processed with the Fourier analysis (as it is commonly done with real data [Pfeiffer *et al.* 2008a]) and refraction angle projections have been retrieved. The number of refraction angle projections obtained in this way was different for the different phase stepping methods. In particular 1700/4=425 refraction angle projections were obtained with the standard and interlaced methods, 1700/3=566 refraction angle projections were retrieved by simulating oversampled zigzag phase stepping and 1700 projections were obtained with the oversampled interlaced method.

The refraction angle sinogram obtained with the oversampled interlaced method is shown in Fig. 10.10 (b), the dashed lines in the sinogram indicate the positions at which the sinograms were truncated. Sinograms like the one shown in Fig. 10.10 (b) (with less projections) have been generated for the standard, interlaced and oversampled zigzag acquisition schemes. Phase reconstructions of the region of interest of 800 pixels width have been obtained from these sinograms with the filtered back-projection algorithm and an imaginary sign filter [Pfeiffer *et al.* 2007b].

The phase reconstructions are shown in Fig. 10.10 (c)-(f) and the results on the histogram analysis is presented in Fig. 10.6 of the main text. Note that the starting slice was noise free, thus, all noise present in the reconstructed tomograms is generated in the reconstruction process.

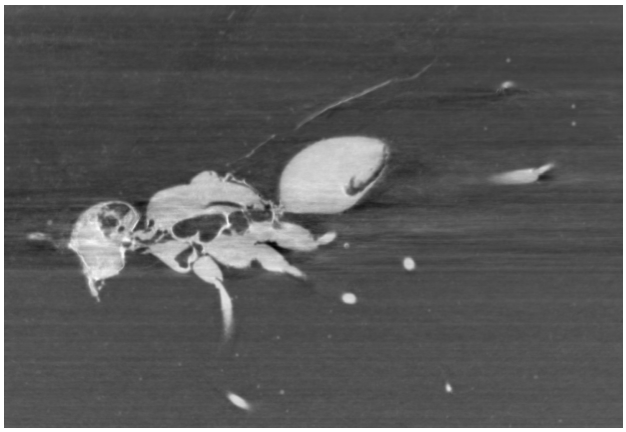

Figure 10.11: Phase tomography of the insect in amber obtained with the oversampled interlaced method. The general contrast in the phase tomography is much higher than the contrast in absorption tomography (Fig. 10.9 (a) of the main paper, allowing easier segmentation process of the data. This makes grating interferometry a promising technique for revealing features in fossils which can not visualized in absorption contrast.

Chapter 11

Two-dimensional grating interferometry

Contents

11.1 Introductory remarks

The standard one-dimensional (1D) grating interferometer yields the component of the differential phase and dark-field signals orthogonal to the grating lines. Applied to the scatter signal, this property is at the basis of a new imaging technique called "directional dark-field imaging", see Ref. [Jensen *et al.* 2010a, Jensen *et al.* 2010b] and Sec. 6.2.2. However, the existence of a blind direction is in most of the cases a limitation, especially when the sample cannot be rotated around the optical axis [Kottler *et al.* 2007].

An example which shows the dependency of image contrast on the orientation of the features in the sample is displayed in Fig. 11.1. The object shown in this figure is a wafer box, used for the storage of silicon wafers such as those used as substrates for gratings. These images were recorded by the author of this thesis at the laboratory setup at PSI. The lines of the gratings in this experiment were oriented in the vertical direction. The differential phase and dark-field contrast produced by the ribs of the wafer box strongly depends on their orientation: the horizontal ribs are almost invisible in the differential phase and dark-field images. These ribs are clearly visible only in the attenuation radiograph, whose signal is isotropic. Horizontal structures with insufficient absorption contrast will remain undetected in this setup.

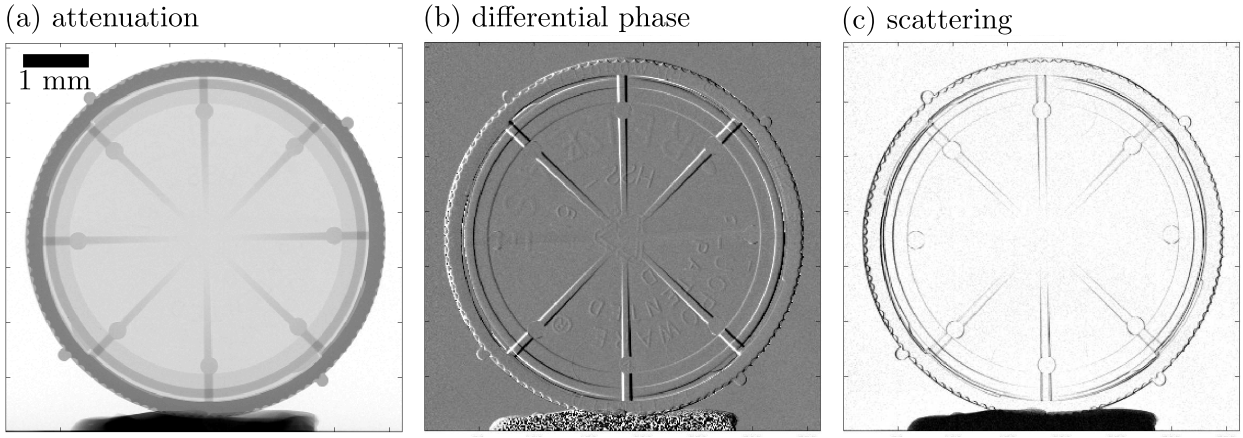

Figure 11.1: Wafer box on a wax support measured with the standard 1D grating interferometer installed at the laboratory source at PSI. This interferometer is described in Sec. 6.1.1. The mean X-ray energy was 28 keV, the periods of the gratings were: $p_0 = 14$ μm, $p_1 = 3.5$ μm and $p_2 = 2.0$ μm. The G0-to-G1 distance was L = 1.383 m and the G1-to-G2 distance, corresponding to the fifth fractional Talbot order was d = 198 mm. The grating lines were vertically orientated.

To overcome the limitations imposed by the existence of the blind direction, a two-dimensional (2D) grating interferometer has been conceived, designed, implemented and characterized during this PhD project. With this instrument, through the use of 2D gratings instead of line gratings, it is possible to measure differential phase and scattering signals simultaneously along different directions, without the need to move the sample. This advanced version of the grating interferometer is described in this chapter.

The next section (Sec. 11.2) is a reprint of a journal article that reports on the first implementation of the 2D grating interferometer [Zanette *et al.* 2010b].

The following sections report results, so far largely unpublished, on the practical implementation (Sec. 11.3) and application of the 2D interferometer for optics characterization (Sec. 11.4) and wavefront sensing (Sec. 11.5).

11.2 Paper IV

This section is a reprint of the paper published as: I. Zanette, T. Weitkamp, T. Donath, S. Rutishauser and C. David. *Two-dimensional grating interferometer.* Physical Review Letters **105**, 248102 (2010).

11.2.1 Abstract

We report on the design and experimental realization of a two-dimensional (2D) X-ray grating interferometer. We describe how this 2D grating interferometer has been practically implemented, discuss its performance and present multi-directional scattering (dark-field) maps and quantitative phase images that have been retrieved using this device.

11.2.2 Introduction

X-ray grating interferometry is a method for hard X-ray wavefront sensing and phase-contrast imaging that has been developed over the past few years [David *et al.* 2002, Momose *et al.* 2003, Weitkamp *et al.* 2005b, Weitkamp *et al.* 2005a, Pfeiffer *et al.* 2008a]. It is highly sensitive to subtle deviations of the local wavefront propagation direction (differential phase contrast) and to scatter in the sample (dark-field contrast), can be used with large fields of view and does not need a high degree of X-ray monochromaticity [Weitkamp *et al.* 2005a]. A grating interferometer implemented on a synchrotron source typically consists of two line gratings, used in an in-line transmission geometry and placed one behind the other. The first grating, termed the "beam splitter", acts as a diffractive element. The second one is used as an absorption mask [Momose *et al.* 2003, Weitkamp *et al.* 2005b] and is often referred to as the "analyzer" grating.

An interferometer of this kind, using specifically developed line gratings [David *et al.* 2007, Reznikova *et al.* 2008], gives contrast for wavefront deviations or scattering in the direction perpendicular to the grating lines. However, structures in the sample that are oriented perpendicular to the lines are not visible. In addition, retrieval of the wavefront phase not only requires exact knowledge of the boundary values, but also induces substantial artifacts due to the lack of information on the "blind" direction.

To overcome these limitations, grating-based imaging systems that use two-dimensional (2D) structures, rather than line gratings, have already been proposed. Some of them are single-grating setups, i.e., without an analyzer grating [Baker 2009, Wen *et al.* 2010]. The grating used in these systems has a period large enough so that the intensity modulations it induces can be directly resolved by the detector.

Other proposed systems [Momose & Kawamoto 2006, Olivo *et al.* 2009] do have an analyzer element in front of the detector or incorporated with the detector itself. However, no experimental scattering images or integrated phase maps are reported in [Momose & Kawamoto 2006, Olivo *et al.* 2009].

In this Letter, we present the design and realization of a device, measurement strategy, and data analysis algorithm that yield high-quality reconstructed phase images and multi-directional dark-field images using a 2D interferometer that includes an analyzer grating.

11.2.3 Design and setup

The device presented here is conceptually similar to the one-dimensional (1D) interferometer we have reported in the past [Weitkamp *et al.* 2005b] except that the gratings are structured in both transverse dimensions. Thus, the beam splitter is a 2D diffraction grating (G1); its active areas are preferably pure phase structures. The diffraction pattern created by G1 is an array of intensity spots. A second absorbing grating G2, the analyzer, encodes the spot positions into intensity values on the detector (Fig. 11.2). The difference to a standard 1D grating interferometer is that diffraction on G1 occurs not only along x *or* y, but in both dimensions, and G2 allows analysis of the signals in both dimensions.

In the 1D case (i.e., the case of line gratings), the variable parameters for a binary grating are only the material, structure thickness t, lateral period p, and duty cycle $\gamma = w/p$ (where

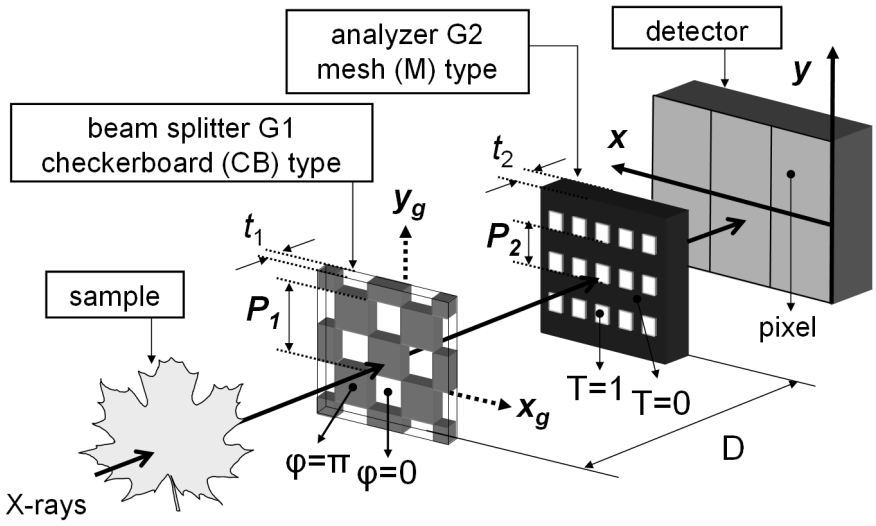

Figure 11.2: Schematic representation of a 2D X-ray grating interferometer setup. The gratings G1 and G2 are placed in series in the X-ray path, separated by a distance D. $\varphi(x, y)$ denotes the phase-shift profile of G1, $T(x, y)$ the intensity transmission of G2.

w is the line width). Usually a duty cycle of $\gamma = 0.5$ is preferred for the beam-splitter grating, to eliminate its non-zero even diffraction orders.

The design of a 2D grating, however, allows a variety of different unit cells. In this paper we consider only the case of cells with fourfold symmetry, equal periods $p_x = p_y = P$ and duty cycles $\gamma_x = \gamma_y = 0.5$. Two of the simplest unit cells are what we shall henceforward refer to as "checkerboard" (CB) and "mesh" (M) type patterns; they are shown in Fig. 11.2. The intensity distribution produced by G1, and the distances at which maximum contrast is observed, will depend on the pattern chosen and on the phase shift induced by the structures. A detailed study [Zanette *et al.* 2010a] shows that a CB-type, π-shifting grating produces a distribution of square intensity spots forming an M-type pattern with half the period of G1. This phenomenon is observed at distances :

$$D_n = \frac{nP_1^2}{8\lambda} \quad , \tag{11.1}$$

with P_1 the period of G1, $n = 1, 3, 5, \ldots$, and λ the wavelength of the radiation. These distances may be different for other designs of a 2D diffraction grating [Zanette *et al.* 2010a].

The analyzer grating G2 has opaque structures [Weitkamp *et al.* 2005a, Zanette *et al.* 2010a]. In our device, it is an M-type grating with period $P_2 = P_1/2$. As in the 1D case, G2 has the same pattern as the (unperturbed) intensity distribution impinging on it.

The gratings forming the 2D grating interferometer can be implemented by using genuine 2D structures. However, for particular G1 and G2 patterns, it is also possible to combine two 1D gratings to create the equivalent of a 2D grating structure. A CB-type, π-shifting grating can be obtained as a superposition of two crossed linear π-shifting gratings; similarly, 2D mesh-type analyzer gratings can be obtained by the combination of two perpendicular linear absorption gratings [Zanette *et al.* 2010a].

The phase-stepping technique [Weitkamp *et al.* 2005a] can be used to separate absorp-

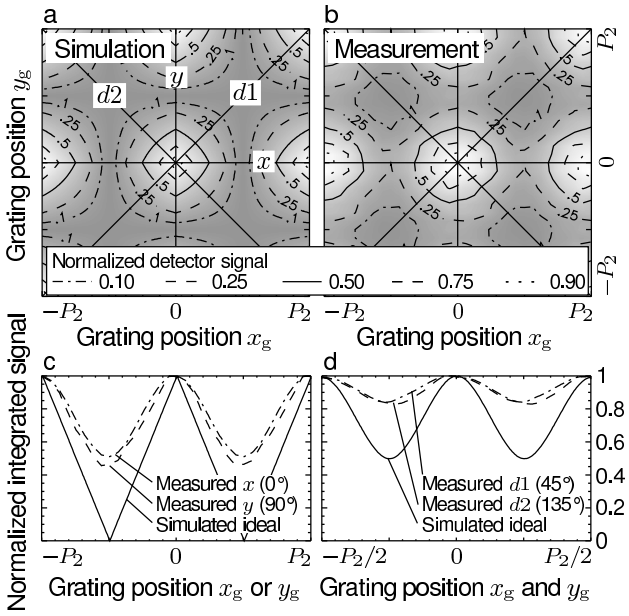

Figure 11.3: Theoretical and experimental results of a 2D raster phase-stepping scan performed over one grating period. The two-period representation used in this figure has been chosen for clarity. It is obtained by tiling the data. Panels a) and b) show the detector signal in a single pixel as a function of the grating coordinates x_g and y_g. Panel a) displays the calculated detector signal for ideal conditions (perfect gratings, fully coherent flat beam). Panel b) shows the experimentally measured signal. The signal integrated along the x and y coordinates is shown in c); the contrast curves along the diagonals $d1$ and $d2$ are shown in d).

tion, phase, and scattering information. In the 2D case, a raster scan of one of the two gratings is performed along the transverse coordinates, x_g and y_g. In order to be able to retrieve the three image signals, the phase-stepping scan should be performed over at least one absorption grating period with a number of steps per period greater than two. The phase-stepping scan produces, in each detector pixel, a 2D intensity distribution which is the convolution of the interference pattern incident on this pixel with the transmission function of the analyzer grating. The simulated 2D convolution in the ideal case of fully coherent flat beam and perfect structures is shown in Fig. 11.3 (a). The experimentally observed convolution resembles a 2D sinusoidal function (Fig. 11.3 (b)).

For data analysis, it is useful to project the 2D signal recorded during a phase-stepping scan along four axes: the x and y coordinates and the diagonals $d1$ and $d2$ that form, respectively, 45° and 135° with the x axis. The resulting contrast curves are shown in Fig. 11.3 (c) and (d); the amplitude of each curve is related to the visibility of the intensity pattern along the respective direction. The visibility V, defined as $V = (I_{max} - I_{min})/(I_{max} + I_{min})$, where I_{max} and I_{min} are the maximum and minimum intensity values observed in the contrast curve, can be considered a figure of merit of the performances of the grating interferometer [Weitkamp *et al.* 2005a]. In an ideal 2D grating interferometer of the type presented here, the visibility along the main axes is 100%, along the diagonals it is 36%; see solid lines in Fig. 11.3 (c) and (d). The limited spatial coherence of the X-ray beam, grating imperfections and limited absorption from G2 structures reduce the visibility to measured values of 37%

along x and y and 10% along the diagonals. The measured visibility value of 37% along the main axes is comparable to the amplitude of the contrast curves obtained in the past with 1D grating interferometers [Weitkamp *et al.* 2005a, Pfeiffer *et al.* 2008a]. The visibility value of 10% measured along the diagonals results in noisier images than along the main axes; however, as we will show in the following, scattering images along these directions give helpful information on the scattering orientation of the sample features.

The 2D intensity pattern in each pixel (X, Y) can be expanded in a 2D Fourier series and, if the phase-stepping scan is performed over one period in each direction, it can be written as

$$I(X, Y, x_\mathrm{g}, y_\mathrm{g}) = I(x_\mathrm{g}, y_\mathrm{g}) \simeq \sum_{k=-1}^{1} \sum_{l=-1}^{1} a_{k,l} \exp\left[\mathrm{i}\left(k\frac{2\pi}{P_2}x_\mathrm{g} + l\frac{2\pi}{P_2}y_\mathrm{g} + \phi_{k,l}\right)\right], \tag{11.2}$$

with the Fourier coefficients $a_{k,l}$ and their corresponding phases $\phi_{k,l}$ (note the analogy of Eq. (11.2) and the following treatment with the ones used for the 1D interferometer [Pfeiffer *et al.* 2008a]). From the Fourier analysis of the signal $I(x_\mathrm{g}, y_\mathrm{g})$ in each pixel, the differential phase images, the scattering properties of the object and the conventional absorption map can be simultaneously retrieved.

The differential phase shift along one transverse direction is related to the refraction angle in that direction by $\partial\Phi/\partial x = 2\pi\alpha_x/\lambda$ (analogous for y) [Weitkamp *et al.* 2005a]. The values of α_x and α_y can be calculated from the experimental data by

$$\alpha_x = \frac{1}{2\pi S}\left(\phi_{0,1}^\mathrm{sam} - \phi_{0,1}^\mathrm{ref}\right),\ \alpha_y = \frac{1}{2\pi S}\left(\phi_{1,0}^\mathrm{sam} - \phi_{1,0}^\mathrm{ref}\right). \tag{11.3}$$

In the formulas above, D is the distance between the two gratings and $S = D/P_2 = 2D/P_1$ is the sensitivity of the interferometer [Donath *et al.* 2009]. The superscripts of Eq. (11.3) indicate values measured when the sample is in the beam path ("sam") and for reference phase-stepping scans ("ref").

Besides the two components x and y of the differential phase shift, a measure of the scattering power of the sample is obtained by calculating the reduction in amplitude of the interference pattern caused by the sample. The scattering maps are usually called dark-field images [Pfeiffer *et al.* 2008a]; we will indicate them with the letter v. With the 2D grating interferometer the scattering signal along four directions can be retrieved [1]:

$$\begin{aligned} v_x &= A^{-1}a_{0,1}^\mathrm{sam}/a_{0,1}^\mathrm{ref} & v_y &= A^{-1}a_{1,0}^\mathrm{sam}/a_{1,0}^\mathrm{ref} \\ v_{d1} &= A^{-1}a_{-1,1}^\mathrm{sam}/a_{-1,1}^\mathrm{ref} & v_{d2} &= A^{-1}a_{1,1}^\mathrm{sam}/a_{1,1}^\mathrm{ref}\,. \end{aligned} \tag{11.4}$$

The term A^{-1} in the above equations corrects for the absorption of the sample: $A = a_{0,0}^\mathrm{sam}/a_{0,0}^\mathrm{ref}$ is the conventional absorption signal.

The experimental data presented here were taken with a setup mounted at the beamline ID19 [Weitkamp *et al.* 2010a] of the European Synchrotron Radiation Facility. The first grating was placed at approximately 150 m from the wiggler source. An X-ray energy

[1] Following the same principle, phase gradient images along the $d1$ and $d2$ directions can also been calculated. They are not presented here because the x and y components of the phase gradient are sufficient to retrieve the phase map.

of 23 keV was selected by a Si-111 double crystal Bragg monochromator. The detector was a lens-coupled CCD system with a magnification of 1.87 and an effective pixel size of 7.5×7.5 μm^2, using a FReLoN CCD with 2048 × 2048 pixels [Labiche *et al.* 2007] and a powder scintillator.

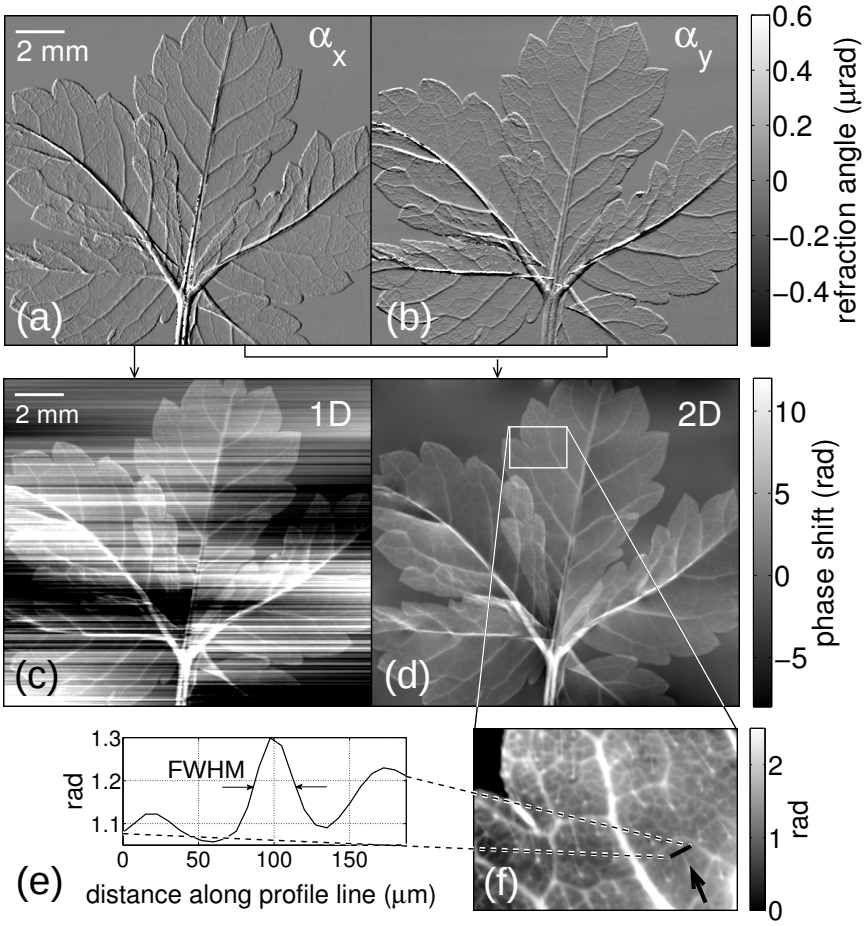

Figure 11.4: Horizontal (a) and vertical (b) components of the refraction angle signal of a leaf recorded with a 2D grating interferometer. Note the superior quality of the 2D phase map retrieved with the 2D interferometer ((d) and detail (f)) over the one that would have been obtained with a 1D interferometer giving signal only along x (c). The section profile across a linear feature in the phase map (plot in (e), profile position indicated by an arrow in (f)) has a full width at half maximum of 3.9 pixels (29.25 μm).

We constructed the interferometer by using two orthogonal linear phase gratings and two orthogonal linear absorption gratings. The phase gratings G1 with a period of P_1 = 4.785 μm and a Si structure thickness of 29 μm were made at the Paul Scherrer Institut [David *et al.* 2007]. The two analyzer gratings G2 with a period of P_2 = 2.4 μm and a Au structure thickness of 50 μm were fabricated at the Karlsruhe Institute of Technology [Reznikova *et al.* 2008]. The grating periods were matched in order to compensate for beam divergence at the 9$^{\text{th}}$ fractional Talbot order with a distance of 479 mm between the G1 and G2 gratings. The sample was placed immediately upstream of the phase grating pair; the detector was positioned as close as possible to the absorption grating pair.

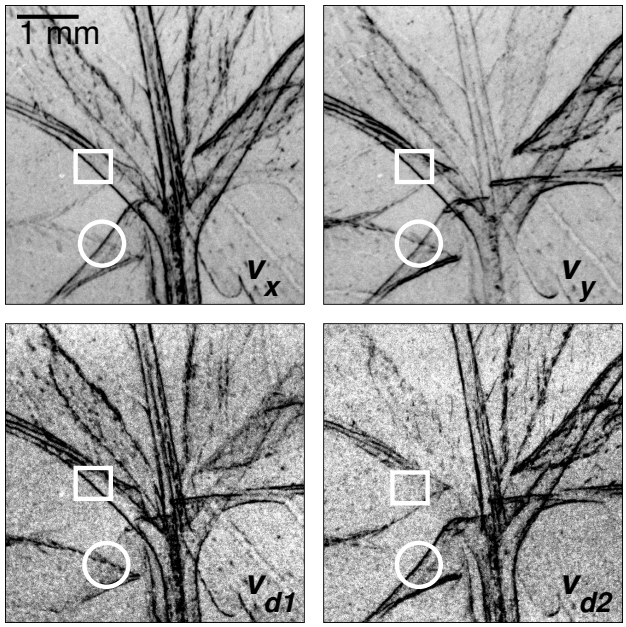

Figure 11.5: Scattering (dark-field) images of the central part of the leaf along the four directions (x, y, $d1$ and $d2$) as indicated in the bottom right of each image. Strong scattering details in the object are represented by dark regions in the images. Images v_x and v_y have a better signal-to-noise ratio than v_{d1} and v_{d2} because the visibility is higher along the main axes than along the diagonals (Fig. 11.3). Details highlighted with circles and squares are examples of features for which the diagonal information helps to determine with more accuracy their preferential scattering direction.

Raster phase-stepping scans were performed over one period and in 4 steps in each direction (16 frames in total) and an exposure time of 1 s per frame.

The two components α_x and α_y of the refraction angle for a leaf are shown in Fig. 11.4 (a) and (b). The phase wrapping phenomenon shows up as a noise-like artifact in areas with a strong X-ray phase gradient; this effect is visible in the petiole and in the veins of the leaf. Together with unknown boundary values, and/or low-frequency errors due to statistical propagation of errors induced by noise, this phenomenon causes the phase map obtained with a 1D interferometer to contain strong stripe artifacts (Fig. 11.4 c). These artifacts are so strong that the phase projection maps are usually unusable as end results and therefore not shown in many publications on 1D interferometers. A substantial advantage of the 2D grating interferometer is the possibility of retrieving quantitative phase maps without these artifacts (Fig. 11.4 (d) and (f)). To obtain the phase map shown in Fig. 11.4 (c) we adopted the Frankot−Chellappa method [Frankot & Chellappa 1988], a widely used method in optical microscopy. From this map, a lower limit of the spatial resolution in the phase image has been estimated by analyzing a section profile of the image (Fig. 11.4 (e)) across a hair on the leaf surface (the smallest structure discernible in the phase image indicated by an arrow in Fig. 11.4 (f)). The full width at half maximum (FWHM) of the curve generated by the hair has been taken as a measure of the spatial resolution: the FWHM is 29.25 μm.

Fig. 11.5 shows the central region of interest of the dark-field images of the leaf. The information in the diagonal directions helps to determine with more accuracy the preferential

scattering direction of the sample features (e.g. details indicated by rectangles and circles in Fig. 11.5). Since the dark-field images obtained with the grating interferometer are sensitive to scattering features smaller than the detector pixel size, the multi-directional scattering images from a 2D X-ray grating interferometer can be used to determine the orientation of structures in the sample with characteristic sizes well beyond the spatial resolution of the device.

11.2.4 Conclusions

With the 2D interferometer presented here, it is possible to retrieve the phase and amplitude profiles of X-ray wavefronts and the scattering in the sample. The results presented show the substantial advantages of the 2D interferometer over a 1D design: higher quality of the retrieved phase images, and directional scattering information in the dark-field signal.

Considerations concerning performance aspects of 1D grating interferometers (e. g., [Weitkamp *et al.* 2005a]), such as chromaticity, effects of imperfect spatial and temporal coherence, and spatial resolution, can also be applied to the 2D grating interferometer presented here.

Compared to other recently-proposed schemes of 2D grating-based imaging [Baker 2009, Wen *et al.* 2010], the effort of using a second grating is rewarded by higher sensitivity and spatial resolution. This is because, when an analyzer G2 is used, the intensity modulation created by G1 need not be resolved by the detector and therefore gratings G1 with period P_1 much smaller than the detector resolution can be used. Moreover, if the instrument is used in phase-stepping mode, the full spatial resolution of the imaging system is retained in the final images. This is not what happens in the single-grating setups where the spatial resolution is limited by the period of the intensity pattern produced by the grating on the observation plane [Wen *et al.* 2010].

While we have demonstrated operation of the instrument in phase-stepping mode, it is also possible to use this device for moiré interferometry. In this mode, the phase profile can be retrieved from a single shot [Weitkamp *et al.* 2005b], albeit at inferior spatial resolution than in phase-stepping. This mode may be interesting for various wavefront-sensing applications, particularly in the photon diagnostics for future X-ray free electron lasers.

11.3 Implementation

The 2D grating interferometer implemented at ID19 is based on the same system of rods, holding plates and motors that is used for the 1D device (Sec. 7.3). The main differences between the 2D grating interferometer and the standard 1D device are:

(i) the 2D phase grating must be scanned along two orthogonal axes in a raster scan;

(ii) the alignment procedure consists in removing 2D moiré fringes which, as shown in Sec. 11.5, form an array of intensity spots rather than lines.

In the first implementations of the 2D grating interferometer, two crossed $\pi-$shifting line gratings and two crossed absorption line gratings were used. Each of the phase gratings was

mounted on a piezo of the type described in Sec. 7.3. The two piezo stages gave access to linear motion along the two transverse axes x and y. The absorption gratings were mounted on two identical rotation stages (the rotation system is described in Sec. 7.3) for independent alignment of each grating to the respective phase grating. The distances between the two phase gratings and the distance between the two absorption gratings were approximately 1 mm.

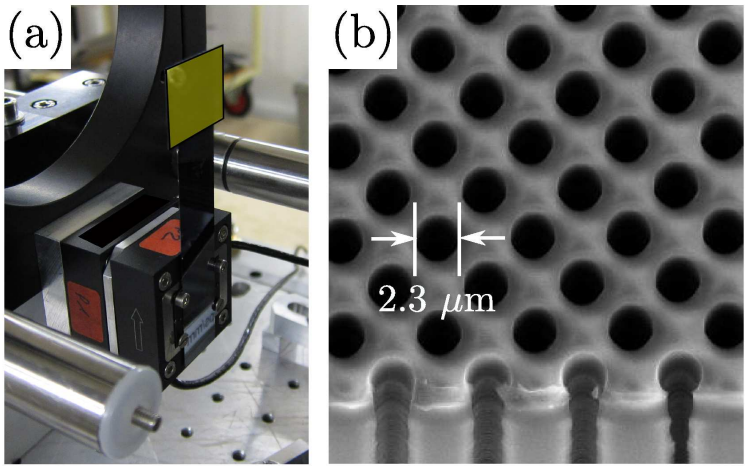

Figure 11.6: (a) Picture of the 2D phase grating (the active area has been coloured in yellow) fixed on two linear piezos mounted on top of each other. (b) Scanning electron microscope image of a 2D phase grating (courtesy S. Rutishauser, PSI).

After the first proof-of-principle implementation, genuine 2D phase gratings were fabricated at PSI and used instead of the two crossed line gratings. These 2D phase gratings were fabricated by deep reactive ion etching (DRIE), using a pulsed etching technique known as "Bosch process". The 2D phase grating was mounted on two piezos placed on top of each other as shown in Fig. 11.6 (a). Panel (b) of the same figure shows a scanning electron micrograph of the 2D phase grating. One immediately notices that void parts in the silicon have a circular shape rather than a square shape as shown in Fig. 11.2. The simulated interference pattern generated by a 2D phase grating with circular holes is shown in Fig. 11.7 (d). This interference pattern is compared to the one generated by the ideal ckeckerboard grating, see Fig. 11.7 (b). The interference pattern produced by the two types of gratings is similar and in both cases the period of the intensity spots is half of the period of the structures in the phase grating. However, while all the spots in Fig. 11.7 (b) have the same intensity, the spots in Fig. 11.7 (d) have different intensities. This, together with the fact that the intensity pattern is not binary and presents intensity modulations in the background as well as in the spots, affects the visibility measured with 2D gratings with circular holes.

The visibility values measured in the horizontal and vertical directions with the 2D phase grating shown in Fig. 11.6 were, respectively, 32% and 35%. In both directions, the visibility was thus slightly smaller than the value of 37% obtained under the same conditions with two crossed line phase gratings [Zanette *et al.* 2010b]. The visibility in the vertical direction is larger because the angular source size in this direction is smaller. Images of a glass-carbon

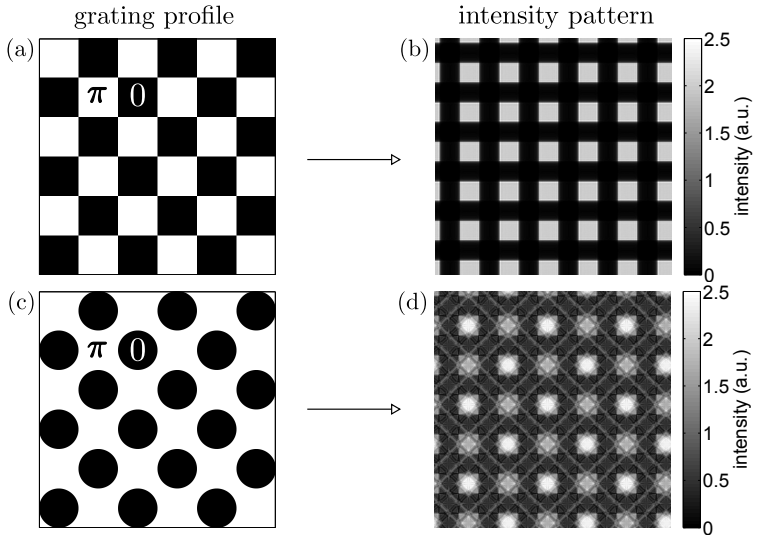

Figure 11.7: (a) Ideal checkerboard phase grating and (b) interference pattern produced at the fractional Talbot distance when it is illuminated by a plane monochromatic wavefront. (c) 2D phase grating used in the 2D grating grating interferometer at ID19 and (d) its interference pattern at the fractional Talbot distance. In the intensity patterns at the right, dark parts are region of less intensity.

mesh taken with a 2D phase grating of the type shown in Fig. 11.6 are shown in Fig. 11.8.

The implementation of the 2D device was further improved with the use of a *de facto* 2D absorption grating, made at KIT, in combination with the 2D phase grating described above. The 2D absorption grating was made by fabricating orthogonal line gratings on both sides of the same wafer. In order for the alignment procedure to yield good results, and particularly to avoid residual moiré fringes, the main axes of the grid structures on both 2D gratings need to be perfectly orthogonal. An image of an ant obtained with the 2D interferometer using two 2D gratings is shown in Fig. 11.9. It is a false color combination of the dark-field signals in two orthogonal directions.

11.4 Application to refractive lens characterization

Since the 2D grating interferometer yields, with high angular sensitivity, the full phase gradient vector downstream of the sample and thus, via suitable reconstruction methods, the phase of the incoming wavefront, this device is particularly interesting for optics characterization and wavefront measurements.

During this PhD project, the potential of the 2D grating interferometer has been exploited for characterizing parabolic refractive X-ray lenses. Stacks of this type of lenses are used at several synchrotron beamlines for microfocusing, collimation and as broad-band monochromators. These lenses are widely described in the literature, see for example References [Lengeler *et al.* 1999, Lengeler *et al.* 2002, Vaughan *et al.* 2011], and have already been inspected with the standard 1D interferometer and polychromatic radiation produced by a microfocus X-ray tube [Engelhardt *et al.* 2007b].

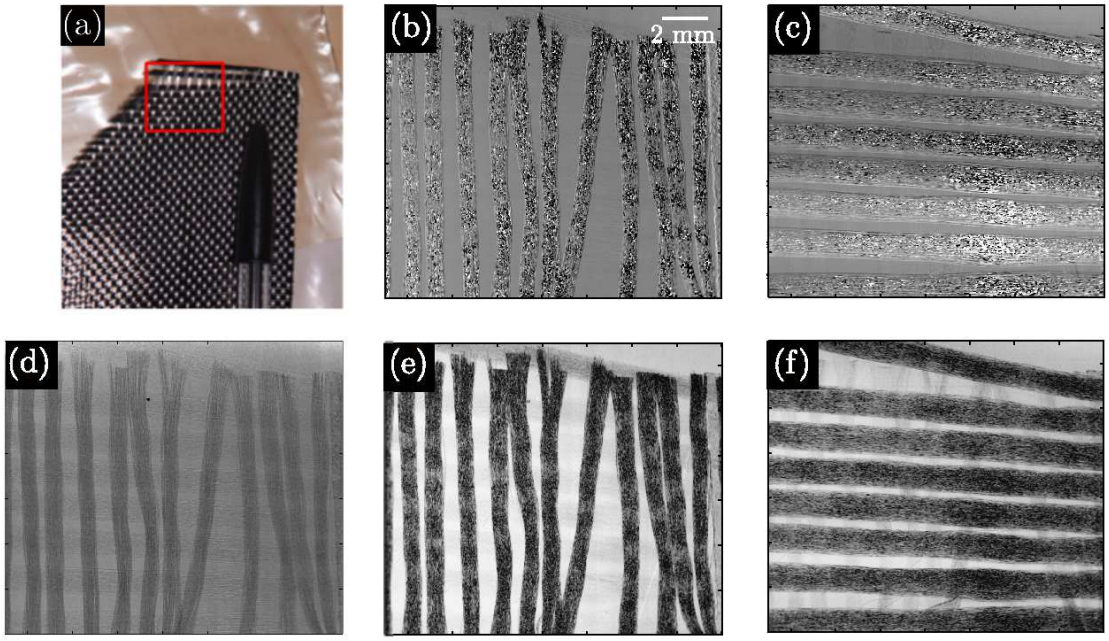

Figure 11.8: (a) Photography of the carbon-glass mesh measured with the 2D grating interferometer. In this picture and in the radiographs, horizontal fibers are made of carbon and vertical fibers are made of glass. (b)-(c) Differential phase images along x and y respectively. (d) Attenuation image. (e)-(f) Dark-field images along x and y respectively. The raster phase-stepping scan was performed over one period in 4×4 points. The exposure time per raw interferogram was 1 s, the pixel size was 7.5 μm.

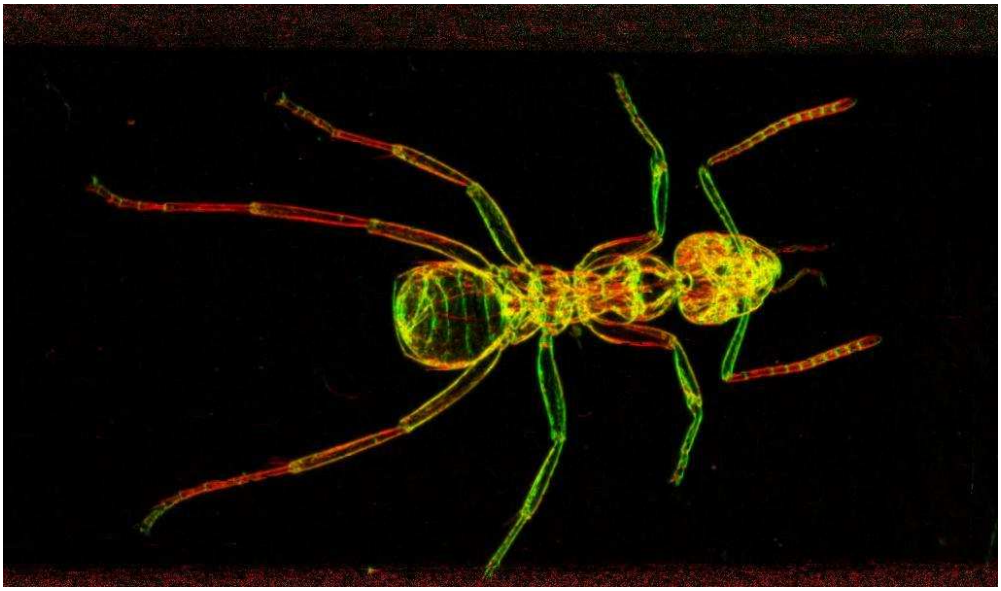

Figure 11.9: Dark-field image of an ant taken with the 2D interferometer consisting of a 2D phase grating and a 2D absorption grating. The green and red channels represent, respectively, the dark-field contrast in the horizontal and vertical directions.

Preliminary results on the characterization of parabolic refractive lenses with a 2D grating interferometer and monochromatic synchrotron radiation within the present PhD work are reported in a co-authored paper [Rutishauser *et al.* 2011b]. The published results are complemented in this section.

In this experiment, single Be refractive lenses with a radius of curvature ρ in the apex from 50 to 1500 μm were inspected with the 2D grating interferometer operating at 23 keV. The focal length as a function of the decrement δ of refractive index of the lens material at the working energy is given by [Lengeler *et al.* 1999]:

$$f = \frac{\rho}{2\delta} \quad , \tag{11.5}$$

and δ=6.437×10^{-7} for Be at 23 keV .

During the measurements, the lens was placed directly upstream the 2D phase grating G1. The 2D grating interferometer was built with two crossed line phase gratings and two crossed line absorption gratings as described in Ref. [Zanette *et al.* 2010b]. The raster phase-stepping scan was performed by moving the phase gratings over 2×2 periods in 8×8 steps. The exposure time per image was 1 s. The detector had an effective pixel size of 7.5 μm.

11.4.1 Measurement of a lens with large radius of curvature

The refraction angle images α_x and α_y of the lens with $\rho = 1.5$ mm are shown in Fig. 11.10. The projected material thickness retrieved from these images with the Frankot-Chellappa algorithm [Frankot & Chellappa 1988] is displayed, as contour plot (concentric circles), in Fig. 11.11. The plot with black arrows of the refraction angle vector in Fig. 11.11 shows that X rays are refracted towards the center of the lens and that refraction is much stronger at the periphery of the lens than in the center.

In order to evaluate the astigmatism of the lens, refraction angle values in the active area of the lens have been fitted with a first-order polynomial. The values $\alpha_x(x, y)$ have been fitted with the function $g_x(x, y) = A_x x + B_x$ and the values $\alpha_y(x, y)$ have been fitted with the function $g_y(x, y) = A_y y + B_y$.

The slopes A_x and A_y of the fit planes directly give the focal lengths f_x and f_y in the two orthogonal directions:

$$f_x = \left(\frac{\partial \alpha_x}{\partial x}\right)^{-1} = \frac{1}{A_x} \quad \text{and} \quad f_y = \left(\frac{\partial \alpha_y}{\partial y}\right)^{-1} = \frac{1}{A_y} \quad . \tag{11.6}$$

The focal lengths measured in this way were $f_x = 1195 \pm 2$ m and $f_y = 1145 \pm 2$ m. These values should be compared with the nominal focal length at this energy which, according to Eq. (11.5), is 1165 m. This means that, in this lens, as in the results published in Ref. [Rutishauser *et al.* 2011b], a slight astigmatism has been detected, in this case of 4%.

Residual aberrations are evaluated by subtracting the linear fits from the original refraction angle images. The resulting images $\Delta\alpha_x = \alpha_x - g_x$ and $\Delta\alpha_y = \alpha_y - g_y$ are plotted in Fig. 11.12. As in Ref. [Rutishauser *et al.* 2011b], a circular shape generated in the fabrication process can be seen at the center of the lenses. Moreover, low-frequency oscillations in

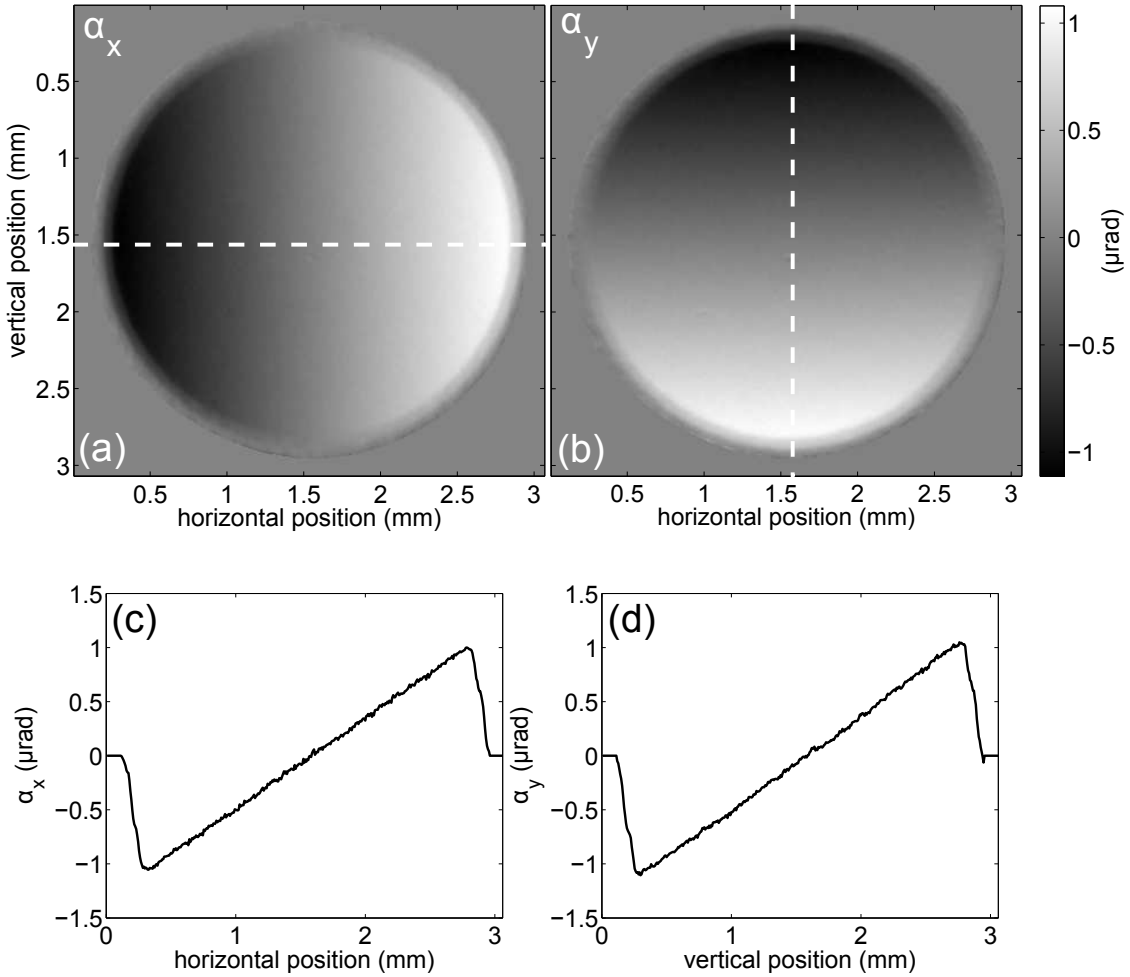

Figure 11.10: (a) and (b): Refraction angle images of a single Be refractive lens with radius of curvature of 1.5 mm measured with the 2D grating interferometer. (c) and (d): Profile plots extracted from the dashed white lines in panels (a) and (b).

$\Delta\alpha_y$ are visible in Fig. 11.12 (b). These oscillations are most probably not lens aberrations but rather artifacts caused by imprecisions in phase stepping. The vertical phase-stepping motor showed some instabilities during the measurements and low-frequency artifacts in this direction have been observed, not only for this particular lens, but for all the lenses measured during the experiment. Despite the presence of such artifacts, the standard deviation of $\Delta\alpha_x$ and $\Delta\alpha_y$ values calculated in a region of interest of 50×50 pixels is as small as 13 nrad.

11.4.2 Measurement of a lens with small radius of curvature

In the previous section and in Ref. [Rutishauser *et al.* 2011b], measurements on single refractive lenses with a large radius of curvature and a focal length on the order of 1 km are reported. This section presents results on characterization of a lens with a shorter focal length and discusses artifacts introduced by the strong focusing of the optical element under test.

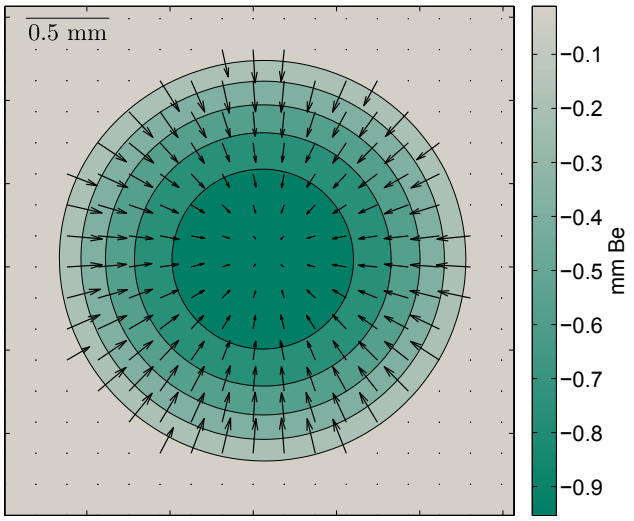

Figure 11.11: Differential phase vector (arrows) and contour plot of the projected material thickness downstream the refractive lens (concentric circles) obtained from the differential phase images of Fig. 11.10 as described in the text.

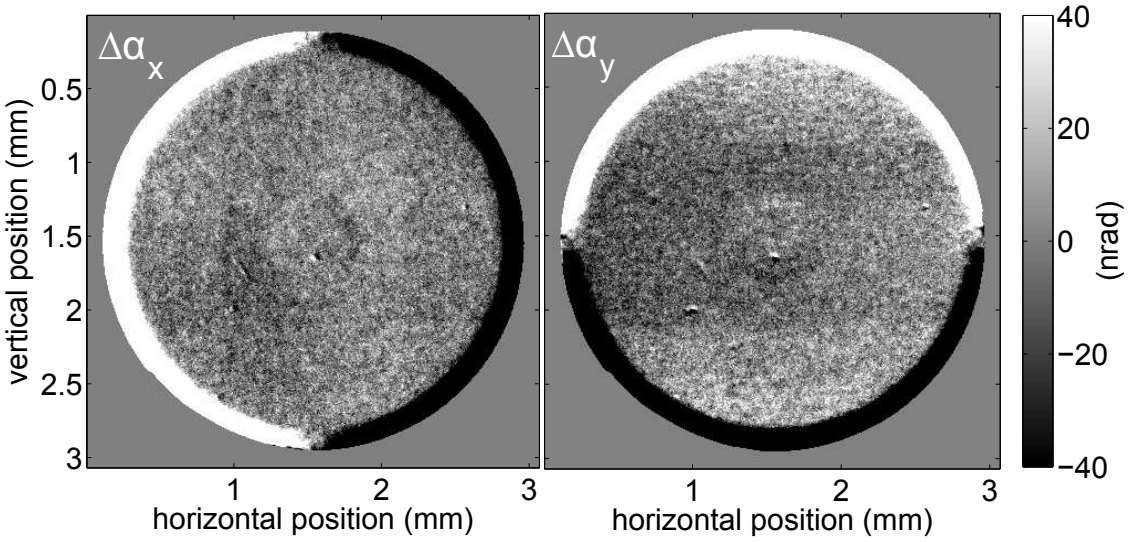

Figure 11.12: Measured refraction angle values minus values obtained with the linear fit. The very small values in the colorbars highlight the high precision of the measurement and the high quality of the lens.

A lens with a radius of curvature of $\rho = 50\,\mu$m was measured at the same experimental conditions than the other lenses, see previous section and Ref. [Rutishauser *et al.* 2011b]. Since this lens is more strongly focusing than the other lenses (the nominal value of the focal length is 38.84 m), the displacement of the 2D interference pattern caused by the lens on the observation plane is larger than the period of the interference pattern. This causes the phase-wrapping phenomenon.

Fig. 11.13 (a) and (b) show the (wrapped) phase obtained from the analysis of the raster phase-stepping scan. A quality-guided phase-unwrapping algorithm known as "Goldstein algorithm" was used to unwrap these images [Ghiglia & Pritt 1998]. The unwrapped images,

scaled to refraction angle values, are shown in Fig. 11.13 (c) and (d).

As in the measurements reported in the previous sections, the refraction angle values have been fitted with a first-degree polynomial. The focal lengths measured in this way were $f_x = 39.1 \pm 0.1$ m and $f_y = 39.0 \pm 0.1$ m which are both slightly larger than but very similar to the nominal value. In this case, unlike for the lenses with a larger radius of curvature, the lens does not show substantial astigmatism. This measurement, however, is affected by the presence of low-frequency intensity oscillations which can be seen when the fitted planes are subtracted from the refraction angle images. The images of $\Delta\alpha_x$ and $\Delta\alpha_y$, obtained with the procedure described in the previous section, are shown in Fig. 11.13 (e) and (f).

These low-frequency artifacts have the same period as the moiré fringes which are present in the active area of the lens of the raw interferogram, see Fig. 11.14. These moiré fringes are caused by the convergent beam behind the lens. With geometrical considerations, it can be shown that, when a lens with focal length f is placed in the X-ray beam path, the period p_i of the interference pattern produced by G1 is given by:

$$p_i = \frac{p_1}{2}\frac{f-d}{f} \quad . \tag{11.7}$$

where p_1 is the period of the phase-shifting grating and d is the inter-grating distance. In this case, $p_1 \approx 4.8$ μm, $d \approx 0.5$ m and $f \approx 39$ m which, according to Eq. (11.7), yield $p_i \approx 2.37$ μm. Since the period p_2 of the absorption grating is 2.4 μm, the period of the moiré fringes should be, using Eq. (B.1), of $2.37^2/(2.4-2.37) \approx 190$ μm in the two transverse directions. This is approximately the period of the low-frequency oscillations in Fig. 11.14 and Fig. 11.13 (e) and (f). Since the moiré fringes present in the raw interferograms do not cancel out with the flat-field correction, other methods, such as moiré imaging or direct fringe detection (i.e. without G2 and a high-resolution detector), might be better adapted to characterize these optical elements.

11.5 Two-dimensional moiré imaging

All the results presented in this thesis have been obtained in phase-stepping mode. However, as discussed in Sec. 4.4, there are certain conditions, e.g. when single-shot imaging is the only way to obtain information on the investigated object or the dose delivered to the sample has to be kept low and the spatial resolution is not an issue, in which moiré imaging is more suitable than phase stepping to retrieve the image signals.

In this section demonstrative images taken at ID19 are presented which show how the 2D grating interferometer developed during this PhD project can be used in moiré mode for wavefront sensing, optics characterization and imaging.

Moiré imaging with a 2D grating interferometer has recently been implemented at a synchrotron facility [Itoh *et al.* 2011] and at a laboratory X-ray source, the latter also with three 2D gratings [Sato *et al.* 2011]. Algorithms which can be used for the analysis of 2D periodic patterns are essentially an extension of Takeda's algorithm [Takeda *et al.* 1982] to the 2D case.

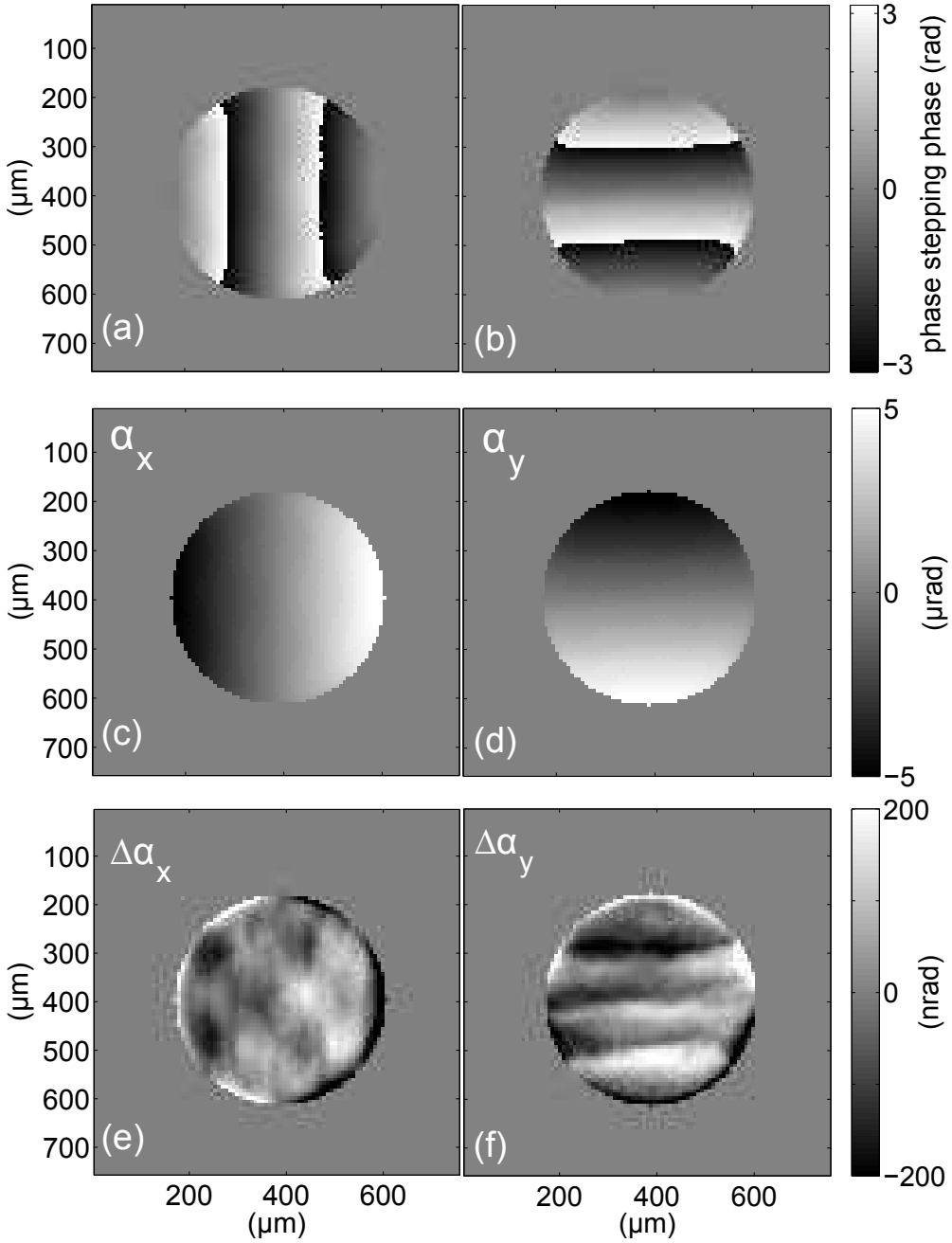

Figure 11.13: (a) and (b): wrapped images of a focusing lens with $r = 50$ μm obtained from the analysis of the 2D raster phase-stepping scan. (c) and (d): refraction angle images obtained by unwrapping images (a) and (b). (e) and (f): measured refraction angle values minus values fitted with a first-order polynomial.

A 2D moiré image of the empty beam is shown in Fig. 11.15 (a). The moiré intensity spots do not form a regular grid but are distorted, especially in the horizontal direction. These distortions are most probably caused by the thermal load on the double crystal monochromator which modifies the shape of the first crystal and thus of the vertical profile of the reflected wavefront. This is confirmed by the fact that when the photon flux on the

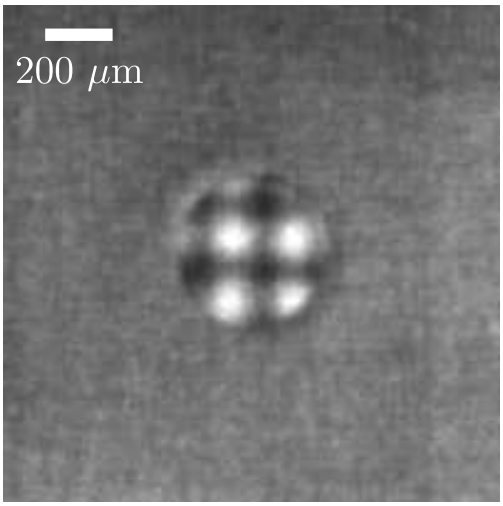

Figure 11.14: Raw image acquired during the raster phase-stepping scan.

double crystal monochromator is increased - in this case by closing the wiggler gap -, the distortion revealed by the 2D moiré image is much stronger, see Fig. 11.15 (b). With the analysis of the 2D moiré pattern, the shape of the surface of the crystal can be retrieved in two directions.

Figures 11.15 (a) and (b) show wavefront distortions mainly in the vertical direction. In Fig. 11.15 (c), a 2D moiré image of a Be refractive lens with radius of curvature $\rho = 50$ μm is displayed. Phase-stepping measurements on this lens are reported in Sec. 11.4. Since in the active area of the lens both horizontal and vertical moiré fringes are shifted, the moiré pattern inside an ideal lens appears rotated with respect to the moiré pattern outside. By measuring the tilt angle with respect to the empty beam, the radius of curvature of the wavefront can be retrieved in the two directions.

As a final example of moiré imaging, Fig. 11.15 (d) shows an image of a leaf on a 2D moiré pattern. The leaf is not only refracting the X rays, and thus shifting the position of the intensity spots, but it also scatters the X-ray photons causing a decrease of the spot visibility.

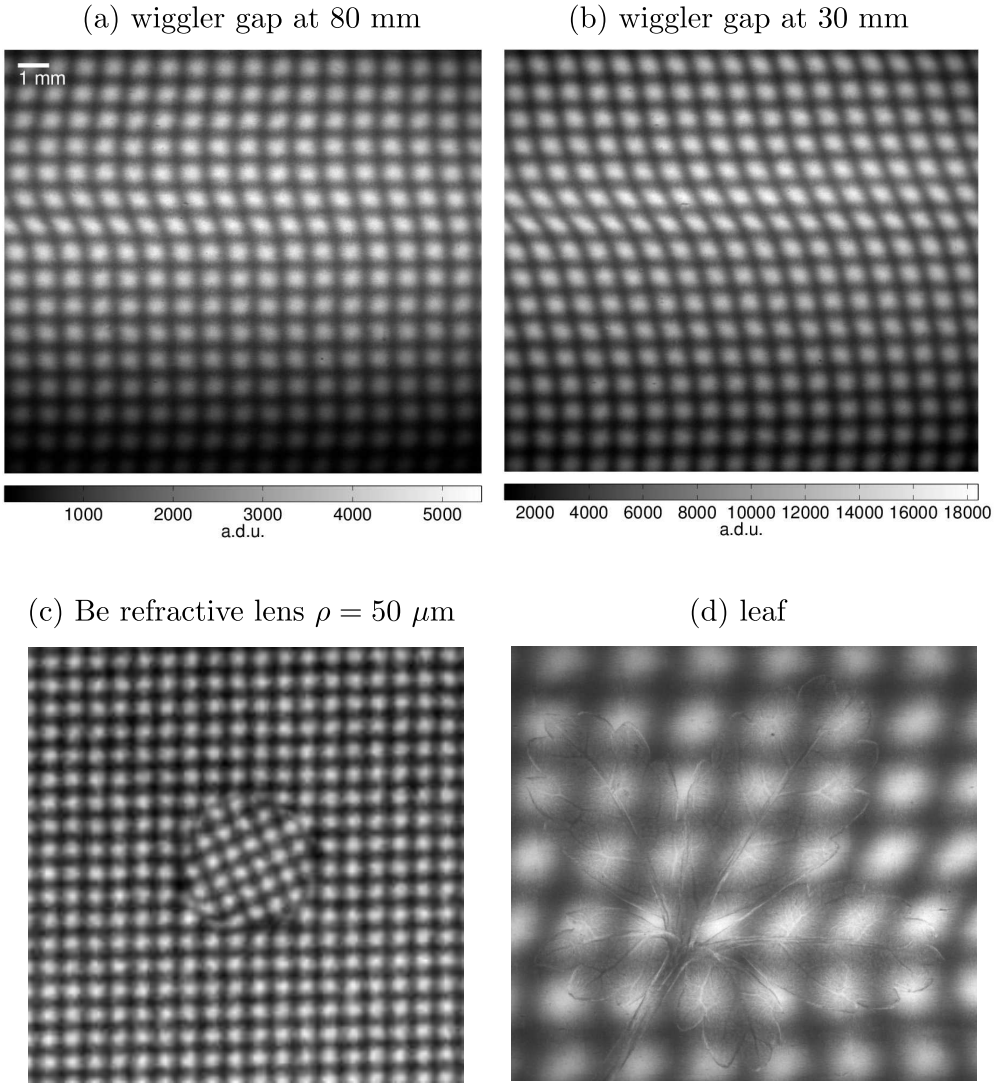

Figure 11.15: Two-dimensional moiré pattern images. (a) and (b): Flat-field images taken without any sample in the beam. These images were recorded at different wiggler gap openings as indicated in the title of the figures. (c) 2D moiré pattern distorted by a refractive beryllium lens. (d) Leaf on a 2D moiré pattern. All these images have been recorded with the 2D interferometer described in Chap. 11 at an X-ray photon energy of 23 keV.

Chapter 12
Conclusions and Perspectives

X-ray grating interferometry is a recently-developed multimodal X-ray imaging technique which yields attenuation, differential phase and dark-field images of the sample. The standard one-dimensional grating interferometer consists of two line gratings placed one behind the other in the X-ray path. The first grating acts as a diffractive element that induces a periodic modulation in the wavefront; the second grating transforms modifications in position or strength of the interference pattern into intensity differences on the detector. Phase and dark-field images provided by the X-ray grating interferometer allow the visualization of object features which can not be accessed with conventional attenuation contrast. While phase contrast is sensitive to variations in the projected electron density, scatter contrast (or "dark-field imaging") detects features that cause small-angle X-ray scattering, i.e., structures with density fluctuations on length scales smaller than the resolution of the imaging system. X-ray grating interferometry bears tremendous potential for medical imaging, non-destructive testing, security screening and many other fields. Moreover, since it allows very accurate and precise refraction angle measurements, it is widely exploited also for optics characterization and wavefront analysis.

The first chapters of this thesis, Chapters 2-6, describe the principles of grating interferometry and give a review of the recent contributions in this field. The author of this PhD thesis has contributed to the two developments listed below.

- We have demonstrated that a *structured scintillator*, used as analyzer element at the place of the conventional absorption grating and the continuous scintillator, helps to circumvent the limitations caused by unwanted transmission by the absorbing grating lines. The structured scintillator has been tested at a laboratory setup with a mean X-ray photon energy of 60 keV. The visibility of the contrast curve obtained with the structured scintillator was 22% while the one measured with the standard setup was only 5%, see Sec. 6.2.1 and Ref. [Rutishauser *et al.* 2011a].

- We have developed a new formalism for describing the *directional dark-field signal* generated by *strongly oriented systems*. This formalism has been applied to data recorded with the grating interferometer built during this PhD project at the beamline ID19 of the European Synchrotron Radiation Facility in Grenoble, France. See Sec. 6.2.2 and Ref. [Jensen *et al.* 2010b].

The main results of the author's work (Chapters 7 to 11), in which she had a leading role, are summarized in the following. Some general research perspectives are discussed at the end of this chapter.

Main contributions of this PhD project

Implementation of an X-ray grating interferometer at ID19 The first achievement of this PhD project was the design and installation of an X-ray grating interferometer for radiography and tomography at the beamline ID19 of the European Synchrotron Radiation Facility in Grenoble, France. The instrument, which is now available to external users, is described in Chap. 7. The availability of different sets of gratings gives access to a wide energy range, from ≈17 keV to more than 100 keV. Inter-grating distances from 150 to 600 mm can be realized with the current setup. The best spatial resolution achieved in the final differential phase and dark-field images is approximately 10 μm and the precision in the refraction angle measurement is of 10 nrad. This interferometer has been used mainly in phase-stepping mode.

Phase-stepping tomography is performed with a step-and-go motion of the tomography rotation axis, the standard implementation consists in recording an entire phase-stepping scan for each angular position of the sample. Advanced acquisition schemes developed during this PhD project are discussed further below.

A largely automated software, relying on the standard ESRF tomographic reconstruction routines, allows to reconstruct attenuation, phase and dark-field tomograms from raw interferograms collected during the phase-stepping tomography scans (Sec. 7.6).

Characterization of the instrument The grating interferometer has been characterized through measurements with monochromatic beam of the refractive index of a phantom sample made of known materials arranged in a systematic geometry. The results, reported in Chap. 8 and in Ref. [Zanette *et al.* 2011d], show the *high precision and accuracy of the phase measurements* provided by this device. This work also discusses the limitations imposed by the *phase-wrapping phenomenon* which reduces the quality of the phase measurement. Numerical simulations show that the stripe features generated by the phase-wrapping phenomenon in the phase tomogram can be qualitatively and quantitatively reproduced by calculations.

Phase tomographies of soft-tissue biological samples The potential of grating interferometry in providing high-sensitivity phase tomograms of soft-tissue biological specimens has been confirmed by measurements of a human cerebellum and a rat testis (Chap. 9).

The results show that grating-based phase tomography gives access to features which cannot be revealed by any other non-destructive technique and that the information obtained with this device is similar to that provided by conventional histological sectioning and staining, but in three dimensions and without the distortions commonly caused by sectioning. Without making use of any staining agent, different strata in the white and grey matter of the cerebellum could be separated and Purkinje cells can be visualized at the periphery of the stratum granulosum (grey matter). In the testis, seminiferous tubules and different stadia of the spermatozoa maturation could be clearly imaged.

The δ (decrement of refractive index) resolution in these phase tomograms was around 2.5×10^{-10} which corresponds to a mass density resolution of 0.5 mg/cm^3 for aqueous specimens.

Preliminary results on the comparison between phase tomograms of soft-tissue samples provided by different phase-contrast imaging techniques (e.g. grating-based phase tomography vs. holotomography) are also presented in this thesis.

New acquisition schemes New phase-stepping tomography methods have been developed in order to reduce the dose delivered to the sample and to increase the quality of the phase reconstructions. These methods are based on *interlaced phase stepping* which consists in recording each raw interferogram of a phase-stepping scan at a slightly different viewing angle of the sample, see Chap. 10 and Ref. [Zanette *et al.* 2011a]. As explained in Sec. 10.2, interlaced phase stepping is beneficial especially in local (or region-of-interest) tomography when the sample is larger than the detector field of view and the imaged region may suffer from artifacts caused by the presence of external features. These artifacts are drastically reduced in interlaced phase stepping.

As shown in Sec. 10.3 and in Ref. [Zanette *et al.* 2011b], interlaced phase stepping has the further advantage that, for the same dose delivered to the sample and with suitable analysis of the raw interferograms (*oversampled interlaced* phase stepping), the effective angular sampling density can be increased with respect to the standard phase-stepping method. With oversampled interlaced phase stepping, the net minimum number of raw interferograms needed per tomographic projection angle is only one, as opposed to three in standard phase stepping. Moreover, interlaced phase-stepping acquisition schemes give a substantially improved signal-to-noise ratio in phase and dark-field tomography with respect to the standard method, as has been demonstrated with numerical simulations and experimental data recorded at ID19 [Zanette *et al.* 2011a, Zanette *et al.* 2011b].

Two-dimensional grating interferometry A two-dimensional (2D) grating interferometer has been conceived, designed, implemented and characterized during this PhD project (Chap. 11). This interferometer uses 2D gratings instead of line gratings used in the standard device and yields differential phase and dark-field signals in multiple directions [Zanette *et al.* 2010a, Zanette *et al.* 2010b]. In the first proof-of-principle implementation of the device, two crossed line phase gratings and two crossed line absorption gratings were used. In more recent implementations, genuine 2D gratings have been employed (Sec. 11.3). The two-dimensional device has been used in phase-stepping mode and in moiré mode. The phase stepping is, in the 2D case, a 2D raster scan. The moiré pattern is a series of spots (instead of the lines observed in the 1D case).

From the orthogonal differential phase images provided by the 2D grating interferometer, the phase of the incoming wavefront can be retrieved with suitable reconstruction methods. This makes the two-dimensional grating interferometer interesting for optics characterization and wavefront sensing. Application examples of characterization of

Be refractive lenses with a 2D grating interferometer are reported in Sec. 11.4 and in Ref. [Rutishauser *et al.* 2011b]. Limitations imposed by the strong focusing of lenses with small radius of curvature are discussed in Sec. 11.4.

Perspectives

The results obtained during this PhD project open up new research perspectives and indicate new directions to further improve the technique; some of them are discussed below.

- Phase wrapping, strong scattering and strong absorption corrupt the differential phase signal. This reduces the accuracy and precision of the phase measurements, see Chap. 8. A situation similar to that observed for the phantom sample reported in Chap. 8 can occur, for example, when different parts of soft tissue need to be distinguished in a sample region in which bones (which are strongly refracting) are also present. In these cases, a significant improvement could come from the development of algorithms which correct the corrupted signal in differential phase projections and/or phase tomograms. Algorithms of this kind could exploit, for example, the information given by the dark-field and attenuation signals.

  The fact that artifacts from the phase-wrapping phenomenon can be completely reproduced by simulations [Zanette *et al.* 2011d] indicates that even the phase-contrast signal alone may possibly be used to eliminate these artifacts, for example, by iterative algorithms.

  Using the absorption or dark-field information to correct for the phase-wrapping effect even when phase jumps can not be unambiguously unwrapped (e.g. when phase jumps are on a scale smaller than the spatial resolution), would also eliminate the need to immerse the sample in a phase-matching liquid during the tomography measurement.

- We believe that a systematic study on the effects of number of steps per phase-stepping scan, angular phase-stepping range and number of desired differential phase projections would be beneficial to further improve the phase reconstruction provided by the interlaced phase-stepping methods. Moreover, fast tomography scans could be implemented based on the interlaced schemes, thus combining high data acquisition speed with the high spatial resolution of the phase-stepping technique.

- The four dark-field images obtained with the 2D grating interferometer could be combined to yield a directional dark-field map similar to the one obtained with the technique developed by Jensen et al. [Jensen *et al.* 2010a, Jensen *et al.* 2010b]. This will allow to visualize preferential orientation of scattering features in the sample without the need to rotate the specimen or the interferometer with promising applications in the medical field and in materials science.

- Benefits could come from combining 2D grating interferometry, either in moiré or phase-stepping mode, with tomography. Tomography reconstructions obtained from phase maps and from directional dark-field images may show features which can not

be revealed with the standard 1D grating interferometer. Ultra-fast tomography scans in moiré mode, with speed comparable to the one reached with the 1D device [Momose *et al.* 2011b], could be performed with a 2D grating interferometer and white-beam synchrotron radiation.

Final remarks

As a result of this thesis project, an X-ray grating interferometer is now available to users at ID19. This X-ray grating interferometer is one of only a few fully-operational instruments in the world so far and is second to none in the world in terms of sensitivity and data quality in general.

Grating interferometry is an ideal complement to existing synchrotron-based X-ray phase-contrast imaging methods, at ID19 and other imaging beamlines, in two main ways:

1. By giving high-sensitivity phase-contrast images in cases where propagation-based techniques are limited by the technically feasible propagation distances (i.e. for high energies and relatively large pixel sizes/fields of view).

2. Through the dark-field imaging modality, grating interferometry makes it possible to detect and obtain contrast from the presence of sub-resolution structures. This will allow to visualize features such as very small fissures, fibres and regions with nanoporosity.

Beyond its value for the user program at beamline ID19 or the ESRF in general, this instrument and the developments made in this thesis project demonstrate the high performance and versatility of X-ray grating interferometry. They pave the way for similar, or improved, instruments on future beamlines at facilities around the globe, in the fields of X-ray imaging and X-ray metrology.

Appendix A

Intensity pattern from a $\pi-$shifting phase grating

In this appendix we show that the intensity pattern generated at the distance $F_{1,16}$ by a $\pi-$shifting phase grating has a rectangular profile with half of the period of the grating. All the quantities used in this appendix are defined in Sec. 3.2.3.2.

When $m_1 = 1$ and $m_2 = 16$, Eq. (3.15) (page 26) becomes

$$E(x, F_{1,16}) = \frac{2}{\sqrt{32}}\left\{ e^{\frac{i\pi}{8}}\left[\mathcal{T}\left(x+\frac{1}{8}p\right) - \mathcal{T}\left(x+\frac{3}{8}p\right) - \mathcal{T}\left(x+\frac{5}{8}p\right) + \mathcal{T}\left(x+\frac{7}{8}p\right)\right] + \cdots \right.$$
$$\left. \cdots + i\left[\mathcal{T}\left(x+\frac{p}{4}\right) + \mathcal{T}\left(x+\frac{3}{4}p\right)\right] + \mathcal{T}\left(x+\frac{p}{2}\right) + \mathcal{T}\left(x+p\right)\right\}. \quad \text{(A.1)}$$

According to Eq. (3.20) (page 27), a binary phase grating with $\phi = \pi$-shifting lines and duty cycle 0.5, has a transmission function $\mathcal{T}(x)$ (Fig. A.1):

$$\mathcal{T}(x) = \begin{cases} 1, & \text{if } 0 \leqslant (x \bmod p) < p/2 \\ -1, & \text{if } p/2 \leqslant (x \bmod p) < p \end{cases}. \quad \text{(A.2)}$$

For this particular transmission function

$$\left[\mathcal{T}\left(x+\frac{p}{4}\right) + \mathcal{T}\left(x+\frac{3}{4}p\right)\right] = 0 \quad \text{and} \quad \mathcal{T}\left(x+\frac{p}{2}\right) + \mathcal{T}\left(x+p\right) = 0 \ ,$$

so that, Eq. (A.1) can be rewritten as

$$E(x, F_{1,16}) = \frac{2}{\sqrt{32}}\left[\mathcal{T}\left(x+\frac{1}{8}p\right) - \mathcal{T}\left(x+\frac{3}{8}p\right) - \mathcal{T}\left(x+\frac{5}{8}p\right)\mathcal{T}\left(x+\frac{7}{8}p\right)\right]. \quad \text{(A.3)}$$

If we now divide the period p in eight intervals of the same width, we can evaluate Eq. (A.3)

in each of these, obtaining the following values.

$$\text{Ⓐ} \qquad E\left(0 < (x \bmod p) \leqslant \frac{1}{8}p\right) = 0$$

$$\text{Ⓑ} \qquad E\left(\frac{1}{8}p < (x \bmod p) \leqslant \frac{2}{8}p\right) = -8/\sqrt{32}$$

$$\text{Ⓒ} \qquad E\left(\frac{2}{8}p < (x \bmod p) \leqslant \frac{3}{8}p\right) = -8/\sqrt{32}$$

$$\text{Ⓓ} \qquad E\left(\frac{3}{8}p < (x \bmod p) \leqslant \frac{4}{8}p\right) = 0$$

$$\text{Ⓔ} \qquad E\left(\frac{4}{8}p < (x \bmod p) \leqslant \frac{5}{8}p\right) = 0$$

$$\text{Ⓕ} \qquad E\left(\frac{5}{8}p < (x \bmod p) \leqslant \frac{6}{8}p\right) = 8/\sqrt{32}$$

$$\text{Ⓖ} \qquad E\left(\frac{6}{8}p < (x \bmod p) \leqslant \frac{7}{8}p\right) = 8/\sqrt{32}$$

$$\text{Ⓗ} \qquad E\left(\frac{7}{8}p < (x \bmod p) \leqslant p\right) = 0$$

Since the intensity is given by the square modulus of the wavefield E, the intensity profile is $I_{\max}(x, F_{1,16}) = 2$ in the intervals Ⓑ, Ⓒ, Ⓗ and Ⓖ and 0 in the others.

With the above results we have shown that the intensity pattern produced by the $\pi-$shifting grating at the distance $F_{1,16}$ is a square profile with half of the period of the grating as shown in Fig. A.1 bottom and in the Talbot carpet of Fig. 3.3 (c). Moreover, since the minimum of the intensity pattern is zero, its visibility as defined in Eq. (3.22) (page 27) is 1.

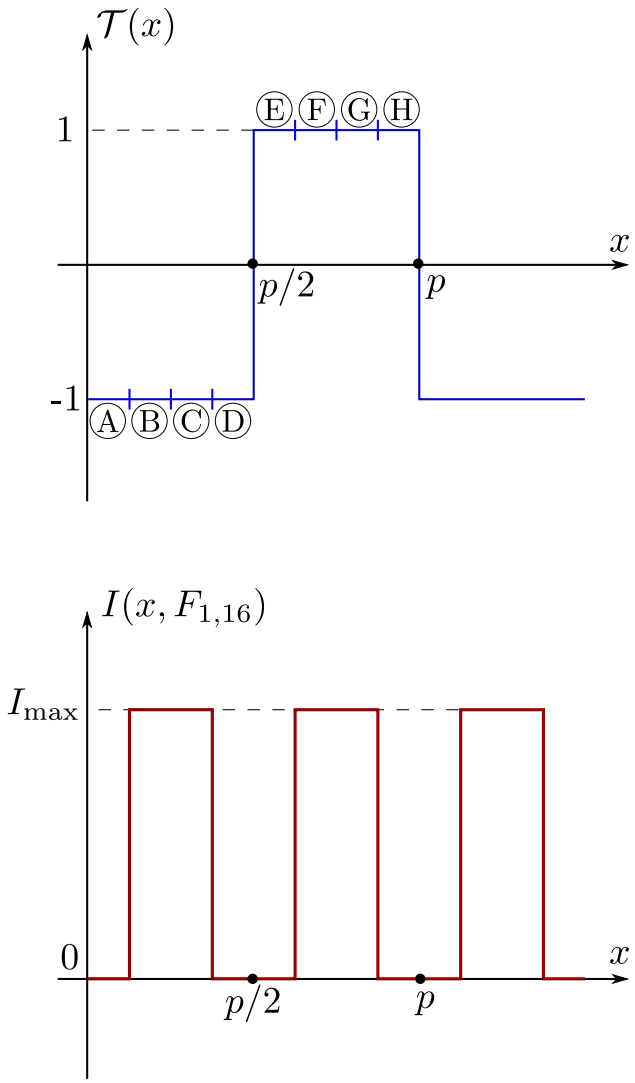

Figure A.1: Top: transmission function of a $\pi-$shifting grating. Bottom: intensity pattern produced by this grating at the fractional Talbot distance $F_{1,16}$.

Appendix B
The moiré effect

The moiré effect (the term *moiré* originates from a type of textile which has a rippled appearance) is a phenomenon observed when two patterns with different periods, different angle or simply laterally shifted one respect to the other, are superimposed. The patterns can have any shape (they can be, for example, mesh grids or concentric circles); the moiré image that the patterns generate depends on the shape of the patterns and on the origin of the effect. The moiré effect is used in many applications, such as metrology, topography and strain analysis [Patorski & Kujawinska 1993].

In grating interferometry the moiré effect has an important role. In moiré imaging, a large number of moiré fringes are created by a deliberate misalignment of the two gratings. Analysis of the fringe pattern yields the differential phase and scattering signals, see Sec. 4.4. On the other hand, when the grating interferometer is used in phase-stepping mode (Sec. 4.1), the moiré effect may disturb the signal in the final images. In this case, the gratings should be carefully aligned in order to minimize the number of moiré fringes.

In the standard one-dimensional grating interferometer, the moiré image, which is a pattern of lines, is generated by superposition of two line patterns. These are:

1. the self image of G1;

2. the lines of G2.

In this appendix we give the basic equations to calculate the period of the moiré lines when the period of the gratings and the interferometer geometry are known. More formulas describing the (one-dimensional) moiré effect in an X-ray grating interferometer with applications in wavefront sensing are presented in Refs. [Weitkamp *et al.* 2004, Wang *et al.* 2011].

In the following we indicate with p_i the period of the self image of G1 (as discussed in Sec. 3.3.1, p_i depends on the period of G1 and on the magnification factor). Moreover, we assume that the lines of G2 (with period p_2) are vertical as shown in Fig. B.1. The quantity ξ in Fig. B.1 (b) indicates the rotation angle between the self image of G1 and G2; when $\xi = 0$ the gratings are parallel.

The moiré fringes generated in this configuration can be:

(a) **vertical** with period p_v if $p_i \neq p_2$ and $\xi = 0$ (see Fig. B.1 (a));

(b) **quasi horizontal** with period p_d if $p_i = p_2$ and $\xi \neq 0$ (see Fig. B.1 (b));

(c) **diagonal** $p_i \neq p_2$ and $\xi \neq 0$, i.e. cases (a) and (b) occur at the same time.

Here, for simplicity, we will consider only cases (a) and (b) separately.

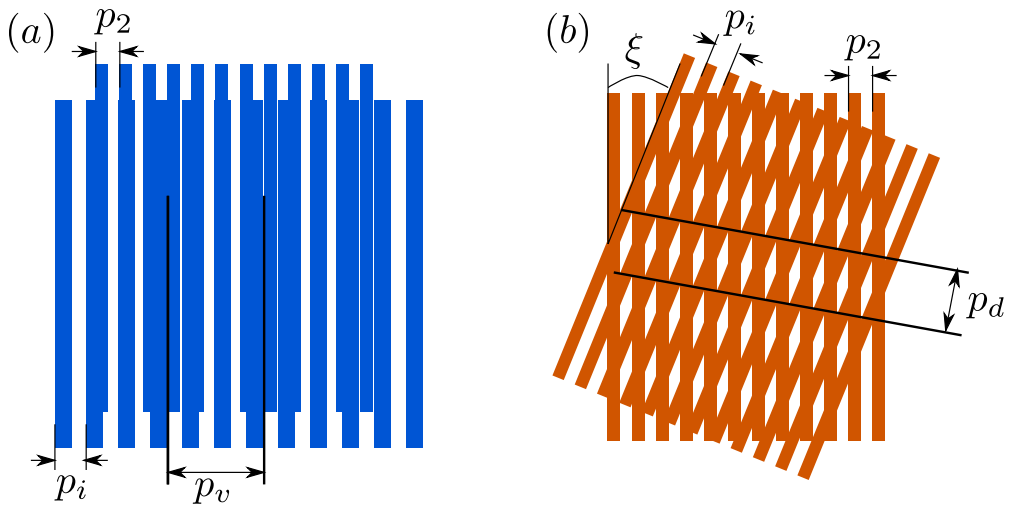

Figure B.1: Schematic representation of the moiré effect in standard one-dimensional grating interferometry. p_i is the period of the interference pattern and p_2 is the period of G2. Vertical fringes with period p_v are observed if $p_i \neq p_2$; quasi-horizontal fringes with period p_d are formed when one of the two gratings is rotated respect to the other.

Period of moiré fringes in case (a) The period p_v of the vertical moiré lines is given by [Patorski & Kujawinska 1993]:

$$p_v = \frac{p_i p_2}{|p_i - p_2|} \quad . \tag{B.1}$$

As an example, let us calculate the period of the moiré lines caused by an absorption grating with period $p_2 = 2.4$ μm and an interference pattern with period $p_i = 2.408$ μm. An interference pattern with this particular period is generated, at ID19, by, for example, a $\pi/2-$shifting grating with period $p_1 = 2.4$ μm at a distance of $d = 0.5$ m (the distance R from the source to the phase grating is 150 m, the magnification factor M is $M = (d+R)/R$ and $p_i = Mp_1$). According to Eq. (B.1), the period of the moiré lines is $p_v \approx 0.7$ mm. This means that 28 fringes are observed in a field of view of 2 cm width.

Period of moiré fringes in case (b) The period p_d of the moiré fringes which are formed if one of the two grating is rotated by an angle ξ respect to the other (case 2.) is given by [Patorski & Kujawinska 1993]:

$$p_d = \frac{p_2}{2\sin\xi} \approx \frac{p_2}{2\xi} \quad , \tag{B.2}$$

In moiré imaging, the rotation of one of the gratings is adjusted so that a suitable number of fringes are present on the observation plane. For example, if $p_2 = 2.4$ μm, the pixel size is 10 μm and fringes with a period that cover 3-5 pixels are desired, the angle ξ should be around 2 degrees.

Further considerations Note that both p_v and p_d are inversely dependent on the quantity causing the moiré images, i.e. the difference in period δ_p and the rotation angle ξ. This

means the *number of fringes* in the field of view, which is inversely proportional to the period of the fringes, is linearly dependent on δ_p and ξ.

When two-dimensional gratings, such as the ones presented in Chap. 11, are used instead of one line structures, the moiré pattern is a superposition of vertical and horizontal fringes, see Chap. 11.

Appendix C
Design of two-dimensional gratings

The first step for the realization of the 2D grating interferometer was the design of 2D gratings. Different possible configurations were investigated with numerical simulations. The results of this study are published in Ref. [Zanette *et al.* 2010a]; the main findings are reported in the following paragraphs.

While in the 1D case the variable parameters for the design of a grating are its duty cycle and the period of the lines, the design of 2D gratings allows for a variety of unit cells. To restrict the number of possible configurations, we considered only 2D gratings with the same period along x and y (Fig. C.1). Furthermore, in analogy to the 1D case, binary gratings with a duty cycle of 0.5 along both axes have been considered. Taking these two constraints into account, two types of unit cells are possible: mesh-type (Fig. C.1 (a)) and checkerboard-type (Fig. C.1 (b)).

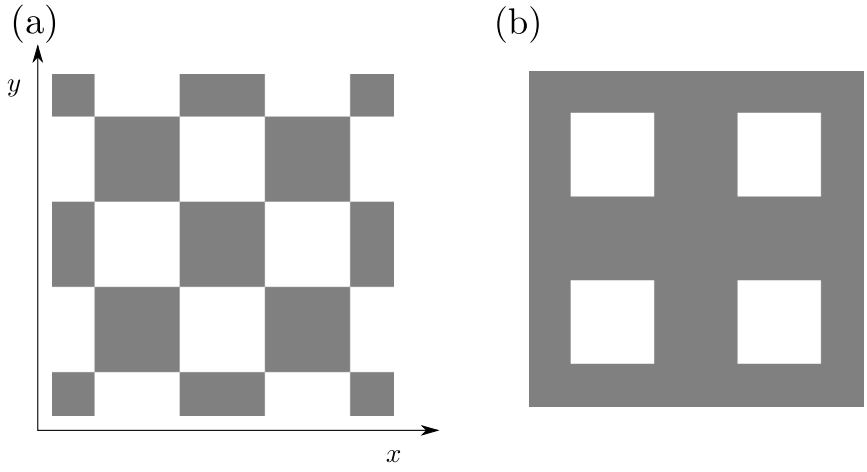

Figure C.1: Checkerboard-type (a) and mesh-type (b) gratings.

Design of the 2D phase grating To further reduce the number of possible candidates, and still in analogy to the 1D case, phase gratings with π and $\pi/2$-shifting pillars have been considered. The four different 2D phase gratings are shown in Fig. C.2 (left column). The simulation code discussed in Sec. 3.1.1 has been extended to two dimensions, and successively been used to simulate the images generated by these gratings. In the simulation, we assumed that the gratings are illuminated by a plane monochromatic wavefront. The binary images produced by these gratings are shown in Fig. C.2 (right column).

Among the four gratings considered in this study, the checkerboard-type π-shifting phase grating generates mesh intensity patterns with half of the period of the grating itself. Moreover, the π-shifting checkerboard can be obtained as superposition of two crossed line π-shifting 1D gratings; in fact, the phase shift caused by the regions in which the two π-shifting lines overlap is $\pi + \pi = 2\pi = 0$. Because of these properties, we have taken the π-shifting checkerboard-type grating as a good candidate for the phase grating of the 2D interferometer.

Design of the absorption grating In analogy to the 1D case, an absorption grating with the the same shape of the interference pattern produced by G1 has been chosen. The 2D absorption grating has the mesh pattern shown in Fig. C.3 (a), where the black parts are the absorbing areas. This grating, analogously the checkerboard $\pi-$shifting phase grating, can be obtained by superposition of two crossed line absorption grating.

The convolution of the 2D mesh interference pattern with the 2D mesh absorption grating gives the image shown in Fig. C.3 (b). This image corresponds to the intensity modulation recorded during a 2D raster phase-stepping scan (see measured 2D intensity pattern in Fig. 11.3). This pattern of intensity spots can be conveniently analyzed by a 2D Fourier analysis as described in Chap. 11. Moreover, the visibility of the contrast curve along x and y, obtained by integrating the convolution image along these axes, is, ideally, 100%. Lower visibilities would be obtained if one of the two patterns, i.e. the interference pattern or the transmission function of the absorption grating, had a checkerboard profile.

With this numerical study, we have designed an appropriate combination of phase and absorption gratings for realizing a 2D interferometer which, as explained in Chap. 11, gives the differential phase and scattering signals along multiple directions without the need of moving the sample or the gratings.

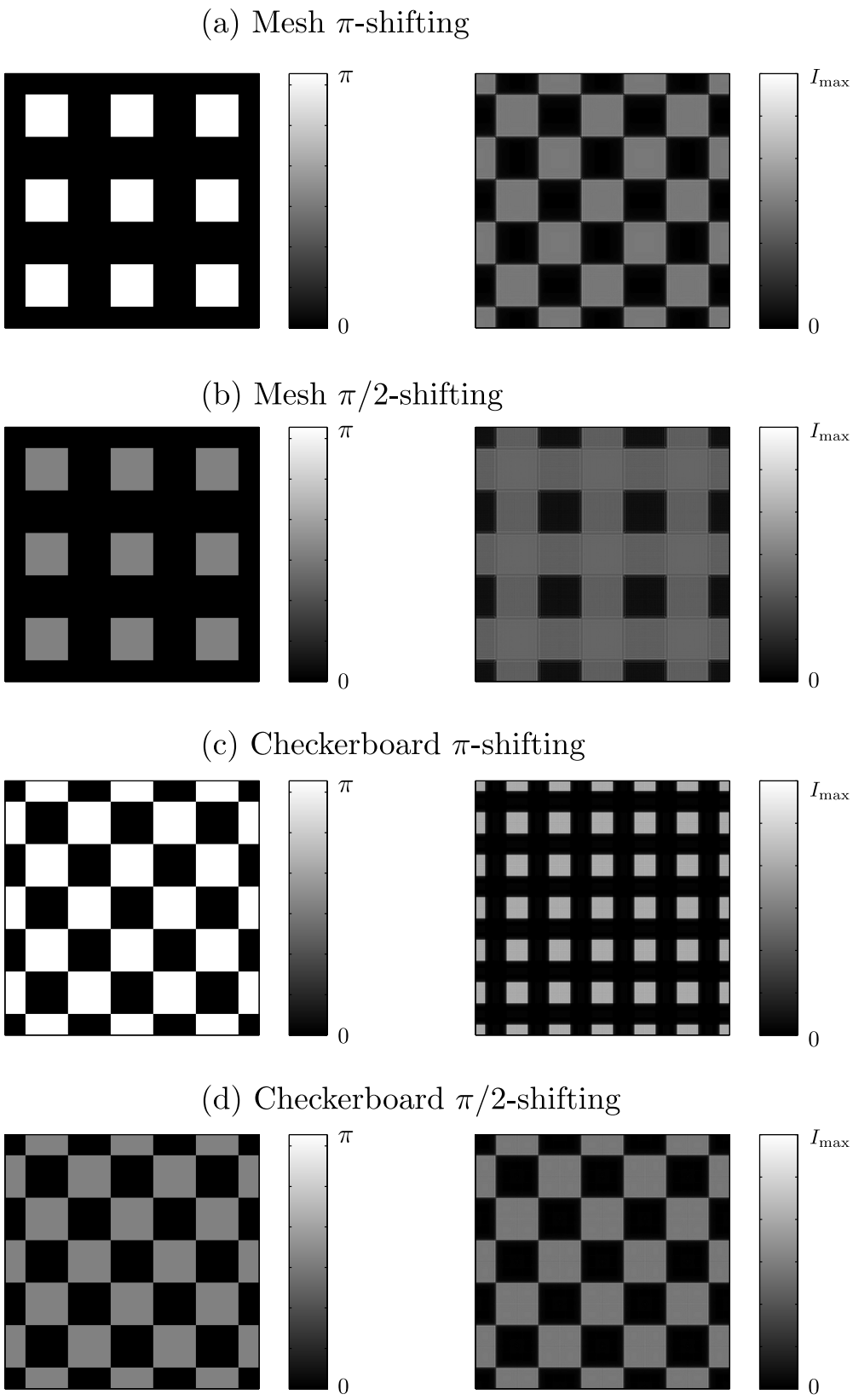

Figure C.2: Left column: phase profiles of four types of 2D phase gratings. Right: binary intensity pattern generated by these gratings.

(a) (b)

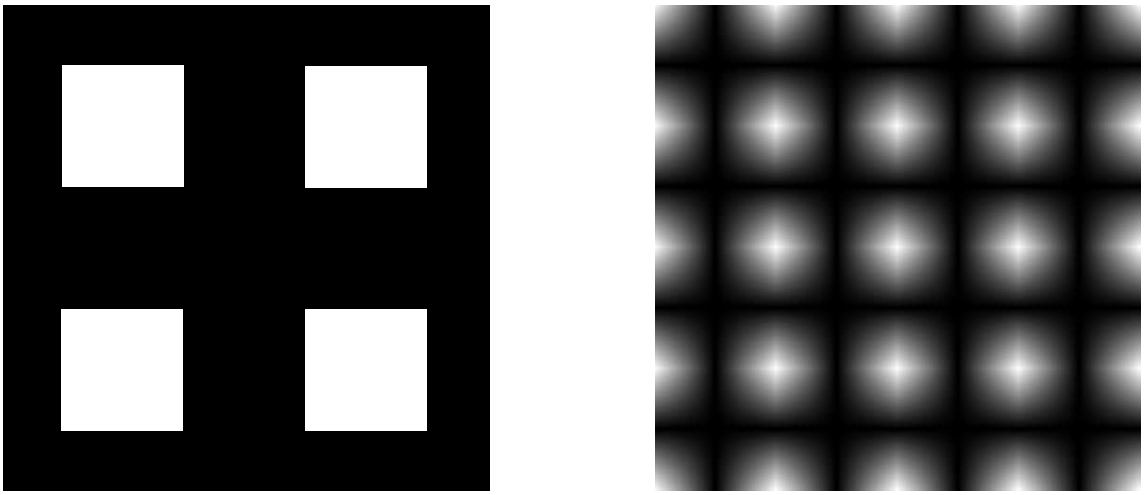

Figure C.3: (a) 2D absorption grating; the opaque parts are represented in black. (b) Image resulting from the convolution of the mesh interference pattern generated by the 2D phase grating with the mesh transmission function of the absorption grating.

References

[Als-Nielsen & McMorrow 2010] J. Als-Nielsen and D. McMorrow. Elements of modern x-ray physics. John Wiley & Sons Inc., England, 2010. (Cited on pages 8, 12 and 70.)

[Arrizón & Rojo-Velázquez 2001] V. Arrizón and G. Rojo-Velázquez. *Fractional Talbot field of finite gratings: compact analytical formulation.* J. Opt. Soc. Am. A, vol. 18, issue no. 6, pages 1252–1256, 2001. (Cited on page 30.)

[Attix 1986] F. H. Attix. Introduction to radiological physics and radiation dosimetry. John Wiley & Sons Inc., New York, 1986. (Cited on page 13.)

[Baker 2009] K. L. Baker. *W-ray wavefront analysis and phase reconstruction with a two-dimensional shearing interferometer.* Opt. Eng., vol. 48, art. no. 086501, 2009. (Cited on pages 133 and 139.)

[Bech *et al.* 2008] M. Bech, O. Bunk, C. David, P. Kraft, C. Brönnimann, E. F. Eikenberry and F. Pfeiffer. *X-ray imaging with the PILATUS 100k detector.* Appl. Radiat. Isotop., vol. 66, issue no. 4, pages 474–478, 2008. (Cited on page 73.)

[Bech *et al.* 2010] M. Bech, O. Bunk, T. Donath, R. Feidenhans'l, C. David and F. Pfeiffer. *Quantitative x-ray dark-field computed tomography.* Phys. Med. Biol., vol. 55, issue no. 18, pages 5529–5539, 2010. (Cited on pages 45, 57 and 125.)

[Bech 2008] M. Bech. *X-ray imaging with a grating interferometer.* PhD thesis, University of Copenhagen, 2008. (Cited on pages 33 and 34.)

[Becker & Bonse 1974] P. Becker and U. Bonse. *The skew-symmetric two-crystal X-ray interferometer.* J. Appl. Cryst., vol. 7, issue no. 6, pages 593–598, 1974. (Cited on page 16.)

[Bennett *et al.* 2010] E. E. Bennett, R. Kopace, A. F. Stein and H. Wen. *A grating-based single-shot x-ray phase contrast and diffraction method for in vivo imaging.* Med. Phys., vol. 37, issue no. 11, pages 6047–6054, 2010. (Cited on page 64.)

[Bonse & Hart 1965] U. Bonse and M. Hart. *An X-ray interferometer.* Appl. Phys. Lett., vol. 6, pages 155–156, 1965. (Cited on pages 15 and 115.)

[Born & Wolf 1998] M. Born and E. Wolf. Principles of optics. Cambridge University Press, 1998. (Cited on pages 22, 31 and 32.)

[Bruning *et al.* 1974] J. H. Bruning, D. R. Herriott, J. E. Gallagher, D. P. Rosenfeld, A. D. White and D. J. Brangaccio. *Digital Wavefront Measuring Interferometer for Testing Optical Surfaces and Lenses.* Appl. Opt., vol. 13, issue no. 11, pages 2693–2703, Nov 1974. (Cited on page 46.)

[Bunk *et al.* 2009] O Bunk, M Bech, T H Jensen, R Feidenhans'l, T Binderup, A Menzel and F Pfeiffer. *Multimodal x-ray scatter imaging.* New J. Phys., vol. 11, issue no. 12, art. no. 123016, 2009. (Cited on page 19.)

[Chabior *et al.* 2011] M. Chabior, T. Donath, C. David, O. Bunk, M. Schuster, C. Schroer and F. Pfeiffer. *Beam hardening effects in grating-based x-ray phase-contrast imaging.* Med. Phys., vol. 38, issue no. 3, pages 1189–1195, 2011. (Cited on page 57.)

[Chapman *et al.* 1997] D. Chapman, W. Thomlinson, R. E. Johnston, D. Washburn, E. Pisano, N. Gmür, Z. Zhong, R. Menk, F. Arfelli and D. Sayers. *Diffraction enhanced x-ray imaging.* Phys. Med. Biol., vol. 42, issue no. 11, pages 2015–2025, 1997. (Cited on page 116.)

[Cloetens *et al.* 1996] P. Cloetens, R. Barrett, J. Baruchel, J.-P. Guigay and M. Schlenker. *Phase objects in synchrotron radiation hard x-ray imaging.* J. Phys. D: Appl. Phys., vol. 29, issue no. 1, pages 133–146, 1996. (Cited on page 16.)

[Cloetens *et al.* 1997] P. Cloetens, J. P. Guigay, C. De Martino, J. Baruchel and M. Schlenker. *Fractional Talbot imaging of phase gratings with hard x rays.* Opt. Lett., vol. 22, issue no. 14, pages 1059–1061, 1997. (Cited on pages 21 and 34.)

[Cloetens *et al.* 1999] P. Cloetens, W. Ludwig, J. Baruchel, D. Van Dyck, J. Van Landuyt, J. P. Guigay and M. Schlenker. *Holotomography: Quantitative phase tomography with micrometer resolution using hard synchrotron radiation x rays.* Appl. Phys. Lett., vol. 75, pages 2912–2914, 1999. (Cited on page 16.)

[Cloetens *et al.* 2006] P. Cloetens, R. Mache, M. Schlenker and S. Lerbs-Mache. *Quantitative phase tomography of Arabidopsis seeds reveals intercellular void network.* Proc. Nat. Acad. Sci., vol. 103, issue no. 39, pages 14626–14630, 2006. (Cited on page 16.)

[Cloetens 1999] P. Cloetens. *Contribution to Phase Contrast Imaging, Reconstruction and Tomography with Hard Synchrotron Radiation.* PhD thesis, Vrije Universiteit Brussel, 1999. (Cited on page 31.)

[Cormack 1963] A. M. Cormack. *Representation of a Function by Its Line Integrals, with Some Radiological Applications.* J. Appl. Phys., vol. 34, issue no. 9, pages 2722–2727, 1963. (Cited on page 53.)

[Creath 1988] K. Creath. *V Phase-Measurement Interferometry Techniques.* Progress in Optics, art. no. 349. Elsevier, 1988. (Cited on page 40.)

[David *et al.* 2002] C. David, B. Nöhammer, H. H. Solak and E. Ziegler. *Differential x-ray phase contrast imaging using a shearing interferometer.* Appl. Phys. Lett., vol. 81, pages 3287–3289, 2002. (Cited on pages 17, 51, 86, 108, 116 and 133.)

[David *et al.* 2005] C. David, F. Pfeiffer and T. Weitkamp. *Interferometer for quantitative phase contrast imaging and tomography with an incoherent polychromatic x-ray source.* European patent application no. EP05012121, filed (priority date) 6 June

2005, international publication no. WO2006131235 (A1), published 14 December 2006, 2005. (Cited on page 63.)

[David *et al.* 2007] C. David, J. Bruder, T. Rohbeck, C. Grünzweig, C. Kottler, A. Diaz, O. Bunk and F. Pfeiffer. *Fabrication of diffraction gratings for hard X-ray phase contrast imaging*. Microelectron. Eng., vol. 84, pages 1172–1177, 2007. (Cited on pages 50, 89, 133 and 137.)

[Davis *et al.* 1995] T. J. Davis, D. Gao, T. E. Gureyev, A. W. Stevenson and S. W. Wilkins. *Phase-contrast imaging of weakly absorbing materials using hard X-rays*. Nature, vol. 373, pages 595 – 598, 1995. (Cited on pages 17 and 116.)

[Diaz *et al.* 2010] A. Diaz, C. Mocuta, J. Stangl, M. Keplinger, T. Weitkamp, F. Pfeiffer, C. David, T. H. Metzger and G. Bauer. *Coherence and wavefront characterization of Si-111 monochromators using double-grating interferometry*. J. Synchrotron Rad., vol. 17, issue no. 3, pages 299–307, 2010. (Cited on page 52.)

[Diemoz *et al.* 2011] P. C. Diemoz, P. Coan, I. Zanette, A. Bravin, S. Lang, C. Glaser and T. Weitkamp. *A simplified approach for computed tomography with an X-ray grating interferometer*. Opt. Express, vol. 19, issue no. 3, pages 1691–1698, 2011. (Cited on pages 63 and 64.)

[Dilmanian *et al.* 2000] F. A. Dilmanian, Z. Zhong, B. Ren, X. Y. Wu, L. D. Chapman, I. Orion and W. C. Thomlinson. *Computed tomography of x-ray index of refraction using the diffraction enhanced imaging method*. Phys. Med. Biol., vol. 45, issue no. 4, pages 933–946, 2000. (Cited on page 17.)

[Donath *et al.* 2009] T. Donath, M. Chabior, F. Pfeiffer, O. Bunk, E. Reznikova, J. Mohr, E. Hempel, S. Popescu, M. Hoheisel, M. Schuster, J. Baumann and C. David. *Inverse geometry for grating-based x-ray phase-contrast imaging*. J. Appl. Phys., vol. 106, issue no. 5, art. no. 054703, 2009. (Cited on pages 62 and 136.)

[Donath *et al.* 2010] T. Donath, F. Pfeiffer, O. Bunk, C. Grünzweig, E. Hempel, S. Popescu, P. Vock and C. David. *Toward Clinical X-ray Phase-Contrast CT: Demonstration of Enhanced Soft-Tissue Contrast in Human Specimen*. Invest. Radiol., vol. 45, issue no. 7, pages 445–452, 2010. (Cited on pages 34 and 63.)

[Engel *et al.* 2011] K. J. Engel, D. Geller, T. Köhler, G. Martens, S. Schusser, G. Vogtmeier and E. Rössl. *Contrast-to-noise in X-ray differential phase contrast imaging*. Nucl. Instrum. Meth. A, vol. 648, Supplement 1, pages S202 – S207, 2011. (Cited on page 46.)

[Engelhardt *et al.* 2007a] M. Engelhardt, J. Baumann, M. Schuster, C. Kottler, F. Pfeiffer, O. Bunk and C. David. *High-resolution differential phase contrast imaging using a magnifying projection geometry with a microfocus x-ray source*. Appl. Phys. Lett., vol. 90, art. no. 224101, 2007. (Cited on page 64.)

[Engelhardt *et al.* 2007b] M. Engelhardt, J. Baumann, M. Schuster, C. Kottler, F. Pfeiffer, O. Bunk and C. David. *Inspection of refractive x-ray lenses using high-resolution differential phase contrast imaging with a microfocus x-ray source*. Rev. Sci. Instrum., vol. 78, issue no. 9, art. no. 093707, 2007. (Cited on page 141.)

[Engelhardt *et al.* 2008] M. Engelhardt, C. Kottler, O. Bunk, C. David, C. Schroer, J. Baumann, M. Schuster and F. Pfeiffer. *The fractional Talbot effect in differential x-ray phase-contrast imaging for extended and polychromatic x-ray sources*. J. Microsc., vol. 232, issue no. 1, pages 145–157, 2008. (Cited on page 34.)

[Espeso *et al.* 1998] J. I. Espeso, P. Cloetens, J. Baruchel, J. Härtwig, T. Mairs, J. C. Biasci, G. Marot, M. Salomé-Pateyron and M. Schlenker. *Conserving the Coherence and Uniformity of Third-Generation Synchrotron Radiation Beams: the Case of ID19, a 'Long' Beamline at the ESRF*. J. Synchrotron Rad., vol. 5, pages 1243–1249, 1998. (Cited on page 72.)

[Fitzgerald 2000] R. Fitzgerald. *Phase-Sensitive X-Ray Imaging*. Phys. Today, vol. 53, issue no. 7, pages 23–27, 2000. (Cited on pages 86, 108 and 115.)

[Förster *et al.* 1980] E. Förster, K. Goetz and P. Zaumseil. *Double crystal diffractometry for the characterization of targets for laser fusion experiments*. Krist. Tech., vol. 15, pages 937–945, 1980. (Cited on pages 17 and 115.)

[Frankot & Chellappa 1988] R. T. Frankot and R. Chellappa. *A Method for enforcing integrability in shape from shading algorithms*. IEEE Transactions on Pattern Analysis and Machine Intelligence, vol. 10, pages 439–451, 1988. (Cited on pages 138 and 143.)

[Ghiglia & Pritt 1998] D. C. Ghiglia and M. D. Pritt. Two-dimensional phase unwrapping: theory, algorithms, and software. John Wiley & Sons Inc., New York, 1998. (Cited on pages 15, 44, 91 and 145.)

[Grodzins 1983] L. Grodzins. *Optimum energies for x-ray transmission tomography of small samples: Applications of synchrotron radiation to computerized tomography I*. Nucl. Instrum. Methods, vol. 206, issue no. 3, pages 541 – 545, 1983. (Cited on page 98.)

[Guigay 1971] J. P. Guigay. *On Fresnel Diffraction by One-dimensional Periodic Objects, with Application to Structure Determination of Phase Objects*. Opt. Acta, vol. 18, pages 677–682, 1971. (Cited on page 25.)

[Hack & Burke 2011] E. Hack and J. Burke. *Measurement uncertainty of linear phase-stepping algorithms*. Rev. Sci. Instrum., vol. 82, art. no. 061101, 2011. (Cited on page 46.)

[Herzen *et al.* 2009] J. Herzen, T. Donath, F. Pfeiffer, O. Bunk, C. Padeste, F. Beckmann, A. Schreyer and C. David. *Quantitative phase-contrast tomography of a liquid phantom using a conventional x-ray tube source*. Opt. Express, vol. 17, issue no. 12, pages 10010–10018, 2009. (Cited on pages 57, 63, 86, 94 and 95.)

[Herzen *et al.* 2010] J. Herzen, F. Beckmann, T. Donath, M. Ogurreck, C. David, F. Pfeiffer, J. Mohr, E. Reznikova, S. Riekehr, A. Haibel, G. Schulz, B. Muller and A. Schreyer. *X-ray grating interferometer for imaging at a second-generation synchrotron radiation source*. Proc. SPIE, vol. 7804, issue no. 1, art. no. 780407, 2010. (Cited on page 63.)

[Hirano & Momose 1999] K. Hirano and A. Momose. *Development of an X-Ray Interferometer for High-Resolution Phase-Contrast X-Ray Imaging*. Jpn. J. Appl. Phys., vol. 38, issue no. 12B, pages L1556–L1558, 1999. (Cited on page 16.)

[Hounsfield 1973] G. N. Hounsfield. *Computerized transverse axial scanning (tomography): Part 1. Description of system*. Br. J. Radiol., vol. 46, issue no. 552, pages 1016–1022, 1973. (Cited on page 53.)

[Hsieh 2003] J. Hsieh. Computed tomography: principles, design, artifacts, and recent advances, volume 114. SPIE Press, Bellingham, WA, 2003. (Cited on page 53.)

[Ingal & Beliaevskaya 1995] V. N. Ingal and E. A. Beliaevskaya. *X-ray plane-wave topography observation of the phase contrast from a non-crystalline object*. J. Phy. D: Appl. Phys., vol. 28, issue no. 11, pages 2314–2317, 1995. (Cited on page 17.)

[Itoh *et al.* 2011] H. Itoh, K. Nagai, G. Sato, K. Yamaguchi, T. Nakamura, T. Kondoh, C. Ouchi, T. Teshima, Y. Setomoto and T. Den. *Two-dimensional grating-based X-ray phase-contrast imaging using Fourier transform phase retrieval*. Opt. Express, vol. 19, issue no. 4, pages 3339–3346, 2011. (Cited on page 146.)

[Jensen *et al.* 2010a] T. H. Jensen, M. Bech, O. Bunk, T. Donath, C. David, R. Feidenhans'l and F. Pfeiffer. *Directional x-ray dark-field imaging*. Phys. Med. Biol., vol. 55, issue no. 12, pages 3317–3323, 2010. (Cited on pages 66, 131 and 154.)

[Jensen *et al.* 2010b] T. H. Jensen, M. Bech, I. Zanette, T. Weitkamp, C. David, H. Deyhle, S. Rutishauser, E. Reznikova, J. Mohr, R. Feidenhans'l and F. Pfeiffer. *Directional x-ray dark-field imaging of strongly ordered systems*. Phys. Rev. B, vol. 82, issue no. 21, art. no. 214103, 2010. (Cited on pages 66, 67, 131, 151 and 154.)

[Kak & Slaney 1987] A. C. Kak and M. Slaney. Principles of Computerized Tomography. IEEE Press, London, 1987. Also available online at `http://www.slaney.org/pct`. (Cited on pages 53 and 56.)

[Kenntner *et al.* 2010] J. Kenntner, T. Grund, B. Matthis, M. Boerner, J. Mohr, T. Scherer, M. Walter, M. Willner, A. Tapfer, M. Bech, F. Pfeiffer, I. Zanette and T. Weitkamp. *Front- and backside structuring of gratings for phase contrast imaging with x-ray tubes*. Proc. SPIE, vol. 7804, issue no. 1, art. no. 780408, 2010. (Cited on page 49.)

[Knoll 1979] G.F. Knoll. Radiation detection and measurement. John Wiley & Sons Inc., New York, 1979. (Cited on page 74.)

[Koch *et al.* 1998] A. Koch, C. Raven, P. Spanne and A. Snigirev. *X-ray imaging with submicrometer resolution employing transparent luminescent screens.* J. Opt. Soc. Am. A, vol. 15, pages 1940–1951, 1998. (Cited on page 73.)

[Kottler *et al.* 2007] C. Kottler, C. David, F. Pfeiffer and O. Bunk. *A two-directional approach for grating-based differential phase contrast-imaging using hard x-rays.* Opt. Express, vol. 15, issue no. 3, pages 1175–1181, 2007. (Cited on page 131.)

[Labiche *et al.* 1996] J.-C. Labiche, J. Segura Puchades, D. van Brussel and J. Moy. ESRF Newsletter, vol. 25, pages 41–43, 1996. (Cited on page 74.)

[Labiche *et al.* 2007] J.-C. Labiche, O. Mathon, S. Pascarelli, M. A. Newton, G. Guilera Ferre, C. Curfs, G. Vaughan, A. Homs and D. Fernandez Carreiras. *The fast readout low noise camera as a versatile x-ray detector for time resolved dispersive extended x-ray absorption fine structure and diffraction studies of dynamic problems in materials science, chemistry, and catalysis.* Rev. Sci. Instrum., vol. 78, art. no. 091301, 2007. (Cited on pages 74 and 137.)

[Lak *et al.* 2008] M. Lak, D. Néraudeau, A. Nel, P. Cloetens, V. Perrichot and P. Tafforeau. *Phase contrast X-ray synchrotron imaging: opening access to fossil inclusions in opaque amber.* Microsc. microanal., vol. 14, issue no. 3, pages 251–259, 2008. (Cited on page 123.)

[Langer 2008] M. Langer. *Phase Retrieval in the Fresnel Region for Hard X-ray Tomography.* PhD thesis, L'Institut National des Sciences Appliquées de Lyon, 2008. (Cited on page 17.)

[Lau 1948] E. Lau. Ann. Phys. (Leipzig), vol. 6, art. no. 417, 1948. (Cited on page 62.)

[Lengeler *et al.* 1999] B. Lengeler, C. Schroer, J. Tümmler, B. Benner, M. Richwin, A. Snigirev, I. Snigireva and M. Drakopoulos. *Imaging by parabolic refractive lenses in the hard X-ray range.* J. Synchrotron Rad., vol. 6, pages 1153–1167, 1999. (Cited on pages 141 and 143.)

[Lengeler *et al.* 2002] B. Lengeler, C. G. Schroer, B. Benner, A. Gerhardus, T. F. Günzler, M. Kuhlmann, J. Meyer and C. Zimprich. *Parabolic refractive X-ray lenses.* J. Synchrotron Rad., vol. 9, issue no. 3, pages 119–124, 2002. (Cited on page 141.)

[Lynch *et al.* 2011] S. K. Lynch, V. Pai, J. Auxier, A. F. Stein, E. E. Bennett, C. K. Kemble, X. Xiao, W.-K. Lee, N. Y. Morgan and H. H. Wen. *Interpretation of dark-field contrast and particle-size selectivity in grating interferometers.* Appl. Opt., vol. 50, issue no. 22, pages 4310–4319, 2011. (Cited on pages 45 and 57.)

[McDonald *et al.* 2009] S. A. McDonald, F. Marone, C. Hintermüller, G. Mikuljan, C. David, F. Pfeiffer and M. Stampanoni. *Advanced phase-contrast imaging using a grating interferometer.* J. Synchrotron Rad., vol. 16, issue no. 4, pages 562–572, 2009. (Cited on pages 61, 97 and 116.)

[Modregger *et al.* 2011] P. Modregger, B. R. Pinzer, T. Thüring, S. Rutishauser, C. David and M. Stampanoni. *Sensitivity of X-ray grating interferometry.* Opt. Express, vol. 19, issue no. 19, pages 18324–18338, 2011. (Cited on page 48.)

[Momose & Kawamoto 2006] A. Momose and S. Kawamoto. *X-ray Talbot Interferometry with Capillary Plates.* Jpn. J. Appl. Phys., vol. 45, pages 314–316, 2006. (Cited on page 133.)

[Momose *et al.* 1996] A. Momose, T. Takeda, Y. Itai and K. Hirano. *Phase-contrast X-ray computed tomography for observing biological soft tissues.* Nature Medicine, vol. 2, 1996. (Cited on page 15.)

[Momose *et al.* 2000] A. Momose, T. Takeda and Y. Itai. *Blood Vessels: Depiction at Phase-Contrast X-ray Imaging without Contrast Agents in the Mouse and Rat - Feasibility Study.* Radiology, vol. 217, issue no. 2, pages 593–596, 2000. (Cited on page 15.)

[Momose *et al.* 2003] A. Momose, S. Kawamoto, I. Koyama, Y. Hamaishi, K. Takai and Y. Suzuki. *Demonstration of X-Ray Talbot Interferometry.* Jpn. J. Appl. Phys., vol. 42, pages L866–L868, 2003. (Cited on pages 17, 18, 24, 25, 51, 86, 108, 109, 116 and 133.)

[Momose *et al.* 2009a] A. Momose, W. Yashiro, H. Kuwabara and K. Kawabata. *Grating-Based X-ray Phase Imaging Using Multiline X-ray Source.* Jpn. J. Appl. Phys., vol. 48, issue no. 7, art. no. 076512, 2009. (Cited on page 63.)

[Momose *et al.* 2009b] A. Momose, W. Yashiro, H. Maikusa and Y. Takeda. *High-speed X-ray phase imaging and X-ray phase tomography with Talbot interferometer and white synchrotron radiation.* Opt. Express, vol. 17, issue no. 15, pages 12540–12545, 2009. (Cited on pages 18, 52 and 113.)

[Momose *et al.* 2009c] A. Momose, W. Yashiro and Y. Takeda. *X-Ray Phase Imaging with Talbot Interferometry.* Biomedical Mathematics Promising Directions in Imaging Therapy Planning and Inverse Problems, art. no. 281, 2009. (Cited on pages 12 and 46.)

[Momose *et al.* 2011a] A. Momose, H. Kuwabara and W. Yashiro. *X-ray Phase Imaging Using Lau Effect.* Appl. Phys. Expr., vol. 4, issue no. 6, art. no. 066603, 2011. (Cited on page 63.)

[Momose *et al.* 2011b] A. Momose, W. Yashiro, S. Harasse and H. Kuwabara. *Four-dimensional X-ray phase tomography with Talbot interferometry and white synchrotron radiation: dynamic observation of a living worm.* Opt. Express, vol. 19, issue no. 9, pages 8423–8432, 2011. (Cited on pages 52, 117 and 155.)

[Momose 2003] A. Momose. *Phase-sensitive imaging and phase tomography using X-ray interferometers.* Opt. Express, vol. 11, issue no. 19, pages 2303–2314, 2003. (Cited on pages 15 and 16.)

[Momose 2005] A. Momose. *Recent Advances in X-ray Phase Imaging.* Jpn. J. Appl. Phys., vol. 44, pages 6355–6367, 2005. (Cited on pages 86, 108 and 109.)

[Natterer 1986] F. Natterer. The mathematics of computerized tomography. John Wiley & Sons Inc., New York, 1986. (Cited on page 53.)

[Nesterets 2008] Ya.I. Nesterets. *On the origins of decoherence and extinction contrast in phase-contrast imaging.* Opt. Commun, vol. 281, issue no. 4, pages 533 – 542, 2008. (Cited on page 19.)

[Noël *et al.* 2011] P. B. Noël, J. Herzen, A. Fingerle, M. K. Stockmar, D. Hahn, M. Willner, M. Settles, E. Drecoll, I. Zanette, T. Weitkamp, E. J. Rummeny and F. Pfeiffer. *Phase-Contrast Computed Tomography for Improved Diagnostics of Liver Cancer.* 2011. Submitted. (Cited on page 98.)

[Nugent *et al.* 1996] K. A. Nugent, T. E. Gureyev, D. F. Cookson, D. Paganin and Z. Barnea. *Quantitative Phase Imaging Using Hard X Rays.* Phys. Rev. Lett., vol. 77, pages 2961–2964, 1996. (Cited on page 16.)

[Olivo & Speller 2007] A. Olivo and R. Speller. *A coded-aperture technique allowing x-ray phase contrast imaging with conventional sources.* Appl. Phys. Lett., vol. 91, issue no. 7, art. no. 074106, 2007. (Cited on page 65.)

[Olivo *et al.* 2009] A. Olivo, S. E. Bohndiek, J. A. Griffiths, A. Konstantinidis and R. D. Speller. *A non-free-space propagation x-ray phase contrast imaging method sensitive to phase effects in two directions simultaneously.* Appl. Phys. Lett., vol. 94, art. no. 044108, 2009. (Cited on pages 65 and 133.)

[Paganin *et al.* 2002] D. Paganin, S. C. Mayo, T. E. Gureyev, P. R. Miller and S. W. Wilkins. *Simultaneous phase and amplitude extraction from a single defocused image of a homogeneous object.* J. Microsc., vol. 206, pages 33–40, 2002. (Cited on page 16.)

[Paganin 2006] D. M. Paganin. Coherent X-ray Optics. Oxford University Press, England, 2006. (Cited on pages 8, 11 and 30.)

[Pagot *et al.* 2003] E. Pagot, P. Cloetens, S. Fiedler, A. Bravin, P. Coan, J. Baruchel, J. Härtwig and W. Thomlinson. *A method to extract quantitative information in analyzer-based x-ray phase contrast imaging.* Appl. Phys. Lett., vol. 82, issue no. 20, pages 3421–3423, 2003. (Cited on pages 17 and 19.)

[Patorski & Kujawinska 1993] K. Patorski and M. Kujawinska. Handbook of the moiré fringe technique. Elsevier, 1993. (Cited on pages 161 and 162.)

[Perrichot *et al.* 2011] V. Perrichot, J. Ortega-Blanco, R.C. McKellar, X. Delclòs, D. Azar, A. Nel, P. Tafforeau, M.S. Engel, V. Perrichot and J. Ortega-Blanco. *New and revised maimetshid wasps from Cretaceous ambers (Hymenoptera, Maimetshidae).* ZooKeys, vol. 130, pages 421–453, 2011. (Cited on page 123.)

[Pfeiffer *et al.* 2005] F. Pfeiffer, O. Bunk, C. Schulze-Briese, A. Diaz, T. Weitkamp, C. David, J. F. van der Veen, I. Vartanyants and I. K. Robinson. *Shearing Interferometer for Quantifying the Coherence of Hard X-Ray Beams*. Phys. Rev. Lett., vol. 94, issue no. 16, art. no. 164801, 2005. (Cited on page 52.)

[Pfeiffer *et al.* 2006] F. Pfeiffer, T. Weitkamp, O. Bunk and C. David. *Phase retrieval and differential phase-contrast imaging with low-brilliance X-ray sources*. Nature Physics, vol. 2, pages 258–261, 2006. (Cited on pages 34, 62, 86, 109 and 116.)

[Pfeiffer *et al.* 2007a] F Pfeiffer, O Bunk, C David, M Bech, G Le Duc, A Bravin and P Cloetens. *High-resolution brain tumor visualization using three-dimensional x-ray phase contrast tomography*. Phys. Med. Biol., vol. 52, issue no. 23, pages 6923–6930, 2007. (Cited on pages 88, 94 and 97.)

[Pfeiffer *et al.* 2007b] F. Pfeiffer, C. Kottler, O. Bunk and C. David. *Hard X-Ray Phase Tomography with Low-Brilliance Sources*. Phys. Rev. Lett., vol. 98, art. no. 108105, 2007. (Cited on pages 55, 56, 57, 109, 112, 119, 127 and 128.)

[Pfeiffer *et al.* 2008a] F. Pfeiffer, M. Bech, O. Bunk, P. Kraft, E. F. Eikenberry, C. Brönnimann, C. Grünzweig and C. David. *Hard-X-ray dark-field imaging using a grating interferometer*. Nat. Mater., vol. 7, pages 134–137, 2008. (Cited on pages 19, 44, 116, 119, 128, 133 and 136.)

[Pfeiffer *et al.* 2008b] F. Pfeiffer, C. David, O. Bunk, T. Donath, M. Bech, G. Le Duc, A. Bravin and P. Cloetens. *Region-of-Interest Tomography for Grating-Based X-Ray Differential Phase-Contrast Imaging*. Phys. Rev. Lett., vol. 101, issue no. 16, art. no. 168101, 2008. (Cited on page 111.)

[Rack *et al.* 2010] A. Rack, T. Weitkamp, M. Riotte, D. Grigoriev, T. Rack, L. Helfen, T. Baumbach, R. Dietsch, T. Holz, M. Krämer, F. Siewert, M. Meduňa, P. Cloetens and E. Ziegler. *Comparative study of multilayers used in monochromators for synchrotron-based coherent hard X-ray imaging*. J. Synchrotron Rad., vol. 17, issue no. 4, pages 496–510, 2010. (Cited on page 34.)

[Rack *et al.* 2011] A. Rack, T. Weitkamp, I. Zanette, Ch. Morawe, A. Vivo Rommeveaux, P. Tafforeau, P. Cloetens, E. Ziegler, T. Rack, A. Cecilia, P. Vagovic, E. Harmann, R. Dietsch and H. Riesemeier. *Coherence preservation and beam flatness of a single-bounce multilayer monochromator (beamline ID19–ESRF)*. Nucl. Instrum. Meth. A, vol. 649, issue no. 1, pages 123 – 127, 2011. (Cited on page 34.)

[Ramm & Katsevich 1996] A. G. Ramm and A. I. Katsevich. The Radon Transform and Local Tomography. CRC Press, Boca Raton, 1996. (Cited on page 109.)

[Raoux 1983] D. Raoux. Neutron and synchrotron radiation for condensed matter studies, volume 1. EDP Sciences - Springer - Verlag, 1983. (Cited on pages 69 and 70.)

[Raupach & Flohr 2011] R. Raupach and T. G Flohr. *Analytical evaluation of the signal and noise propagation in x-ray differential phase-contrast computed tomography.* Phys. Med. Biol., vol. 56, issue no. 7, pages 2219–2244, 2011. (Cited on page 46.)

[Rayleigh 1881] L. Rayleigh. *On copying diffraction gratings, and some phenomena connected therewidth.* Phil. Mag., vol. 11, pages 196–205, 1881. (Cited on page 21.)

[Revol *et al.* 2010] V. Revol, C. Kottler, R. Kaufmann, U. Straumann and C. Urban. *Noise analysis of grating-based x-ray differential phase contrast imaging.* Rev. Sci. Instrum., vol. 81, issue no. 7, art. no. 073709, 2010. (Cited on page 46.)

[Revol *et al.* 2011] V. Revol, C. Kottler, R. Kaufmann, I. Jerjen, T. Lüthi, F. Cardot, P. Niedermann, U. Straumann, U. Sennhauser and C. Urban. *X-ray interferometer with bent gratings: Towards larger fields of view.* Nucl. Instrum. Meth. A, vol. 648, Supplement 1, issue no. 0, pages S302 – S305, 2011. (Cited on page 63.)

[Reznikova *et al.* 2008] E. Reznikova, J. Mohr, M. Börner, V. Nazmov and P. J. Jakobs. *Soft X-ray lithography of high aspect ratio SU8 submicron structures.* Microsyst. Technol., vol. 14, pages 1683–1688, 2008. (Cited on pages 49, 89, 133 and 137.)

[Rizzi *et al.* 2011] J. Rizzi, T. Weitkamp, N. Guérineau, M. Idir, P. Mercère, G. Druart, G. Vincent, P. da Silva and J. Primot. *Quadriwave lateral shearing interferometry in an achromatic and continuously self-imaging regime for future x-ray phase imaging.* Opt. Lett., vol. 36, issue no. 8, pages 1398–1400, 2011. (Cited on pages 34 and 116.)

[Rutishauser *et al.* 2011a] S. Rutishauser, I. Zanette, T. Donath A. Sahlholm, J. Linnros and C. David. *Structured scintillator for hard x-ray grating interferometry.* Appl. Phys. Lett., vol. 98, art. no. 171107, 2011. (Cited on pages 65, 66 and 151.)

[Rutishauser *et al.* 2011b] S. Rutishauser, I. Zanette, T. Wetikamp, T. Donath and C. David. *At-wavelength characterization of refractive X-ray lenses using a two-dimensional grating interferometer.* Appl. Phys. Lett., vol. 99, issue no. 22, art. no. 221104, 2011. (Cited on pages 143, 144, 145 and 154.)

[Sanchez del Rio & Dejus 2004] Manuel Sanchez del Rio and Roger J. Dejus. *Status of XOP: an X-ray optics software toolkit.* Proc. SPIE, vol. 5536, issue no. 1, pages 171–174, 2004. (Cited on pages 13 and 89.)

[Sato *et al.* 2011] G. Sato, T. Kondoh, H. Itoh, S. Handa, K. Yamaguchi, T. Nakamura, K. Nagai, C. Ouchi, T. Teshima, Y. Setomoto and T. Den. *Two-dimensional gratings-based phase-contrast imaging using a conventional x-ray tube.* Opt. Lett., vol. 36, issue no. 18, pages 3551–3553, 2011. (Cited on page 146.)

[Schulz *et al.* 2010a] G. Schulz, A. Morel, M. S. Imholz, H. Deyhle, T. Weitkamp, I. Zanette, F. Pfeiffer, C. David, M. Müller-Gerbl and B. Müller. *Evaluating the microstructure of human brain tissues using synchrotron radiation-based micro-computed tomography.* Proc. SPIE, vol. 7804, issue no. 1, art. no. 78040F, 2010. (Cited on page 98.)

[Schulz *et al.* 2010b] G. Schulz, T. Weitkamp, I. Zanette, F. Pfeiffer, F. Beckmann, C. David, S. Rutishauser, R. Reznikova and B. Müller. *High-resolution tomographic imaging of a human cerebellum: comparison of absorption and grating-based phase contrast.* J. R. Soc. Interface, vol. 7, issue no. 53, pages 1665–1676, 2010. (Cited on pages 94, 97, 98, 99, 100 and 116.)

[Smith 2003] G. Smith. *The optical properties of the crystalline lens and their significance.* Clinical and Experimental Optometry, vol. 86, pages 3–18, 2003. (Cited on page 123.)

[Snigirev *et al.* 1995] A. Snigirev, I. Snigireva, V. Kohn, S. Kuznetsov and I. Schelokov. *On the possibilities of x-ray phase contrast microimaging by coherent high-energy synchrotron radiation.* Rev. Sci. Instrum., vol. 66, pages 5486–5492, 1995. (Cited on page 16.)

[Stampanoni *et al.* 2011] M. Stampanoni, Z. Wang, T. Thüring, C. David, E. Roessl, M. Trippel, R. Kubik-Huch, G Singer, M. Hohl and N Hauser. *The First Analysis and Clinical Evaluation of Native Breast Tissue Using Differential Phase-Contrast Mammography.* Invest. Radiol., vol. 46, pages 801–806, 2011. (Cited on page 63.)

[Stetson & Brohinsky 1985] K. A. Stetson and W. R. Brohinsky. *Electrooptic holography and its application to hologram interferometry.* Appl. Opt., vol. 24, issue no. 21, pages 3631–3637, 1985. (Cited on page 46.)

[Suleski 1997] Thomas J. Suleski. *Generation of Lohmann images from binary-phase Talbot array illuminators.* Appl. Opt., vol. 36, issue no. 20, pages 4686–4691, 1997. (Cited on page 27.)

[Swank 1973] Robert K. Swank. *Calculation of Modulation Transfer Functions of X-Ray Fluorescent Screens.* Appl. Opt., vol. 12, issue no. 8, pages 1865–1870, 1973. (Cited on page 74.)

[Tafforeau *et al.* 2006] P. Tafforeau, R. Boistel, E. Boller, A. Bravin, M. Brunet, Y. Chaimanee, P. Cloetens, M. Feist, J. Hoszowska, J.J. Jaeger*et al.* *Applications of X-ray synchrotron microtomography for non-destructive 3D studies of paleontological specimens.* Appl. Phys. A, vol. 83, issue no. 2, pages 195–202, 2006. (Cited on page 123.)

[Takeda *et al.* 1982] M. Takeda, H. Ina and S. Kobayashi. *Fourier-transform method of fringe-pattern analysis for computer-based topography and interferometry.* J. Opt. Soc. Am., vol. 72, issue no. 1, pages 156–160, 1982. (Cited on pages 51, 65 and 146.)

[Takeda *et al.* 2008] Y. Takeda, W. Yashiro, T. Hattori, A. Takeuchi, Y. Suzuki and A. Momose. *Differential Phase X-ray Imaging Microscopy with X-ray Talbot Interferometer.* Appl. Phys. Expr., vol. 1, issue no. 11, art. no. 117002, 2008. (Cited on page 64.)

[Talbot 1836] H. F. Talbot. *Facts related to optical science.* Phil. Mag., vol. 9, pages 401–407, 1836. (Cited on pages 18 and 21.)

[Vaughan *et al.* 2011] G. B. M. Vaughan, J. P. Wright, A. Bytchkov, M. Rossat, H. Gleyzolle, I. Snigireva and A. Snigirev. *X-ray transfocators: focusing devices based on compound refractive lenses.* J. Synchrotron Rad., vol. 18, issue no. 2, pages 125–133, 2011. (Cited on page 141.)

[Wang *et al.* 2009] Z. T. Wang, K. J. Kang, Z. F. Huang and Z. Q. Chen. *Quantitative grating-based x-ray dark-field computed tomography.* Appl. Phys. Lett., vol. 95, issue no. 9, art. no. 094105, 2009. (Cited on pages 45 and 57.)

[Wang *et al.* 2011] H. Wang, K. Sawhney, S. Berujon, E. Ziegler, S. Rutishauser and C. David. *X-ray wavefront characterization using a rotating shearing interferometer technique.* Opt. Express, vol. 19, issue no. 17, pages 16550–16559, 2011. (Cited on page 161.)

[Wang 2007] Y. Wang. *Intuitive dimensional analyses of the energy and atomic number dependences of the cross sections for radiation interaction with matter.* J. X-Ray Sci. Technol., vol. 15, pages 169–175, 2007. (Cited on page 12.)

[Weitkamp *et al.* 2004] T. Weitkamp, A. Diaz, B. Nöhammer, F. Pfeiffer, M. Stampanoni, E. Ziegler and C. David. *Moiré interferometry formulas for hard X-ray wavefront sensing.* Proc. SPIE, vol. 5533, pages 140–144, 2004. (Cited on page 161.)

[Weitkamp *et al.* 2005a] T. Weitkamp, A. Diaz, C. David, F. Pfeiffer, M. Stampanoni, P. Cloetens and E. Ziegler. *X-ray phase imaging with a grating interferometer.* Opt. Express, vol. 13, pages 6296–6304, 2005. (Cited on pages 18, 87, 88, 108, 109, 116, 127, 133, 134, 135, 136 and 139.)

[Weitkamp *et al.* 2005b] T. Weitkamp, B. Nohammer, A. Diaz, C. David and E. Ziegler. *X-ray wavefront analysis and optics characterization with a grating interferometer.* Appl. Phys. Lett., vol. 86, issue no. 5, art. no. 054101, 2005. (Cited on pages 52, 133 and 139.)

[Weitkamp *et al.* 2006] T. Weitkamp, C. David, C. Kottler, O. Bunk and F. Pfeiffer. *Tomography with grating interferometers at low-brilliance sources.* Proc. SPIE, vol. 6318, issue no. 1, art. no. 63180S, 2006. (Cited on pages 28, 29 and 33.)

[Weitkamp *et al.* 2010a] T. Weitkamp, P. Tafforeau, E. Boller, P. Cloetens, J.-P. Valade, P. Bernard, F. Peyrin, W. Ludwig, L. Helfen and J. Baruchel. *Status and evolution of the ESRF beamline ID19.* AIP Conf. Proc., vol. 1221, issue no. 1, pages 33–38, 2010. (Cited on pages 72, 86, 89 and 136.)

[Weitkamp *et al.* 2010b] T. Weitkamp, I. Zanette, C. David, J. Baruchel, M. Bech, P. Bernard, H. Deyhle, T. Donath, J. Kenntner, S. Lang, J. Mohr, B. Muller, F. Pfeiffer, E. Reznikova, S. Rutishauser, G. Schulz, A. Tapfer and J.-P. Valade. *Recent developments in x-ray Talbot interferometry at ESRF-ID19.* Proc. SPIE, vol. 7804, issue no. 1, art. no. 780406, 2010. (Cited on pages 86, 89 and 121.)

[Weitkamp *et al.* 2011] T. Weitkamp, D. Haas, D. Wegrzynek and A. Rack. *ANKAphase: software for single-distance phase retrieval from inline X-ray phase-contrast radiographs.* J. Synchrotron Rad., vol. 18, issue no. 4, pages 617–629, 2011. (Cited on page 16.)

[Weitkamp 2002] T. Weitkamp. *Imaging and Tomography with High Resolution Using Coherent Hard Synchrotron Radiation.* PhD thesis, Universität Hamburg, Göttingen, 2002. (Cited on pages 23 and 100.)

[Wen *et al.* 2009] H. Wen, E. E. Bennett, M. M. Hegedus and S. Rapacchi. *Fourier X-ray Scattering Radiography Yields Bone Structural Information.* Radiology, vol. 251, issue no. 3, pages 910–918, June 2009. (Cited on pages 64 and 117.)

[Wen *et al.* 2010] H. H. Wen, E. E. Bennett, R. Kopace, A. F. Stein and V. Pai. *Single-shot x-ray differential phase-contrast and diffraction imaging using two-dimensional transmission gratings.* Opt. Lett., vol. 35, issue no. 12, pages 1932–1934, 2010. (Cited on pages 64, 133 and 139.)

[Wilkins *et al.* 1996] S. W. Wilkins, T. E. Gureyev, D. Gao, A. Pogany and A. W. Stevenson. *Phase-contrast imaging using polychromatic hard X-rays.* Nature, vol. 384, pages 335–337, 1996. (Cited on page 16.)

[Yashiro *et al.* 2008] W. Yashiro, Y. Takeda and A. Momose. *Efficiency of capturing a phase image using cone-beam x-ray Talbot interferometry.* J. Opt. Soc. Am. A, vol. 25, issue no. 8, pages 2025–2039, 2008. (Cited on page 46.)

[Yashiro *et al.* 2009] W. Yashiro, Y. Takeda, A. Takeuchi, Y. Suzuki and A. Momose. *Hard-X-Ray Phase-Difference Microscopy Using a Fresnel Zone Plate and a Transmission Grating.* Phys. Rev. Lett., vol. 103, issue no. 18, art. no. 180801, 2009. (Cited on page 64.)

[Yashiro *et al.* 2010a] W. Yashiro, S. Harasse, A. Takeuchi, Y. Suzuki and A. Momose. *Hard-x-ray phase-imaging microscopy using the self-imaging phenomenon of a transmission grating.* Phys. Rev. A, vol. 82, issue no. 4, art. no. 043822, 2010. (Cited on page 64.)

[Yashiro *et al.* 2010b] W. Yashiro, Y. Terui, K. Kawabata and A. Momose. *On the origin of visibility contrast in x-ray Talbot interferometry.* Opt. Express, vol. 18, issue no. 16, pages 16890–16901, 2010. (Cited on page 45.)

[Yashiro *et al.* 2011] W. Yashiro, S. Harasse, K. Kawabata, H. Kuwabara, T. Yamazaki and A. Momose. *Distribution of unresolvable anisotropic microstructures revealed in visibility-contrast images using x-ray Talbot interferometry.* Phys. Rev. B, vol. 84, art. no. 094106, 2011. (Cited on page 125.)

[Zambelli *et al.* 2010] J. Zambelli, N. Bevins, Z. Qi and G.-H. Chen. *Radiation dose efficiency comparison between differential phase contrast CT and conventional absorption CT.* Med. Phys., vol. 37, issue no. 6, pages 2473–2479, 2010. (Cited on page 86.)

[Zanette *et al.* 2010a] I. Zanette, C. David, S. Rutishauser and T. Weitkamp. *2D grating simulation for X-ray phase-contrast and dark-field imaging with a Talbot interferometer*. AIP Conf. Proc., vol. 1221, pages 73–79, 2010. (Cited on pages 30, 77, 134, 153 and 165.)

[Zanette *et al.* 2010b] I. Zanette, T. Weitkamp, T. Donath, S. Rutishauser and C. David. *Two-Dimensional X-Ray Grating Interferometer*. Phys. Rev. Lett., vol. 105, issue no. 24, art. no. 248102, 2010. (Cited on pages 77, 132, 140, 143 and 153.)

[Zanette *et al.* 2011a] I. Zanette, M. Bech, F. Pfeiffer and T. Weitkamp. *Interlaced phase stepping in phase-contrast x-ray tomography*. Appl. Phys. Lett., vol. 98, issue no. 9, art. no. 094101, 2011. (Cited on pages 108, 116, 117, 118, 120 and 153.)

[Zanette *et al.* 2011b] I. Zanette, M. Bech, A. Rack, G. Le Duc, P. Tafforeau, C. David, J. Mohr, F. Pfeiffer and T. Weitkamp. *Trimodal low-dose X-ray tomography*. 2011. Submitted. (Cited on pages 108 and 153.)

[Zanette *et al.* 2011c] I. Zanette, S. Rutishauser, C. David and T. Weitkamp. *X-ray Interferometry with Two-Dimensional Gratings*. AIP Conf. Proc., vol. 1365, issue no. 1, pages 325–328, 2011. (Cited on page 77.)

[Zanette *et al.* 2011d] I. Zanette, T. Weitkamp, S. Lang, M. Langer, J. Mohr, C. David and J. Baruchel. *Quantitative phase and absorption tomography with an X-ray grating interferometer and synchrotron radiation*. Physica Status Solidi (A), vol. 208, issue no. 11, pages 2526–2532, 2011. (Cited on pages 57, 85, 152 and 154.)

[Zhu *et al.* 2010] P. Zhu, K. Zhang, Z. Wang, Y. Liu, X. Liu, Z. Wu, S. A. McDonald, F. Marone and M. Stampanoni. *Low-dose, simple, and fast grating-based X-ray phase-contrast imaging*. Proc. Nat. Acad. Sci., vol. 107, issue no. 31, art. no. 13576, 2010. (Cited on pages 63, 64, 113 and 117.)

List of publications

Peer-reviewed publications as first author:

1. I. Zanette, M. Bech, A. Rack, G. Le Duc, P. Tafforeau, C. David, J. Mohr, F. Pfeiffer, and T. Weitkamp, **Trimodal low-dose X-ray tomography**, submitted (2011).

2. I. Zanette, T. Weitkamp, S. Lang, M. Langer, J. Mohr, C. David and J. Baruchel **Quantitative phase and absorption tomography with an X-ray grating interferometer and synchrotron radiation**, *Physica Status Solidi A*, **208**, 2526 (2011).

3. I. Zanette, M. Bech, F. Pfeiffer, and T. Weitkamp, **Interlaced phase stepping in phase-contrast x-ray tomography**, *Applied Physics Letters*, **98**, 094101 (2011).

4. I. Zanette, T. Weitkamp, T. Donath, C. Rutishauser, and C. David, **Two-dimensional X-ray grating interferometer**, *Physical Review Letters*, **105**, 248102 (2010).

Peer-reviewed publications as co-author:

5. S. Rutishauser, I. Zanette, T. Weitkamp, T. Donath, and C. David, **At-wavelength characterization of refractive X-ray lenses using a two-dimensional grating interferometer**, *Applied Physics Letters*, **99**, 221104 (2011).

6. S. Rutishauser, I. Zanette, T. Donath, A. Sahlholm, J. Linnros, and C. David, **Structured scintillator for hard X-ray grating interferometry**, *Applied Physics Letters*, **98**, 171107 (2011).

7. T. H. Jensen, A. Böttiger, M. Bech, I. Zanette, T. Weitkamp, S. Rutishauser, C. David, E. Reznikova, J. Mohr, L. B. Christensen, E. V. Olsen, R. Feidenhans'l, and F. Pfeiffer, **X-ray phase-contrast tomography of porcine fat and rind**, *Meat Science*, **88**, 379 (2011).

8. L. Helfen, F. Xu, B. Schillinger, E. Calzada, I. Zanette, T. Weitkamp, and T. Baumbach, **A Novel Approach to Three-Dimensional Imaging of Flat Objects with Neutrons**, *Nuclear Instruments and Methods in Physics Research A*, **651**, 135 (2011).

9. P. Diemoz, P. Coan, I. Zanette, A. Bravin, S. Lang, C. Glaser, and T. Weitkamp, **A simplified approach for computed tomography with an X-ray grating interferometer**, *Optics Express*, **19**, 1691 (2011).

10. T. H. Jensen, M. Bech, I. Zanette, T. Weitkamp, C. David, H. Deyhle, R. Feidenhans'l, and F. Pfeiffer, **Directional x-ray dark-field imaging of strongly ordered systems**, *Physical Review B*, **105**, 214103 (2010).

11. G. Schulz, T. Weitkamp, I. Zanette, F. Pfeiffer, F. Beckmann, C. David, S. Rutishauser, E. Reznikova, and B. Müller, **High-resolution tomographic imaging of a human cerebellum: comparison of absorption and grating-based phase contrast**, *Journal of The Royal Society Interface*, **7**, 1665 (2010).

12. A. Rack, T. Weitkamp, I. Zanette, Ch. Morawe, A. Vivo Rommeveaux, P. Tafforeau, P. Cloetens, E. Ziegler, T. Rack, A. Cecilia, P. Vagovic, E. Harmann, R. Dietsch, and H. Riesemeier, **Coherence preservation and beam flatness of a single-bounce multilayer monochromator (beamline ID19-ESRF)** *Nuclear Instruments and Methods in Physics Research A*, **649**, 123 (2010).

Conference proceedings as first author:

13. I. Zanette, S. Rutishauser, C. David, and T. Weitkamp, **X-ray interferometry with two-dimensional gratings**, *AIP Conference Proceedings*, **1365**, 325 (2011).

14. I. Zanette, C. David, S. Rutishauser, and T. Weitkamp, **2D grating simulations for X-ray phase-contrast and dark-field imaging with a Talbot interferometer**, *AIP Conference Proceedings*, **1221**, 73 (2010).

Conference proceedings as co-author:

15. T. Weitkamp, I. Zanette, G. Schulz, M. Bech, S. Rutishauser, S. Lang, T. Donath, A. Tapfer, H. Deyhle, P. Bernard, J.-P. Valade, E. Reznikova, J. Kenntner, J. Mohr, B. Müller, F. Pfeiffer, C. David, and J. Baruchel, **X-ray grating interferometry at ESRF: applications and recent technical developments**, *AIP Conference Proceedings*, **1365**, 28 (2011).

16. T. Weitkamp, I. Zanette, C. David, J. Baruchel, M. Bech, P. Bernard, H. Deyhle, T. Donath, J. Kenntner, S. Lang, J. Mohr, B. Müller, F. Pfeiffer, E. Reznikova, S. Rutishauser, G. Schulz, A. Tapfer, and J-P. Valade, **Recent developments in X-ray Talbot interferometry at ESRF-ID19**, *Proceedings of SPIE*, **7804**, 780406 (2010).

17. G. Schulz, A. Morel, M. S. Imholz, H. Deyhle, T. Weitkamp, I. Zanette, F. Pfeiffer, C. David, M. Müller-Gerbl, and B. Müller, **Evaluating the microstructure of human brain tissues using synchrotron radiation-based micro computed tomography**, *Proceedings of SPIE*, **7804**, 78040F (2010).

18. J. Kenntner, T. Grund, B. Matthis, M. Boerner, J. Mohr, T. Scherer, M. Walter, M. Willner, A. Tapfer, M. Bech, F. Pfeiffer, I. Zanette, and T. Weitkamp, **Front- and backside structuring of gratings for phase contrast imaging with x-ray tubes**, *Proceedings of SPIE*, **7804**, 780408 (2010).

Talks, Seminars and Awards

Invited talks at conferences and workshops:

1. Title: *Instrumental Developments in Grating-based X-ray Imaging at the ESRF Beamline ID19*, International Workshop on X-ray and Neutron Phase Imaging, 5th - 7th March 2012, Tokyo (Japan).

2. Title: *High-sensitivity Phase Imaging with an X-ray Grating Interferometer*, **International Congress in X-ray Optics and Microanalysis (ICXOM21)**, 5th - 8th September 2011, Indaiatuba (SP-Brazil).

Seminars:

1. Title: *"One- and Two-dimensional X-ray Grating Interferometry at ESRF-ID19"*, seminar at **Technische Universität** München, 28th March 2011, Munich (Germany).

2. Title: *"Recent Developments in X-ray Imaging with a Grating Interferometer at the ESRF"*, seminar at the **Paul Scherrer Institute**, 23th November 2010, Villigen (Switzerland).

3. *"X-ray Imaging with a Grating Interferometer: Principles and Recent Developments at the ESRF"*, XSD Presentation at the **Advanced Photon Source**, 23th March 2010, Chicago (Illinois U.S.A.).

Awards:

1. **ESRF Young Scientist Award 2012** award given during the ESRF Users' Meeting 2012, 6th-8th February, Grenoble (France). The work has been presented with a lecture during the plenary session of the meeting.

2. **XRM2010 (a)** *Outstanding Poster Award* at the International Conference on X-Ray Microscopy in Chicago, 15th-20th August 2010 (Illinois U.S.A.).

3. **XRM2010 (b)** *Student Grant* for attending the International Conference on X-Ray Microscopy in Chicago, 15th-20th August 2010 (Illinois U.S.A.).

4. **SSD 2009** *Best Student Poster Award* at the Science and Students Days, 7th-9th October 2009, Val Cenis (France).

Acknowledgements

First and foremost, I want to thank my supervisors Timm Weitkamp and José Baruchel for giving me the opportunity to work on this exciting project and for their formative guidance during these three years. Thanks, Timm, especially for all the things you taught me on X-ray optics; thanks, José, especially for always indicating the right way when I most needed it.

I acknowledge the jury members of this thesis, for attentively reading this book and being present at my defense. In particular, I thank the referees Dr. Francois Polack and Prof. Atsushi Momose for their constructive comments.

My gratitude goes to Prof. Franz Pfeiffer for accepting to be in the jury of this thesis and for giving me opportunity of continuing my career at the Technische Universität München.

This thesis work has been performed within a successful collaboration with the Technische Universität München (TUM), the Laboratory of Micro- and Nanotechnology (LMN) of Paul Scherrer Institute, the Biomaterials Science Center (BMC) at the University of Basel and the Institute of Microstructure Technology (IMT) of Karlsruhe Institue of Technology.

I thank the group of Prof. Franz Pfeiffer from TUM, in particular Franz, Martin, Arne, Simone, Astrid, Julia and Marco for sharing their invaluable knowledge on phase-contrast imaging, for providing interesting samples and for creating a very nice atmosphere during beamtimes. Deep gratitude goes to Martin and Franz for fruitful discussions on interlaced phase-stepping methods.

I thank the LMN group of Dr. Christian David. Christian provided fundamental help in the first stages of the design and installation of the interferometer at ID19; he also warmly welcomed me at PSI and gave me the opportunity to perform formative experiments at his laboratory setups. Special thanks to Simon for our stimulating collaboration: I very much enjoyed experimenting, analysing data and writing papers with you.

My gratitude goes to the group of Prof. Bert Müller (BMC), especially to Bert, Georg, Sabrina and Hans for bringing extremely interesting scientific cases at ID19 and for bringing my attention to different imaging methods.

Many thanks to Dr. Jürgen Mohr, Johannes and Martin from IMT, for providing incredibly good gratings with impressive aspect ratios. The excellent performance of the interferometer at ID19 is largely due to your superb structures.

Thanks to Torben Jensen, formerly at the University of Copenhagen, for insightful discussions on directional dark-field imaging.

During this thesis, I had the opportunity to consult knowledgeable ESRF scientists; my gratitude goes to Eric Ziegler, Paul Tafforeau, Hélène Elleaume, Alexander Rack and Geraldine Le Duc for exciting discussions.

Thanks to two *magnifiques* ESRF engineers: P. Bernard and J.-P. Valade who helped in the different stages of the interferometer installation and, with their prompt and invaluable support, efficiently solved last-minute problems, making experiments possible even when I had lost all my hopes!

Parts of this book have been proof read by Michele, Maria, Alexander, Sophie and Pierre.. I thank you all for your kind help!

Last but not least, thanks to the ID19 team for creating a nice atmosphere at the working place and for the support, particularly strong and helpful in the last stages of this work. *Merci*, especially to Maria, Sophie, Carmen and Pei Dong.